Investigation of dielectric and optical properties of perovskite materials with possible applications in promising energy harvesting

THESIS SUBMITTED FOR THE DEGREE OF

DOCTOR OF PHILOSOPHY (SCIENCE)

OF

JADAVPUR UNIVERSITY

2024

BY

PAYAL SENGUPTA

DEPARTMENT OF PHYSICS

JADAVPUR UNIVERSITY,

KOLKATA 700032,

INDIA

Dedicated to. . .

My beloved Parents: Late Kamal Sengupta & Hasi Sengupta

Though you never got to see this,

But you're on every page Baba

&

My closest friend

Prof. (Dr.) Ruma Ray
Professor
Department of Physics
Jadavpur University
Kolkata-700032
India

CERTIFICATE FROM THE SUPERVISOR

This is to certify that the thesis entitled "**Investigation of dielectric and optical properties of perovskite materials with possible applications in possible energy harvesting**" submitted by **Ms. Payal Sengupta**, who got her name registered on **November 05, 2019 (Index no. 120/19/Phys./26)** for the award of **Doctor of Philosophy (Science) degree** of Jadavpur University, is absolutely based upon her own work under the supervision of **Prof. Ruma Ray** in the department of Physics, Jadavpur University, Jadavpur, Kolkata-700032 and that neither the results reported in this thesis not any part of it has been submitted for either any degree / diploma or any other academic award anywhere before.

Ruma Ray 02.05.2024

Dr. Ruma Ray
Professor
Department of Physics
Jadavpur University
Jadavpur, Kolkata-700 0

(Ruma Ray)
Signature of the supervisor

Acknowledgment

At last, the moment has come when I am going, to sum up, all the research work I have done in the last few years. At the edge of the submission of this dissertation, I would like to express my heartiest gratitude to my family members, teachers, and friends for their constant support and encouragement.

Foremost, I would like to convey my deepest gratitude to my supervisor Prof. (Dr.) Ruma Ray (Department of Physics, Jadavpur University, Kolkata, India) for her continuous support throughout my research work. She has always encouraged me to choose my research problems from the very first day. She made an amazing comfort zone in her research laboratory that helped me to shape my work in my own way. Every time, her insightful guidance and immense patience aided me to sort out problems, may they be related to research or else. Thank you so much Ma'am for being there, believing in me unconditionally, and allowing me to work under your supervision. I consider myself lucky to have a wonderful supervisor like you.

I am thankful to Dr. Subrata Sarkar (Department of Physics, Jadavpur University), the subject expert of my Ph.D. Research Advisory Committee, for his valuable input and feedback during my Ph.D. work.

I would like to express my sincere gratitude to Prof. Satyaranjan Bhattacharyya (senior professor and Head (retired) of Surface Physics and Material Science Division, Saha Institute of Nuclear Physics, Kolkata) for always inspiring me to become a good researcher and to achieve my goal. He has always guided me to choose the right way and helped me in doing some of the experimental research works related to this thesis.

My earnest gratitude goes to Prof. Sourav Giri (School of Physical Sciences, Indian Association for the Cultivation of Science, Kolkata) for providing his valuable feedback and allowing me to carry out some of the experimental research works in his laboratory.

I wish to thank Dr. Sachindranath Das (Department of Instrumentation Science, Jadavpur University) for his important suggestions regarding my Ph.D. work and for allowing me to use a few instruments in his research laboratory.

I wish to acknowledge Dr. Anar Singh (Department of Physics, University of Lucknow, Lucknow, India) for his valuable contribution to one of my research works.

I am grateful to Prof. Nabin Baran Manik (Department of Physics, Jadavpur University) for always inspiring me and allowing me to carry out a few experiments in his research laboratory.

I would like to thank all my senior and junior lab mates Sanchari Sarkar, Archita Mondal, Neepamala Giri, Simantini Majumder, Ashik Ikbal, and Arijit Ghosal for their harmonic cooperation throughout my Ph.D. tenure. I have nice memories with each of you. I would like to thank Dr. Priyabrata Sadhukhan (former Ph.D. scholar at the Department of Instrumentation Science, Jadavpur University) for being a kind senior and mentoring me in the initial days of my research life. I wish to express my thanks to Dr. Apurba Ray and Dr. Samik Saha (former Ph.D. scholars, Department of Instrumentation Science, Jadavpur University) for some constructive discussions related to my research work. I also want to thank Pradeepta Kumar Ghose (Ph.D. scholar, Indian Association for the Cultivation of Science, Kolkata) for his kind help with a few experimental measurements at IACS. I especially thank Roshni Begum and Sudip Kundu (Ph.D. scholars, Department of Material Science and Nanotechnology, Jadavpur University) for being there whenever I need any help. I would like to convey my heartiest thanks to Dipankar Sahoo, Arnab Kanti Karan, Subhra Rakshit, and Sudipta Sen (Ph.D. scholars, Department of Physics, Jadavpur University) for being amazing friends and seniors. Whenever I required any kind of support, may it be related to research or anything else, I found them to stand there. I thank Government of West Bengal for providing Swami Vievekananda Merit-Cum-Means (V3.0) (WBP191577101374) fellowship in the initial days of my research career, and University Grant Commission (UGC), Government of India for awarding me Savitribai Jyotirao Phule Single Girl Child Fellowship (SJSGC) (Award no. 202223-UGCES-22-GE-WES-F-7062) for the financial support. I am thankful to all the faculties and staffs of the Department of Physics, members of the research section, fellowship section, Dean Office, and Ph.D. cell in Jadavpur University for their support and assistance on various occasions.

Finally, I wish to share my heartiest gratitude to my beloved parents without whom I would not come this far. I lost my father when I was in B.Sc. 1st year, still I can imagine the shine in his eyes seeing his daughter writing her Ph.D. thesis. I used to aim to be an astronaut when I was a kid. My father told me a popular phrase at that time “Aim high so that even if you fall, you will float among stars”. That inspired my childish mind a lot. I always wanted to be as honest, kind, humble, courageous, and hard-working as him. I hope, one day, I shall make you proud. Today, when I look back, I can understand the pain behind his incomparable efforts

to give me a better life. The financial and emotional struggle we (me and Ma) have gone through after you left us Dad, made us very strong, and emotionally controlled individuals. I cannot express how much I feel for you Ma, by just writing a few lines on a piece of paper. Your countless efforts, continuous inspiration, unconditional love, and care give me the strength to fight against all odds and stand keeping my head straight. You were my very first teacher and to date, you are the best teacher I have ever come across. You are my best friend, my most secure place on earth. I hope, one day, I shall be able to gift you the tension-free, more comfortable life that you deserve. I cannot even think of my life without you.

I wish to share my happiness with my beloved grandparents (Late Brajagopal Dev, Usha Rani Dev). Dadu, you were my first role model. You pampered me and gave me unconditional love till your last breath. You always believed that one day your granddaughter would make you proud. Hope, you and baba are having good times in heaven and pouring blessings on me. I promise I will never let you down. Dida, I am grateful to you too for whatever you have done for me. I wish to express my gratitude to my maternal uncle (Partha Pratim Dev) for his contribution to my life.

Last but not least, I wish to thank my closest friend for being such an amazing support system throughout the years. Your continuous encouragement and inspiration always motivate me to run a long way. You never fail to keep faith in me. Truly, I wish to believe, “Grow old with me, and the best is yet to be”.

Payal Sengupta
02.05.2024

Jadavpur University
Kolkata
2024

Payal Sengupta

Synopsis

In the 21st century, green and renewable sources of energy have become a global concern not only to meet the rapidly growing power need due to the rapid urbanization but also to face various panicking challenges like energy calamities, limited stock of fossil fuels, unusual climate changes, frightening growth of environmental pollution caused by the usage of fossil fuels, etc. Among various sustainable energy sources, wind, tide, geothermal, etc. are used in heavy power grids to generate power in the range of mega to gigawatt. In recent years, the rapid progress in miniaturized devices, the Internet of Things (IoTs), and sensors has brought a revolution in the field of microelectronics. These miniaturized devices and sensors that have immense utilization in each corner of our day-to-day life as wearable biomedical devices, environmental monitoring sensors, climate monitoring sensors, etc. require minimal power to be operated. Acquiring abundant mechanical energy from our everyday life in the form of any kind of human motions, acoustic noises, vibrations etc. and converting it to electrical energy can be an ideal option to harvest sustainable, clean, maintenance-free energy that can not only run these low-powered sensors and devices but also the self-powering ability of these devices eliminate the necessity of external battery. These piezoelectric and triboelectric generators are lightweight, flexible, and thus wearable, portable, and self-powered that partially meet the power need. Solar energy, available in the maximum portion of the earth, is another important source of renewable energy. Thus, designing integrated devices that can harvest both solar and mechanical energy can be an optimum choice to serve wide purposes. Besides renewable energy harvesting, addressing the inflated energy requirements of modern society results in cutting-edge research interest in developing energy storage systems. Despite following two different working mechanisms, researchers have dedicated their tremendous efforts to the fabrication of sustainable energy sources that integrate energy harvesting and storage units in a single device. Commonly, a sustainable energy system comprises an energy harvesting unit, power management circuits, and an energy storing unit. The internal integration of energy harvesting and storing units into a sole unit eliminates the requirement for additional power management circuits. Hence, in recent years, the development of self-powered, self-charging devices has been of high interest.

Perovskite materials have gained immense attention among researchers during past decades owing to the unusual transport and magnetic properties of oxide perovskites,

fascinating optical properties of hybrid perovskites, long carrier diffusion length, tunable band gap, etc., and their utilization in a wide range of optoelectronic devices. It is required to study various intrinsic properties of the perovskites in detail to understand their potential in different application domains. Hence, the motivation of this dissertation is to extensively investigate the dielectric and optical properties of some potential perovskite systems and incorporate them in the fabrication of cost-effective, integrated energy harvesting devices.

Organic inorganic hybrid perovskites have drawn keen interest due to their inexpensiveness, interesting photovoltaic properties, simple synthesis process, etc. but facing some important issues that need to be worked on for commercial implementation like poor stability in the presence of moisture, UV-light, and high temperature. I have synthesized propylammonium lead halide ($C_3H_7NH_3PbX_3$, with X = I, Br) that exhibited excellent stability in the presence of moisture, temperature, and UV exposure. Sol-gel driven $C_3H_7NH_3PbI_3$ possessed a rod-like structure and an optimal band gap of ~ 2.38 eV. We have performed an extensive study on frequency-dependent dielectric properties of $C_3H_7NH_3PbX_3$, with X = I, Br for $273\ K \leq T \leq 373\ K$. $C_3H_7NH_3PbBr_3$ showed giant dielectric constant and appreciable conductivity. The impedance spectra were analyzed by considering the effect of grain and grain boundaries. The suppressed Nyquist plot at different temperatures, the asymmetric nature of the imaginary part of the electric modulus, etc. illustrated the non-Debye type nature of the samples that varied over the temperatures. The role of ionic conduction in the enhancement of conductivities of the samples at elevated temperatures was analyzed in detail. Moreover, we designed a UV photodetector using $C_3H_7NH_3PbBr_3$ that yielded satisfactory output.

Among various ferroelectric materials, polyvinylidene difluoride (PVDF) is one of the widely used polymers ascribing to its low cost, high piezo output, simple fabrication process, and ability to be designed in the desired shape. In PVDF, the non-polar α phase is predominant, in general. To bring out the dominance of the polar β phase that is responsible for ferroelectricity, various methods such as mechanical stretching, annealing at high temperatures, hydrated salt addition, etc. have been employed over the years. Among these practices, adding an appropriate external agent is the most convenient one. We incorporated $C_3H_7NH_3PbI_3$ in PVDF in different proportions (3.21, 4.76, and 6.20 wt %) to form nanofibers by the method of electrospinning. Electrospinning was chosen to prepare homogeneous, flexible, sensitive nanofibers with a significant amount of β phase within it. It has been evaluated that 4.76 wt% of $C_3H_7NH_3PbI_3$ decorated PVDF nanofiber contains significantly high electroactive phase component ~ 92.5 %, remarkable crystallinity with superior

piezoelectric coefficient ~ 138 pC/N. The obtained band gap of the aforementioned nanofiber (~2.2 eV) ensured that the intrinsic properties of the perovskite remained intact. The optically active nanofiber was then used to fabricate a flexible, ultra-sensitive piezoelectric nanogenerator that produced a remarkably high ~ 60 V open circuit voltage and 27.5 μA short circuit current under hammering with a free hand. The generated power was sufficient to light up several green and blue LEDs. Moreover, the developed power was stored in a commercially available capacitor that was further used to charge a digital wristwatch. The device showed excellent stability and a high energy conversion efficiency of ~ 42.03 %. We have also designed a piezo-active photodetector using the aforesaid composite and obtained satisfactory performance. The sensitivity, portability, and significant yield confirm its efficacy in the IoTs, sensors, etc.

Next, we synthesized different self-poled flexible films of the same perovskite and PVDF in larger proportions (5, 10, 15, 20 wt %) than that of nanofibers. The inclusion of $C_3H_7NH_3PbI_3$ in PVDF in 15 wt % produced appreciably high ferroelectric phase content of ~ 66.7 %, a degree of crystallinity of ~ 69 % with the polymer matrix. This composite was employed in the fabrication of piezoelectric energy harvester that produced 80 V open circuit voltage and 17.8 $\mu A/cm^2$ short circuit current when subjected to the free hand hammering. The obtained outcome was substantially large compared to that of a reference energy harvester made of neat PVDF. The flexibility of the piezo energy harvester provided an added advantage for the film to be used as a wearable bio-sensor. A piezo-active photodetection ability of the same composite was also successfully explored and investigated in detail.

Here, we fabricated self-charging, flexible piezoelectric supercapacitor that can not only convert the mechanical energy into the electrical energy but also store the energy as a sole unit. Despite being potential candidates, the abovementioned perovskites contain toxicity content lead though the amount of lead is quite low in the ultimate composite and the fabricated devices. To address the eco-friendly need, we have synthesized lead-free $NdMnO_3$ nanoparticles via sol-gel method and incorporated them in PVDF in 3, 5, 7, and 10 wt % to prepare self-poled films. The film containing 7 wt % of $NdMnO_3$ nanoparticles in PVDF possesses an enhanced β phase content of 89.71 %. To have a glimpse of the tribo effect, we designed a piezoelectric-triboelectric hybrid nanogenerator following the configuration Cu electrode/ $NdMnO_3$@PVDF / Air gap (~100 μm)/ PDMS layer/ Cu electrode that produced enormously large open circuit voltage ~ 160 V in response to free hand hammering. The intrinsic effect of piezoelectricity of the $NdMnO_3$@PVDF films only was isolated by

minimizing the tribo effect and we fabricated piezoelectric nanogenerator using $NdMnO_3$@PVDF films with sincere care to get rid of any trapped air bubbles between the films and the electrodes. The piezo nanogenerator exhibited a significant response of open circuit voltage ~50 V and short circuit current ~30 μA under periodic dynamic strain. The output response assured its utility in IoTs. The generated energy was stored in commercially available capacitors and was sufficient to illuminate several green and blue LEDs. Furthermore, the piezoelectric generator revealed excellent stability even in a water medium. Moreover, the degradation of a dye by piezocatalysis exhibited by this film made it a multifunctional composite. The potential of self-charging piezoelectric supercapacitor using $NdMnO_3$@PVDF as a separator has also been explored which demonstrated energy storing behavior under the periodic mechanical deformation. The areal capacitance was significant ~ 41.37 mF cm^{-2} and 99% of capacitance retention after 2000 cycles. The study of the overall performance of the multifunctional device opens a window for the fabrication of self-powered piezoelectric wearable devices in union with supercapacitors.

Payal Sengupta
02.05.2024

List of publications included in the thesis

1. **Payal Sengupta**, Priyabrata Sadhukhan, Samik Saha, Sachindranath Das, Ruma Ray, Improved energy harvesting ability of $C_3H_7NH_3PbI_3$ decorated PVDF nanofiber based flexible nanogenerator, **Nano Energy,** 109 (2023) 108277.

2. **Payal Sengupta**, Ruma Ray, Tailoring of dielectric and transport properties of $C_3H_7NH_3PbI_xBr_{3-x}$, **Materials Letters,** 302 (2021) 130456.

3. **Payal Sengupta**, Priyabrata Sadhukhan, Apurba Ray, Souvik Mal, Anar Singh, Ruma Ray, Satyaranjan Bhattacharyya, Sachindranath Das, Influence of activation energy on charge conduction mechanism and giant dielectric relaxation of sol-gel derived $C_3H_7NH_3PbBr_3$ perovskite; Act as high performing UV photodetector, **Journal of Alloys and Compounds,** 892 (2021) 162216.

4. **Payal Sengupta**, Priyabrata Sadhukhan, Apurba Ray, Ruma Ray, Satyaranjan Bhattacharyya, and Sachindranath Das, Temperature and frequency dependent dielectric response of $C_3H_7NH_3PbI_3$: A new hybrid perovskite, **Journal of Applied Physics**, 127, 204103 (2020).

5. **Payal Sengupta,** Arijit Ghosal, Ruma Ray, Probing the piezoelectric energy harvesting to self-charging storage process using $NdMnO_3$@PVDF composite: A lead-free piezo-supercapacitor (**under peer review**).

6. **Payal Sengupta,** Dipankar Sahoo, Ashik Ikbal, Ruma Ray, $C_3H_7NH_3PbI_3$@PVDF porous piezo-active film: A wearable phototronic potential bio-sensor (**communicated**).

Other publications

7. Dipankar Sahoo, **Payal Sengupta**, Arnab Kanti Karan, Nabin Baran Manik, Improvement in conductivity of lead-free $CH_3NH_3SnI_3$ perovskite thin film using multi-walled carbon nanotubes as a transporter, **Surfaces and Interfaces**, 2023, 41, 103222.

8. Neepamala Giri, Bohnni Shikha Biswas, **Payal Sengupta** and Ruma Ray, Exchange bias and magnetic memory effect in hole doped $Nd_{0.78}Sr_{0.22}CoO_3$ nanoparticles, **RSC Advance**, 2022, 12, 26470.

9. Priyabrata Sadhukhan, Dibyendu Ghosh, **Payal Sengupta**, Sayan Bhattacharyya, and Sachindranath Das, Unraveling the Charge Transport Mechanism in Mechanochemically Processed Hybrid Perovskite Solar Cell, **Langmuir** 2021, 37, 5513−5521.

10. Priyabrata Sadhukhan, Anway Pradhan, Suman Mukherjee, **Payal Sengupta**, Atanu Roy, Satyaban Bhunia, and Sachindranath Das, Low temperature excitonic spectroscopy study of mechano-synthesized hybrid perovskite, **Applied Physics Letter**, 2019, 114, 131102.

11. Subhasish Patra, **Payal Sengupta**, Apurba Ray, Atanu Roy, Sachindranath Das, Discrete Dipole Approximation for Calculating Optical Properties of ZnO nanoparticles and ZnO-PVP composites, **Ceramic International**, 2018, 44, 14236-14241.

Conference contribution

1. Enhanced performance of self-powered photoactive piezoelectric energy harvester using organohalide perovskite decorated PVDF nanofiber, **Payal Sengupta**, Ruma Ray, Condensed Matter Research Centre & Department of Physics, Jadavpur University, Kolkata, India, February 7, 2024 (Oral presentation). **Selected for best oral presentation award.**
2. Improved photoactive piezoelectric performance of flexible nanogenerator using methylammonium bismuth iodide embedded PVDF film, **Payal Sengupta**, Ruma Ray, 6th Regional Science and Technology Congress, University of Calcutta and Department of Science and Technology and Biotechnology, Government of West Bengal, India, December 22, 2023 (Oral presentation).
3. A flexible piezo-triboelectric energy harvester employing $NdMnO_3$-PVDF composite: A promising lead-free piezocatalyst, **Payal Sengupta**, Ruma Ray, 4th International Conference on Advanced Functional Materials for Sustainable Energy Applications, Department of Physics, Koneru Lakshmaiah Education Foundation (Deemed to be university), India, December 6-8, 2023 (Oral presentation).
4. $C_3H_7NH_3PbI_3$ decorated PVDF electrospun nanofiber: A potential candidate for self-powered photoactive piezoelectric energy harvester, **Payal Sengupta**, Ruma Ray, Young Physicists' Colloquium, Indian Physical Society, India, August 24-25, 2023 (Oral presentation).
5. Study on temperature dependent dielectric and transport properties of K-doped $NdMnO_3$ nanoparticles, **Payal Sengupta**, Ruma Ray, 7th International Conference on Nanoscience and Nanotechnology, Department of Science and Nanotechnology, SRM Institute of Science and Technology, March 27-29, 2023 (Oral presentation).
6. Highly stable organo-halide perovskite regulated β phase formation in PVDF film and its potential efficacy as mechanical energy harvester and photodetector, **Payal Sengupta**, Ruma Ray, Internation e-symposium on Materials Development and Scale-up for Membrane Separation, Sensing, Energy and Biological Applications (MDS-MESB), Department of Chemical Engineering, SRM Institute of Science and Technology, Kattankulathur, India, January 24-25, 2023. (Poster presentation)
7. Tailoring of dielectric and transport properties of $C_3H_7NH_3PbI_xBr_{3-x}$, **Payal Sengupta**, Ruma Ray, 6th International Conference on Nanoscience and Nanotechnology,

Department of Physics and Technology, SRM Institute of Science and Technology, Kattankulathur, India, February 01-03, 2021 (Poster presentation).

Table of Contents

Motivation and arrangement of the thesis

Motivation and objectives

The day-by-day increasing power needs across the globe and the limitation of fossil fuels ignite the requirement for renewable energy sources. Nowadays, there is rapid progress in microelectronics and sensors that are widely used in different segments as wearable biomedical devices, environmental monitoring sensors, climate monitoring sensors, etc., and need minimal power to run. Mechanical energy is the most abundant sustainable source of energy in our surroundings. Therefore, it can be an ideal choice to harvest abundant mechanical energy that we can gather from various kinds of vibration, noise, human motion, etc. of our daily life and convert it to electrical energy to run these low-powered sensors. These self-powered, flexible sensors often require photodetection for intended functioning. Solar energy is another sustainable source that is abundant in the maximum portions of the earth. In the pace of solar energy harvesting, organic-inorganic hybrid perovskites (OIHP) that are considered to be 3rd generation photovoltaic materials have already set a benchmark in the solar cell domain in a few years owing to their several fascinating properties such as easy synthesis process, cost-effectivity, tunable band gap, long charge diffusion length, good photovoltaic properties, etc. These promising optically active OIHPs need to be studied more to cultivate their potential in energy harvesting devices other than solar cells. On the other hand, rare earth oxide perovskites have garnered immense attention over the last decades ascribing to their abundant physical properties like magnetic ordering, interesting transport properties, etc. and potential usage in magnetic storage media, spintronics, ferroelectromagnets, etc. The interesting behavior of these perovskites motivates me to cultivate their potential in the development of multifaceted energy harvesting devices. Besides renewable energy harvesting and conversion, ambient energy storage is another vital research topic to deal with the energy challenges. Despite following two different mechanisms, the integration of both energy harvesting and storage devices in a sole unit is of utmost importance.

In this dissertation, I have performed a detailed analysis of the compositional, optical, and dielectric response of different types of perovskite materials to construct a path of understanding their intrinsic properties that can add remarkable values in energy harvesting,

especially in mechanical and solar, and storing. Polyvinylidene difluoride (PVDF) is a widely used bio-degradable, inexpensive piezoelectric polymer that consists of four phases α, β, γ and δ. Among these phases, α is the non-electroactive and predominant one whereas the polar β phase is the electroactive component. To bring out the dominance of the β phase, assisting appropriate filler within PVDF is one of the most convenient procedures. I have incorporated different perovskite materials as external fillers in PVDF not only to enhance the β phase formation required for significant piezoelectric response but also to utilize the intrinsic characteristics of the perovskites to fabricate versatile devices. Therefore, the main objectives of this dissertation are

- ♠ To perform an extensive study on several important properties such as impedance and dielectric, ionic conduction, optical, etc. of some promising perovskite materials,
- ♠ To analyze the experimental outcomes with different theoretical models,
- ♠ To fabricate and analyze the output performance of versatile energy harvesting devices based on these perovskites incorporated PVDF composites.
- ♠ To design integrated self-charging energy harvester cum storage unit employing the aforesaid composites.

Organization of the thesis

This dissertation consists of nine chapters as discussed below.

Chapter 1: Introduction

This chapter provides a broad, general overview of different types of perovskite materials, their properties, and wide applications. Moreover, this chapter includes the basic concepts of piezoelectric, triboelectric, and solar energy harvesting and storage.

Chapter 2: Literature review

This chapter focuses on the literature review that includes the national and international status of the proposed research work.

Chapter 3: Methods and characterization

This chapter demonstrates the methods we used in the proposed work to synthesis the chosen perovskites and the perovskite decorated PVDF composites. Moreover, the working principle

along with the instrumentation of all the characterization tools that we have utilized to carry out this research work is explained in this chapter.

The following chapters explain the results and discussions we obtained in this work.

Chapter 4: Temperature and frequency dependent dielectric response of $C_3H_7NH_3PbI_3$: A new hybrid perovskite

In this chapter, we report the extensive study on temperature and frequency dependent dielectric properties of sol-gel derived propylammonium lead iodide ($C_3H_7NH_3PbI_3$), an OIHP following generic formula ABX_3 (A denotes the organic cation, B represents the inorganic component and X refers to the halogen). This hybrid perovskite exhibits appreciable stability in the presence of moisture. Moreover, the optimal energy band gap ~ 2.38 eV of this perovskite affirms its potential in optoelectronic applications. The variation of ionic conduction, AC conductivity, electric modulus, and the dielectric response of the sample with frequency (10 Hz $\leq$ f $\leq$ 8 MHz) as well as temperature (273 K $\leq$ T $\leq$ 373 K) has been analyzed in detail.

Chapter 5: Influence of activation energy on charge conduction mechanism and giant dielectric relaxation of sol-gel derived $C_3H_7NH_3PbBr_3$ perovskite; Act as high performing UV photodetector

In this work, we synthesized propylammonium lead bromide ($C_3H_7NH_3PbBr_3$) via sol-gel method and we report a study on the dielectric behavior and conductivity of the sample over a wide range of frequency (4 Hz $\leq$ f $\leq$ 8 MHz) and temperature (273 K $\leq$ T $\leq$ 373 K). The optimal energy band gap and thermal stability analysis ensure the capability of the material in device fabrication. Possessing a wide band gap, this perovskite fascinatingly serves as UV detector. Moreover, this perovskite is found to achieve a giant dielectric constant at room temperature. Enhancement of dielectric constant, conductivity along with reduction of dielectric loss make this perovskite a potential candidate in energy harvesting.

Chapter 6: Tailoring of dielectric and transport properties of $C_3H_7NH_3PbI_xBr_{3-x}$

Here, we report a comparative study on the dielectric behavior and improved conductivity of the $C_3H_7NH_3PbI_xBr_{3-x}$ at various temperatures. It has been found that at elevated temperatures, the conductivity of $C_3H_7NH_3PbBr_3$ is 10 times that of $C_3H_7NH_3PbI_3$.

Chapter 7: Improved energy harvesting ability of $C_3H_7NH_3PbI_3$ decorated PVDF nanofiber based flexible nanogenerator

In this chapter, we incorporated $C_3H_7NH_3PbI_3$ in different concentrations (3.21, 4.76, and 6.1 wt %) in PVDF matrix to produce flexible, lightweight nanofibers by the method of electrospinning. The perovskite-embedded PVDF nanofibers possess significantly enhanced β phase content along with a remarkably high piezoelectric coefficient in comparison with neat PVDF. 4.76 wt% $C_3H_7NH_3PbI_3$ decorated PVDF exhibits improved crystallinity, elastic properties, etc. that distinctly reflects in the striking response of piezoelectric energy harvester based on the aforesaid composite nanofiber. The concerned piezoelectric nanogenerator is flexible, ultra-sensitive, and highly stable ensuring its utility as wearable sensors, IoTs. The device not only detects the vibration even in the ultrasonic range but also exhibits an exotic mechano-sensitivity. Furthermore, the energy conversion efficiency of this device is very high ~ 42.03 %. The generated open circuit voltage, short circuit current by the device under periodic hammering with a free hand is adequate to generate enough power required to light up several green and blue LEDs, as well as a digital wristwatch. This generated electricity is further stored in several commercially available capacitors. The aforesaid composite (4.76 wt% $C_3H_7NH_3PbI_3$@PVDF) was further used to form porous, self-polarized films that were employed in the fabrication of a well-responded piezo-active photodetector. Thus, we perform a detailed study of the performance of a multifaceted device as mentioned.

Chapter 8: $C_3H_7NH_3PbI_3$@PVDF porous piezo-active film: A wearable phototronic potential bio-sensor

Here, we formed highly porous films using different wt % of $C_3H_7NH_3PbI_3$ in PVDF (5, 10, 15, 20 wt %) to investigate the enhancement of ferroelectric phase content within the polymer matrix. It has been observed that the piezoelectric energy harvester based on 15 wt % of $C_3H_7NH_3PbI_3$@PVDF yields superior response under different applied dynamic strains. The

flexibility of the energy harvester assures their wearability and utilization as a potential bio-sensor. This particular composite is further used to fabricate piezo-active photodetector that performs quite satisfactorily under irradiation with white light. Hence, this report contains an elaborate analysis of the response and performance of the multi-folded device.

Chapter 9: Environmental friendly multifunctional energy harvester along with energy storage application of an oxide perovskite composite

In this chapter, to avoid the toxicity content of the hybrid perovskite, we synthesized rare earth oxide perovskite, $NdMnO_3$, via sol-gel method and encapsulated this perovskite in PVDF in different wt % (3, 5, 7, 10 wt %) to fabricate mechanical energy harvesters (hybrid piezoelectric-triboelectric generator). The addition of 7 wt % of $NdMnO_3$ in PVDF significantly improved the content of the polarized β phase. To evaluate the piezoelectric contribution of the $NdMnO_3$@PVDF composite, the piezoelectric coefficient was measured and observed as remarkably high. Moreover, the composite assures its efficacy as a promising piezocatalyst for dye degradation. The corresponding hybrid piezoelectric-triboelectric nanogenerator exhibits substantially high output response under free hand hammering. To isolate the sole contribution of piezoelectricity, we designed piezoelectric nanogenerators that also produced improved output under different applied forces such as hammering with various lightweight objects, acoustic vibrations, etc. One of the most interesting features is the excellent stability of the device even after drowning in water. The impressive outcomes of the device ensure its utility as mechanical energy harvester. Furthermore, a self-charging piezoelectric supercapacitor was constructed using the same composite that exhibited significant performance assuring its potential as self-charging sensor.

Chapter 10: General Conclusion

This chapter includes a general conclusion of this dissertation.

CHAPTER 1

1. Introduction

This chapter draws an outline and overview of the importance and development of different perovskite materials. The chapter also provides a general understanding of the contribution of different properties of the perovskites in renewable energy harvesting in the form of polymer composites.

1.1. Perovskites

Following the discovery of calcium titanium oxide or calcium titanate ($CaTiO_3$) in 1839, German mineralogist Gustav Rose referred to this mineral as "perovskite" after the Russian mineralogist Lev Perovski [1]. Later, several compounds having analogous crystal structures to that of $CaTiO_3$ such as $BaTiO_3$ were discovered rapidly. Nowadays, the word "perovskite" is used as a general term to describe crystal structures that

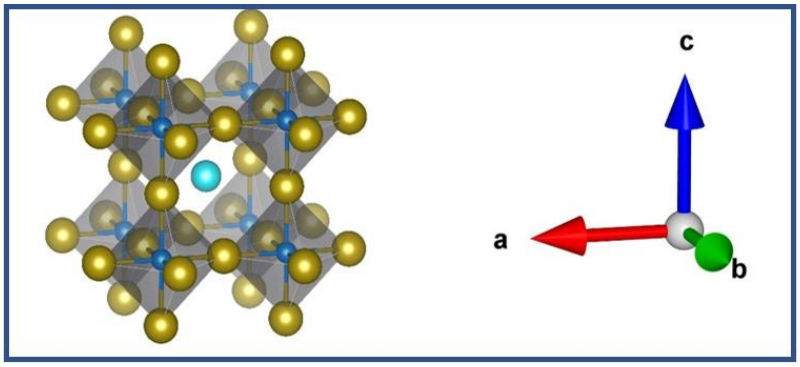

Fig. 1.1. Schematic diagram of a perovskite structure

are similar to $CaTiO_3$. The generic chemical formula that the perovskite structure follows is ABO_3 or ABX_3 within which the A-sited cation sits at the body centre position and the B-sited cation occupies the eight corners of the lattice forming the BX_6 or BO_6 octahedron as shown in Fig. 1.1 [2]. The structure ABX_3 categorizes the halide perovskites where X represents the halide anions. A new compound possessing ABO_3 or ABX_3 structure can be termed as "perovskite" if the compound satisfies Goldschmidt tolerance factor (t) proposed by Victor Goldschmidt [3].

$$t = \frac{R_A + R_X}{\sqrt{2}(R_B + R_X)} \qquad (1.1)$$

Here, R_A, R_B, R_X refers to the ionic radius of A-sited cation, B-sited cation, and X-sited anion, respectively. The value of t for an ideally packed perovskite is 1. However, a compound can be named "perovskite" if the value of t lies between 0.7 to 1.1. Another parameter referred to as the "Octahedral factor" ($m = \frac{R_B}{R_X}$) determines the deformation of the perovskites. Therefore, the ionic radius of the ions forming the perovskite materials should be organized in such a way as to form a stable compound. Any slight deformation or structural defect can bring a remarkable change in the intrinsic properties such as optical, structural, dielectric, etc. of the perovskite materials. Therefore, the optoelectronic, electrical properties of the perovskite materials can be tuned by intended deformation. Thus, perovskite materials can be considered a class of a wide range of compounds that can be categorized into different types depending on the type of constituent elements.

1.2. Classification of perovskite

Perovskite materials can be classified into different categories as shown in Fig. 1.2 based on their compositions. Compositional changes can bring change to the different properties of the perovskites.

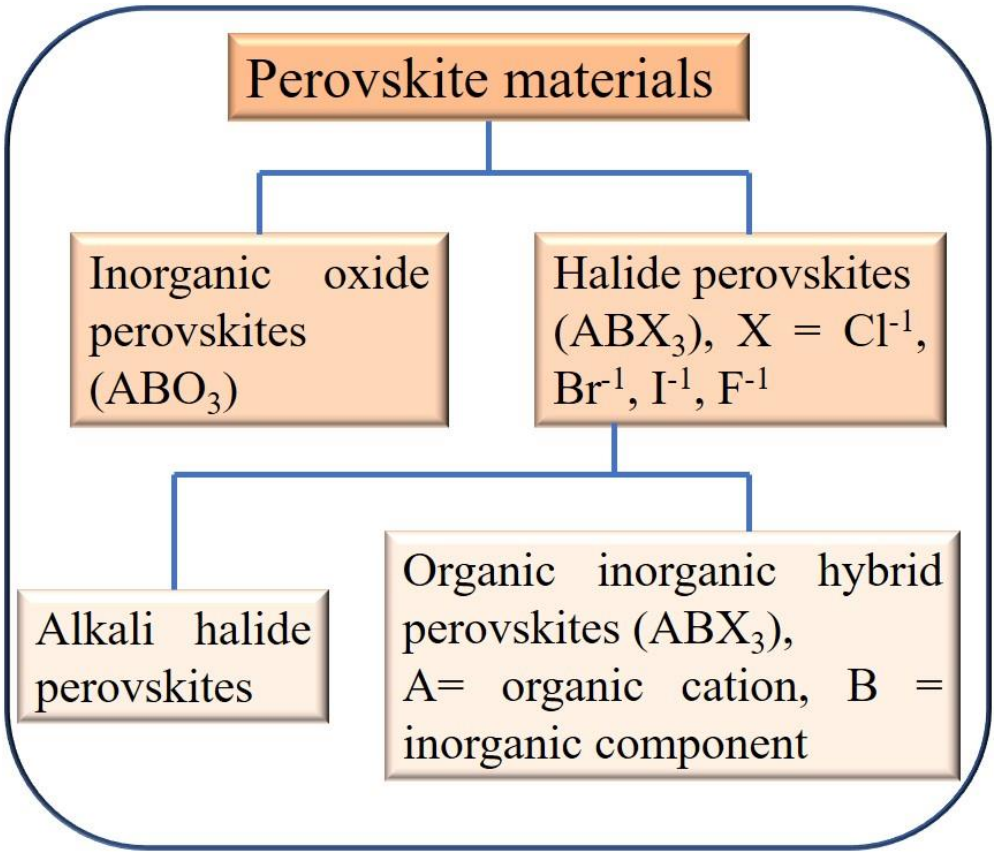

Fig. 1.2. Classification of perovskite materials

1.2.1. Oxide perovskites

Over the years, oxide perovskites such as rare earth manganates, alkaline earth stannates, etc. have gained popularity among researchers owing to their different merits and a variety of physical properties such as [4–9]

- ♠ High stability
- ♠ Excellent magnetic and electrical properties
- ♠ Superconductivity
- ♠ Metal-insulator transition
- ♠ Photovoltaic effect
- ♠ Ferroelectricity
- ♠ Transparent conductivity
- ♠ Long carrier diffusion length, etc.

Besides extensive studies, these oxide perovskites have wide applications in catalysis, high-temperature superconductors, giant magnetoresistance devices, ferroelectricity, magnetic storage media, sensors, spintronics, etc. The ferroelectricity and non-toxicity content of these perovskites lead to expanding their utility in energy harvesting devices. However, these perovskites are very expensive and follow a prolonged and complicated synthesis process.

The emergence of halide anions in place of oxygen ions has brought a significant change in the perovskite domain.

1.2.2. Organic-inorganic hybrid perovskites (OIHPs)

The coexistence of organic and inorganic cations in OIHP brings the intriguing properties of both components. These materials have been in the limelight over the past few years ascribing to their different qualities as mentioned below [10,11]

- ♠ Inexpensive
- ♠ High light absorption coefficient
- ♠ Long charge diffusion length
- ♠ High power conversion efficiency
- ♠ Tunable band gap
- ♠ Easy synthesis process

- Structural versatility, etc.

These OIHPs are widely used in various optoelectronic devices like light emitting diodes (LEDs), solar cells, lasers, photodiodes, X-ray detectors, etc.[12] Moreover, nowadays, extensive research is carried out globally to utilize the aforesaid qualities of the OIHPs to develop different kinds of energy harvesting devices. Despite these advantages, the main disadvantage of these OIHPs is the stability issue of these materials in the presence of moisture, temperatures, and UV light. This issue can be addressed by either changing the alkylammonium cation or substituting the halogen anion. These structural changes can bring a lot of change in the electrical as well as optoelectronic properties of the OIHPs that on the other may be an added advantage in the fabrication of multifaceted energy harvesting devices.

1.3. Dielectric properties and ionic conduction

An ideal dielectric is an electrical insulator that can be polarized by the influence of an applied electric field. Under the application of an external electric field, charges inside the material shift from their average equilibrium position giving rise to polarization. Therefore, positive, and negative charges move in the opposite direction leading to the formation of an internal electric field that reduces the effective field within the dielectric itself.

As previously mentioned, perovskites are very rich in different material properties. These materials host both ionic and electronic conductivity. Impedance spectroscopy is frequently used to perform a thorough analysis of the charge transport mechanism, dielectric behavior over a wide range of frequency and temperature, ionic movement, the contribution of grain and grain boundary over the total impedance more precisely recombination resistance, etc. of the sample. The dielectric properties of a material deal with the storage and dissipation of the electrical energy of the material. The formation and the orientation of the dipole moment in the presence of an external electric field play a key role in the polarization of the dielectric molecules.

a) Electronic polarization

If in a dielectric material, the molecules generating elementary dipole moments consist of neutral particles such as atoms, then in the presence of an external electric field, positive and negative charges (electrons and nucleus) get displaced producing an “induced dipole moment.”.

b)Ionic polarization

If in a dielectric material, the molecules producing elementary dipole moments comprise ions of opposite charges, then in the presence of an electric field, the positively charged ions move in the direction of the electric field whereas the negatively charged ion moves opposite to the direction of the electric field. Thus, the displacement of the ions initiates “ionic polarization”.

c) Orientational polarization

The asymmetric charge distribution between the different atoms of the same molecule introduces permanent dipole moments inside the molecules of a dielectric material. In the presence of an external electric field, the permanent dipole moments rotate into the direction of the applied field inducting a polarization.

d)Interfacial polarization

Interfacial polarization holds an essential role in the enhancement of dielectric constant in the low-frequency region. According to Maxwell-Wagner's interfacial polarization theory, dielectric materials are composed of two layers ~ of highly conducting grain separated by a poorly conducting grain boundary. As a result, charge carriers get trapped at the interface of grain boundaries to restrict the charge flow. In this polarization, the exchange of electrons between the ions of the same molecules occurs. The deformities and imperfections influence the alternation of the position and distribution of positive and negative charge carriers. Under the action of the electric field, positive and negative charges move towards the negative and positive poles of the electric field giving rise to a large number of dipole moments.

To perform the detailed analysis of the dielectric behavior along with ionic conduction of the sample, an AC signal was applied across the material under test to measure the complex impedance ($Z^* = Z' - jZ''$) at different frequencies and temperatures. Cole-Cole plot or Nyquist plot (imaginary impedance component (Z'') is plotted against the real impedance component (Z')) is a very important tool not only to figure out the total bulk impedance of the sample but also to determine the Debye/non-Debye type nature [13]. The individual contribution of grain, grain boundary, and electrode-material interface to the total impedance of the sample can be resolved from Maxwell-Wagner equivalent circuit model as displayed in Fig. 1.3.

$$Z'(\omega) = \frac{R_g}{[1+(\omega R_g C_g)^2]} + \frac{R_{gb}}{[1+(\omega R_{gb} C_{gb})^2]} \qquad (1.2)$$

$$Z"(\omega) = \frac{\omega C_g R_g^2}{[1+(\omega R_g C_g)^2]} + \frac{\omega C_{gb} R_{gb}^2}{[1+(\omega C_{gb} R_{gb})^2]} \quad (1.3)$$

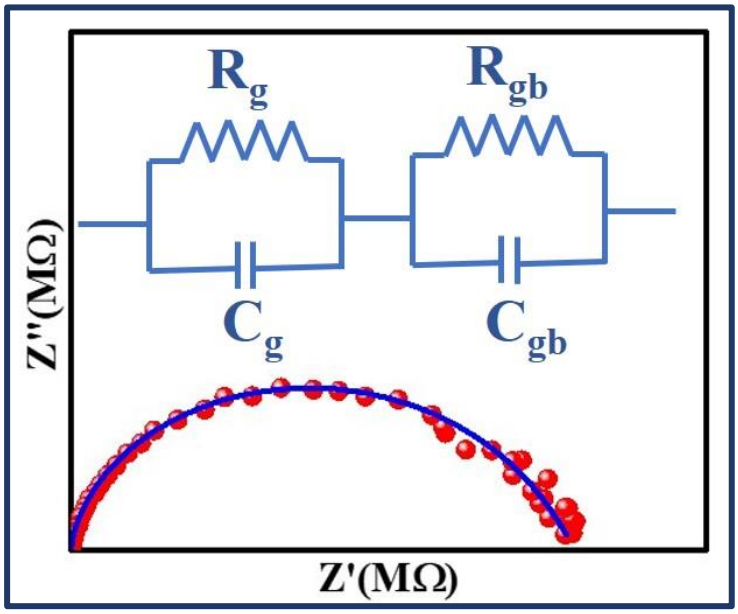

Fig. 1.3. Cole-cole plot and the equivalent Maxwell-Wagner circuit.

Here, R_g, R_{gb}, C_g and C_{gb} represent the grain resistance, grain boundary resistance, grain capacitance, and grain boundary capacitance, respectively. The complex dielectric response of the sample can be expressed as $\varepsilon^* = \varepsilon' - j\varepsilon"$.

$$\varepsilon'(\omega) = \frac{Z"}{\omega C_0 (Z'^2 + Z"^2)} \quad (1.4)$$

$$\varepsilon"(\omega) = \frac{Z'}{\omega C_0 (Z'^2 + Z"^2)} \quad (1.5)$$

Here, $C_0 = \frac{\varepsilon_0 A}{L}$, ε_0 is the permittivity in vacuum (8.854×10^{-14} F/m), A and L represent the effective area and thickness of the sample.

Electric modulus (M^*) is used to investigate the conduction relaxation of the sample.

$$M^* = \frac{1}{\varepsilon^*} = \frac{1}{\varepsilon' + j\varepsilon"} = \frac{\varepsilon'}{\varepsilon'^2 + \varepsilon"^2} + \frac{\varepsilon"}{\varepsilon'^2 + \varepsilon"^2} \quad (1.6)$$

Maxwell-Wagner proposed circuit model (comprising of a parallel combination of resistance and capacitance) is one of the most recognized models to fit the imaginary and real part of the dielectric permittivity or electric modulus. Modified Kahlrausch-William-Watts functions (KWW) were used to determine the deviation of the sample from the ideal Debye-type nature. Electrical conductivity (σ_{ac}) of the sample was evaluated from

$$\sigma_{ac} = \omega \varepsilon_0 \varepsilon' tan\delta \quad (1.7)$$

Here, $tan\delta$ refers to the loss tangent of the sample.

The ionic conduction that plays a key role in the AC and DC conductivity of the sample can be explained by the jump relaxation model (JRM). Using Jonscher's power law, the individual contribution of AC and DC conductivity over the whole conduction mechanism can be evaluated. Activation energy that influences the ionic movement of the samples can also be computed.

1.4. Mechanical and solar energy harvesting

Utilizing renewable sources of energy to produce power is not a choice today, it has become an ultimate necessity to provide the rising power need due to the worldwide rapid urbanization and to fight against

- Limited stock of fossil fuels
- Energy calamities
- Environmental pollution that caused by excessive usage of fossil fuels, etc.

The most acquainted sustainable energy sources such as solar, wind, hydro, geothermal, etc. [14] are widely used in power grids to accomplish the requirement in mega to giga-watt power scale. At the edge of modernization, miniaturized devices, IoTs, MEM-based sensors, etc. [15] are required on a large scale in each segment of mankind. These devices need to be recharged at a certain interval and can be run on nominal power. Here, mechanical energy harvesting can play a remarkable role. Scavenging mechanical energy from our surroundings especially from our day-to-day lives in the form of human motion (walking, talking, running), Acoustic noise, vehicle vibrations, etc., and converting it to electrical energy can be considered to be a sustainable solution to run these low-powered sensors and miniaturized devices. Moreover, the generation of self-power within the device leads to the elimination of the external battery portion that on the other hand, reduces expenses, and pollution and initiates hassle-free operation. Another source of energy i.e. solar energy is the most abundant in the maximum portions of the world, especially in a tropical country like India. Therefore, harvesting solar energy is a clean, biocompatible, and economic choice. The zero-emission solar cell has already built a mass opening in most developed countries. In India also, electric vehicles, and solar firms get huge financial support through government subsidies. This solar energy can also be integrated into mechanical energy to design multipurpose devices that we often require for various purposes, especially in the biomedical domain. The sensors about

which we have already talked, frequently require photodetection. Thus, harvesting mechanical and solar energy individually or simultaneously as an integrated unit can be an optimum solution for the required power production.

1.5. Fundamentals of piezoelectricity

The word "piezoelectricity" comes from the Greek word "piezein" which means squeeze or press and "electron" which means "amber". The piezoelectricity or piezoelectric effect is defined as a linear electromechanical interaction between the mechanical and electrical states

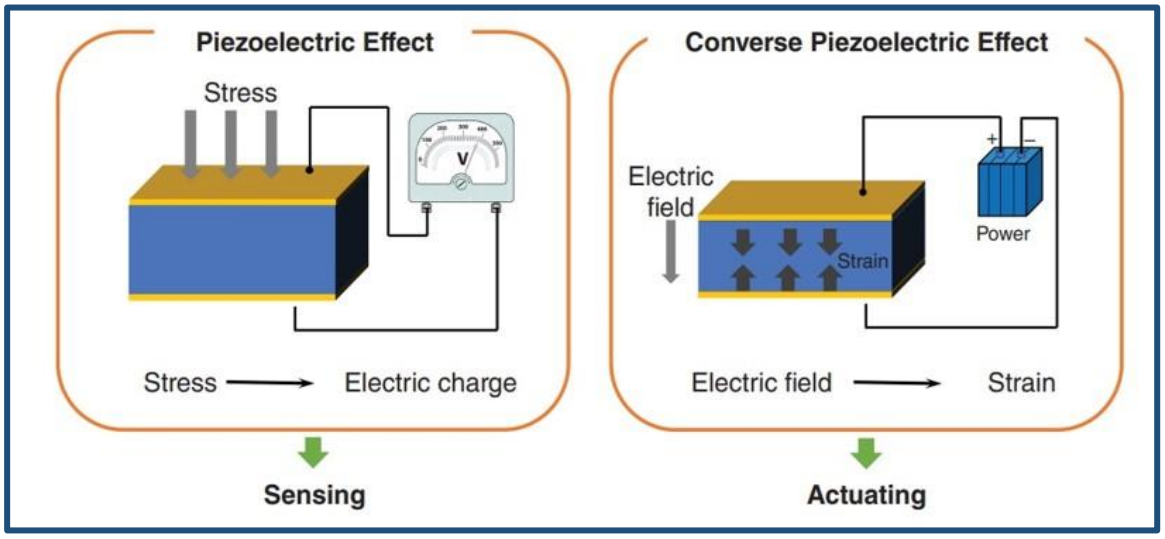

Fig. 1.4. illustrates the direct and reverse/converse piezoelectric effect. Source: [16]

of certain non-centric materials. It is noteworthy that the piezoelectric effect is reversible [16].

i) Direct piezoelectric effect

It is defined as the production of electric charges on the surface of certain non-centrosymmetric materials under the influence of applied mechanical stress. In the presence of applied stress, proportional electric polarization is generated in the material. Under the temporal distortion, centres of gravity of positive and negative charges dislocate that polarize the material. The change in polarization results in the accumulation of charges that we get in terms of voltage across the terminals. Fig. 1.5. describes the dislocation of centres of gravity of positive and negative charges of the piezoelectric materials when subjected to temporal distortion.

ii) Reverse piezoelectric effect

It is defined as the generation of mechanical strain in the aforesaid materials in response to an applied electric field.

In general, the term “piezoelectricity” is lucidly used to refer to the general of electricity when

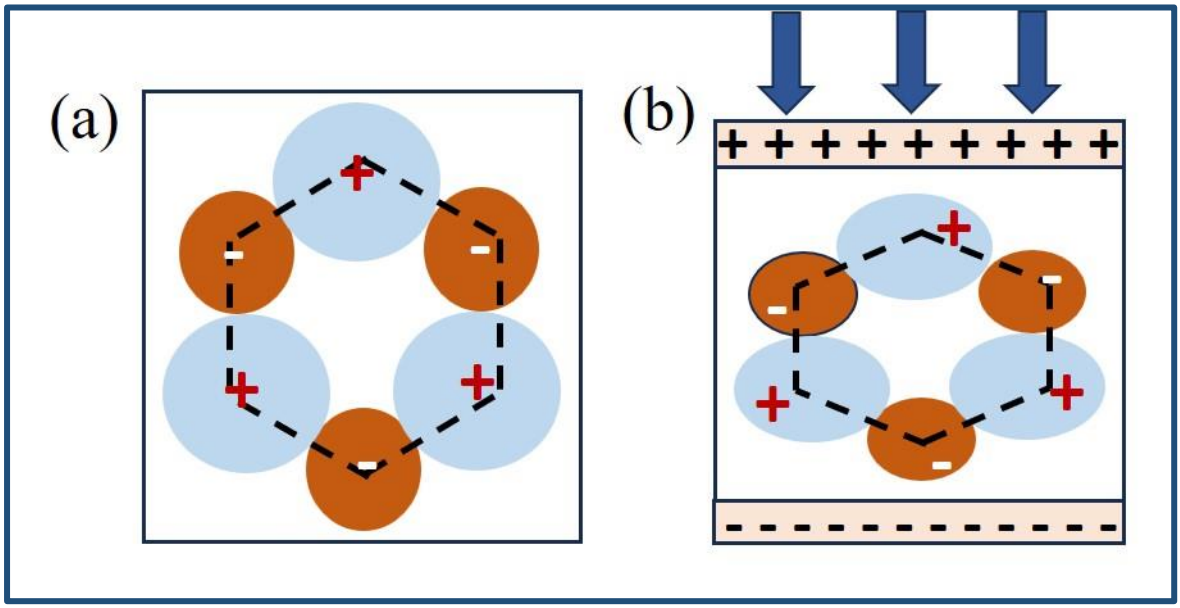

Fig. 1.5. depicts the (a) distribution of centre of charges in absence of any external stress and (b) displacement of centres of charges under the influence of mechanical stress.

the concerned material is subjected to any mechanical force. Fig. 1.4. emphasizes schematically the direct and reverse or converse piezoelectric effect. As I already mentioned the electrical state of a system is linearly proportional to the mechanical state in piezoelectricity, a constant may be defined for this linear relation. This constant is defined as the piezoelectric coefficient (d), a third-rank tensor, that couples the first-rank tensor (electric displacement or field) with the second-rank tensor (stress or strain) [17].

$$D_k = d_{kij} T_{ij} \tag{1.8}$$

$$S_{ij} = d^*_{kij} E_k \tag{1.9}$$

Here, D_k is the electric displacement (C/m^2), E_k is the electric field component (V/m), S_{ij} and T_{ij} refers to the strain and stress component (N/m^2), respectively, d_{kij} or d^*_{kij} represents the component corresponding to the piezoelectric charge or strain constant. Generally, the piezoelectric constant is expressed as d_{km} using reduced Voigt matrix rotation where k denotes the component of D or E in the Cartesian reference frame (x_1, x_2, x_3), and the index m = 1, 2, 3,..,6 defines the mechanical stress or strain. It is noteworthy that m = 1, 2, 3 corresponds to the normal stresses along the x_1, x_2, and x_3 axes, respectively, whereas m = 4, 5, 6 represents the shear stresses T_{23}, T_{13}, and T_{12}, respectively. Both d and d^* are called the piezoelectric

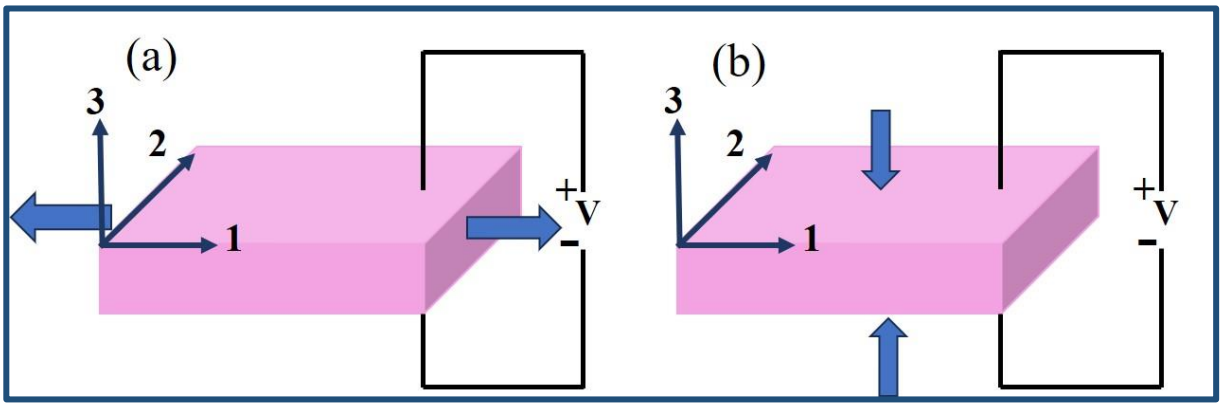

Fig. 1.6. shows the piezoelectric energy harvester working in (a) 31 mode and (b) 33 mode.

coefficient having different units ~ pC/N and pm/V, respectively. In a nutshell, piezoelectric constants are listed below

d = piezoelectric charge or strain coefficient,

$$d_{ij} = \left(\frac{\partial D_i}{\partial T_j}\right)_E = \left(\frac{\partial S_j}{\partial E_i}\right)_T \tag{1.10}$$

g = piezoelectric voltage coefficient,

$$g_{ij} = -\left(\frac{\partial E_i}{\partial T_j}\right)_D = \left(\frac{\partial S_j}{\partial D_i}\right)_T \tag{1.11}$$

e = piezoelectric stress coefficient,

$$e_{ij} = -\left(\frac{\partial T_j}{\partial E_i}\right)_S = \left(\frac{\partial D_i}{\partial S_j}\right)_E \tag{1.12}$$

h = piezoelectric stiffness coefficient,

$$h_{ij} = -\left(\frac{\partial E_i}{\partial S_j}\right)_D = \left(\frac{\partial T_j}{\partial D_i}\right)_S \tag{1.13}$$

Commonly, the piezoelectric generators perform in 31 and 33 modes. The first digit implies the direction of the voltage generation across the device and the second digit refers to the direction of the applied stress. Fig. 1.6. depicts the schematic diagram of the operation of piezoelectric devices in the two modes.

1.6. Relationship between dielectric, piezoelectric and ferroelectric properties

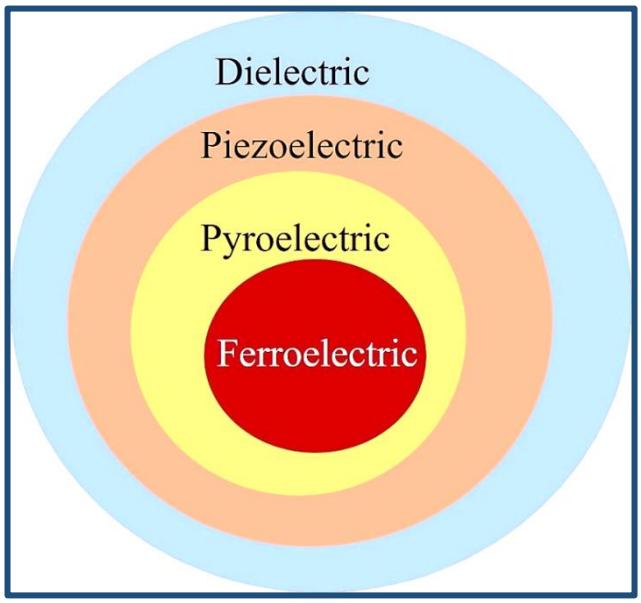

Fig. 1.7. demonstrates the Venn diagram that represents the relationship between dielectric, piezoelectric and ferroelectric material.

Since most of the high-yield piezoelectric materials are also ferroelectric materials, it is necessary to discuss the contribution of ferroelectric properties to piezoelectricity. Ferroelectricity corresponds to the spontaneous electric polarization of some materials that can be reversed when subjected to an applied electric field. With the help of a Venn diagram (Fig. 1.7.), we are trying to demonstrate that dielectrics are a big family with the core subset of ferroelectrics. Dielectric materials, when placed between the plates of a capacitor, become polarized under the application of an external electric field. Piezoelectric materials having non-centrosymmetric crystal structures belong to the dielectric family within which positive and negative charges can be separated when applied to an external strain. It can be concluded that all ferroelectric materials are piezoelectric, however, all piezoelectric materials are not necessarily ferroelectric.

1.7. Piezoelectric parameters

1.7.1. Open circuit voltage (V_{OC})

Under the influence of mechanical stress, a change in polarization takes place within the piezoelectric material that creates charge accumulation. These accumulated charges across the

terminals can be measured as the output voltage of the piezoelectric device. In the absence of any load, the generated output voltage across infinite resistance is considered as open circuit voltage (V_{OC}) and the current flowing through the device is negligible or ideally zero.

1.7.2. Short circuit current (I_{SC})

The produced current with minimum or ideally zero resistance across the terminals of the piezoelectric device is considered as short circuit current (I_{SC}). The free charge carriers present in the piezoelectric material are responsible for generating I_{SC}.

1.7.3. Piezoelectric charge constant

The piezoelectric charge coefficient or constant is expressed as the electric charge generated per unit area under the application of external mechanical force. It is frequently used to estimate the goodness of a piezoelectric material.

$$d = \frac{strain\ developed}{applied\ field} = \frac{Charge\ density}{Applied\ stress} \tag{1.14}$$

The two important d constants are [18]

$$d_{31} = k_{31}\sqrt{\varepsilon_0 k_3^T S_{11}^E}\ \text{(C/N)} \tag{1.15}$$

$$d_{33} = k_{33}\sqrt{\varepsilon_0 k_3^T S_{33}^E}\ \text{(C/N)} \tag{1.16}$$

Here, k represents the electro-mechanical coupling coefficient, k^T refers to the relative dielectric constant at constant stress and S^E is the elastic compliance at a constant electrical field. The relation between d_{33} and d_{31} is $d_{33} \cong 2.5\ d_{31}$.

1.7.4. Piezoelectric voltage coefficient

The piezoelectric voltage coefficient is the ratio of the generated electric field in response to the applied mechanical force

$$g = \frac{Field\ developed}{Applied\ mechanical\ force} \tag{1.17}$$

The g constants are computed from the piezoelectric coefficient and relative permittivity mentioned as

$$g = \frac{d}{\varepsilon} \tag{1.18}$$

1.7.5. Figure of merit

The figure of merit of a piezoelectric material ($F_O M_P$) is a salient parameter that validates the ability of the material to design a piezoelectric energy harvester. The value of $F_O M_P$ can be evaluated from the piezoelectric charge coefficient and piezoelectric voltage coefficient.

$$F_O M_P = d \times g \tag{1.19}$$

1.7.5.1. Energy conversion efficiency

Energy conversion efficiency (η_{piezo}) can be defined as the efficiency of the piezoelectric generator to convert the mechanical energy to the corresponding electrical energy.

$$\eta_{piezo} = \frac{E_{elec}}{W_{mech}} \times 100\% \tag{1.20}$$

Here, W_{mech} denotes the amount of mechanical energy and E_{elec} refers to the corresponding converted electrical energy.

1.8. Piezoelectric materials

Over the years, several high-yield piezoelectric materials such as PZT (lead zirconium titanate), $ZnSO_3$, $PbTiO_3$, ZnO, etc. have been extensively studied. Despite possessing a high piezoelectric coefficient, the rigidity, brittle nature, high expense, and complicated fabrication process, somehow limit the practical and commercial implementation of piezoelectric nanogenerators (PNGs) made of these materials on a large scale. On the other hand, piezoelectric polymers have gained immense attention nowadays owing to several merits such as low fabrication cost, flexibility, biodegradability, etc. The piezoelectric polymers can be categorized in different sections as observed in Fig. 1.8.

Among various polymers, polyvinylidene difluoride (PVDF) and its copolymers are the most popular, synthetic, ferroelectric polymers due to their synthesis simplicity, thermal stability, high dielectric constant compared to other polymers, cost-effectivity, biocompatibility, durability, and ability to be shaped in the desired form. PVDF is a semi-crystalline, homopolymer that contains repetitive CH_2-CF_2 monomers [19]. There are four

existing polymorphs namely predominant non-polar α (TGTG conformation), electroactive,

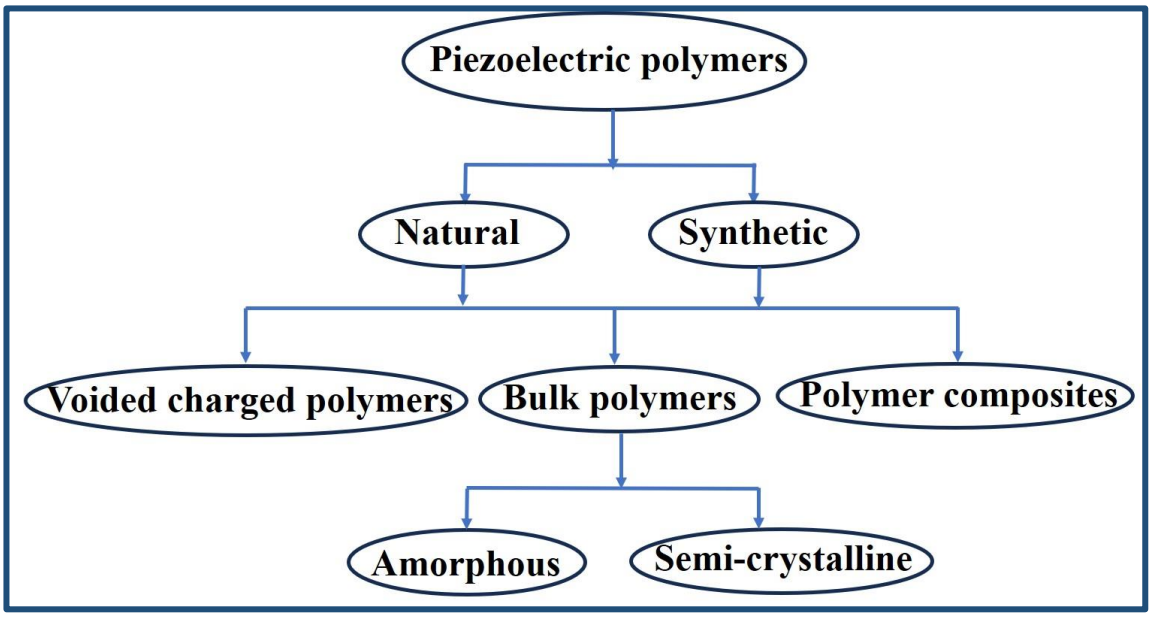

Fig. 1.8. illustrates the classification of piezoelectric polymers

polar β (TTTT conformation), γ (T_3GT_3G conformation), δ (polarised α phase) in PVDF. The α, β, and γ phases of PVDF have been illuminated in Fig. 1.9 [20]. Among these phases, the β phase acquires the highest value of dipole moments per unit volume along with maximum ferroelectric content that consequently assures its key role in piezoelectric energy harvesting.

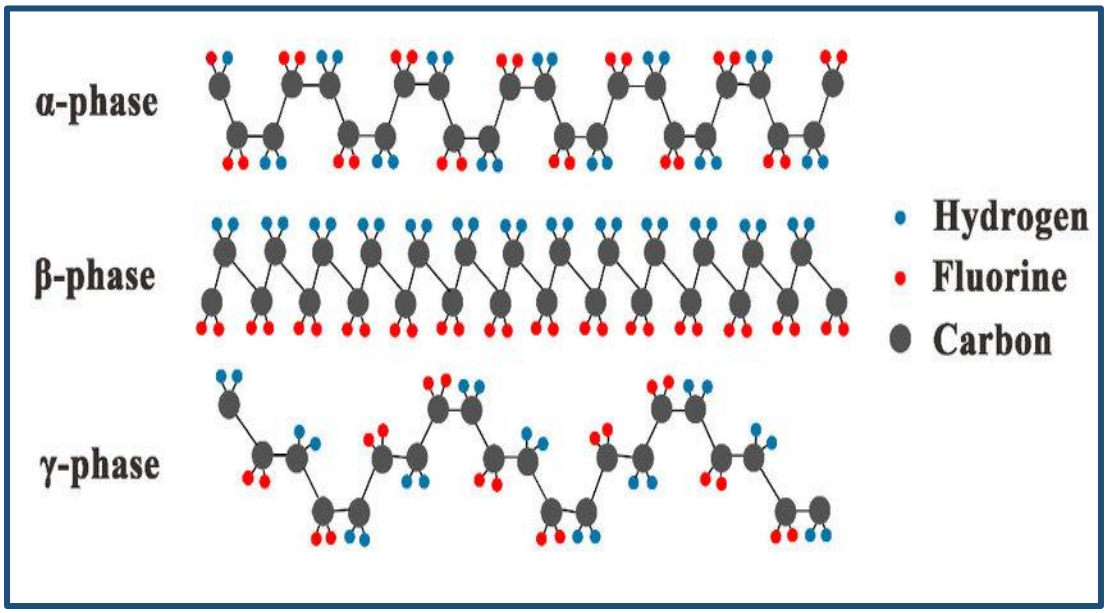

Fig. 1.9. illuminates the schematic representation of α, β, and γ phase of PVDF. Source: [20]

To bring out the dominance of the β phase in PVDF, various techniques have been used over the years such as

- ♠ Annealing at high temperature
- ♠ Mechanical stretching
- ♠ Addition of hydrated salts
- ♠ Electrical polling
- ♠ Assisting external filler within the polymer matrix, etc.

Adding an external agent within the polymer is one of the best choices among all these techniques. The main concerns on incorporating external filler within the PVDF matrix to significantly improve the β phase are

i) Choosing the appropriate filler not only participates in improving the electroactive content of the polymer but also makes the composite multifunctional by contributing to its intrinsic properties.

ii) The suitable method of inclusion of the filler plays a vital role in the electroactive content enhancement process.

The 1st concern can be addressed by choosing different perovskite materials as key fillers within the PVDF framework. Considering hybrid perovskites as external fillers provide an added advantage as the photovoltaic properties of these perovskites can be used to harvest solar energy as well. The toxicity content of the hybrid perovskites can be removed by adding appropriate oxide perovskite as a filler within the PVDF.

The 2nd concern is approaching the suitable methods to add the filler inside the polymer mat to properly increase the efficacy of the composite can be considered by employing various useful techniques such as electrospinning, fabrication of self-poled porous film, etc.

1.9. Fundamentals of triboelectricity

The word “triboelectricity” comes from the Greek word “tribo” which defines “friction”. The triboelectric effect arises from “contact electrification” which states the flow of electric charges from the surface of one material to that of the other when they keep in contact with each other. When the two materials are in contact, opposite static charges are generated on the surfaces due to contact electrification.

Triboelectric generators can be operated and structured in the following ways [21].

a) Vertical contact-separation mode

This mode describes a motion direction that is normal to the charged surfaces of a triboelectric

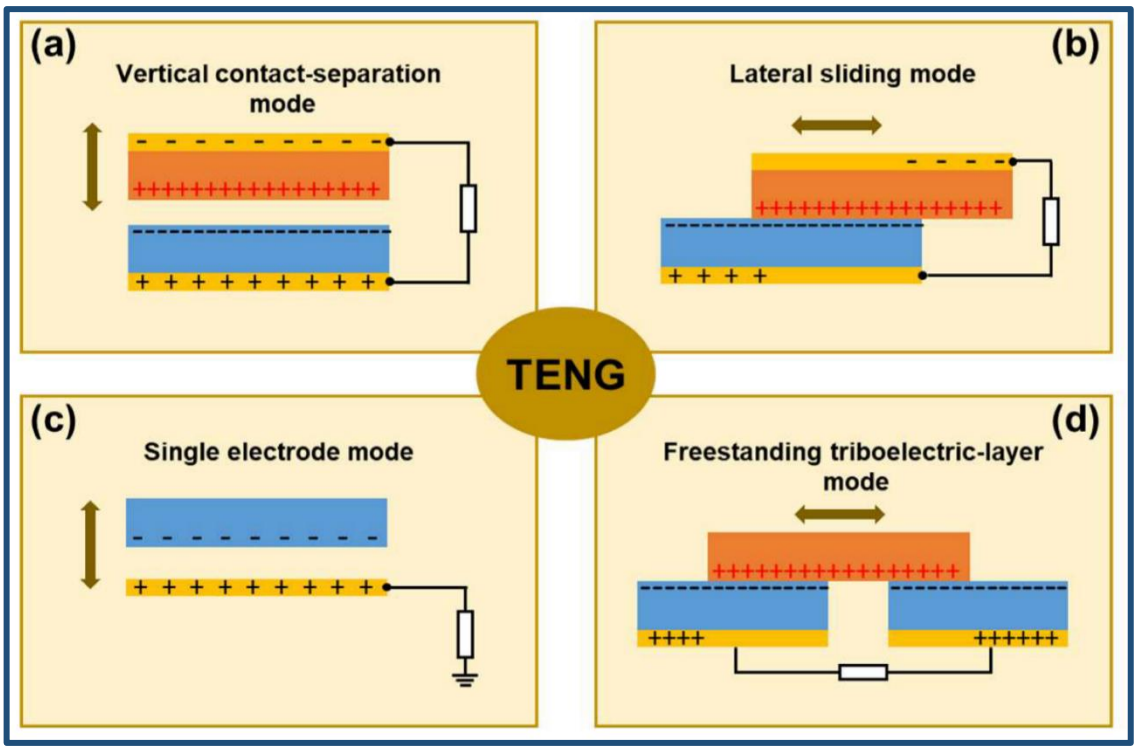

Fig. 1.10. schematically demonstrates the four modes of triboelectric generators. Source: [21]

nanogenerator. In a designed triboelectric generator, no triboelectric charges are generated in the original state since induced charges cannot be exchanged between two electrodes in open-circuit mode. When an external force is applied on the upper surface of the device, the surface comes into contact with the other surface and hence the exchange of charges takes place resulting in two oppositely charged surfaces of the device (Fig. 1.10a). On the removal of the force, the two surfaces get separated inducing a potential difference across the top and bottom electrodes. Thus, electrical energy can be harvested implying any contact modes viz. pressing, shock, etc.

b) Lateral sliding mode

In this mode, the two constituting surfaces of the triboelectric generator are brought in contact in such a way that one surface can slide smoothly against the other one resulting in a relative motion that is parallel to the charged surface plane (Fig. 1.10b). Once the upper surface slides outward, the contact area reduces that leads to the flow of electrons through the external circuit since the in-plane charge separation develops an electric field parallel to the plates. Again,

when the upper surface comes back to the initial position, the electrons on the top electrode will transfer back through the external circuit to the bottom electrode in a similar way.

c) Single electrode mode

In this mode, the triboelectric generator contains only one electrode since the other electrode is connected to the ground. The surfaces of the dielectric material and metal electrode are brought in contact to transfer the charge between them. Once the electrode and the dielectric materials get separated, free electrons flow from the electrode to the ground, and consequently current is generated. The corresponding schematic diagram is shown in Fig. 1.10c.

d)Free standing mode

In this mode, two electrodes of the triboelectric generator lie beneath the dielectric layer and a frictional layer as displayed in Fig. 1.10d. During the to-and-fro movement of the frictional layer from the dielectric layer, a disturbance occurs due to the unstable charge distribution. To balance the potential drop, the exchange of carriers occurs between two electrodes.

1.10. Triboelectric materials

Table 1.1. Some of the name of common triboelectric materials and their affinity to lose or gain electrons

Material Name	Electron affinity (nC/J)
Hair, oily skin	+45
Nylon, dry skin	+30
Paper	+10
Pine wood	+7
Cotton	+5
Wool	0
Acrylic (polymethyl methacrylate)	-10
Epoxy (circuit board)	-32
Solvent based spray paints	-38
Gum rubber	-60
Polymide	-70

Various materials are found to be promising candidates to harvest triboelectric energy according to the triboelectric series (series containing some common materials as exhibited in Table 1.1) [22]. PVDF is tested to be a potential material that can be considered an effective

dielectric in the triboelectric generator. PVDF is highly non-reacting with an appreciable piezoelectric response. As already stated, the β phase of PVDF possesses the highest amount of crystallinity content that consists of fluorine atom and hydrogen atom in the opposite direction resulting in a high dipole density. The large electron affinity of these fluorine functional groups enhances the carrier acceptance from the metal during the instantaneous contact. Thus, PVDF and its composite can be used to harvest triboelectric energy with significant energy conversion efficacy [22].

1.11. Piezo-catalysis

The rapid development of industrialization throughout the globe results in the production of environmental pollutants that accumulate in the water. Consequently, the aquatic ecosystem is in danger and requires environmental remediation urgently. Piezo-catalysis that takes advantage of piezo and triboelectric effect has gained keen attention as a potential environmental remediation technique. Without employing any additional electrical energy, piezo-catalysis is capable of degrading the pollutants effectively. Moreover, these processes do not require any supply of energy in the form of a light source as is required in conventional photocatalysis. The built-in electric field appearing from the piezo effects of materials makes it advantageous for the degradation of pollutants. Piezo-catalysis develops from an intimate interaction between the native electronic state and the strain state of the piezoelectric material. To get more insight into the piezo-catalysis process, it is required to understand electrocatalysis first in which the applied electric field from an external power source triggers the electron transfer reaction. The applied potential either lowers the electronic energy levels of unoccupied states within the electrode to a magnitude lower than that of the highest occupied molecular orbital (HOMO) in the solution or increases the occupied states within the electrode above the lowest unoccupied molecular orbital (LUMO) in the solution. In piezo-catalysis, piezoelectric potential plays the role of an external power source that results from piezoelectric polarization. Thus, piezo-potential will move the electronic energy levels to the occupied or unoccupied states within the material. Piezo-catalysis can be induced in a solution in the form of different kinds of mechanical energy such as sonic waves, tides, wind, etc.

1.12. Photodetector

Photodetectors, an integral wing of solar energy harvesting, have the utmost necessity in imaging, automation, high-speed optical communications, etc., and have a broad spectrum of applications ranging from smartphone cameras to Mars rovers [23]. Depending on the mode and principle of operations, architecture, etc., photodetectors can be divided into two categories ~ photo conductors and photo transistors. In photoconductors, the depletion region of the p-n junction structure is used to generate and capture incident photons. When the photon energy is higher than the band gap of the material, photo-generated electron-hole pairs are separated by the electric field across the depletion region. As the depletion region is the active region that captures light, a larger depletion area will enable higher sensitivity. Hence, photo detectors are used with reverse bias that widens the depletion region.

In this context, a brief discussion is necessary about a dynamic parameter ~ response time. The response time of a photodetector denotes the time taken by the device to reach 63.2 % (1/e) of its steady state when subjected to a periodic switching of optical state. The response time of a device can be fast as well as slow. The fast segment of response time is ascribed to the transit time of the carriers inside the device. The slow response of a device denotes the charge accumulation and RC delay of the total network. Junction capacitance also plays a significant role in slowing down the response time.

1.13. Hybrid energy harvesting

A hybrid energy harvester integrates two or more energy harvesting techniques in a sole unit that not only produces sufficient power to operate the microelectronics but also can function simultaneously in different directions. Generally, a hybrid system acquires renewable energies from different sources and generates more power than an individual energy harvester. These devices can work even in the absence of one source of energy. Depending upon the requirement, these hybrid systems can harvest several energies individually or simultaneously. Hybridising piezo and triboelectric energy in a single system can produce high energy density whereas harvesting solar and mechanical energy in a single unit can serve the purpose of the low-powered sensors that need photodetection at the same time. Therefore, it is very important as well as challenging nowadays to first choose different energy sources that can be harvested together and then design a robust multifaceted energy harvesting unit.

1.14. Supercapacitor as energy storage device

Generally, an energy system consists of three very important segments- an energy harvesting unit, a power management circuit, and a storage unit. Nowadays, apart from exploring sustainable energy sources to address the global energy crisis, storing energy for future usage according to the requirements along with independence on the condition of weather, timing, and ambiance is another challenge. In recent times, the electrochemical charge storage units like batteries, supercapacitors, etc. being used to run portable microelectronics, are extensively investigated followed by a continuous modification to meet the consumers' need. Supercapacitors which offer high power density but low energy density as compared to the batteries, reversible charge-discharge cycle form the bridge between traditional capacitors and rechargeable batteries. In a conventional capacitor, two parallel metal plates are separated by a dielectric material such as air to generate an electric potential and store charge electrostatically in the electric field whereas in a supercapacitor, two metal plates, coated with a porous material to encompass a large surface area, are immersed in an ion rich liquid electrolyte to create charge separation and consequent generation of electric potential [24]. A separator is placed between the porous electrodes of the supercapacitor to provide a safeguard to the device from the electrical short circuits. Depending on the electrode design and charge storage mechanism, supercapacitors can be classified into three categories [25].

a) Electric double layer capacitors (EDLC)

EDLC undergoes a non-faradic process since no electron transfer is involved here. In EDLC, the two conducting electrodes are separated by a liquid electrolyte. The double layer capacitance forms at the electrode-electrolyte interface due to the polarization as a result of charge separation when voltage is applied. In EDLC, the charge stores electrostatically and the amount of stored charge is linearly proportional to the voltage applied. The electrochemical performance of EDLC depends on specific surface area, and porosity of the electrodes. Commonly, carbon-based materials such as activated carbon, carbon nanotubes, graphene, etc. are used as electrode materials in EDLC owing to their wide availability, appreciable stability in the presence of high temperature and moisture, high conductivity, high surface area, etc.[26–28]

b)Pseudocapacitors

Pseudocapacitors follow a faradic nature as a reversible redox reaction is involved between the electrode and electrolyte at the surface of the electrode. The produced pseudocapacitance also depends on the surface area, structure, and material of the electrode. The amount of charge stored in a pseudocapacitor is also linearly proportional to the applied voltage. Generally, conducting polymers and transition metal oxides are used to prepare the electrodes of the pseudocapacitors [29–31].

c) Hybrid supercapacitors

A hybrid supercapacitor is fabricated by combining the characteristics of both EDLC and pseudocapacitors to attain better performance. The coupling of faradic pseudocapacitor electrodes with high pseudocapacitance and non-faradic electric double layer capacitor electrode provides high energy density along with high power density. Hybrid supercapacitors are designed by integrating different EDLC materials and redox materials such as activated charcoals, transition metal oxides, conducting polymers, etc. These hybrid capacitors yield higher working potential as well as much higher capacitance as compared to the EDLCs and pseudocapacitors.

1.15. Piezoelectric supercapacitor

Since renewable energy harvesting and energy storing are two key pillars of a sustainable energy system not only to convert the ambient energy to an electrical signal but also to provide consistent power supply to the portable electronic devices, it is necessary to hybridize the individual harvesting and storing unit into a single unit. It is a highly challenging task to integrate energy harvesting and storage devices that operate in different working mechanisms in a single unit. Commonly, a full wave rectifier circuit is used as a power management circuit between a piezoelectric energy harvester and a storage device. The integration of harvesting and storage devices not only eases the process of power supply but also minimizes unnecessary power loss at the rectifier circuit. That is why, self-charging piezoelectric supercapacitor is a new trend for one step solution of energy conversion and storage. In this integrated piezo-supercapacitor device, a piezoelectric film is used as the separator, as well as an energy harvester between two electrodes, and a polymer gel electrolyte is used to avoid the disadvantages of a liquid electrolyte such as the possibility of electrolyte leakage, short circuit of the electrodes, etc. When the device is subjected to external mechanical stress, a piezo-

potential develops across the piezoelectric film resulting in the ion migration between the electrodes and electrolyte towards the interface of the electrodes, and the charge is stored as the electrochemical energy.

References

[1] P.C. Reshmi Varma, Low-Dimensional Perovskites, in Perovskite Photovoltaics, Elsevier, 2018: pp. 197–229. https://doi.org/10.1016/B978-0-12-812915-9.00007-1.

[2] A. Kubacka, M. Fernández-García, G. Colón, Advanced Nanoarchitectures for Solar Photocatalytic Applications, Chem. Rev. 112 (2012) 1555–1614. https://doi.org/10.1021/cr100454n.

[3] P. Gao, M. Grätzel, M.K. Nazeeruddin, Organohalide lead perovskites for photovoltaic applications, Energy Environ. Sci. 7 (2014) 2448–2463. https://doi.org/10.1039/C4EE00942H.

[4] H. He, Z. Yang, Y. Xu, A.T. Smith, G. Yang, L. Sun, Perovskite oxides as transparent semiconductors: a review, Nano Converg. 7 (2020) 32. https://doi.org/10.1186/s40580-020-00242-7.

[5] M.N. Grisolia, J. Varignon, G. Sanchez-Santolino, A. Arora, S. Valencia, M. Varela, R. Abrudan, E. Weschke, E. Schierle, J.E. Rault, J.-P. Rueff, A. Barthélémy, J. Santamaria, M. Bibes, Hybridization-controlled charge transfer and induced magnetism at correlated oxide interfaces, Nat. Phys. 12 (2016) 484–492. https://doi.org/10.1038/nphys3627.

[6] A. Mercy, J. Bieder, J. Íñiguez, P. Ghosez, Structurally triggered metal-insulator transition in rare-earth nickelates, Nat. Commun. 8 (2017) 1677. https://doi.org/10.1038/s41467-017-01811-x.

[7] S. Kumari, N. Ortega, A. Kumar, J.F. Scott, R.S. Katiyar, Ferroelectric and photovoltaic properties of transition metal doped $Pb(Zr_{0.14}Ti_{0.56}Ni_{0.30})O_{3-\delta}$ thin films, AIP Adv. 4 (2014) 037101. https://doi.org/10.1063/1.4868380.

[8] J. Biscaras, N. Bergeal, A. Kushwaha, T. Wolf, A. Rastogi, R.C. Budhani, J. Lesueur, Two-dimensional superconductivity at a Mott insulator/band insulator interface $LaTiO_3/SrTiO_3$, Nat. Commun. 1 (2010) 89. https://doi.org/10.1038/ncomms1084.

[9] J.H. Haeni, P. Irvin, W. Chang, R. Uecker, P. Reiche, Y.L. Li, S. Choudhury, W. Tian, M.E. Hawley, B. Craigo, A.K. Tagantsev, X.Q. Pan, S.K. Streiffer, L.Q. Chen, S.W. Kirchoefer, J. Levy, D.G. Schlom, Room-temperature ferroelectricity in strained SrTiO3, Nature. 430 (2004) 758–761. https://doi.org/10.1038/nature02773.

[10] D.O. Demchenko, N. Izyumskaya, M. Feneberg, V. Avrutin, Ü. Özgür, R. Goldhahn, H. Morkoç, Optical properties of the organic-inorganic hybrid perovskite, Phys. Rev. B. 94 (2016) 075206. https://doi.org/10.1103/PhysRevB.94.075206.

[11] P. Sadhukhan, S. Kundu, A. Roy, A. Ray, P. Maji, H. Dutta, S.K. Pradhan, S. Das, Solvent-Free Solid-State Synthesis of High Yield Mixed Halide Perovskites for Easily Tunable Composition and Band Gap, Cryst. Growth Des. 18 (2018) 3428–3432. https://doi.org/10.1021/acs.cgd.8b00137.

[12] P. Sadhukhan, D. Ghosh, P. Sengupta, S. Bhattacharyya, S. Das, Unraveling the Charge Transport Mechanism in Mechanochemically Processed Hybrid Perovskite Solar Cell, Langmuir. 37 (2021) 5513–5521. https://doi.org/10.1021/acs.langmuir.1c00200.

[13] A. Ray, A. Roy, S. Chatterjee, K. Centre, S. Das, Frequency and temperature dependent dielectric properties of TiO_2 -V_2O_5 nanocomposites Frequency and temperature dependent dielectric properties of TiO_2-V_2O_5, J. Appl. Phys. 123 (2018) 104102. https://doi.org/10.1063/1.5012586.

[14] S. Guo, X. Duan, M. Xie, K.C. Aw, Q. Xue, Composites, Fabrication and Application of Polyvinylidene Fluoride for Flexible Electromechanical Devices: A Review, Micromachines. 11 (2020) 1076. https://doi.org/10.3390/mi11121076.

[15] S.K. Ghosh, D. Mandal, Synergistically enhanced piezoelectric output in highly aligned 1D polymer nanofibers integrated all-fiber nanogenerator for wearable nano-tactile sensor, Nano Energy. 53 (2018) 245–257. https://doi.org/10.1016/j.nanoen.2018.08.036.

[16] J. Rödel, J.-F. Li, Lead-free piezoceramics: Status and perspectives, MRS Bull. 43 (2018) 576–580. https://doi.org/10.1557/mrs.2018.181.

[17] A. American, N. Standard, IEEE Standard on IEEE Standard on Piezoelectricity, ANSI/IEEE Std 176-1987. (1988) 8–10. https://doi.org/10.1109/IEEESTD.1988.79638.

[18] J.-F. Li, Lead-Free Piezoelectric Materials, Wiley. (2021) 240. https://doi.org/ISBN: 978-3-527-34512-0.

[19] L. Ruan, X. Yao, Y. Chang, L. Zhou, G. Qin, X. Zhang, Properties and Applications of the β Phase Poly(vinylidene fluoride), Polymers (Basel). 10 (2018) 228. https://doi.org/10.3390/polym10030228.

[20] T. Tansel, High beta-phase processing of polyvinylidenefluoride for pyroelectric applications High beta-phase processing of polyvinylidenefluoride for pyroelectric applications, J. Polym. Res. (2022). https://doi.org/10.1007/s10965-020-02073-w.

[21] J. Lee, J. Lee, J. Baik, The Progress of PVDF as a Functional Material for Triboelectric Nanogenerators and Self-Powered Sensors, Micromachines. 9 (2018) 532. https://doi.org/10.3390/mi9100532.

[22] O. MOLNAR, Triboelectricity and construction of power generators based on it, PRZEGLĄD ELEKTROTECHNICZNY. 1 (2018) 169–173. https://doi.org/10.15199/48.2018.01.41.

[23] T. Kirchartz, F. Deledalle, P.S. Tuladhar, J.R. Durrant, J. Nelson, On the Differences between Dark and Light Ideality Factor in Polymer:Fullerene Solar Cells, J. Phys. Chem. Lett. 4 (2013) 2371–2376. https://doi.org/10.1021/jz4012146.

[24] A. Ray, A. Roy, M. Ghosh, J. Alberto Ramos-Ramón, S. Saha, U. Pal, S.K. Bhattacharya, S. Das, Study on charge storage mechanism in working electrodes fabricated by sol-gel derived spinel $NiMn_2O_4$ nanoparticles for supercapacitor application, Appl. Surf. Sci. 463 (2019) 513–525. https://doi.org/10.1016/j.apsusc.2018.08.259.

[25] T.U.R. Bijoy Krishna Roy, Ishmam Tahmid, Chitosan-based materials for supercapacitor applications : a review, JJurnal Mater. Chem. A. 9 (2021) 17592–17642. https://doi.org/10.1039/d1ta02997e.

[26] Z. Fan, D. Qi, Y. Xiao, J. Yan, T. Wei, One-step synthesis of biomass-derived porous carbon foam for high performance supercapacitors, Mater. Lett. 101 (2013) 29–32. https://doi.org/10.1016/j.matlet.2013.03.064.

[27] E. Frackowiak, K. Metenier, V. Bertagna, F. Beguin, Supercapacitor electrodes from multiwalled carbon nanotubes, 2421 (2012) 4–7. https://doi.org/10.1063/1.1290146.

[28] L.T. Le, M.H. Ervin, H. Qiu, B.E. Fuchs, W.Y. Lee, Electrochemistry Communications Graphene supercapacitor electrodes fabricated by inkjet printing and thermal reduction of graphene oxide, Electrochem. Commun. 13 (2011) 355–358. https://doi.org/10.1016/j.elecom.2011.01.023.

[29] A. Eftekhari, L. Li, Y. Yang, Polyaniline supercapacitors, J. Power Sources. 347 (2017) 86–107. https://doi.org/10.1016/j.jpowsour.2017.02.054.

[30] G.M. Subbukalai Vijayakumar, Sadayappan Nagamuthu, Supercapacitor Studies on NiO Nanoflakes Synthesized Through Microwave Route, ACS Appl. Mater. Interfaces. 5 (2013) 2188–2196. https://doi.org/10.1021/am400012h.

[31] S.K. Meher, G.R. Rao, Ultralayered Co_3O_4 for High-Performance Supercapacitor Applications, J. Phys. Chem. C. 115 (2011) 15646–15654. https://doi.org/10.1021/jp201200e.

CHAPTER 2

2. Literature review

This section will provide a clear vision of the national and international status of this dissertation.

2.1. Perovskites

A BO_3 based ideal cubic perovskite oxide structures are very familiar in inorganic compounds where A-sited cation is mainly an alkaline-earth, a rare earth or an alkali element, and B-sited cation is a transition, or post transition metal element that constructs the BO_6 octahedra. The structure of these perovskites can remain stable even if A or B-sited cation is substituted with a larger element. Various studies have been carried out over the decades on these oxide perovskites because of their variety of physical properties including superconductivity, metal-insulator transition, photovoltaic effect, transparent conductivity, ferroelectricity, and magnetism [1]. $BaTiO_3$ was first discovered during World War II. In 1947, Robert discovered the good piezoelectric effect in $BaTiO_3$ that is almost 100 times higher than that of quartz (SiO_2, in 1880, Pierre Curie and Jacques Curie discovered that SiO_2 exhibits a direct piezoelectric effect that produces an electric charge in response to a mechanical stress) [2]. In 1956, the first photo generated current effect was observed in $BaTiO_3$ [3]. Later, $LiNbO_3$ was also observed to show ferroelectricity and photovoltaic properties [4]. Afterward, poled $BaTiO_3$ in high voltage was rapidly used in sensors and transducers, especially in Japan. In 1954, enhanced ferroelectricity and antiferroelectricity were observed by Jaffle in the solid solution of $PbTiO_3$ and $PbZrO_3$ (commonly known as PZT) [5].

Another class of perovskites is halide perovskites (ABX_3) which have become a point of interest among researchers in the past few years because of their promising optical, structural, and dielectric properties. In alkali-based halide perovskites, a monovalent alkali metal ion (Li^+, Na^+, K^+) sits in the position of A. In OIHPs, an aromatic or aliphatic ammonium organic cation ($CH_3NH_3^+$, $CHN_2H_4^+$) occupies position A and a divalent cation (Pb^{2+}, Sn^{2+}, Ni^{2+}, etc.) placed in the B-site. The ionic radii of the halide ions I^-, Br^-, Cl^- that occupy the X-site are 2.07 Å, 1.84 Å, 1.67 Å, respectively. The most common and widely used OIHPs are

methylammonium lead halide ($CH_3NH_3PbX_3$, $MAPbX_3$) and formamidium lead halide ($CH(NH_2)_2PbX_3$, $FAPbX_3$) that exhibit direct bandgap with superior semiconducting properties. The values of band gap of these OIHPs range from 1.48 ($FAPbI_3$) [6], 1.55 eV ($MAPbI_3$) [7], 2.23 eV ($FAPbBr_3$) [8], 2.35 eV ($MAPbBr_3$) [7] to 3 eV ($MAPbCl_3$) [9]. The main challenge faced by these OIHPs is the stability issue in the presence of moisture, high temperature, and light illumination. The degradation processes are briefly discussed here.

2.2. Stability issues of OIHPs

The main disadvantage of these hybrid perovskites is the poor stability in ambient conditions. Degradation of these perovskites draws a restriction on the solar cells based on OIHPs. Absorption of moisture and degradation in the presence of UV light are the most common. Various types of degradation processes are discussed below.

➢ Degradation in the presence of moisture

Hybrid perovskites degrade very fast in moisture or an oxygen environment due to the presence of organic components in it. Moisture induced degradation initiates from the surface of OIHPs. Polar H_2O molecules form a strong hydrogen bond with the organic cation of OIHPs which on the other hand weakens the bond strength between the organic cation and the BX_6 octahedra. Moreover, water molecules protonate the halide ions to release them as hydrogen halide leaving behind the lead halides in case of lead contained OIHPs [10]. External stimuli like electric field [11], and heat [12] boost the degradation reaction. $CH_3NH_3PbI_3$ degrades in the presence of moisture easily. Compositional engineering to substitute or add the organic cations and halide ions can effectively reduce degradation.

➢ Degradation under light irradiation

Stability under illumination is the utmost requirement of a photovoltaic material like OIHPs. During the early days of OIHP solar cell, Lee et al. explained that an insulated $CH_3NH_3PbI_3$ solar cell can tolerate 1000 hours in 1 sun light illumination without significantly deteriorating the performance [13]. However, in 2018 DeQuiletts et al. reported the ion migration under the influence of light illumination and halide segregation in $CH_3NH_3PbI_3$ [14]. In 2016, Kim et. al. supported this fact [15]. Hoke et. al. reported that Br^- and I^- ions of a mixed halide OIHP separate to form isolated areas of Br^- and I^- rich sections. This halide segregation disturbs the uniformity of the spatial distribution of different halides in the perovskite film. All these studies

were performed under the irradiation of full sun spectrum. The UV light exposure can also cause damage to the OIHPs.

➢ Temperature induced degradation

Generally, the working temperature of any energy harvesting device lies in between -10 ^{o}C to 65 ^{o}C. In summer, the upper temperature can even go up further in few places. Moreover, processing of an OIHP solar cell requires temperature over 120 ^{o}C at various steps. On the other hand, some piezoelectric films are required to anneal at 130 ^{o}C. Therefore, the stability of OIHP at high temperatures is highly required. From the TGA (thermogravimetric analysis) analysis, it has been reported that $CH_3NH_3PbI_3$ decomposes into volatile CH_3NH_2 and HI leaving behind PbI_2. PbI_2 requires a higher temperature to degrade. The degradation process is stated as [16–18]

$$CH_3NH_3PbI_3\ (s) \rightarrow\ PbI_2\ (s) +\ CH_3NH_2\ (g) + HI\ (g) \qquad (2.1)$$

In this dissertation, we address the stability issue of OIHP by introducing a larger cation $C_3H_7NH_3$ that exhibited excellent stability in the presence of moisture, temperature, and UV light.

2.3. Piezoelectric materials

Piezoelectric materials are mainly referring to piezoceramics and piezopolymers. InN, GaN, CdS, ZnO, etc. are well explored over the years owing to their high piezoelectric response and superior energy conversion efficiency [19–21]. Besides these ceramics, various perovskites like $BaTiO_3$, PZT, etc. as already mentioned previously, exhibit piezoelectric coefficients as high as 200 – 900 pC/N [22]. Despite having high piezoelectric efficacy, these materials are expensive, brittle, and rigid to some extent and need high end complicated processes to synthesize on a large scale. These demerits mainly put a limitation on the production of wearable devices made of these materials on a large scale.

In contrast, among various piezopolymers like nanocellulose, Nylon 11, etc., PVDF and its copolymers such as PVDF-TrFe, PVDF-HEP, etc. have become immensely popular in wearable energy harvesting devices mainly because of its low-expense and ability to be shaped in the desired form [23–26]. PVDF is a semi-crystalline polymer that consists of α, β, γ, δ, ε phases. Among these phases, α phase is non-polar and can be easily achieved directly from the melt by crystallization [27]. In contrast, β and γ phases that are responsible for the

ferroelectric content possess a significant amount of dipole moment [28]. Hence, it is necessary to bring out the supremacy of the polar β phase in PVDF that can be achieved using the following ways.

2.3.1. Phase transition method

The dominance of the β phase obtained from direct melting not only requires high temperature and pressure but also needs some other specified conditions. Doll et al. and Yang et al. reported a detailed study on high-pressure crystallized PVDF that comprised both low and high melting phases [29,30]. Yang et al. also showed earlier how quenching and annealing at high temperatures can induce the β phase formation in PVDF [30]. In 1969, Kawai reported the β phase formation from the uniaxial drawing of α film [31]. Later, various investigations were performed on the conversion from α to β phase by the method of mechanical stretching at different stretching temperatures with a range of stretch ratio [32–34]. In 1996, Hattori explained that the piezoelectric response of PVDF can be enhanced effectively by crystallizing the PVDF films at high pressure [35]. However, the β phase obtained by "drawing at low temperature" was not piezoelectric because of their random orientation. A Poling was necessary to orient the β phases to make it effective for piezoelectricity. This can be achieved using electrical poling and emerging self-poling methods.

2.3.1.1. Electrical poling

Well, electrical poling includes both electrode poling and corona poling. In electrode poling, all the dipoles align inside the piezoelectric materials on the influence of a strong electric field generated by the application of a high voltage across the electrodes.

Compared to electrode poling, corona poling is a bit complicated. In this method, a metal grid with a voltage of around 0.2 – 3 kV is placed about 3 mm above the sample. The high voltage will ionize the neighboring ion molecules resulting in the surface charge of the sample. The charged surface consequently generates a potential difference that induces the poling of the sample [36,37].

2.3.1.2. Self-poling

This emerging and simplified poling method is widely used to align the dipoles inside PVDF without applying an external electrical potential. Self-poling can be achieved by assisting external filler [38,39], hydrated salts [40,41], hydroxides [42], and coagulation of ultra-thin

film in water [43]. In these processes, dipoles of PVDF can be oriented enormously due to the electrostatic interaction or formation of hydrogen bonds with CF_2 and CH_2 dipoles of PVDF [42–44].

2.3.2. Solvent casting

Besides the aforementioned techniques, researchers have focused on developing other solvent casting techniques to form β phase enormously.

2.3.2.1. Electrospinning

This method can produce flexible and consistent nanofibers of PVDF and PVDF composites with enhanced β phase content. In this method, the solution containing PVDF and its composites are triggered to pump out with immense force from a syringe placed at the spinneret under the influence of high applied voltage. The generated potential difference can be optimized by changing the distance between the tip of the syringe and the collector plate. The high stretching ratio that is responsible for the conversion of α phase to β phase is somehow similar to the elongation during mechanical stretching. Despite this similarity, some parameters like flow rate, electrospinning temperature, solvent evaporation temperature, and distance between the collector plate and the syringe tip are capable of producing highly crystalline PVDF nanofibers [45,46]. Ribeiro et. al. reported an improved crystallinity of PVDF was achieved with 85 % β phase fraction by the method of electrospinning [47].

2.3.2.2. Spin coating

A thin, uniform polymer film with a superior β phase portion can be achieved by spin coating the solution on a specific substrate at a controlled temperature [48]. Benz et. al. prepared 2 μm thick PVDF film by the method of spin coating the PVDF solutions [40].

We have used electrospinning and self-poling methods in our work to form piezoelectric and triboelectric composites.

2.4. Dielectric properties

As discussed, the dielectric property is one of the most important properties of perovskite materials. As reported by Li et al, Ghosh et al, $CH_3NH_3PbX_3$ (X = I. Br) exhibits a giant dielectric constant at low frequency region [49,50]. Perez et al. introduced the effect of light

illumination on the dielectric constant [51]. According to the report, the value of the dielectric constant is significantly high under irradiation. However, the explanation of light illumination effect was rejected by Almond et al. [52]. Various reports exhibit the giant dielectric constant of oxide perovskites that is further explained with interfacial polarization and polaronic relaxation [53,54]. Ionic migration is an essential parameter in many applications like energy harvesting devices.

To the best of our knowledge, extensive study on the temperature and frequency dependent dielectric properties of $C_3H_7NH_3PbI_{3-x}Br_x$ was reported for the first time in our works. We have observed that $C_3H_7NH_3PbBr_3$ possesses a giant dielectric constant at low frequency range. We have discussed the ion migration process and the influence of activation energy in detail.

2.5. Recent development of piezoelectric and triboelectric energy harvesting

Wang et al. termed piezoelectric nanogenerator (PENG) in 2006 following the discovery of piezoelectric response in ZnO nanowire [55]. Recently, after gaining huge attention in the photovoltaic domain, hybrid perovskites having ferroelectric response are broadly used in the PENGs to harvest mechanical energy. Kim et al reported for the first time the piezoelectric response of PENG that was fabricated by sandwiching a 500 nm thick $MAPbI_3$ in between two flexible PET electrodes via an adhesive polydimethylsiloxane (PDMS) layer. The PDMS layer acted as a potential barrier that led to the reduction of leakage current. After poling with a very high electric field ~ 80 kV/cm, the output response of the PENG was quite promising ~ 2.7 V open circuit voltage (V_{OC}) and 140 nA/cm^2 short circuit current (I_{SC}) [56]. Ippili et al. reported that PENG comprised of PVDF-$MASnI_3$ composite exhibited ~ 12.0 V V_{OC} and ~ 4 μA/cm^2 I_{SC} [57]. Again in 2018, Ippili et al. reported the response of PENG made of PVDF-$MAPb_{1-x}Fe_xI_3$ ($0.01 \leq x \leq 0.50$) composite that exhibited ~7.20 V V_{OC} and 0.88 μA/cm^2 I_{SC} for x = 0.07 after poling at 30 kV/cm [58]. Pandey et al. reported the performance of a PENG made of PVDF-$FASnI_3$ in 2019 that delivered ~ 23 V V_{OC} under periodic hammering [59]. Ding et al. showed an interesting response of PENG made of $FAPbBr_3$ nanoparticles and PDMS that was capable to produce 8.5 V V_{OC} and 3.8 μA/cm^2 I_{SC} in 2016 [60]. In 2017, the same group reported an enhanced performance of a PENG ~ 30 V V_{OC} and 6.2 μA/cm^2 I_{SC} that made of $FAPbBr_3$ nanoparticles and PVDF composite [61]. In 2018, Jella et al. reported a very high V_{OC}

and I_{SC} as 45.6 V and 4.7 μA/cm^2, respectively of PENGs made of PVDF-$MAPbI_3$ composite with different concentrations [62]. Sultana et al. reported the enhanced performance of an acoustic generator based on $MAPbBr_3$ -PVDF nanofiber in 2018 [63]. Again, Sultana et al. reported the significant performance of piezoelectric-pyroelectric generator based on $MAPbI_3$-PVDF nanofiber [64]. Su et al. reported an enhanced performance of a photoinduced triboelectric generator made of PVDF-$MAPbI_3$ [65]. Wang et al. reported the outstanding dielectric and electrical properties of triboelectric nanogenerator based on an inorganic halide perovskite $CsPbBr_3$ [66]. The device was fabricated by sandwiching the PVDF- $CsPbBr_3$ composite in between silver and FTO electrodes. After doping Ba^{2+} into the $CsPbBr_3$, surface potential, dielectric property, electron binding energy, etc. were optimized in the $CsPb_{1-x}Ba_xBr_3$. The device made of PVDF-$CsPb_{0.91}Ba_{0.09}Br_3$ exhibited 220 V V_{OC} and 228 mA/m^2 I_{SC} with higher stability [67]. Du et al. showed that partial substitution of halide ions in $CsPbBr_3$ can effectively enhance the performance of triboelectric generators made of this perovskite doped PVDF composites [68]. Jung et al. developed hybrid piezo and triboelectric generator in 2015 based on PVDF and polytetrafluoroethylene that produced remarkably high output [69]. In 2016, Wang et al. reported the satisfactory performance of a hybrid tribo and piezoelectric generator made of P(VDF-TrFE) nanofibers and PDMS/MWCNT composites [70]. In 2018, He et al. reported the ultra-high response of a hybrid piezo and triboelectric nanogenerator based on ZnO nanoflakes-PDMS composite films [71].

2.6. Piezo-catalysis

Various studies show the piezocatalysis. In 2020, Bagchi et al. reported the piezocatalytic effect of MoS_2-PVDF composite [72].

2.7. Hybrid mechanical and solar energy harvesting

Over the years, various attempts have been made to harvest mechanical and solar energy together. The photodetection of ZnO nanowire-based photodetector has been enhanced owing to the piezo-phototronic effect [73]. Rai et al. reported the enhanced performance of photodetection of CdSe / ZnTe core / shell nanowire array through piezo-phototronic effect [74]. Bao et al. mentioned the significant performance of pressure mapping sensor matrix by ZnO nanowire/p-polymer LED array employing piezo-phototronic effect [75]. Zhang et al.

demonstrated in detail the theory behind the piezo-phototronics effect of LEDs [76]. Recently, Maity et al. reported the enhanced response of piezo-phototronic effect using $CsPbI_3$-PVDF composite [77]. Sultana et al. mentioned the outcome of piezo-active photodetector using an optically active hybrid perovskite incorporated polymer matrix in their study [78].

2.8. Piezoelectric supercapacitor

In recent years, self-charging piezoelectric supercapacitors have gained keen interest among researchers. In 2015, Ramadoss et al. fabricated the piezoelectric driven self-charging supercapacitor using PVDF-ZnO as piezo-active separator, soaked in gel electrolyte made of H_3PO_4/PVA, between two MnO_2 electrodes [79]. In 2017, a group of researchers in China reported a significant response to a flexible, self-charging power cell using a piezo-electrolyte [80]. Enhanced performance of a self-charging supercapacitor has been observed using piezo-polymer as the separator between two graphene electrodes. The device exhibited remarkable specific device capacitance ~ 28.46 F g-1 and could be charged up to 112 mV when subjected to external compressive force [81]. Rasheed et al. reported the outcome of a rectifier free, self-charging power unit designed by PVDF-ZnO-RGO piezoelectric matrix [82]. In 2020, Krishnamoorthy et al. reported the self-charging property of the piezo-driven supercapacitor that was able to self charge up to a maximum of 207 mV [83]. The piezo-active supercapacitor was fabricated using siloxane-PVDF piezofibers and a gel electrolyte.

References

[1] H. He, Z. Yang, Y. Xu, A.T. Smith, G. Yang, L. Sun, Perovskite oxides as transparent semiconductors: a review, Nano Converg. 7 (2020) 32. https://doi.org/10.1186/s40580-020-00242-7.

[2] S. Roberts, Dielectric and Piezoelectric Properties of Barium Titanate, Phys. Rev. 71 (1947) 890–895. https://doi.org/10.1103/PhysRev.71.890.

[3] Z. Fan, K. Sun, J. Wang, Perovskites for photovoltaics: a combined review of organic–inorganic halide perovskites and ferroelectric oxide perovskites, J. Mater. Chem. A. 3 (2015) 18809–18828. https://doi.org/10.1039/C5TA04235F.

[4] F.S. Chen, Optically Induced Change of Refractive Indices in $LiNbO_3$ and $LiTaO_3$, J. Appl. Phys. 40 (1969) 3389–3396. https://doi.org/10.1063/1.1658195.

[5] M.R. Das, A. Mukherjee, P. Mitra, Influence of Cu incorporation on ionic conductivity and dielectric relaxation mechanism in NiO thin films synthesized by CBD, J. Mater. Sci. Mater. Electron. 29 (2018) 1216–1231. https://doi.org/10.1007/s10854-017-8024-x.

[6] W.S. Yang, J.H. Noh, N.J. Jeon, Y.C. Kim, S. Ryu, J. Seo, S. Il Seok, High-performance photovoltaic perovskite layers fabricated through intramolecular exchange, Science (80-.). 348 (2015) 1234–1237. https://doi.org/10.1126/science.aaa9272.

[7] J.H. Noh, S.H. Im, J.H. Heo, T.N. Mandal, S. Il Seok, Chemical Management for Colorful, Efficient, and Stable Inorganic–Organic Hybrid Nanostructured Solar Cells, Nano Lett. 13 (2013) 1764–1769. https://doi.org/10.1021/nl400349b.

[8] G.E. Eperon, S.D. Stranks, C. Menelaou, M.B. Johnston, L.M. Herz, H.J. Snaith, Formamidinium lead trihalide: a broadly tunable perovskite for efficient planar heterojunction solar cells, Energy Environ. Sci. 7 (2014) 982. https://doi.org/10.1039/c3ee43822h.

[9] R. Comin, G. Walters, E.S. Thibau, O. Voznyy, Z.-H. Lu, E.H. Sargent, Structural, optical, and electronic studies of wide-bandgap lead halide perovskites, J. Mater. Chem. C. 3 (2015) 8839–8843. https://doi.org/10.1039/C5TC01718A.

[10] J.M. Frost, K.T. Butler, F. Brivio, C.H. Hendon, M. van Schilfgaarde, A. Walsh, Atomistic Origins of High-Performance in Hybrid Halide Perovskite Solar Cells, Nano Lett. 14 (2014) 2584–2590. https://doi.org/10.1021/nl500390f.

[11] T. Leijtens, E.T. Hoke, G. Grancini, D.J. Slotcavage, G.E. Eperon, J.M. Ball, M. De Bastiani, A.R. Bowring, N. Martino, K. Wojciechowski, M.D. McGehee, H.J. Snaith, A. Petrozza, Mapping Electric Field-Induced Switchable Poling and Structural Degradation in Hybrid Lead Halide Perovskite Thin Films, Adv. Energy Mater. 5 (2015) 1500962. https://doi.org/10.1002/aenm.201500962.

[12] S.N. Habisreutinger, T. Leijtens, G.E. Eperon, S.D. Stranks, R.J. Nicholas, H.J. Snaith, Carbon Nanotube/Polymer Composites as a Highly Stable Hole Collection Layer in Perovskite Solar Cells, Nano Lett. 14 (2014) 5561–5568. https://doi.org/10.1021/nl501982b.

[13] M.M. Lee, J. Teuscher, T. Miyasaka, T.N. Murakami, H.J. Snaith, Efficient Hybrid Solar Cells Based on Meso-Superstructured Organometal Halide Perovskites, Science (80). 338 (2012) 643–647. https://doi.org/10.1126/science.1228604.

[14] G.Y. Kim, A. Senocrate, T. Yang, G. Gregori, M. Grätzel, J. Maier, Large tunable photoeffect on ion conduction in halide perovskites and implications for photodecomposition, Nat. Mater. 17 (2018) 445–449. https://doi.org/10.1038/s41563-018-0038-0.

[15] D.W. deQuilettes, W. Zhang, V.M. Burlakov, D.J. Graham, T. Leijtens, A. Osherov, V. Bulović, H.J. Snaith, D.S. Ginger, S.D. Stranks, Photo-induced halide redistribution in organic–inorganic perovskite films, Nat. Commun. 7 (2016) 11683. https://doi.org/10.1038/ncomms11683.

[16] I. Deretzis, A. Alberti, G. Pellegrino, E. Smecca, F. Giannazzo, N. Sakai, T. Miyasaka, A. La Magna, Atomistic origins of CH 3 NH 3 PbI 3 degradation to PbI_2 in vacuum, Appl. Phys. Lett. 106 (2015) 131904. https://doi.org/10.1063/1.4916821.

[17] B. Brunetti, C. Cavallo, A. Ciccioli, G. Gigli, A. Latini, On the Thermal and Thermodynamic (In)Stability of Methylammonium Lead Halide Perovskites, Sci. Rep. 6 (2016) 31896. https://doi.org/10.1038/srep31896.

[18] A. Dualeh, P. Gao, S. Il Seok, M.K. Nazeeruddin, M. Grätzel, Thermal Behavior of Methylammonium Lead-Trihalide Perovskite Photovoltaic Light Harvesters, Chem. Mater. 26 (2014) 6160–6164. https://doi.org/10.1021/cm502468k.

[19] C. Huang, J. Song, W. Lee, Y. Ding, Z. Gao, Y. Hao, L.-J. Chen, Z.L. Wang, GaN Nanowire Arrays for High-Output Nanogenerators, J. Am. Chem. Soc. 132 (2010) 4766–4771. https://doi.org/10.1021/ja909863a.

[20] S.-H. Shin, Y.-H. Kim, M.H. Lee, J.-Y. Jung, J. Nah, Hemispherically Aggregated BaTiO 3 Nanoparticle Composite Thin Film for High-Performance Flexible Piezoelectric Nanogenerator, ACS Nano. 8 (2014) 2766–2773. https://doi.org/10.1021/nn406481k.

[21] J. Chun, K.Y. Lee, C.-Y. Kang, M.W. Kim, S.-W. Kim, J.M. Baik, Embossed Hollow Hemisphere-Based Piezoelectric Nanogenerator and Highly Responsive Pressure

Sensor, Adv. Funct. Mater. 24 (2014) 2038–2043. https://doi.org/10.1002/adfm.201302962.

[22] H. Liu, X. Lin, S. Zhang, Y. Huan, S. Huang, X. Cheng, Enhanced performance of piezoelectric composite nanogenerator based on gradient porous PZT ceramic structure for energy harvesting, J. Mater. Chem. A. 8 (2020) 19631–19640. https://doi.org/10.1039/D0TA03054F.

[23] H. Wu, Y. Huang, F. Xu, Y. Duan, Z. Yin, Energy Harvesters for Wearable and Stretchable Electronics: From Flexibility to Stretchability, Adv. Mater. 28 (2016) 9881–9919. https://doi.org/10.1002/adma.201602251.

[24] C. Chang, V.H. Tran, J. Wang, Y.-K. Fuh, L. Lin, Direct-Write Piezoelectric Polymeric Nanogenerator with High Energy Conversion Efficiency, Nano Lett. 10 (2010) 726–731. https://doi.org/10.1021/nl9040719.

[25] M. Lee, C.-Y. Chen, S. Wang, S.N. Cha, Y.J. Park, J.M. Kim, L.-J. Chou, Z.L. Wang, A Hybrid Piezoelectric Structure for Wearable Nanogenerators, Adv. Mater. 24 (2012) 1759–1764. https://doi.org/10.1002/adma.201200150.

[26] S. Cha, S.M. Kim, H. Kim, J. Ku, J.I. Sohn, Y.J. Park, B.G. Song, M.H. Jung, E.K. Lee, B.L. Choi, J.J. Park, Z.L. Wang, J.M. Kim, K. Kim, Porous PVDF As Effective Sonic Wave Driven Nanogenerators, Nano Lett. 11 (2011) 5142–5147. https://doi.org/10.1021/nl202208n.

[27] H. Pan, B. Na, R. Lv, C. Li, J. Zhu, Z. Yu, Polar phase formation in poly(vinylidene fluoride) induced by melt annealing, J. Polym. Sci. Part B Polym. Phys. 50 (2012) 1433–1437. https://doi.org/10.1002/polb.23146.

[28] P. Martins, C.M. Costa, M. Benelmekki, G. Botelho, S. Lanceros-Mendez, On the origin of the electroactive poly(vinylidene fluoride) β-phase nucleation by ferrite nanoparticles via surface electrostatic interactions, CrystEngComm. 14 (2012) 2807. https://doi.org/10.1039/c2ce06654h.

[29] W.W. Doll, J.B. Lando, The polymorphism of poly(vinylidene fluoride) IV. The structure of high-pressure-crystallized poly(vinylidene fluoride), J. Macromol. Sci. Part B. 4 (1970) 889–896. https://doi.org/10.1080/00222347008217130.

[30] D. Yang, Y. Chen, β-phase formation of poly(vinylidene fluoride) from the melt induced by quenching, J. Mater. Sci. Lett. 6 (1987) 599–603. https://doi.org/10.1007/BF01739296.

[31] H. Kawai, The Piezoelectricity of Poly (vinylidene Fluoride), Jpn. J. Appl. Phys. 8 (1969) 975. https://doi.org/10.1143/JJAP.8.975.

[32] B.-E. El Mohajir, N. Heymans, Changes in structural and mechanical behaviour of PVDF with processing or thermal treatment., Polymer (Guildf). 42 (2001) 7017–7023. https://doi.org/10.1016/S0032-3861(01)00184-7.

[33] R. Gregorio, E.M. Ueno, Effect of crystalline phase, orientation and temperature on the dielectric properties of poly (vinylidene fluoride) (PVDF), J. Mater. Sci. 34 (1999) 4489–4500. https://doi.org/10.1023/A:1004689205706.

[34] B. Mohammadi, A.A. Yousefi, S.M. Bellah, Effect of tensile strain rate and elongation on crystalline structure and piezoelectric properties of PVDF thin films, Polym. Test. 26 (2007) 42–50. https://doi.org/10.1016/j.polymertesting.2006.08.003.

[35] T. Hattori, M. Kanaoka, H. Ohigashi, Improved piezoelectricity in thick lamellar β-form crystals of poly(vinylidene fluoride) crystallized under high pressure, J. Appl. Phys. 79 (1996) 2016–2022. https://doi.org/10.1063/1.361055.

[36] T.R.T. Dargaville, M.C. Celina, J. Elliot, P.M. Chaplya, J.M. Elliott, G.D. Jones, D.M. Mowery, R. a Assink, R.L. Clough, J.W. Martin, Characterization, performance and optimization of PVDF as a piezoelectric film for advanced space mirror concepts, Optimization. (2005). https://doi.org/SAND2005-6846.

[37] S.K. Mahadeva, J. Berring, K. Walus, B. Stoeber, Effect of poling time and grid voltage on phase transition and piezoelectricity of poly(vinyledene fluoride) thin films using corona poling, J. Phys. D. Appl. Phys. 46 (2013) 285305. https://doi.org/10.1088/0022-3727/46/28/285305.

[38] P. Thakur, A. Kool, N.A. Hoque, B. Bagchi, F. Khatun, P. Biswas, D. Brahma, S. Roy, S. Banerjee, S. Das, Superior performances of in situ synthesized ZnO/PVDF thin film based self-poled piezoelectric nanogenerator and self-charged photo-power bank with high durability, Nano Energy. 44 (2018) 456–467.

https://doi.org/10.1016/j.nanoen.2017.11.065.

[39] T.K. Sinha, S.K. Ghosh, R. Maiti, S. Jana, B. Adhikari, D. Mandal, S.K. Ray, Graphene-Silver-Induced Self-Polarized PVDF-Based Flexible Plasmonic Nanogenerator Toward the Realization for New Class of Self Powered Optical Sensor, ACS Appl. Mater. Interfaces. 8 (2016) 14986–14993. https://doi.org/10.1021/acsami.6b01547.

[40] M. Benz, W.B. Euler, O.J. Gregory, The Role of Solution Phase Water on the Deposition of Thin Films of Poly(vinylidene fluoride), Macromolecules. 35 (2002) 2682–2688. https://doi.org/10.1021/ma011744f.

[41] S.K. Ghosh, A. Biswas, S. Sen, C. Das, K. Henkel, D. Schmeisser, D. Mandal, Yb3+ assisted self-polarized PVDF based ferroelectretic nanogenerator: A facile strategy of highly efficient mechanical energy harvester fabrication, Nano Energy. 30 (2016) 621–629. https://doi.org/10.1016/j.nanoen.2016.10.042.

[42] R. Tian, Q. Xu, C. Lu, X. Duan, R.-G. Xiong, Spontaneous polarization switching and piezoelectric enhancement of PVDF through strong hydrogen bonds induced by layered double hydroxides, Chem. Commun. 53 (2017) 7933–7936. https://doi.org/10.1039/C7CC04240J.

[43] S. Maji, P.K. Sarkar, L. Aggarwal, S.K. Ghosh, D. Mandal, G. Sheet, S. Acharya, Self-oriented β-crystalline phase in the polyvinylidene fluoride ferroelectric and piezo-sensitive ultrathin Langmuir–Schaefer film, Phys. Chem. Chem. Phys. 17 (2015) 8159–8165. https://doi.org/10.1039/C5CP00218D.

[44] A. Tamang, S.K. Ghosh, S. Garain, M.M. Alam, J. Haeberle, K. Henkel, D. Schmeisser, D. Mandal, DNA-Assisted β-phase Nucleation and Alignment of Molecular Dipoles in PVDF Film: A Realization of Self-Poled Bioinspired Flexible Polymer Nanogenerator for Portable Electronic Devices, ACS Appl. Mater. Interfaces. 7 (2015) 16143–16147. https://doi.org/10.1021/acsami.5b04161.

[45] W.A. Yee, M. Kotaki, Y. Liu, X. Lu, Morphology, polymorphism behavior and molecular orientation of electrospun poly(vinylidene fluoride) fibers, Polymer (Guildf). 48 (2007) 512–521. https://doi.org/10.1016/j.polymer.2006.11.036.

[46] J. Zheng, A. He, J. Li, C.C. Han, Polymorphism Control of Poly(vinylidene fluoride)

through Electrospinning, Macromol. Rapid Commun. 28 (2007) 2159–2162. https://doi.org/10.1002/marc.200700544.

[47] C. Ribeiro, V. Sencadas, J.L.G. Ribelles, S. Lanceros-Méndez, Influence of Processing Conditions on Polymorphism and Nanofiber Morphology of Electroactive Poly(vinylidene fluoride) Electrospun Membranes, Soft Mater. 8 (2010) 274–287. https://doi.org/10.1080/1539445X.2010.495630.

[48] V.F. Cardoso, G. Minas, C.M. Costa, C.J. Tavares, S. Lanceros-Mendez, Micro and nanofilms of poly(vinylidene fluoride) with controlled thickness, morphology and electroactive crystalline phase for sensor and actuator applications, Smart Mater. Struct. 20 (2011) 087002. https://doi.org/10.1088/0964-1726/20/8/087002.

[49] W. Li, Z. Man, J. Zeng, L. Zheng, G. Li, A. Kassiba, Relationship of Giant Dielectric Constant and Ion Migration in $CH_3NH_3PbI_3$ Single Crystal Using Dielectric Spectroscopy, J. Phys. Chem. C. 124 (2020) 13348–13355. https://doi.org/10.1021/acs.jpcc.0c02971.

[50] T. Ghosh, S.K. Sharma, D. Pradhan, Giant Dielectric Constant and Superior Photovoltaic Property of the Mechanochemically Synthesized Stable $CH_3NH_3PbBr_3$ in a Hole Transporter-Free Solar Cell, ACS Sustain. Chem. Eng. 8 (2020) 1445–1454. https://doi.org/10.1021/acssuschemeng.9b05678.

[51] E.J. Juarez-Perez, R.S. Sanchez, L. Badia, G. Garcia-Belmonte, Y.S. Kang, I. Mora-Sero, J. Bisquert, Photoinduced Giant Dielectric Constant in Lead Halide Perovskite Solar Cells, J. Phys. Chem. Lett. 5 (2014) 2390–2394. https://doi.org/10.1021/jz5011169.

[52] D.P. Almond, C.R. Bowen, An Explanation of the Photoinduced Giant Dielectric Constant of Lead Halide Perovskite Solar Cells, J. Phys. Chem. Lett. 6 (2015) 1736–1740. https://doi.org/10.1021/acs.jpclett.5b00620.

[53] P. Thongbai, S. Tangwancharoen, T. Yamwong, S. Maensiri, Dielectric relaxation and dielectric response mechanism in (Li, Ti)-doped NiO ceramics, J. Phys. Condens. Matter. 20 (2008) 395227. https://doi.org/10.1088/0953-8984/20/39/395227.

[54] J. Shanker, J. Ananthaiah, N. Pavan Kumar, K. Venkataramana, M. Anand pandarinath,

U.P. Ujwal, P. Raju, E. Meher Abhinav, D. Suresh babu, Giant dielectric behavior in $NdCrO_3$ perovskite nanoparticles, IOP Conf. Ser. Mater. Sci. Eng. 1233 (2022) 012011. https://doi.org/10.1088/1757-899X/1233/1/012011.

[55] Z.L. Wang, J. Song, Piezoelectric Nanogenerators Based on Zinc Oxide Nanowire Arrays, Science (80). 312 (2006) 242–246. https://doi.org/10.1126/science.1124005.

[56] Y.-J. Kim, T.-V. Dang, H.-J. Choi, B.-J. Park, J.-H. Eom, H.-A. Song, D. Seol, Y. Kim, S.-H. Shin, J. Nah, S.-G. Yoon, Piezoelectric properties of $CH_3NH_3PbI_3$ perovskite thin films and their applications in piezoelectric generators, J. Mater. Chem. A. 4 (2016) 756–763. https://doi.org/10.1039/C5TA09662F.

[57] S. Ippili, V. Jella, J.-H. Eom, J. Kim, S. Hong, J.-S. Choi, V.-D. Tran, N. Van Hieu, Y.-J. Kim, H.-J. Kim, S.-G. Yoon, An eco-friendly flexible piezoelectric energy harvester that delivers high output performance is based on lead-free $MASnI_3$ films and $MASnI_3$-PVDF composite films, Nano Energy. 57 (2019) 911–923. https://doi.org/10.1016/j.nanoen.2019.01.005.

[58] S. Ippili, V. Jella, J. Kim, S. Hong, S. Yoon, Enhanced piezoelectric output performance via control of dielectrics in Fe2+-incorporated $MAPbI_3$ perovskite thin films: Flexible piezoelectric generators, Nano Energy. 49 (2018) 247–256. https://doi.org/10.1016/j.nanoen.2018.04.031.

[59] R. Pandey, G. SB, S. Grover, S.K. Singh, A. Kadam, S. Ogale, U. V. Waghmare, V.R. Rao, D. Kabra, Microscopic Origin of Piezoelectricity in Lead-Free Halide Perovskite: Application in Nanogenerator Design, ACS Energy Lett. 4 (2019) 1004–1011. https://doi.org/10.1021/acsenergylett.9b00323.

[60] R. Ding, H. Liu, X. Zhang, J. Xiao, R. Kishor, H. Sun, B. Zhu, G. Chen, F. Gao, X. Feng, J. Chen, X. Chen, X. Sun, Y. Zheng, Flexible Piezoelectric Nanocomposite Generators Based on Formamidinium Lead Halide Perovskite Nanoparticles, Adv. Funct. Mater. 26 (2016) 7708–7716. https://doi.org/10.1002/adfm.201602634.

[61] R. Ding, X. Zhang, G. Chen, H. Wang, R. Kishor, J. Xiao, F. Gao, K. Zeng, X. Chen, X.W. Sun, Y. Zheng, High-performance piezoelectric nanogenerators composed of formamidinium lead halide perovskite nanoparticles and poly(vinylidene fluoride),

Nano Energy. 37 (2017) 126–135. https://doi.org/10.1016/j.nanoen.2017.05.010.

[62] V. Jella, S. Ippili, J.-H. Eom, J. Choi, S.-G. Yoon, Enhanced output performance of a flexible piezoelectric energy harvester based on stable $MAPbI_3$-PVDF composite films, Nano Energy. 53 (2018) 46–56. https://doi.org/10.1016/j.nanoen.2018.08.033.

[63] A. Sultana, M.M. Alam, P. Sadhukhan, U.K. Ghorai, S. Das, T.R. Middya, D. Mandal, Organo-lead halide perovskite regulated green light emitting poly(vinylidene fluoride) electrospun nanofiber mat and its potential utility for ambient mechanical energy harvesting application, Nano Energy. 49 (2018) 380–392. https://doi.org/10.1016/j.nanoen.2018.04.057.

[64] A. Sultana, S.K. Ghosh, M.M. Alam, P. Sadhukhan, K. Roy, M. Xie, C.R. Bowen, S. Sarkar, S. Das, T.R. Middya, D. Mandal, Methylammonium Lead Iodide Incorporated Poly(vinylidene fluoride) Nanofibers for Flexible Piezoelectric–Pyroelectric Nanogenerator, ACS Appl. Mater. Interfaces. 11 (2019) 27279–27287. https://doi.org/10.1021/acsami.9b04812.

[65] L. Su, Z. Zhao, H. Li, Y. Wang, S. Kuang, G. Cao, Z. Wang, G. Zhu, Photoinduced enhancement of a triboelectric nanogenerator based on an organolead halide perovskite, J. Mater. Chem. C. 4 (2016) 10395–10399. https://doi.org/10.1039/C6TC03513B.

[66] Y. Wang, J. Duan, X. Yang, L. Liu, L. Zhao, Q. Tang, The unique dielectricity of inorganic perovskites toward high-performance triboelectric nanogenerators, Nano Energy. 69 (2020) 104418. https://doi.org/10.1016/j.nanoen.2019.104418.

[67] J. Du, X. Yang, J. Duan, Y. Wang, Q. Tang, Tailoring all-inorganic cesium lead halide perovskites for robust triboelectric nanogenerators, Nano Energy. 70 (2020) 104514. https://doi.org/10.1016/j.nanoen.2020.104514.

[68] J. Du, J. Duan, X. Yang, Y. Wang, Y. Duan, Q. Tang, Charge boosting and storage by tailoring rhombus all-inorganic perovskite nanoarrays for robust triboelectric nanogenerators, Nano Energy. 74 (2020) 104845. https://doi.org/10.1016/j.nanoen.2020.104845.

[69] W.-S. Jung, M.-G. Kang, H.G. Moon, S.-H. Baek, S.-J. Yoon, Z.-L. Wang, S.-W. Kim, C.-Y. Kang, High Output Piezo/Triboelectric Hybrid Generator, Sci. Rep. 5 (2015)

9309. https://doi.org/10.1038/srep09309.

[70] X. Wang, B. Yang, J. Liu, Y. Zhu, C. Yang, Q. He, A flexible triboelectric-piezoelectric hybrid nanogenerator based on P(VDF-TrFE) nanofibers and PDMS/MWCNT for wearable devices, Sci. Rep. 6 (2016) 36409. https://doi.org/10.1038/srep36409.

[71] W. He, Y. Qian, B.S. Lee, F. Zhang, A. Rasheed, J.-E. Jung, D.J. Kang, Ultrahigh Output Piezoelectric and Triboelectric Hybrid Nanogenerators Based on ZnO Nanoflakes/Polydimethylsiloxane Composite Films, ACS Appl. Mater. Interfaces. 10 (2018) 44415–44420. https://doi.org/10.1021/acsami.8b15410.

[72] B. Bagchi, N.A. Hoque, N. Janowicz, S. Das, M.K. Tiwari, Re-usable self-poled piezoelectric/piezocatalytic films with exceptional energy harvesting and water remediation capability, Nano Energy. 78 (2020) 105339. https://doi.org/10.1016/j.nanoen.2020.105339.

[73] Q. Yang, X. Guo, W. Wang, Y. Zhang, S. Xu, D.H. Lien, Z.L. Wang, Enhancing Sensitivity of a Single ZnO Micro-/Nanowire Photodetector by Piezo-phototronic Effect, ACS Nano. 4 (2010) 6285–6291. https://doi.org/10.1021/nn1022878.

[74] S.C. Rai, K. Wang, J. Chen, J.K. Marmon, M. Bhatt, S. Wozny, Enhanced Broad Band Photodetection through Piezo- Phototronic Effect in CdSe / ZnTe Core / Shell Nanowire Array, Adv. Electron. Mater. 1 (2015) 1–7. https://doi.org/10.1002/aelm.201400050.

[75] R. Bao, C. Wang, L. Dong, R. Yu, K. Zhao, Z.L. Wang, Flexible and Controllable Piezo-Phototronic Pressure Mapping Sensor Matrix by ZnO NW / p-Polymer LED Array, Adv. Funct. Mater. 25 (2015) 2884–2891. https://doi.org/10.1002/adfm.201500801.

[76] Y. Zhang, Z.L. Wang, Theory of Piezo-Phototronics for Light-Emitting Diodes, Adv. Mater. 24 (2012) 4712–4718. https://doi.org/10.1002/adma.201104263.

[77] K. Maity, U. Pal, H. Krishna, P. Maji, P. Sadhukhan, Z. Mallick, S. Das, B. Mondal, D. Mandal, Nano Energy Piezo-phototronic effect in highly stable $CsPbI_3$ -PVDF composite for self-powered nanogenerator and photodetector, Nano Energy. 92 (2022) 106743. https://doi.org/10.1016/j.nanoen.2021.106743.

[78] A. Sultana, P. Sadhukhan, M.M. Alam, S. Das, T.R. Middya, D. Mandal, Organo-Lead

Halide Perovskite Induced Electroactive β-Phase in Porous PVDF Films: An Excellent Material for Photoactive Piezoelectric Energy Harvester and Photodetector, ACS Appl. Mater. Interfaces. 10 (2018) 4121–4130. https://doi.org/10.1021/acsami.7b17408.

[79] A. Ramadoss, B. Saravanakumar, W. Lee, Y. Kim, S.J. Kim, Z.L. Wang, Piezoelectric Driven Self-Charging Supercapacitor Power Cell, ACS Nano. 9 (2015) 4337–4345. https://doi.org/https://doi.org/10.1021/acsnano.5b00759.

[80] H. He, Y. Fu, T. Zhao, X. Gao, L. Xing, Y. Zhang, X. Xue, All-solid-state flexible self-charging power cell basing on piezo-electrolyte for harvesting/storing body-motion energy and powering wearable electronics, Nano Energy. 39 (2017) 590–600. https://doi.org/10.1016/j.nanoen.2017.07.033.

[81] S. Sahoo, K. Krishnamoorthy, P. Pazhamalai, V.K. Mariappan, S. Manoharan, S. Kim, High performance self-charging supercapacitors using a porous PVDF-ionic liquid electrolyte sandwiched between two-dimensional graphene electrodes, J. Mater. Chem. A. 7 (2019) 21693–21703. https://doi.org/10.1039/c9ta06245a.

[82] A. Rasheed, W. He, Y. Qian, H. Park, D.J. Kang, Flexible Supercapacitor Type Rectifier-free Self-charging Power Unit Based on a Multifunctional PVDF-ZnO-RGO Piezoelectric Matrix, ACS Appl. Mater. Interfaces. 12 (2020) 20891–20900. https://doi.org/10.1021/acsami.9b22362.

[83] K. Krishnamoorthy, P. Pazhamalai, V.K. Mariappan, S.S. Nardekar, S. Sahoo, S. Kim, Probing the energy conversion process in piezoelectric-driven electrochemical self-charging supercapacitor power cell using piezoelectrochemical spectroscopy, Nat. Commun. 11 (2020) 2351. https://doi.org/10.1038/s41467-020-15808-6.

CHAPTER 3

3. Methods and Characterization

3.1. Introduction

This chapter will encompass different experimental methods and characterizations used in my research work. It has been divided into three parts. The first part comprises the synthesis and preparation methods of the perovskites and the PVDF-perovskite composites I have used in this dissertation. The second part will cover the description of the experimental procedures used to characterize different properties of the prepared samples. The fabrication methods of the energy harvesting devices are discussed in the last part of this chapter.

I have synthesized one of the potential OIHPs propylammonium lead halide ($C_3H_7NH_3PbX_3$) via sol-gel method. To avoid the lead content, a promising oxide perovskite neodymium manganate ($NdMnO_3$) was prepared via sol-gel method. Nanofiber of PVDF@$C_3H_7NH_3PbI_3$ was prepared by electrospinning method. $C_3H_7NH_3PbI_3$ and $NdMnO_3$ were also incorporated in the PVDF through self-poling method. Structural confirmation of the synthesized samples was obtained from X-ray diffraction technique (XRD). Surface morphology of the samples was gained from Field emission scanning electron microscopy (FESEM). Complex impedance spectroscopy was employed to characterize the dielectric properties of the samples. High-resolution transmission electron microscopy (HR-TEM) was used to perform the microstructural study. X-ray photoelectron spectroscopy (XPS) was used to analyze the elemental composition and the chemical states in the material. The optical properties of the optically active samples were attained using UV-Vis and photoluminescence spectroscopy (PL). The ferroelectric content of the ferroelectric films and fiber was computed from Fourier transform infrared spectroscopy (FTIR). Thermal stability along with the crystallinity of the samples was assessed with the help of Thermogravimetric analysis (TGA) and Differential scanning calorimetry (DSC). The elastic property of the ferroelectric fiber and films was studied using Universal testing machine (UTM). A solar simulator was employed to

irradiate the fabricated photodetectors. The output performance of the piezo and triboelectric nanogenerators was investigated based on V_{OC} and I_{SC}.

3.2. Material synthesis

3.2.1. Sol-gel synthesis of $C_3H_7NH_3PbX_3$

To prepare $C_3H_7NH_3PbX_3$, firstly, propylammonium salt ($C_3H_7NH_3I$, $C_3H_7NH_3Br$) was prepared. Hyrdoiodic / hydrobromic acid was mixed in an equimolar ratio with propylamine ($C_3H_7NH_2$) and stirred continuously for 2 hours at 0 ^oC. The resulting solution was dried and washed by diethyl ether for several times to pull out the unreacted acid. Next, the mixture was dried in a vacuum at 60 ^oC for 12 hours to form propylammonium iodide/bromide.

In the next step, the equimolar ratio of $C_3H_7NH_3I$ / $C_3H_7NH_3Br$ and PbI_2 / $PbBr_2$ were dissolved in dimethylformamide (DMF) at 60 ^oC and stirred for 10 hours. The solution was filtered and dried at 65 ^oC to obtain the desired perovskite ~ yellow coloured $C_3H_7NH_3PbI_3$ and white $C_3H_7NH_3PbBr_3$. Fig. 3.1a-b exhibits the digital photograph of the solution of $C_3H_7NH_3I$-PbI_2 in DMF before filtration and the powder form of $C_3H_7NH_3PbI_3$, c. represents the powder

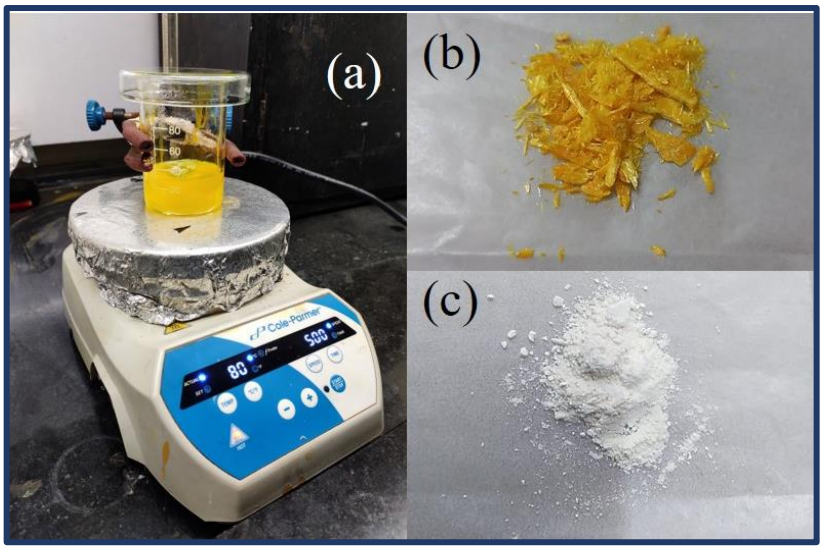

Fig. 3.1a-b. The digital photograph of $C_3H_7NH_3I$-PbI_2 in DMF and $C_3H_7NH_3PbI_3$ in powder form, c. The powder form of $C_3H_7NH_3PbBr_3$.

form of $C_3H_7NH_3PbBr_3$.

3.2.2. Sol-gel synthesis of $NdMnO_3$ nanoparticles

Neodymium oxide (Nd_2O_3) and manganese acetate tetrahydrate $(CH_3COO)_2Mn.\ 4H_2O$) were mixed in a stoichiometric ratio and converted to the respective nitrates by adding a few drops of conc. HNO_3 to the precursors. The nitrate solution was then allowed to boil for 15 minutes

Fig. 3.1c. The powder form of $NdMnO_3$ nanoparticles

to remove excess HNO_3. To mix the metal ions in an atomic scale, a proper amount of citric acid was added to the solution. Considering that only two of the citrate ions take part in chemical bonding with metal ions, the amount of citric acid was estimated such that all the metal ions form metal citrate. Ethylene glycol was added later to the mixture and stirred for 4 hours to form a homogeneous solution. The solution was then kept at 80 ^oC for 12 hours to obtain the gel. The gel was kept at 200 ^oC until it became brownish powder. The powder was heated at 600 ^oC and 800 ^oC respectively, each step for 6 hours, followed by intermediate grinding to form well-crystallized oxides. The digital photograph of the prepared sample is displayed in Fig. 3.1c.

3.2.3. Preparation of $C_3H_7NH_3PbI_3$-PVDF nanofiber by the method of electrospinning

To prepare the stock solution, 10 wt% PVDF was dissolved in a mixture of DMF and acetone (3:5) by stirring continuously for 3 hours at 60 ^oC. A transparent solution was formed in which 3.21, 4.76, and 6.20 wt% (w/w) of previously synthesized $C_3H_7NH_3PbI_3$ was added and stirred for another 3 hours at the same temperature. The presence of DMF turned the transparent solution into a yellow color with the addition of $C_3H_7NH_3PbI_3$ as shown in Fig. 3.2a.

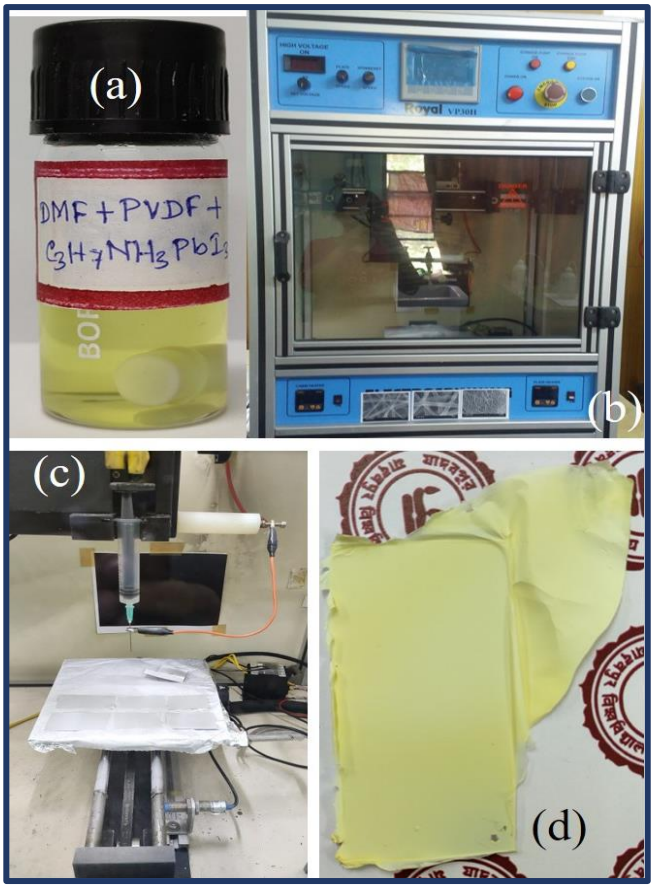

Fig. 3.2. a) The solution of $C_3H_7NH_3PbI_3$+PVDF+DMF, b) Electrospin set-up, c) PVDF nanofiber formation, d) 4.76 wt% of $C_3H_7NH_3PbI_3$ incorporated PVDF nanofiber.

For electrospinning, a 10 ml hypertonic syringe of diameter 8 mm was filled with the homogeneous solutions and placed in the electrospinning set-up. The solution was squeezed out by the pump through the needle of the syringe at a flow rate of 0.8 ml/hour and so formed nanofibers were deposited on the aluminium foil-wrapped collector plate. The temperature of the collector plate was sustained at 70 ^oC to evaporate the solvent. The distance between the collector plate and the needle tip of the syringe was maintained at 6.5 cm during the formation of nanofibers. All the nanofibers were prepared under a high voltage of 19 kV. The prepared nanofibers were collected from the aluminium foil for further characterization and device fabrication. Fig. 3.2b shows the digital photograph of the electrospinning set-up. The formation of PVDF nanofiber is illuminated in Fig. 3.2c. In Fig. 3.2d, the photograph of 4.76 wt % of $C_3H_7NH_3PbI_3$ incorporated PVDF nanofibers is illustrated.

3.2.4. Self-poled $C_3H_7NH_3PbI_3$-PVDF films

Firstly, 10 wt% of PVDF solution was prepared by dissolving the PVDF powder in DMF and stirring continuously for 3 hours at 60 ^oC. Next, 5, 10, 15, and 20 wt% of freshly synthesized $C_3H_7NH_3PbI_3$ powder was mixed in the PVDF solution and stirred for another 4 hours at 60 ^oC to form homogeneous precursor solutions of $C_3H_7NH_3PbI_3$@PVDF composites. Lastly, self-poled $C_3H_7NH_3PbI_3$@PVDF films were achieved by consecutive annealing of the respective precursor solutions at 90 ^oC for 2.5 hours and 130 ^oC for 3.5 hours. A reference film using neat PVDF was also formed following the same procedure to perform a comparative study. Fig. 3.3a-c exhibit the digital photographs of the solution of 15 wt% of $C_3H_7NH_3PbI_3$@PVDF in DMF, prepared films and the flexibility of the prepared film.

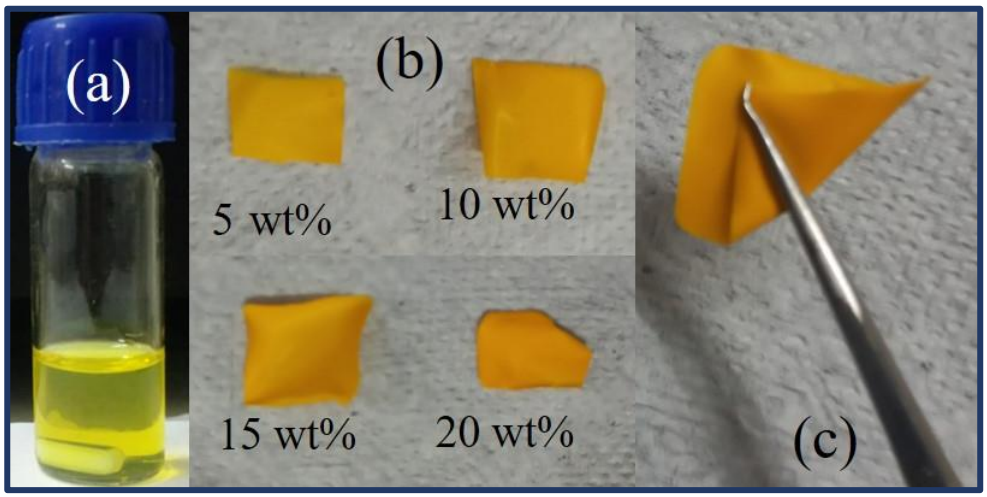

Fig. 3.3. Digital photographs of a) Solution of 15 wt% of $C_3H_7NH_3PbI_3$@PVDF in DMF, b) Prepared films, c) Flexibility of the as prepared film.

3.2.5. Self-poled $NdMnO_3$-PVDF films

PVDF solution was prepared by dissolving 100 mg pure PVDF in 1 ml DMF by continuously stirring the mixture at 60 ^oC for 4 hours. Next, 3, 5, 7, 10, vol % (v/v) of $NdMnO_3$ nanoparticles were added to the stock solution and kept stirring at room temperature for 24 hours. The transparent stock solution became black with the addition of $NdMnO_3$ nanoparticles. The composite precursor solutions were ultrasonicated for 45 minutes and then cast on a glass slide to obtain the composite films by annealing at 90 ^oC for 2 hours followed by annealing at 130 ^oC for 3 hours. This annealing procedure helps to enhance the piezo-active phase of the film.

as three-dimensional gratings for X-ray wavelengths similar to the spacing of planes in a crystal lattice.

This characterization technique is based on the diffraction of X-ray from the lattice plane of a material. In the crystalline and polycrystalline materials, lattice cells are periodically arranged in a repetitive way forming a diffraction grating for X-ray as shown in Fig. 3.4a. When X-ray beam falls at the planes, it gets diffracted. The angle of diffraction is controlled by the lattice planes. In the instrument, a goniometer is used to rotate the detector along the incident beam at an angle 2θ. On the other hand, the sample is placed at an angle θ. The schematic diagram of the instrumental set-up is illustrated in Fig. 3.4b. A new diffraction peak appears depending on the crystal structure and orientation of the sample. This phenomenon is governed by the Bragg's equation

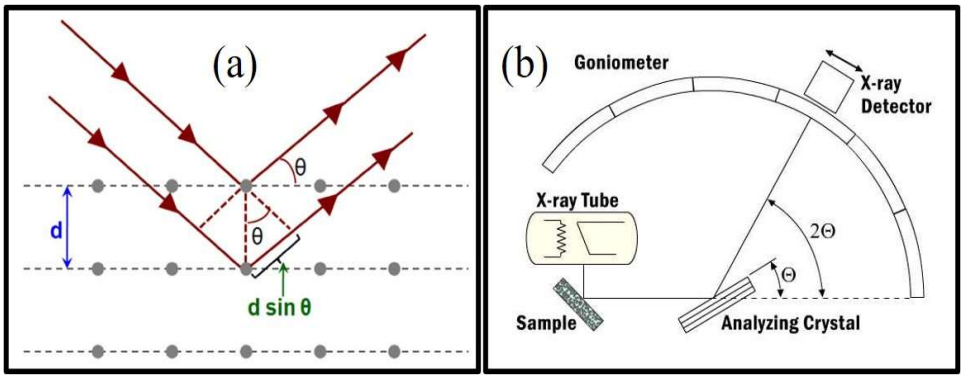

Fig. 3.4. a) Schematic diagram of X-ray diffraction, b) Schematic diagram of XRD set up.

$$2dsin\theta = n\lambda \tag{3.1}$$

Here, d refers to the distance between the diffracting planes, n represents the order of diffraction, and λ denotes the wavelength of the x-ray. An X-ray diffraction pattern is obtained for different scanned θ. From analyzing θ, various information such as lattice phase, microstrain, and grain size of the sample can be computed. The grain size of the samples can be evaluated using Scherrer's formula

$$D = \frac{0.89}{\beta cos\theta} \tag{3.2}$$

D is the crystallite size in the direction normal to the reflecting planes and β denotes the FWHM of the peak in radian. Williamson and Hall modified Scherrer's formula as given below

microstrain, and grain size of the sample can be computed. The grain size of the samples can be evaluated using Scherrer's formula

$$D = \frac{0.89\lambda}{\beta cos\theta} \tag{3.2}$$

D is the crystallite size in the direction normal to the reflecting planes and β denotes the FWHM of the peak in radian. Williamson and Hall modified Scherrer's formula as given below

$$\beta cos\theta = \frac{0.89\lambda}{D} + 2\varepsilon sin\theta \tag{3.3}$$

Here, ε is the microstrain of the sample.

The crystalline content ($\times_{ct}$) of the polymer can also be investigated from XRD

Fig. 3.4c. displays the X-ray powder diffractometer (Bruker D-8 Advance (Germany)).

analysis using the relation

$$\times_{ct} = \frac{\sum A_{crys}}{\sum A_{crys} + \sum A_{amorph}} \times 100\% \tag{3.4}$$

Here, $\sum A_{crys}$ and $\sum A_{amorph}$ denote the integral area of the crystalline and amorphous portions of the concerned samples.

In my research work, all our XRD has been carried out in X-ray powder diffractometer Bruker D-8 Advance (Germany) (λ = 1.5406 Å) and PETRA III beamline P 2.2 at DESY, Germany (λ = 0.2074 Å). Fig. 3.4c. exhibits the digital photograph of X-ray powder diffractometer Bruker D-8 Advance (Germany).

3.3.2. Field Emission Scanning Electron Microscopy (FESEM)

Field emission scanning electron microscopy (FESEM) is a high-resolution imaging spectroscopy used to investigate the surface morphology and topology of the samples. Electron beam is used as a source in SEM resulting in a number of advantages over optical microscopy.

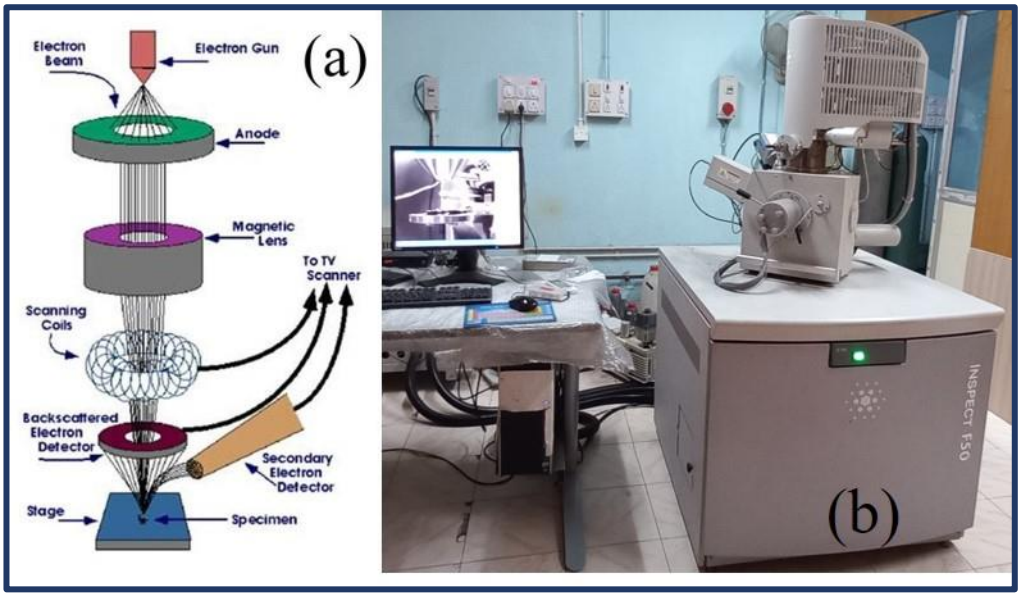

Fig. 3.5. a) Schematic diagram of SEM machine, b) Digital image of FESEM FEI INSPECT F50.

The schematic diagram of a typical SEM is depicted in Fig. 3.5a that shows a high energy electron gun is placed at the top. The electron gun can yield electron beams of energy ~ 1 kV to 30 kV. The filament used here is generally made up of high melting point materials like tungsten of lanthanum hexaboride and is operated under high applied voltage. The electron beam is shaped and focused on the sample through a no. of electromagnetic lens and aperture system. The SEM column and sample chamber are maintained at a high vacuum to avoid the loss of electrons during the collision with air molecules. Electron beam produces secondary

electrons, back scattered electrons, auger electrons, characteristic X-ray etc. that provide different information about the samples. For elemental analysis, characteristic X-ray is used in energy dispersive X-ray spectroscopy (EDX). Secondary and back scattered electrons are collected with the help of two detectors for imaging. As the electron beam is focused on a highly confined region, it is necessary to scan the entire surface of the sample to form a 2D image. Surface morphology of samples in any solid form like powder, thin film, single crystal, etc. can be obtained using SEM. Sometimes, a thin layer of gold or platinum is used to coat poorly conducting samples to remove the accumulated charges on the sample during exposure to the electron beam.

In this dissertation, all the SEM analyses were carried out using FESEM of Zeiss, Germany, model: SUPRA 40 and FEI, INSPECT F50. In Fig. 3.5b, the digital photograph of FESEM FEI, INSPECT F50 is shown.

3.3.3. Energy Dispersive X-ray spectrometer (EDX)

As discussed in the SEM analysis, characteristic X-ray is used for elemental analysis. Energy and intensity of the X-ray are used to detect which element at what amount is present in the sample at that portion. Along with the compositional investigation, this technique is used for chemical mapping. As the emitted X-ray is a byproduct of bombarded electrons, the EDX detector is attached to the SEM or TEM system. Investigation of the data is performed with the help of an internal database. However, a prior idea about the composition of the sample is necessary as the same energy with different X-ray lines can be emitted from more than one element in the periodic table.

3.3.4. High-Resolution Transmission Electron Microscopy (HR-TEM)

HR-TEM is another important imaging technique that works in transmission geometry. A high energy electron beam is allowed to transmit through the specimen and hence various detailed information such as the size, and shape of the particles can be gained using this technique. As the electron beam is incident on a sample, part of the beam interacts with the sample whereas the rest part of the beam transmits through the sample. The transmitted electron beam bears the information regarding the specimen structure that is necessary to get an image of the whole sample. TEM is capable of imaging at a significantly higher resolution than any other optical

microscope due to the smaller de Broglie wavelength of electrons. This technique is further used to study the defects, inter planar spacing, dislocations, etc. Special care is taken to prepare and place the sample on the TEM grid. The sample should be well dispersed in the relevant volatile solvent. Then, the mixture is poured on the TEM grid by drop-casting method to form a very thin layer. The grid is then dried well in the air before placing it in the instrument.

In this research work, all the TEM analysis has been performed using HRTEM ~ FEI, Tecnai G^2, S-Twin microscope with HAADF detector (Fischione, model 3000) and JEOL, JEM, 2100 F.

3.3.5. X-ray Photoluminescence Spectroscopy (XPS)

XPS is one of the most important quantitative techniques that measure the elemental composition of the surface of a material along with the binding states of the elements. Kai Siegbahn got the Nobel prize in Physics in 1981 for his work in XPS. In XPS, X-rays (photons) are incident onto the sample, and when electrons in the sample absorb sufficient energy, they

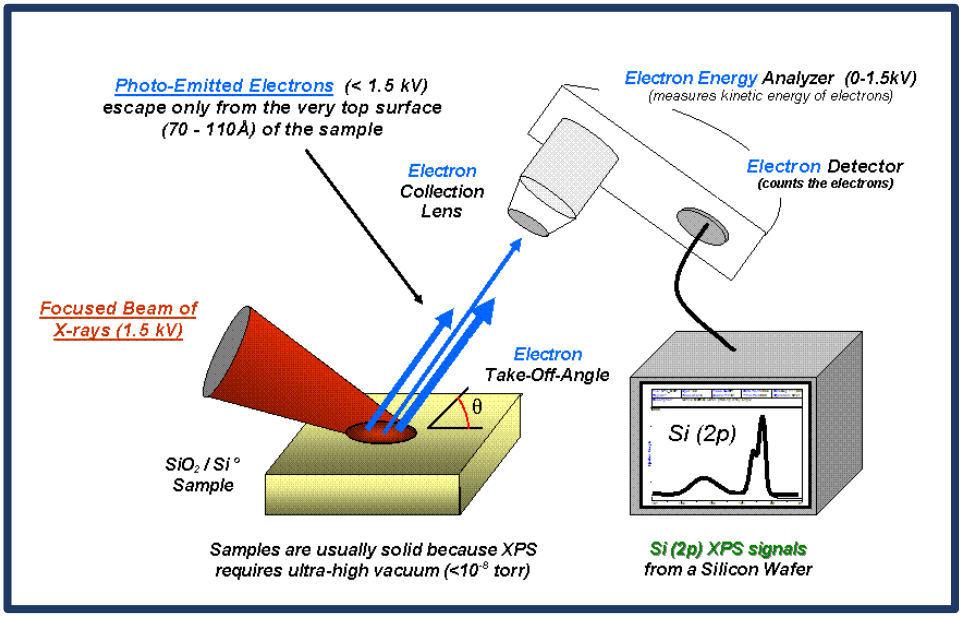

Fig. 3.6 exhibits the schematic diagram of XPS.

are ejected with specific kinetic energy from the sample generating a photoelectric effect. The emitted electrons are referred to as photoelectrons. Generally, the surface of the specimen is excited with a monochromatic or unfiltered Al K_α X-ray to generate photoelectrons. The energy of the ejected electrons is detected by a detector. Electrons with different energies follow different paths through the detector that helps to differentiate and generated the required XPS

spectra. The elements present in the compound can be determined by using the following equation

$$E_{binding} = E_{photon} - (E_{kinetic} + \varphi) \quad (3.5)$$

An atom when bonded with other atoms within a specimen may be in a different energy state or valence state leads to the alteration of the binding energy of the photoelectron that causes a change in the measured kinetic energy. The bonding information can be derived from these chemical shifts. XPS can measure all the elements other than hydrogen and helium and the experiment must be carried out in ultra-high vacuum. Fig. 3.6 represents the schematic diagram of XPS.

In my research work, XPS of VSW Ltd., UK was used.

3.3.6. UV-Vis Absorption Spectroscopy

When a broad light spectrum is shot on a material, some of the light gets absorbed whereas the rest of the portion gets reflected or transmitted. The optical character of an optically active material determines the amount of light absorbed at different wavelengths. Thus, if the wavelength of the incident light is scanned and the corresponding transmitted light intensity is recorded, the absorption characteristics of the specimen can be identified. In the UV-Vis spectrophotometer, a dual source of tungsten-halogen lamp combined with a deuterium lamp is used to provide the broad light spectrum to the monochromator with a range of wavelength from 200 nm to 1100 nm.

Fig. 3.7 shows the digital image of UV-Vis spectrophotometer.

In this dissertation, I have used the Tauc plot analysis to determine the energy band gap of the samples. The Tauc equation is given below

$$\alpha h\vartheta = A(h\vartheta - E_g)^n \quad (3.6)$$

Here, α (= 2.303 A/t, A is the absorbance and t represents the thickness of the sample) represents the absorption coefficient of the material, h is the Planck's constant, ϑ is the frequency of the wavelength and E_g is the energy band gap of the material. The value of "n" can be 2 for direct band gap and ½ for indirect band gap material. Therefore, from the intersection of the extrapolated linear region of the plot $(\alpha h\vartheta)^n$ vs. $h\vartheta$ in x-axis, the band gap of the material can be determined. Fig. 3.7 represents the digital diagram of the UV-Vis spectrophotometer.

We have used OPTIZEN POP UV-Vis spectrophotometer and Jasconic V-650 spectrophotometer.

3.3.7. Photoluminescence Spectroscopy

When a light spectrum is incident on a material with energy greater than the band gap energy, the material emits light. PL spectroscopy is based on this fact. It is a non-invasive technique that can dig up a huge amount of information on the energy bands, impurity states, lattice defects dynamics, optical band gap of the material, etc. When a specimen is irradiated by light of higher photon energy than that of the band gap of the sample, electrons from the valence band get excited and move to the conduction band. After releasing extra energy, the excited electrons move back spontaneously to the ground level. In the case of direct band gap material, radiative emission is predominant and thus released energy comes out in the form of light which is called PL emission. The wavelength of this emission is characteristic of the energy band diagram of the sample. Therefore, we can obtain information regarding the optoelectronic properties of the sample by analyzing the emission spectra.

We have used PTI QuantaMaster 400 spectrofluorometer and Fluoromax-4C_1505D-33 to obtain the PL spectra of all the optically active samples.

3.3.8. Thermogravimetric Analysis (TGA)

TGA is conducted by a thermogravimetric analyzer that is used to detect the mass of the material continuously with time in the presence of heat flow. Mass, temperature, and time are considered the primary measurements. A typical thermogravimetric analyzer is made of a precision balance with a sample pan placed inside a temperature-controlled furnace. The temperature is generally increased at a constant rate to experience a thermal reaction. The thermal reaction can be carried out in a variety of atmospheres such as ambient air, inert gas,

vacuum, etc. The thermogravimetric data obtained from a thermal reaction is plotted keeping the % of initial mass in the y-axis and the temperature or time on the x-axis. This plot is referred to as a TGA curve. The first derivative of the TGA curve is used to compute the inflection points along with differential thermal analysis. Three variations of TGA are commonly employed:

♠ Dynamic TGA

In this case, the temperature of the sample is increased continuously over time, and the mass of the sample is recorded.

♠ Static TGA

Here, the temperature is kept constant as the mass of the material is measured. This can be used to gain more insights into a decomposition that happens at a particular temperature.
In other words, this method is used to investigate a material's stability at a certain temperature.

♠ Quasistatic TGA

Here, the sample is heated in multiple temperature intervals and held at those intervals for a time, until the mass stabilizes. This method is the ideal one to investigate the materials that are known to degrade in various ways at different temperatures and get better information about the way of decomposing.

3.3.9. Differential Scanning Calorimetry (DSC)

DSC is a thermal analysis apparatus that measures the change in physical properties of a sample against time when the sample is exposed to heat flux. In other words, this tool determines the temperature and heat flow associated with the transition in material as a function of time and temperature. In 1962, E. S. Watson and M. J. O'Neil developed this procedure. This method is used to investigate the crystallinity, melting point, etc. of the polymer and polymer composite in my research work. This system is made of a measurement chamber attached to a computer. A sample pan and a reference pan are heated in the measurement chamber. The change in the rate of the temperature of the sample pan is regulated with the help of the computer. From the recorded data, various information about the polymer sample can be evaluated. The melting point of the samples can be detected and from the melting enthalpy, the crystallinity of the polymer samples can be identified.

In this work, two DSC set up was used – TG-DSC (model:449C) made by NETZSCH and DSCQ 2000 TA (Walter India).

3.3.10. Fourier Transform Infrared Spectroscopy (FTIR)

FTIR spectroscopy is a powerful method to identify different chemical compositions along with the functional groups in a molecule by projecting an infrared spectrum as a molecular "fingerprint". In this process, infrared light is incident on the sample, and the absorption of the infrared light by the sample is measured which is plotted against the wavenumber of the infrared radiation. In the elastic collision between the molecules of the material and the infrared light, characteristic vibrations of varying modes generate a specific vibrational frequency known as resonance frequency (depending on the bond nature). Vibrational energy increases with the increase in absorbed energy (quanta) by the material. A molecular bond vibrates at different frequencies that correspond to the ground or any of a higher excited state. If E_0 is the energy of the ground state and E_1 is the energy of the first excited state, $E_1 - E_0 = \frac{hc}{\lambda}$. Here, λ is the wavelength of light, c is the speed of light, h is Planck's constant. FTIR spectroscopy provides information regarding the chemical bonding or molecular structure of samples. The term "Fourier transform infrared spectroscopy" implies that a Fourier transform is necessary for the conversion of the raw data into the actual spectrum. The basic mechanism of a Fourier transform spectrometer is quite simple as it uses an interferometer to modulate the wavelength and the corresponding signal is analyzed by converting it to a single-beam infrared spectrum. FTIR spectrometer works by taking a very small quantity of a sample and introducing it to the infrared cell which is then subjected to an infrared light source and scanned usually from 4000 cm^{-1} to 400 cm^{-1}. The intensity of transmitted light is measured at each wave number. This is known as the infrared spectrum of the sample.

In my research work, I have used FTIR to analyze the electroactive phase content of all the polymer composites. The crystallinity of the polymer samples can be computed using the relation

$$F_{EA} = \frac{A_{842}}{\left(\frac{K_{842}}{K_{764}}\right)A_{764} + A_{842}} \times 100\% \qquad (3.7)$$

Here, A_{842} and A_{764} represent the integral area of the absorbance band corresponding to the ferroelectric β phase at 842 cm^{-1} and non-polar α phase at 764 cm^{-1}. K_{842} and K_{764} are

the corresponding absorption coefficients. The interfacial interaction between the -CH_2- and -CF_2- dipoles of PVDF and the filler plays the key responsibility of enhancing the ferroelectric component due to the addition of external filler. The asymmetric and symmetric stretching of the vibrational bands results in the formation of a damping source. The damping constant (r_{dc}) can be evaluated from the angular frequency of damped vibration (ω) and free vibration (ω_0)

$$\omega^2 = \omega_0^2 - r_{dc}^2 \qquad (3.8)$$

In this dissertation, Fourier transform infrared spectroscopy (FTIR) was performed using IR Prestige-21, Shimadzu spectrophotometer.

3.3.11. Complex impedance spectroscopy

To measure the impedance of the samples, the powder of the perovskites was pelletized at a pressure of 50 kg/cm^2 with a pelletizer machine. Diameter of each pallet was maintained at 8 mm to 10 mm. AC signal was applied across the pallet with Cu / Au electrodes on either side of the pallet. Sample temperature was varied with a built open cycle liquid nitrogen cryostat that can control the temperature.

In my work, Hioki LCR Q meter (IM3536) was used to analyze the dielectric properties of the samples.

3.3.12. Elastic properties of the films

A Universal testing machine (UTM) is used to test the mechanical properties (tension, compression, etc.) of a given test specimen by exerting tensile, compressive, or transverse stresses. The machine has been named so because of the wide range of tests it can perform over different kinds of materials. A specimen of a standard size and shape made of the material is pulled in tension while the load and elongation are continuously (or periodically) monitored. The data thus collected are used to generate a stress-strain curve. Modern machines have an intelligent computer interface and have the facility to perform tests under various user-defined modes (for example load control, displacement control, and strain control). Usually, tensile tests are performed under displacement control mode where the moveable end of the grip is made to move at a constant speed. The load and displacement (strain) records are stored at specified intervals of time. Once the sample breaks the machine stops. Tensile strength, break load, elongation, Young's modulus of the samples are derived from this measurement.

Tinius Olsen H50KS was used in my research work.

3.3.13. Photovoltaic performance measurement

Photovoltaic performance measurement is mainly based on recording the current-voltage (I-V) curve of the device under a dark and simulated solar spectrum. I-V data is recorded by sweeping the bias voltage across the device within a certain range while recording the current at the same time. Under light illumination, charge carriers are generated within the device, and that gives rise to a photocurrent in the reverse bias region. I-V data were recorded with a Keithley 2602B two-channel source- measure unit. 80-100 mW/cm^2 AM1.5 simulated solar radiation is used to irradiate the photodetector. Simulated sunlight was supplied by a Royal enterprise (India) solar simulator to our fabricated photodetectors.

3.3.14. Electrochemical analysis

The electrochemical response which includes cyclic voltammetry (CV) and galvanostatic charge-discharge (GCD) behavior of the designed piezoelectric supercapacitor was recorded by PGSTAT302N autolab.

CV is a well-known tool to study the performance of the fabricated supercapacitor. In this technique, the potential of the supercapacitor is scanned between a potential window limiting from V1 to V2. The applied potential acts as a driving force to generate current which is measured as a function of potential by a potentiostat. The nature of the cyclic voltammogram (represented by plotting current vs. potential) depicts the capacitive, pseudocapacitive or ideal double layer capacitive behavior of the supercapacitor.

In GCD method, at constant current, the supercapacitor is charged until the voltage reaches from its discharged state (V1) to its charged or operating voltage state (V2). After reaching V2, the current drives in reverse direction to discharge back the supercapacitor to V1 state. The specific capacitance of the supercapacitor can be evaluated from the CV curves using the following formula

$$C_A = \frac{\int I\, dv}{vA\Delta V} \qquad (3.9)$$

Here, C_A denotes the areal capacitance of the device, $\int I\, dv$ represents the integral area of the CV curve, A is the area of the device, v refers to the scan rate and ΔV is the working potential window. From GCD curves, the specific capacitance can also be estimated using the formula

$$C_A = \frac{I \times \Delta t}{A \times \Delta V} \quad (3.10)$$

Here, I is the constant discharging current in A, Δt refers to the discharge time and ΔV denotes the working potential window. The energy (E) and power (P) of the device can also be determined from CV curves following the relations

$$E = \frac{C_A \times \Delta V^2}{2} \quad (3.11)$$

$$P = \frac{E}{\Delta t} \quad (3.12)$$

3.3.15. Working mechanism of self-charging piezoelectric supercapacitor

A piezoelectric potential is generated across the piezo-separator of the device under the influence of external force. This potential serves as a driving force to initiate electrochemical oxidation-reduction at both electrodes. At first, in the absence of any external force, the device stays at the discharging condition and an electrochemical equilibrium is sustained between the electrodes and electrolyte. The piezo-potential, developed under temporal distortion, produces positive potential at one electrode and negative potential at the other electrode which initiates the migration of electrolyte ions towards positive and negative electrodes. As a result, a non-equilibrium electrochemical state is developed between the electrodes. To attain the chemical equilibrium, oxidation-reduction reaction takes place at the surface of both the electrodes. When the external force is removed, piezo-potential disappears at the piezo-separator. Consequently, to compensate for the disturbed electrochemical equilibrium, few ions traverse back to the electrolyte but the electrons do not move back to the positive electrode resulting in no current flow in the reverse direction. Under repeated distortion, the V_{OC} of the device increases that signifies the self-charging process of the device. The working mechanism of self-charging piezoelectric supercapacitors is still controversial.

3.4. Fabrication of devices

3.4.1. Fabrication of UV detector

Firstly, a fluorine-incapacitated tin oxide (FTO) coated glass substrate was cleaned and ultrasonicated in deionized water and isopropyl alcohol for 20 min each and then dried in air. Next, a mildly acidic solution of titanium isopropoxide (TiO_2) was spin-coated on the cleaned FTO substrate at 3000 rpm for 60 s followed by consecutive annealing in ambient conditions

at 100 °C for 15 min and 500 °C for 30 min, respectively. In this way, the layer of compact

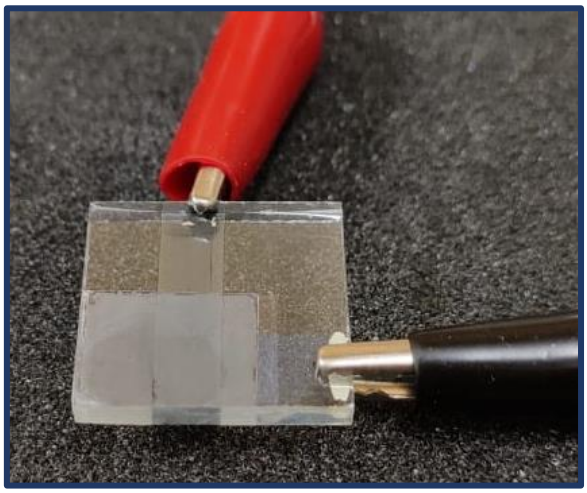

Fig. 3.8 The fabricated UV detector.

TiO_2 forms that serves as an electron transportation layer (ETL). A thin layer of (propylammonium lead bromide) optically active $PAPbBr_3$ is spin-coated on C-TiO_2 at 1000 rpm for 20 s and 4000 rpm for 20 s respectively. Then, the substrate containing multi- layers was annealed at 100 °C for 10 min. Next, a layer of carbon paste was then blade coated onto the perovskite layer to form the sandwich structure and annealed at 100 °C for 5 min. The carbon paste contains 1 g carbon black, 3 g of graphite nanopowder, 40 mg carbon nanotube (CNT) in 8 g α-terpeniol, and 10 ml of ethanol. The digital photograph UV detector is illuminated in Fig. 3.8.

3.4.2. Spin coating

Spin coating is the simplest method to apply a uniform film onto a solid surface by using centrifugal force and requires a liquid-vapor interface. The machine used for spin coating is called a spin coater. The spin-coating process starts with the dilution of the material to be deposited in a solvent. The thickness of the coated film depends upon the spinning speed, surface tension, and viscosity of the solvent. The applied solvent is usually volatile and evaporates simultaneously. After evaporation of the solvent, spin coating results in a thin film ranging from a few nanometers to a few microns in thickness.

In this research work, I have used EZspin-A1, apex instruments for spin coating that have been shown in Fig. 3.9.

Fig. 3.9. The digital diagram of spin coating.

3.4.3. Designing of piezoelectric nanogenerator

The piezoelectric nanogenerator was fabricated by sandwiching the polymer composite between two copper (Cu) electrodes and two copper wires were soldered on the electrodes. Finally, the fabricated nanogenerator, configured as Cu electrode / PVDF composite / Cu electrode, was laminated by PDMS (polydimethylsiloxane) layer to enhance its durability as depicted in Fig. 3.10. In our latest work, we have laminated the nanogenerators by laminating machine.

Fig. 3.10. The fabrication of piezoelectric nanogenerators.

3.4.4. Fabrication of piezo-active photodetector

At first, the prepared PVDF-filler solution was cast drop-wise slowly on an ITO-coated flexible PET substrate and kept at 90 ◦C for 2 h. The coated ITO serves as a top electrode of the obtained film. An aluminium electrode is attached to the other side to design a sandwich-structured piezo-active photodetector. Finally, the device is laminated to provide a safeguard and to increase its lifetime.

3.4.5. Fabrication of hybrid piezo and triboelectric nanogenerator

To design a hybrid piezoelectric and triboelectric nanogenerator, the Cu electrode was attached to a PVDF-perovskite composite that serve as the top electrode. A uniform layer of polydimethylsiloxane (PDMS) is cast on a separate Cu electrode and dried at 60 ^{o}C for 2 hours. Then the hybrid device was configured as Cu electrode / PVDF composite / air gap / a very thin layer of PDMS/ Cu electrode. The digital photograph of the fabricated device is shown in

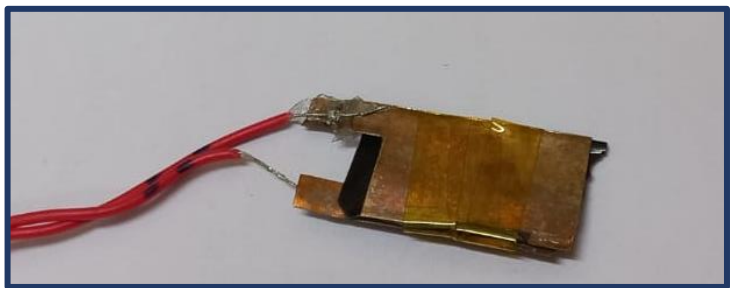

Fig. 3.11. The designed hybrid piezoelectric-triboelectric nanogenerator.

Fig. 3.11.

3.4.6. Designing of piezoelectric supercapacitor

At first, $NdMnO_3$ (as an active material), graphite powder, and PVDF were mixed in the ratio 85:10:5 and dispersed in N-methyle pyrrolidine to prepare a homogeneous slurry. The slurry was coated uniformly on the surface of two flexible steel plates used as symmetric electrodes (the effective area of each plate is 1.5 cm × 1.5 cm) and dried at 50^{o}C for 5 hours. To fabricate the self-charging piezoelectric supercapacitor, $NdMnO_3$ incorporated PVDF self-poled, piezo-active film was used as piezo-separator soaked in gel electrolyte H_3PO_4/PVA. The gel electrolyte was prepared by mixing 1g of H_3PO_4, 3g of PVA, and 20 ml of DI water following rigorous stirring at 90 ^{o}C until a homogeneous solution was achieved. The separator was then sandwiched between two prepared electrodes to design the device. Furthermore, the device was laminated to provide safeguard.

CHAPTER 4

4. Temperature and Frequency Dependent Dielectric Response of $C_3H_7NH_3PbI_3$: A New Hybrid Perovskite

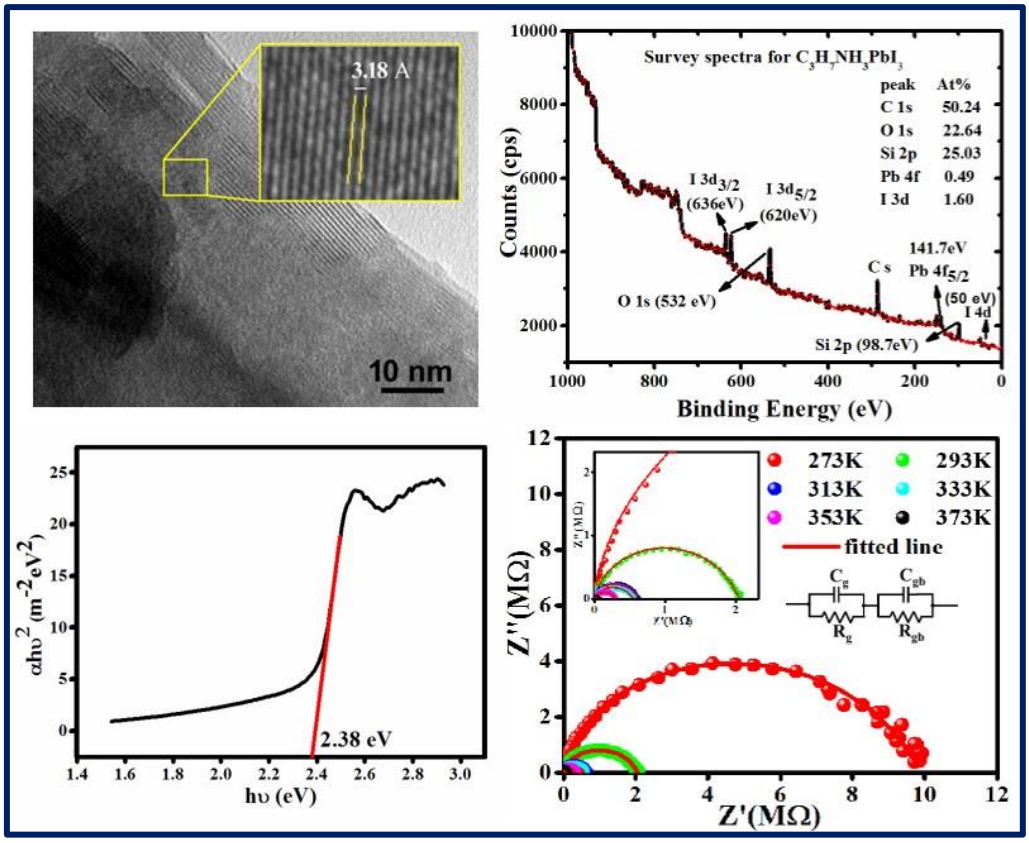

4.1. Introduction

Organic-inorganic hybrid perovskites have become a point of interest among researchers due to its immense utility in solar energy harvesting. Previously, pure organic materials were introduced in the field of photovoltaics to replicate the natural photo-synthesis method. Their high light absorption coefficient, long carrier diffusion length, good photo-voltaic properties, and many other interesting properties boosted its growth. However, their low mechanical as well as thermal stability brings down the lifetime of the devices. In the meantime, hybrid perovskite materials exhibit various desirable properties for optoelectronic applications due to the benefaction of both organic and inorganic components [1-3]. These hybrid perovskites possess improved structural, optical, and electronic properties concerning the organic or inorganic component alone. All these have affirmed hybrid perovskite materials as a promising new-generation photovoltaic with its simple fabrication procedure, appreciably low manufacturing expense, and high-power conversion efficiency over the last few years. The generic form of this type of hybrid perovskite is ABX_3 where A is a cation of any organic compound, B is a bivalent inorganic cation like Sn or Pb and X refers to monovalent halogen ion like Cl, Br or I. The most popular material in light harvesting is methylammonium lead iodide ($CH_3NH_3PbI_3$) for its attractive optoelectronic properties [4,5]. Irrespective of its tunable band gap, high extinction coefficient, and excellent optical response, the stability of the material is still a problem. $CH_3NH_3PbI_3$ is highly unstable in the open ambiance as it degrades quickly in the presence of air, moisture, and ultraviolet light [6]. Moreover, methylammonium lead halide based solar cells can easily be dissociated in its electrolyte solution possessing remarkable loss in solar cell function.[7] To get rid of this adverse nature of the material, researchers nowadays are far more eager to work with other hybrid perovskites either by replacing organic cation with other alkylammonium cation or by varying halogen ion [7]. Replacement of new organic components may lead to a change in the bandgap of the material which in turn influences its opto-electronic properties. The incorporation of new organic components can lead to a change in the structural and dielectric properties along with the band structure of the material significantly which in turn influences its stability and optoelectronic performance [8]. In the large family of hybrid perovskites, propylammonium lead iodide $C_3H_7NH_3PbI_3$ ($PAPbI_3$) is comparatively a newcomer. Unlike $CH_3NH_3PbX_3$, pore free thin film of propylammonium lead iodide is easily achievable using simple lab-scale deposition techniques like spin coating. However, to assess this new material's compatibility

with the field of next generation photovoltaics and optoelectronics, an extensive investigation of its structural and dielectric properties is very important.

Here, the synthesis, structural, and optical characterization of $PAPbI_3$ have been reported. Since this hybrid perovskite material is quite unexplored, it demands a detailed investigation of optical and electrical properties. Impedance spectroscopy is a very convenient and powerful tool to investigate the dielectric properties. The temperature and frequency dependent dielectric study of $PAPbI_3$ can provide detailed information about the performance of the localized charge carriers, conduction mechanism, permittivity, loss factor, etc. To the best of our knowledge, very few literature is available regarding the detailed study of optical properties, AC conductivity, and dielectric relaxation of $PAPbI_3$. In this article, the study of dielectric relaxation using impedance spectroscopy, electric modulus and conductivity of $PAPbI_3$ has been extensively carried out as a function of frequency and temperature. The outcomes of dielectric studies have been scrutinized minutely with the help of different theoretical models. Detailed discussions on dielectric loss, dielectric constant, impedance study, electric modulus, AC and DC conductivity of this perovskite have been reported here.

4.2. Experimental details

4.2.1. Chemicals

n – Propylamine [($C_3H_7NH_2$), Spectrochem, 98%] Hydroiodic acid [57 wt. % in water, Loba Chemie], Dimethylformamide [anhydrous, 99.8%, Merck Chemicals], lead iodide [(PbI_2), Loba Chemie] were used to carry out the synthesis of the required sample. All the chemicals utilized here were of analytical grade and used without any further purification.

4.2.2. Synthesis of propylammonium lead iodide ($C_3H_7NH_3PbI_3$)

To synthesize propylammonium lead iodide, propylammonium salt ($CH_3CH_2NH_3I$) was prepared at first. Hydroiodic acid (HI) was mixed with propylamine ($CH_3CH_2NH_2$) in an equimolecular ratio and stirred continuously for 2 hours at 0 ^oC. The resulting solution thus obtained was dried and washed with diethyl ether several times to remove unreacted HI. Finally, the mixture was dried under vacuum at 60 ^oC for 12 hours to form propylammonium iodide.

In the presence of ambient surroundings, equimolar propylammonium iodide ($CH_3CH_2NH_3I$) and PbI_2 were dissolved in dimethylformamide at 60 ^oC and stirred for 10 hours [9]. The solution was filtered to pull apart the precipitate through a syringe filter having pore size of 0.45 μm. The solvent was evaporated at 65 ^oC to obtain the required yellow sample powder ($C_3H_7NH_3PbI_3$).

4.2.3. Characterization

The structural behavior of synthesized $PAPbI_3$ was examined by the powder X-ray diffraction (XRD). The XRD analysis was carried out by Rigaku miniflex – 600 bench top diffractometer using Cu K_α line radiation (λ = 1.54 Å) in the range of $2\theta = 10^o – 50^o$ with a step size of 0.04^o at room temperature. Sample morphology was characterized by transmission electron microscope (HRTEM, FEI, Tecnai G^2, S-Twin microscope). A HAADF detector (Fischione, model 3000) was used to record scanning transmission electron microscopy high angle annual dark field pictures. For compositional information of the surface of the sample, X-ray Photoelectron Spectroscopy (XPS) analysis was carried out using an XPS facility (VSW Ltd., UK) attached in a UHV (base pressure in the XPS chamber was 5×10^{-10} mbar) compatible nanocluster deposition unit.[10] In this experiment, Mg K_α x-ray, having an energy of 1253 eV (or wavelength of 9.89 Å) was used, and the photoelectrons produced were analyzed by a hemispherical electron analyzer of a mean radius of 150 mm at an operating pass energy of 20 eV and a dwell time of 1 second. XPS spectra were analyzed by using commercially available Casa XPS processing Software. To study the optical characteristic and to evaluate the optical bandgap, Ultraviolet – visible spectroscopy (UV – Vis spectrophototmeter, Optizen POP) of spin coated glass film has been carried out. The absorbance spectrum thus obtained was between 450 nm - 800 nm. The luminescence properties of the sample are analyzed by room temperature photoluminescence spectroscopy (PTI QuantaMaster 400 spectro – fluorometer). The dielectric constant, impedance studies, loss tangent, electric modulus, ac conductivity, and the Nyquist plot of this hybrid perovskite was estimated from the complex impedance spectra. complex impedance spectra were recorded by inserting a material pellet (diameter – 8 mm) of measured thickness between two Cu electrodes in Hioki LCR Q meter (IM3536) instrument. The dielectric studies have been performed for different temperatures (273 K – 383 K) over an appreciable wide range of frequencies (10 Hz – 8 MHz).

4.3. Results and discussions

4.3.1. Microstructural study

The obtained XRD pattern of $PAPbI_3$ is shown in Fig. 4.1a. It matches well with the reported data exhibiting the monoclinic structure with Cc space group [9]. The significant diffraction peaks were observed at 2θ at 12.19°, 18.28°, 24.44°, 25.88°, 30.68°, 31.92°, 31.92° corresponding to 001, 220/310, 221/13-1, 311, 240, 202 lattice planes, respectively. To check the robustness of this material, the sample was kept in 75% relative humidity for 168 hours.

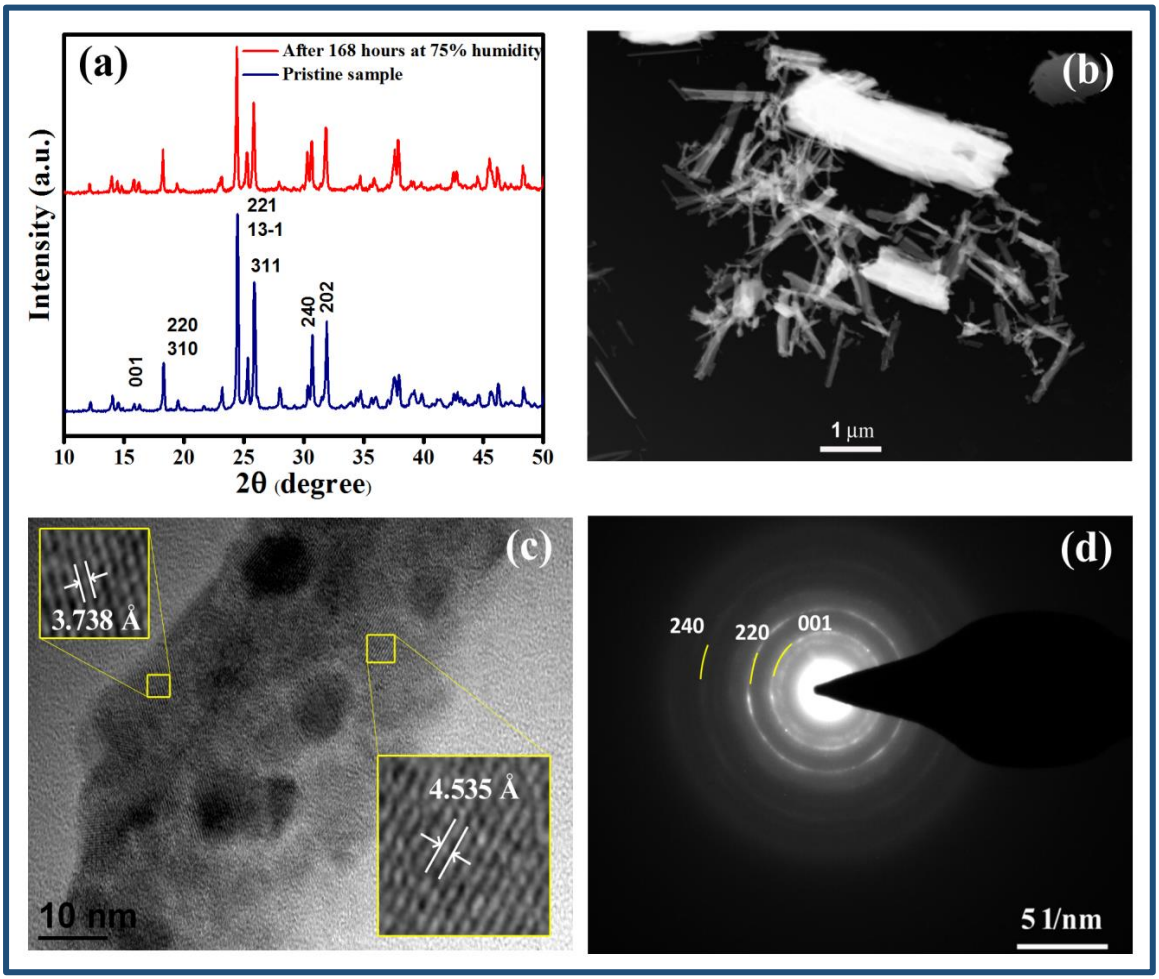

Fig. 4.1. (a) X-Ray diffraction pattern of pristine and moisture exposed $PAPbI_3$ shows no visible change of peaks. (b) Dark field TEM image showing micro rods of $PAPbI_3$. (c) d-spacing calculated from HRTEM image. (d) Well resolved diffraction rings of SAED pattern confirming polycrystalline nature.

The constant relative humidity in a closed container was achieved by using a saturated NaCl solution.[11] After 168 hours, no deviation of the XRD peak was observed which indicates the

remarkable stability of $C_3H_7NH_3PbI_3$ (Fig. 4.1a). The morphology of the synthesized sample is directly observed by transmission electron microscopy study (TEM). The micrograph (Fig. 4.1b) exhibits that the microfibres of the sample are of stem-like structure with an average length of around 1 μm and width of 100 nm. Figure 4.1c depicts HRTEM image showing the lattice planes of the samples. The d-spacings found for several planes of single calculated microfibre are 3.738, 4.363, 7.262 Å which correspond to the respective miller indices as 221/13-1, 220/310 and 001 respectively [4]. The sample is found to be polycrystalline from X-Ray pattern as well as from the resolved circular SAED pattern displayed in Fig. 4.1d. d-spacing TEM from the SAED are 2.909, 4.590 and 6.463 Å corresponding to 240, 220/310, and 001 planes, respectively.

4.3.2. Spectroscopic characterization: XPS, UV-Vis spectroscopy and photoluminescence Study

Figure 4.2a shows the XPS survey spectrum of $C_3H_7NH_3PbI_3$ along with normalized atomic concentrations shown for different peaks coming out from the photoelectrons of representative signals. The atomic concentrations of the main elements present in the sample are estimated from the corresponding XPS peaks. The dominant peaks are C 1s (B.E. 284 eV), O 1s (532 eV), and Si 2p (98.7 eV), whereas, I 3d and Pb 4f doublets are observed with trace amounts of respective atomic concentrations. The sample was dispersed on a silicon substrate and the dominant peaks of Si came from that substrate. The high-resolution XPS spectra of Pb 4f and I 3d were analyzed and the elemental peaks along with the corresponding satellite peaks were de-convoluted as shown in Fig. 4.2b and c respectively. The binding energies of Pb $4f_{7/2}$ (binding energy = 138 eV) and Pb $4f_{5/2}$ (binding energy = 143 eV) having binding energies difference of 5 eV have appeared from pure Pb present in the sample $C_3H_7NH_3PbI_3$. No other compound or Pb-oxide is seen in the spectra. Similarly high resolution XPS peaks attributed to I 3d electrons are seen in Fig. 4.2c where a splitting of I 3d bond into I $3d_{3/2}$ (B.E. = 620 eV) and $I3d_{5/2}$ (B.E. = 631 eV) has occurred upon interacting with x-ray beam. These two peaks also signify that Iodine did not form any bonds with Pb. The peaks I $3d_{5/2}$ and Pb $4f_{7/2}$ also correspond to PbI_2 compound. In semiconductors, optical absorption defines the transition of electrons from the valence band to the conduction band and it can be of two types – direct

transition and indirect transition. This phenomenon is useful for the determination of optical energy band gap (E_g) and it can be derived from the well – known Tauc plot equation (4.1),

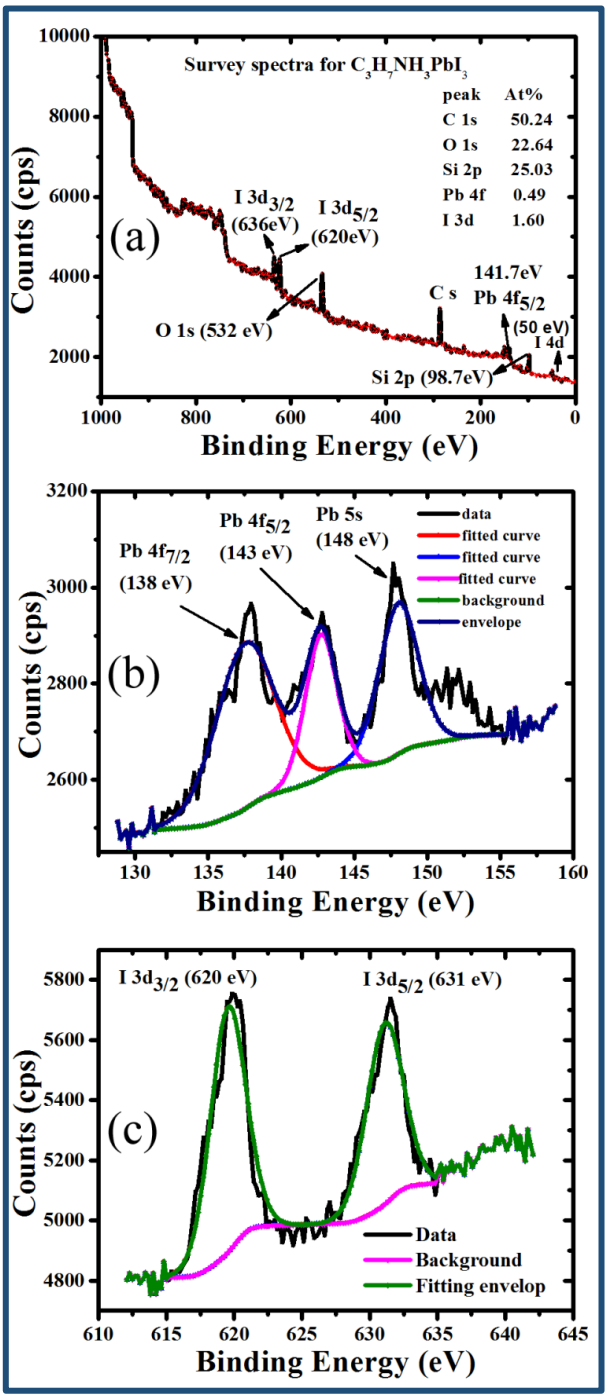

Fig. 4.2. (a) XPS Survey spectrum from the $CH_3H_7NH_3PbI_3$. (b) High resolution XPS spectra of Pb 4f and Pb 5s peaks of the sample. The background subtraction curve is shown by green, while the deconvoluted curves of Pb $4f_{7/2}$ and Pb $4f_{5/2}$ are highlighted by red and magenta colors. Pb 5s is shown in blue. (c) High resolution XPS spectra of I 3d doublet from the sample. The background subtraction curve is shown by magenta, while the de-convoluted curves of I $3d_{3/2}$ and I $3d_{5/2}$ are highlighted by green colors.

$$(\alpha h\vartheta)^{\frac{1}{n}} = A\,(h\vartheta - E_g) \qquad (4.1)$$

where α is absorption coefficient, h is the Planck constant, ϑ is frequency, E_g refers to

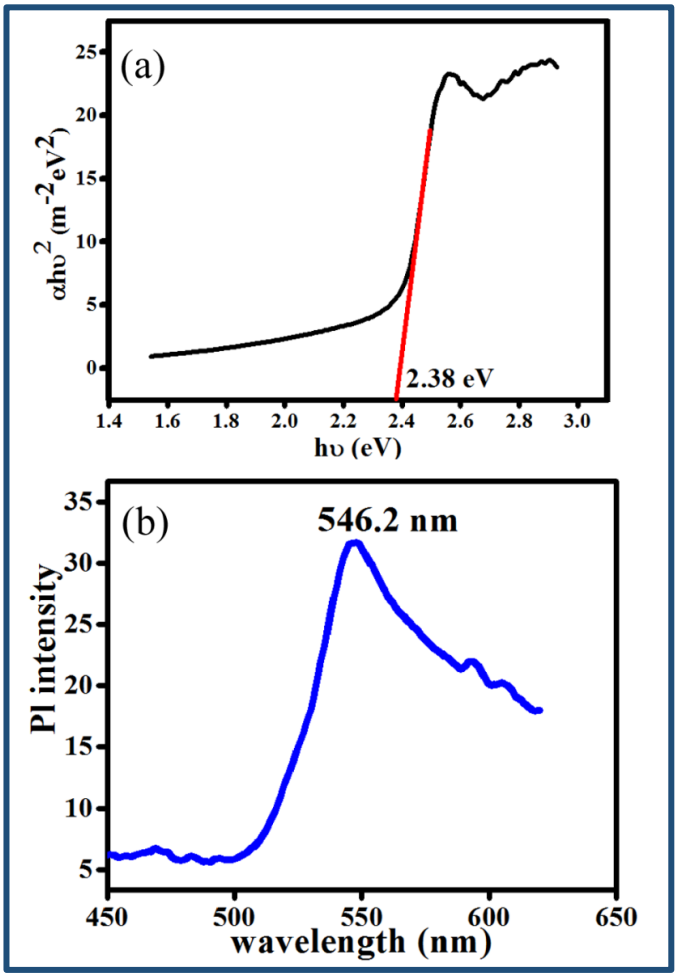

Fig. 4.3. (a) UV-Vis spectroscopy of the sample, (b) Room temperature PL of $CH_3H_7NH_3PbI_3$.

the optical energy band gap and A corresponds to a temperature independent normalizing constant [7]. Generally, direct electronic transition is observed in this kind of hybrid perovskite. To determine the optical energy band gap, $(\alpha h\vartheta)^2$ was plotted against $h\vartheta$ using the Tauc plot equation as shown in Fig. 4.3a. By extrapolating the straight-line segment to $h\vartheta$ axis, the intersection position provides the value of E_g as to be 2.38 eV making it a competitive choice for light emitting diodes and different next generation photovoltaic applications like tandem solar cells, building integrated photovoltaics and transparent photovoltaics, etc.

Room temperature photoluminescence spectrum (PL) shows strong excitation emission peak at around 546 nm (Fig. 4.3b). The sharp peak is close to the band gap value obtained from the absorption band edge in ultraviolet–visible spectroscopy.

4.3.3. Impedance Spectroscopy Results

Complex impedance spectroscopy (CIS) is an essential and well established method to analyze the electrical behavior of material. It furnishes information about the movement of ions inside the material, relaxation time, electrical conductivity, etc. The frequency dependent real part of complex impedance ($Z'(\omega)$) vs. imaginary part of impedance ($Z''(\omega)$) at different temperatures is shown in Fig. 4.4a. This diagram is commonly known as Cole – Cole plot or Nyquist diagram. Generally, for any dielectric material, three distinct semicircles appear in Nyquist diagram which indicate the contribution of grain, grain boundary, and electrode-material interface as the total impedance of the dielectric material. Semicircles which appear in high frequency region represents the contribution of grain whereas the presence of semicircles in low frequency region is due to the contribution of the grain boundary of the material. Lastly, the semicircles in ultra-low frequency region are due to the presence of electrode material interface [12]. Figure 4.4a shows the complete impedance spectra of the samples in the temperature range 273 K≤ T ≤ 373 K demonstrating single depressed semicircles. This single depressed semicircle comprises two successive semicircles which encompass the overall distribution of grain and grain boundary. For the hybrid perovskite $PAPbI_3$, the contribution of electrode - material interface is absent. It is very difficult to differentiate the involvement of grain and grain boundary from this single depressed semicircle. To resolve the contribution of grain and grain boundary distinctly from the single semicircles, Maxwell – Wagner equivalent circuit model which comprises of parallel combination of a number of resistors (R) and capacitor (C) is employed. The impedance spectra of all temperatures are fitted with the help of EC lab software. In this case, the desired circuit model is obtained by connecting two parallel R C elements in series as displayed in the inset of Fig. 4.4a [12]. Figure 4.4a also indicates that with the rise in temperature, the diameter of the semicircle i.e. the intersection point on the real axis diminishes observably which represents the enhancement of DC conductivity with higher temperatures. The formalism of complex impedance can be expressed as the following:

$$Z(\omega) = Z'(\omega) + jZ''(\omega) \tag{4.2}$$

Where $Z'(\omega)$ and $Z''(\omega)$ indicate their usual expression as stated above.

$$Z'(\omega) = \frac{R_g}{[1+(\omega R_g C_g)^2]} + \frac{R_{gb}}{[1+(\omega R_{gb} C_{gb})^2]} \tag{4.3}$$

$$Z"(\omega) = \frac{\omega C_g R_g^2}{[1+(\omega R_g C_g)^2]} + \frac{\omega C_{gb} R_{gb}^2}{[1+(\omega R_{gb} C_{gb})^2]} \tag{4.4}$$

Where, R_g is the grain resistance, C_g refers to grain capacitance, R_{gb} indicates the grain boundary resistance and C_{gb} represents the grain boundary capacitance. Table 4.1 consists of all the obtained values of R and C of the sample for various temperatures.

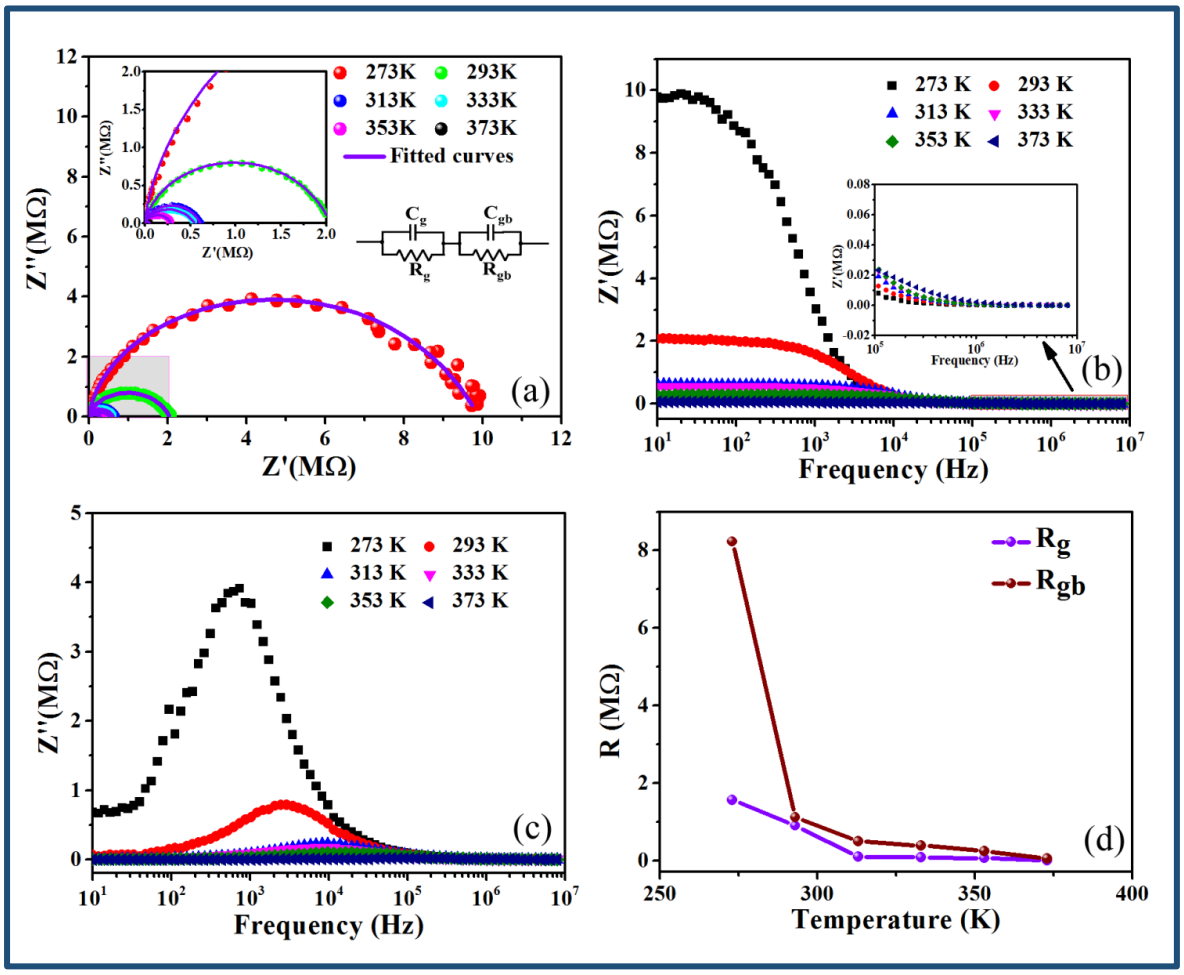

Fig. 4.4. (a) Cole-Cole plot of $CH_3H_7NH_3PbI_3$ at different temperature, inset of (a) Maxwell Wagner equivalent circuit. Frequency dependence of (b) $Z'(\omega)$ and (c) $Z''(\omega)$ of the $PAPbI_3$ at different temperature, inset of (b) Impedance study in high frequency range. (d) Variation of R_g and R_{gb} with temperatures.

Variation of R_g and R_{gb} at different temperatures is illustrated in Fig. 4.4d. The frequency variation of $Z'(\omega)$ at different temperatures in the range 273 K ≤ T ≤ 373 K as shown in Fig. 4.4b exhibits sigmoidal type variation with frequency. It is observed that the magnitude of the real part of the impedance $Z'(\omega)$ is higher in low frequency region. The values of $Z'(\omega)$ decrease with the increase in frequency as well as temperature following the negative temperature coefficient of resistance which in turn causes the rise in AC conductivity with temperature. Eventually, the contribution of grain boundaries in the total impedance reduces at higher frequency region as $Z'(\omega)$ tends to decrease with the elevation of frequency

and temperature. No variation of $Z'(\omega)$ is observed with temperatures in high frequency region resulting in converging to each other (inset of Fig. 4.4b). The reason behind this behavior may be due to the release of space charges along with the reduction of barrier properties which subsequently enhance the AC conductivity [12-17].

Table 4.1. The variation of different resistance and capacitance values for different temperatures

Temperature (K)	R_g (Ω)	R_{gb} (Ω)	$C_{overall}$ (F)	Goodness of fitting factor (χ^2)
273	1.56×10^6	8.23×10^6	4.972×10^{-10}	0.00253
293	8.98×10^5	1.12×10^6	2.55×10^{-10}	0.03701
313	0.952×10^5	4.923×10^5	5.955×10^{-9}	0.01619
333	0.797×10^5	3.865×10^5	1.116×10^{-9}	0.0132
353	0.58×10^5	2.432×10^5	1.709×10^{-7}	0.0243
373	0.327×10^4	4.889×10^4	3.568×10^{-6}	0.0161

The variation of the imaginary part of impedance $Z''(\omega)$ with frequency can be considered as loss spectrum. The variation of $Z''(\omega)$ with frequency demonstrates a significant relaxation peak which is remarkably temperature dependent as shown in Fig. 4.4c. When the frequency of the external field matches with the frequency of localized hopping electrons, relaxation peaks appear [14, 18]. The observed relaxation peaks are much broader than the ideal Debye curve and hence $PAPbI_3$ exhibits non Debye type of relaxation. The width of the peak is responsible for the relaxation time and it is observed that the peak width is proportional to the temperature [14]. The width of the relaxation peak increases gradually with the rise in temperature.

4.3.4. Dielectric studies

The dielectric response of a material can be expressed in the form of a complex dielectric constant

$$\varepsilon(\omega) = \varepsilon'(\omega) - j\varepsilon''(\omega) \quad (4.5)$$

Here, $\varepsilon'(\omega)$ is the real part of the complex dielectric constant and represents the stored energy while $\varepsilon''(\omega)$ represents the imaginary part of the dielectric constant as well as the energy

dissipation of the applied electric field as polarization. The real and imaginary part of the dielectric constant can be stated as equation 4.6-7.

$$\varepsilon'(\omega) = \frac{Z''}{\omega C_0 (Z'^2 + Z''^2)} \tag{4.6}$$

$$\varepsilon''(\omega) = \frac{Z'}{\omega C_0 (Z'^2 + Z''^2)} \tag{4.7}$$

Here, $C_0 = \varepsilon_0 A/d$ (C_0 is the free space capacitance, ε_0 is the permittivity of free space, A is the area of the concerned electrode, and d is the thickness of the pellet). The variation of the dielectric constant as a function of angular frequency has been investigated in the temperature 273 K ≤ T ≤ 373 K. Figure 4.5a-b demonstrate that at a particular temperature, the dielectric constant is large in low frequency region and decreases gradually with the increase in frequency. $\varepsilon'(\omega)$ and $\varepsilon''(\omega)$ play a significant role in the ionic conduction process which is governed by mainly four types of polarization viz. ionic, electronic, orientational, and interfacial. Ionic and electronic polarizations are the deformational component of polarizability while orientational and interfacial polarizations refer to the relaxation component of polarizability [19]. The variation of the real part of permittivity with frequency can be explained by Maxwell Wagner's interfacial polarization which is in union with Koop's phenomenological theory [20]. According to Koops's theory, interfacial polarization is important in low frequency region which is due to the presence of double layers in the dielectric material. Koop proposed that dielectric materials comprise of low-resistive layer of grains which is separated by a comparatively poor conducting layer of grain boundary. Hence, charge carriers get trapped at the interface of grain boundaries to restrain the flow of charge carriers [20, 21]. In the interfacial polarization process, the exchange of electrons between the ions of the same molecules takes place. The deformities and imperfections present in the material are responsible for altering the position and distribution of positive and negative space charges. This hopping mechanism emerges from propylammonium cation ($C_3H_7NH_3^+$) orientation. Under the influence of the applied electric field, positive and negative charges move towards the negative and positive poles of the applied field respectively [17, 22]. As a result, a large number of dipoles are formed. In $PAPbI_3$, molecules having permanent dipole moments can change their orientation along the direction of the electric field in low frequency region. Hence, in low frequency region, dipoles follow the quasi-static field ($\omega << 1/\tau$) easily, so the dielectric constant $\varepsilon'(\omega)$ is increased. However, with the increase in frequency, the dielectric constant gradually decreases as the dipoles are unable to follow the electric field. This fact can be

attributed to the periodic setback of the applied field which occurs in such a rapid manner that

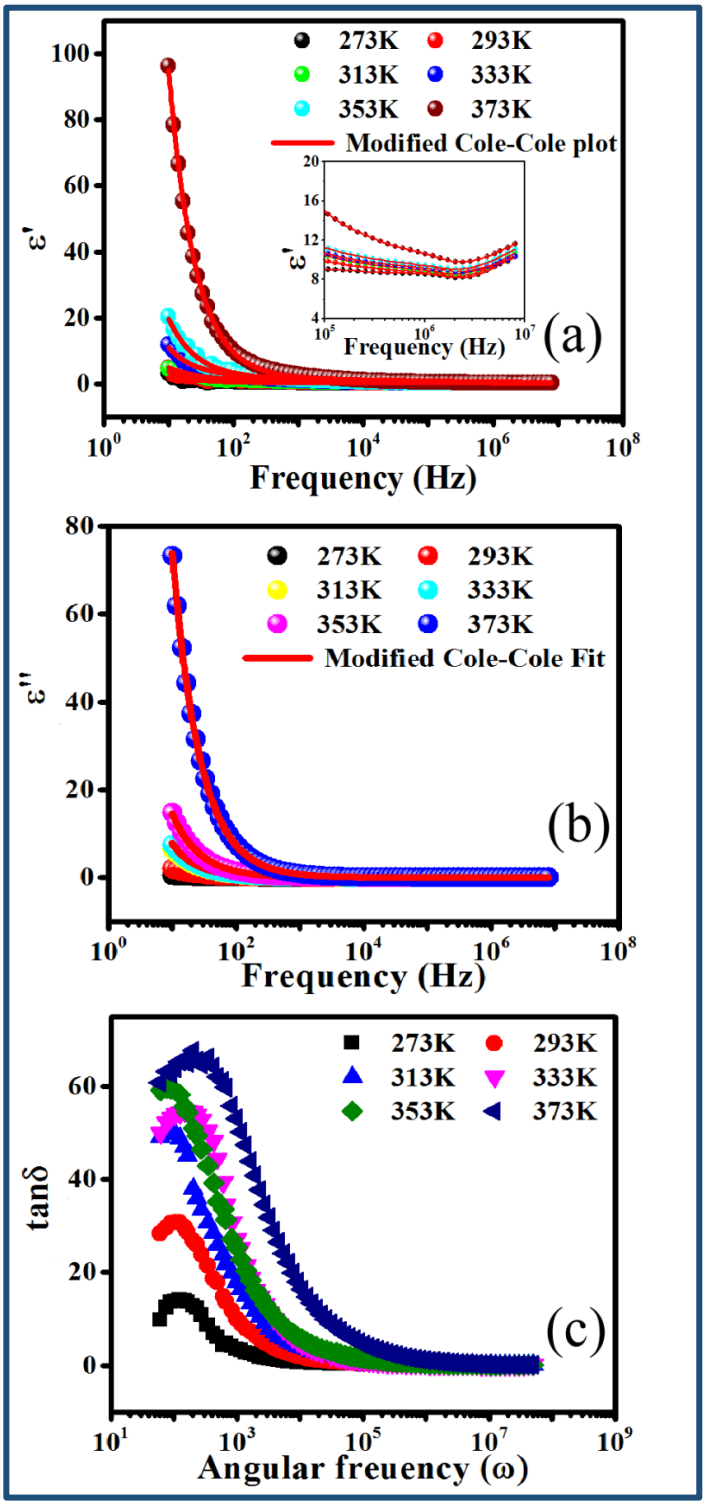

Fig. 4.5. (a) Variation of ε' of the sample at various temperature and fitted by modified Cole-Cole model, inset of (a) variation of ε' in high frequency region. (b) Variation of ε'' of the material at several temperatures and fitted by modified Cole-Cole model. (c) tanδ vs. angular frequency spectra of $CH_3H_7NH_3PbI_3$.

the dipoles are unable to align themselves along the direction of the applied field. As a result,

the number of electrons decreases at the grain boundary at high frequency region. Therefore, the behavior of the real part of dielectric response in low frequency region is governed by orientational polarization and interfacial polarization which confirms the non-Debye behavior [16, 17, 22]. The effect of ionic and electronic polarization is observed in high frequency region which leads to a lowering of the value of the dielectric constant ($\varepsilon'(\omega)$). Among the above-stated four polarizations, dipolar and space charge polarizations are strongly dependent on temperature. The increasing trend of $\varepsilon'(\omega)$ with temperature as shown in the inset of Fig. 4.5a is mainly due to the presence of thermally activated charge carriers and the moment of electric dipoles [18, 23]. Under the influence of the electric field, the rotation of temperature dependent dipoles in propylammonium cation causes fluctuation in energy and hence the dielectric constant is increased with temperature (inset of Fig. 4.5a).

The dielectric loss factor is found to decrease with an increase in frequency. According to the Koop's theory, imperfections or impurities present in the material form a potential barrier for the transportation of the charge carriers. The space charge polarization restricts the partial conduction of charges until they are clogged at a potential barrier or grain boundary. Therefore, due to the dominant effect of grain boundary in low frequency region, electrons require more energy for hopping which in turn gives rise to the high dielectric loss. On the other hand, with the increase in frequency, the effect of low-resistive layers of grain becomes prominent, and hopping electrons fail to follow the applied electric field. Thus, a very small amount of energy is required for the exchange of electrons between the ions of the same molecules which causes a decrease in dielectric loss in high frequency region. Orientational polarization requires more time than ionic or electronic polarization in high frequency region. Although, all four types of polarizations are present in the low frequency region, only ionic and electronic polarizations perform a significant role in high frequency region which causes the decrease in dielectric loss factor in high frequency region for all the specified temperatures [24, 25].

To study the variation of frequency of dielectric constant and dielectric loss for various temperatures, modified Cole-Cole model with a DC conductivity, correction term has been employed among several popular theoretical models [22, 26]. According to the modified Cole-Cole model, the complex permittivity can be expressed as

$$\varepsilon^* = \varepsilon_\infty + \frac{\varepsilon_s - \varepsilon_\infty}{1+(j\omega\tau)^\beta} - \frac{j\sigma^*}{\epsilon_0 \omega^m} \qquad (4.8)$$

Here, σ^* refers to the summation of space charge career conductivity (σ_{sp}) and free charge career conductivity (σ_{fc}), ε_s is the low-frequency limit of permittivity and ε_∞ is the high-frequency limit of permittivity. m is known as the frequency exponent and β refers to the modified Cole-Cole parameter whose value lies between 0 and 1. τ represents the relaxation time. The real (ε') and imaginary (ε'') part of dielectric constant can also be represented as equation (4.9,4.10).

$$\varepsilon' = \varepsilon_\infty + \left[\frac{(\varepsilon_s-\varepsilon_\infty)\left\{1+(\omega\tau)^\beta \cos\left(\frac{\beta\pi}{2}\right)\right\}}{1+2(\omega\tau)^\beta \cos\left(\frac{\beta\pi}{2}\right)+(\omega\tau)^{2\beta}}\right] + \frac{\sigma_{sp}}{\epsilon_0 \omega^m} \quad (4.9)$$

$$\varepsilon'' = \left[\frac{(\varepsilon_s-\varepsilon_\infty)(\omega\tau)^\beta \sin\left(\frac{\beta\pi}{2}\right)}{1+2(\omega\tau)^\beta \cos\left(\frac{\beta\pi}{2}\right)+(\omega\tau)^{2\beta}}\right] + \frac{\sigma_{fc}}{\epsilon_0 \omega^m} \quad (4.10)$$

The experimental data of ε' and ε'' are fitted with modified Cole-Cole equation and the derived values of several parameters β, m, σ_{sp}, σ_{fc}, τ are enlisted in Table 4.2. From Table 4.2, the value of space charge conductivity (σ_{sp}) and free charge conductivity (σ_{fc}) increases with the increase in temperature. The value of β lies between 0 and 1 which further confirms the non-Debye nature. The relaxation time is found to decrease with the increase in temperature.

Table 4.2: Estimated values of relaxation time, parameter, exponent, space charge, free charge conductivity froom the fitting of modified Cole-Cole model of frequency and temperature dependent dielectric constant and dielectric loss of $PAPbI_3$.

Parameter	Temperature					
	273 K	293 K	313 K	333 K	353 K	373 K
τ	0.091	1.018×10^{-4}	1.392×10^{-4}	4.209×10^{-4}	1.729×10^{-5}	2.795×10^{-6}
β	0.754	0.288	0.412	0.559	0.479	0.831
m	0.690	0.835	0.902	0.967	0.989	0.993
σ_{sp}	6.388×10^{-9}	2.214×10^{-8}	3.684×10^{-8}	2.112×10^{-7}	2.810×10^{-7}	1.273×10^{-6}
σ_{fc}	1.041×10^{-7}	9.904×10^{-7}	4.545×10^{-6}	1.631×10^{-5}	3.616×10^{-5}	8.222×10^{-5}

In this aspect, loss tangent is defined as the ratio of dielectric loss and the real part of the dielectric constant, and the variation of loss tangent with frequency for a given range of temperature is depicted in Fig. 4.5c.

$$\tan(\delta) = \frac{\varepsilon''(\omega)}{\varepsilon\prime(\omega)} \quad (4.11)$$

Loss tangent decreases with the increase in frequency and acquires a constant nature in high frequency region in a specific temperature. The appearance of peaks in low frequency region may be attributed to the dominant nature of dipolar polarization. Values of loss tangent increase and accordingly peaks shift with the increase in temperature which confirms that dipolar polarization is a thermally controlled mechanism. Interestingly, a loss peak arises when the hopping frequency matches appreciably with the frequency of the applied external AC field. Moreover, the hopping mechanism suggests that electrical conductivity increases with temperature which triggers the thermally activated charge carriers [27].

4.3.5. Analysis of electric modulus

To get an idea about the relaxation procedure in $PAPbI_3$, detailed complex modulus spectra have been studied. The complex electric modulus is the reciprocal of complex permittivity proposed by Macedo which is a very convenient tool to study the electrical relaxation mechanism of space charge distribution by suppressing the electrode effect. Electric modulus represents the relaxation of the electric field within the material when the dielectric displacement is constant. The electric modulus is given by the following formula:

$$M^* = \frac{1}{\varepsilon^*} = \frac{1}{(\varepsilon' + j\varepsilon")} = \frac{\varepsilon'}{\varepsilon'^2 + \varepsilon"^2} + i\frac{\varepsilon"}{\varepsilon'^2 + \varepsilon"^2} = M' + iM" \qquad (4.12)$$

Where M', $M"$, $\varepsilon'$and $\varepsilon"$are the real part and imaginary part of the electric modulus, M^*, and dielectric constant, ε^*, respectively [22, 28].

Figure 4.6a shows the real part of electric modulus spectra as a function of frequency for a range of temperatures. The variation of M' with frequency of $PAPbI_3$ depicts that M' acquires very small value (nearly zero) in low frequency region for all temperatures. Low value of M' in low frequency region and the sigmoidal nature of M' are ascribed to the long range mobility of charge careers in the conduction mechanism as well as the negligence of electrode polarization. There is a slight shift in the peak of M' along the high frequency region with the rise in temperature. The variation of the imaginary part of electric modulus, $M"$, with frequency is represented in Fig. 4.6b at different temperatures. At a particular temperature, $M"$ acquires its maximum value giving rise to a peak at a certain frequency which corresponds to the relaxation frequency. No peak is found in low frequency region whereas a broad, distinct, significant peak is observed in high frequency region. In lower frequency region, charge

carriers can move freely over a long distance which indicates the successful hopping of charge carriers from one site to its neighbouring site while charge carriers are confined in their

Table 4.3: Values of shape parameters a and b evaluated from the fitting of frequency and temperature dependent imaginary part of electric modulus of sample

Temperature (K)	a	b
273	0.79316	0.28773
293	0.80041	0.36876
313	0.84	0.41
333	0.86748	0.73641
353	0.87	0.738
373	0.87128	0.743

potential well and make restricted motion within the short range of the well in high frequency region. Thus, the occurrence of peak furnishes information about the transition from long range to short range mobility of charge carriers. The peaks in M'' are found to shift towards high frequency region with the increase in temperature which can be explained by the hopping mechanism. The asymmetrical nature of peaks in M'' indicates the non-Debye response of the sample. To explain the asymmetric nature of peaks in the imaginary part of electric modulus, Bergman, in 2000, proposed a general function, considering a modified Kohlrausch –Williams –Watts (KWW) function having two independent shape parameters for low and high frequency sides and a smoothing parameter of M'' spectra as enunciated in equation 4.13 [22, 26].

$$M''(\omega) = \frac{M''_{max}}{\frac{(1-c)}{(a+b)}\left[b\left(\frac{f}{f_{max}}\right)^{-a} + a\left(\frac{f}{f_{max}}\right)^{b}\right] + c} \qquad (4.13)$$

Here, M''_{max} is the maximum value of the imaginary part of the electric modulus and the corresponding frequency is denoted as f_{max}, a and b signify two independent shape parameters for low and high frequency sides respectively and c denotes the smoothing parameter. If a = b = 1 and c = 0, then equation 4.13 is reduced to equation 4.14 which refers to the ideal Debye type behavior. The ideal Debye type response provides the symmetrical nature of M'' spectra as a function of frequency. The solid line shows the fitting of modified KWW function in Fig. 4.6b and the values of shape parameters for different temperatures are summarized in Table 4.3. The values of a and b are found to increase with the rise in

temperature and tend very close to unity which suggests that with the rise in temperature, $M"(\omega)$ becomes close to the ideal Debye response. The deviation of the ideal Debye response happening in low and high frequency sides of experimental data points at 353 K for the sample is shown in the inset of Fig. 4.6(b).

$$M"(\omega) = \frac{M"_{max}}{\frac{1}{2}[\left(\frac{fmax}{f}\right)+\left(\frac{f}{fmax}\right)]} \quad (4.14)$$

The relaxation time has been calculated using the relations equation (4.15).

$$\tau = \frac{1}{f_{max}} \quad (4.15)$$

The average activation energy of charge carriers can be estimated from the Arrhenius equation stated as equation 4.16.

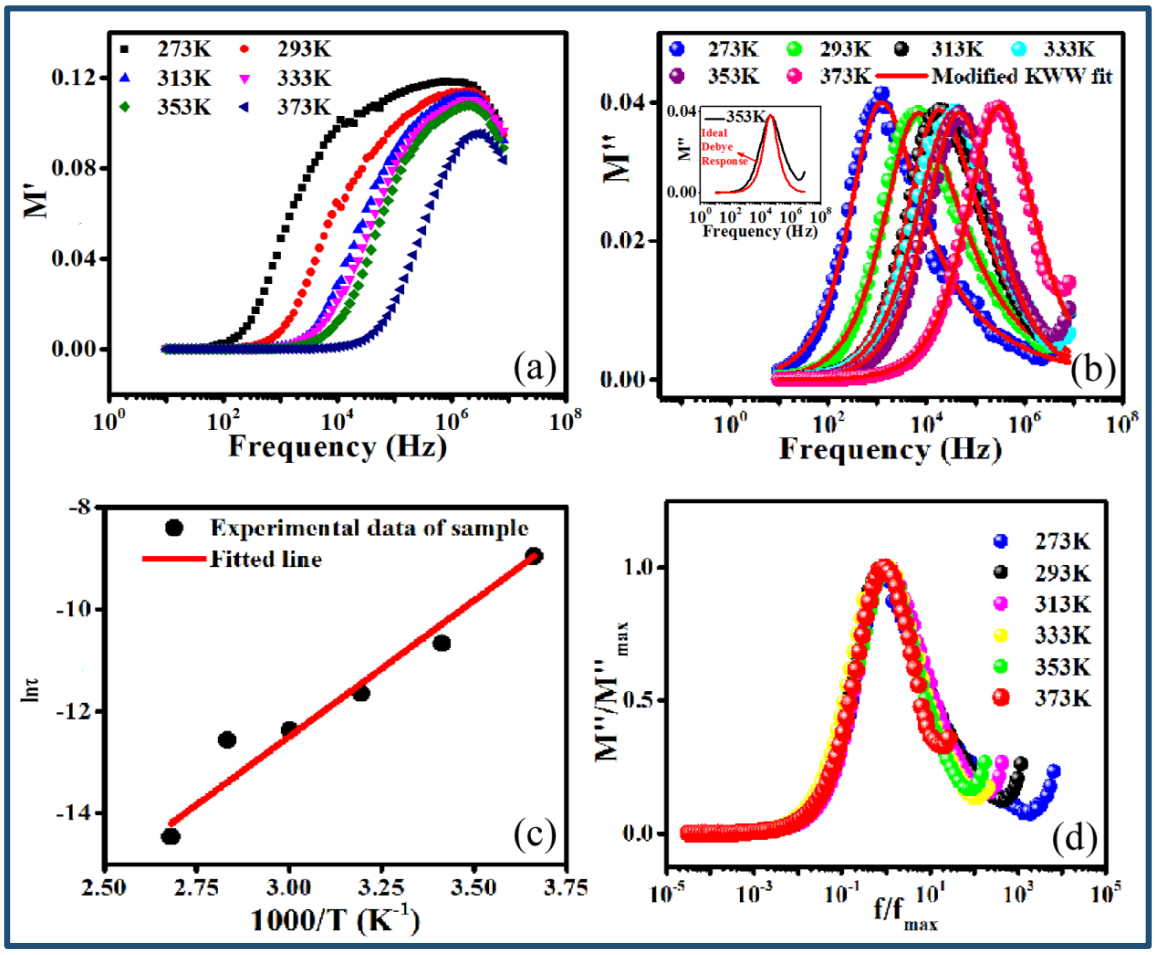

Fig. 4.6. (a) Frequency dependence of real part of electric modulus of $CH_3H_7NH_3PbI_3$. (b) Frequency dependence of imaginary part of electric modulus of the sample, inset of (b) Deviation from ideal Debye response at 353K. (c) Arrhenius plot of frequency maximum of $M"(\omega)$ of the sample. (d) Normalised imaginary electric modulus $M"/M"_{max}$ vs. f/f_{max} at different temperatures.

$$\tau = \tau_0 \exp(-\frac{E_a}{K_\beta T}) \quad (4.16)$$

The derived activation energy from the slope of the least square fitting of ln τ vs 1000/T plot (Fig. 4.6c) is 0.461 eV. This also proves the conduction mechanism in $PAPbI_3$ is due to the thermally stimulated charge carriers. The variation of the normalized imaginary part of the electric modulus with the normalized frequency of the studied sample for different temperatures has been shown in Fig. 4.6d. The peak positions of the normalized spectrum also exhibit the transition from long range mobility to short range mobility of charge carriers along with the hopping method of charge carriers as already explained in detail in the case of M'' spectra [29]. The coincidence of all the peaks at specified temperatures indicates the temperature independent performance of dynamic processes taking place within the sample.

4.3.6. Electrical conductivity

To interpret the electrical conduction mechanism, the AC conductivity of the sample has been studied extensively. The variation of temperature dependent AC conductivity as a function of frequency is shown in Fig. 4.7a. The AC electrical conductivity has been estimated using the relation $\sigma_{ac} = \omega\varepsilon'\varepsilon_0 tan\delta$ where ε_0 corresponds to the permittivity of free space. Here, the estimated conductivity in low frequency region is attributed to DC conductivity, and conductivity in high frequency region is attributed to AC conductivity. The curves seem flattened in low frequency region which is due to the contribution of frequency independent and temperature dependent DC conductivity [25]. However, the curves of electrical conductivity become much wider and show strong frequency dispersion with the increase in frequency which is due to the contribution of AC conductivity. In this type of frequency dependent conductivity, the frequency at which the transition of conductivity takes place is known as “hopping frequency” (ω_P). The hopping frequency is found to shift towards a high frequency region with the elevation of temperature. The observed frequency independent DC conductivity and frequency dependent AC conductivity can be illuminated by the theory of jump relaxation model (JRM) proposed by Funke [17]. According to this theory, in low frequency region, the ions can hop successfully to its neighboring vacant sites. Availability of long time period supports these successful jumps which lead to a long-range translational motion of ions devoted to DC conductivity. On the other hand, in high frequency region, both successful and unsuccessful hopping takes place. The jumping ions can jump back to its initial site (forward-backward-forward motion) giving rise to unsuccessful hopping. In successful

hopping, the excited jumping ion jumps to the new site and becomes stable in the new position

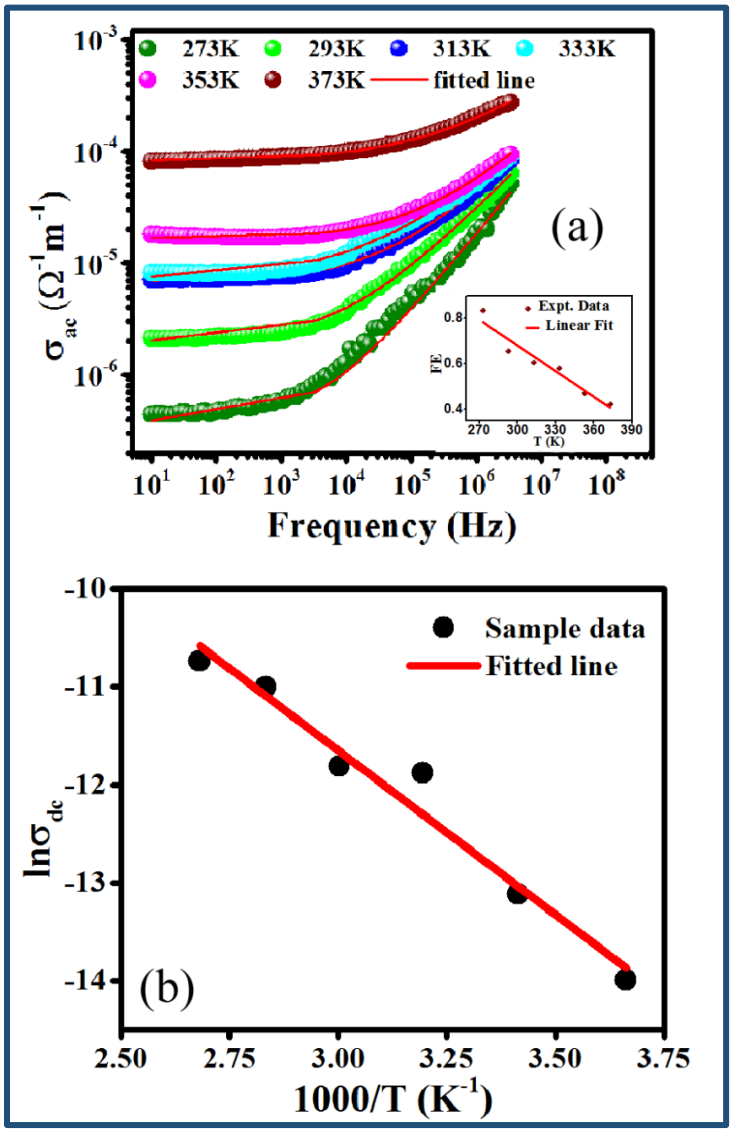

Fig. 4.7. (a) Variation of AC conductivity with frequency at different temperatures of $CH_3H_7NH_3PbI_3$, inset of (a) Variation of frequency exponent (FE) with temperature. (b) σ_{dc} vs. 1000/T plot of $CH_3H_7NH_3PbI_3$.

and the neighbouring ions become relaxed with this stationary ion. The ratio of successful and unsuccessful hopping is found to increase in high frequency region giving rise to dispersive conductivity in high frequency region. Now, among various conduction mechanisms, the measured electrical conductivity is ascribed to universal dielectric response (UDR) model proposed by Jonscher which is known as Jonscher's power law [30,31]

$$\sigma_{ac} = \sigma_{dc} + \sigma_0 f^s \qquad (4.17)$$

where, σ_{ac} and σ_{dc} refer to the AC and DC contribution of total conductivity respectively, σ_0 is a constant and *S* is known as the frequency exponent, the value of which lies

between 0 and 1. *S* follows the interaction of charge carriers with the lattice of the sample. UDR model is employed to fit the experimental data of frequency dependent conductivity of the sample (Fig. 4.7a). It can be observed from the inset of Fig. 4.7a that values of *S* tend to decrease with the increase in temperature which recommends the correlated barrier hopping (CBH) conduction mechanism expressed in equation 4.18. [17,26]

$$S = 1 - \frac{6K_\beta T}{W_m - K_\beta T ln\left(\frac{1}{\omega\tau_0}\right)} \quad (4.18)$$

where, W_m represents the maximum barrier height, K_β is Boltzmann constant, ω is the angular frequency and τ_0 refers to relaxation time.

For an ideal dielectric system, the value of *S* becomes equal to 1 which indicates the minimum ideal Debye type dipole-dipole interaction. In this case, the value of *S* is found to be 0.83049 for 273 K which is quite lower than the ideal dielectric material. The linear decline of frequency exponent can be analyzed with the help of simpler form of CBH model as stated in equation 4.19.

$$S = 1 - \frac{6K_\beta T}{W_m} \quad (4.19)$$

The value of effective barrier height can be calculated from the linear fitting of temperature dependent frequency exponent. The value of W_m is found to be 0.2329 eV in this case.

In this context, σ_{dc} values have been calculated for different temperatures by non-linear curve fitting of σ_{ac} with the help of UDR model. The activation energy (E_a) of $PAPbI_3$ has further been estimated from the σ_{dc} vs. 1000/T plot (Fig. 4.7b) using Arrhenius equation$\sigma_{dc} = \sigma_0 \exp\left[-\frac{E_a}{KT}\right]$, where, σ_0 is considered as a pre-exponential factor. The value of E_a of $PAPbI_3$ is assessed to be 0.372 eV which is very close to the value obtained from the M'' spectra. σ_{dc} at 293 K is calculated to be 2.013 $x10^{-6}$ $S.m^{-1}$ which is comparable to 1.29E-6 $S.m^{-1}$ of $CH_3NH_3PbI_3$.[32]

4.4. Conclusion

In summary, propyl-ammonium lead iodide has been synthesized by sol gel method, and its structural, optical, and extensive dielectric properties are investigated. The XRD analysis confirms the formation of polycrystalline propyl-ammonium lead iodide. High dielectric constant with low dielectric loss in high frequency region makes this perovskite attractive for

applications. Space charge and free charge conductivity are measured from the modified Cole-Cole plot which are found to increase with the rise in temperature. AC conductivity has been studied in detail and described based on CBH conduction mechanism and it indicates a satisfactory response for applications. Dielectric study furnishes information about the contribution of grain and grain boundary on the total impedance. Asymmetric electric modulus curves obtained from the measurement are evaluated with the KWW equation. It has also been found that with the elevation in temperature, the non-Debye nature of the imaginary part of the electric modulus decreases. Activation energy has been calculated from both modulus spectra as well as DC conductivity. The very close values of activation energy suggest that the process of relaxation behavior and conduction mechanism are similar. The structural simplicity as well as the ease of fabrication process may make this material attractive in the formation of multi-layered devices for energy harvesting. The estimated favorable energy band gap, evaluated dielectric constant, relaxation time, and above all conductivity indicate this sample is a new promising perovskite which can be employed in energy harvesting systems.

References

[1] D.O. Demchenko, N. Izyumskaya, M. Feneberg, V. Avrutin, Ü. Özgür, R. Goldhahn, H. Morkoç, Optical properties of the organic-inorganic hybrid perovskite, Phys. Rev. B. 94 (2016) 075206. https://doi.org/10.1103/PhysRevB.94.075206.

[2] Y.-F. Ding, Q.-Q. Zhao, Z.-L. Yu, Y.-Q. Zhao, B. Liu, P.-B. He, H. Zhou, K. Li, S.-F. Yin, M.-Q. Cai, Strong thickness-dependent quantum confinement in all-inorganic perovskite Cs_2PbI_4 with a Ruddlesden–Popper structure, J. Mater. Chem. C. 7 (2019) 7433–7441. https://doi.org/10.1039/C9TC02267H.

[3] X.-Z. Deng, Q.-Q. Zhao, Y.-Q. Zhao, M.-Q. Cai, Theoretical study on photoelectric properties of lead-free mixed inorganic perovskite $RbGe_{1-x}Sn_xI_3$, Curr. Appl. Phys. 19 (2019) 279–284. https://doi.org/10.1016/j.cap.2018.12.007.

[4] X. Zhang, C. Sun, Y. Zhang, H. Wu, C. Ji, Y. Chuai, P. Wang, S. Wen, C. Zhang, W.W. Yu, Bright Perovskite Nanocrystal Films for Efficient Light-Emitting Devices, J. Phys. Chem. Lett. 7 (2016) 4602–4610. https://doi.org/10.1021/acs.jpclett.6b02073.

[5] Y.-Q. Zhao, Q.-R. Ma, B. Liu, Z.-L. Yu, J. Yang, M.-Q. Cai, Layer-dependent transport and optoelectronic property in two-dimensional perovskite: $(PEA)_2PbI_4$, Nanoscale. 10 (2018) 8677–8688. https://doi.org/10.1039/C8NR00997J.

[6] Y.-Q. Zhao, Q.-R. Ma, B. Liu, Z.-L. Yu, M.-Q. Cai, Pressure-induced strong ferroelectric polarization in tetra-phase perovskite $CsPbBr_3$, Phys. Chem. Chem. Phys. 20 (2018) 14718–14724. https://doi.org/10.1039/C8CP01338A.

[7] P. Sadhukhan, S. Kundu, A. Roy, A. Ray, P. Maji, H. Dutta, S.K. Pradhan, S. Das, Solvent-Free Solid-State Synthesis of High Yield Mixed Halide Perovskites for Easily Tunable Composition and Band Gap, Cryst. Growth Des. 18 (2018) 3428–3432. https://doi.org/10.1021/acs.cgd.8b00137.

[8] P. Gao, M. Grätzel, M.K. Nazeeruddin, Organohalide lead perovskites for photovoltaic applications, Energy Environ. Sci. 7 (2014) 2448–2463. https://doi.org/10.1039/C4EE00942H.

[9] M. Safdari, A. Fischer, B. Xu, L. Kloo, J.M. Gardner, Structure and function relationships in alkylammonium lead iodide solar cells, J. Mater. Chem. A. 3 (2015) 9201–9207. https://doi.org/10.1039/C4TA06174H.

[10] S. Mondal, S.R. Bhattacharyya, Performance of a size-selected nanocluster deposition facility and in situ characterization of grown films by x-ray photoelectron spectroscopy, Rev. Sci. Instrum. 85 (2014) 065109. https://doi.org/10.1063/1.4882315.

[11] M. Das, S. Roy, Methyl red/polycarbazole composites: Humidity sensing characteristics and its adsorption kinetics study, IOP Conf. Ser. Mater. Sci. Eng. 561 (2019) 012092. https://doi.org/10.1088/1757-899X/561/1/012092.

[12] A. Ray, A. Roy, S. Bhattacharjee, S. Jana, C.K. Ghosh, C. Sinha, S. Das, Correlation between the dielectric and electrochemical properties of TiO_2-V_2O_5 nanocomposite for energy storage application, Electrochim. Acta. 266 (2018) 404–413. https://doi.org/10.1016/j.electacta.2018.02.033.

[13] M. Ahmad, M.A. Rafiq, M.M. Hasan, Transport characteristics and colossal dielectric response of cadmium sulfide nanoparticles, J. Appl. Phys. 114 (2013) 133702. https://doi.org/10.1063/1.4823810.

[14] N. Ortega, A. Kumar, P. Bhattacharya, S.B. Majumder, R.S. Katiyar, Impedance spectroscopy of multiferroic $PbZr_xTi_{1-x}O_3$Õ$CoFe_2O_4$ layered thin films, Phys. Rev. B. 77 (2008) 014111. https://doi.org/10.1103/PhysRevB.77.014111.

[15] Z. Imran, M.A. Rafiq, M.M. Hasan, Charge carrier transport mechanisms in perovskite CdTiO 3 fibers, AIP Adv. 4 (2014) 067137. https://doi.org/10.1063/1.4885462.

[16] D.K. Pradhan, S. Kumari, V.S. Puli, P.T. Das, D.K. Pradhan, A. Kumar, J.F. Scott, R.S. Katiyar, Correlation of dielectric, electrical and magnetic properties near the magnetic phase transition temperature of cobalt zinc ferrite, Phys. Chem. Chem. Phys. 19 (2017) 210–218. https://doi.org/10.1039/C6CP06133H.

[17] D.K. Pradhan, P. Misra, V.S. Puli, S. Sahoo, D.K. Pradhan, R.S. Katiyar, Studies on structural, dielectric, and transport properties of $Ni_{0.65}Zn_{0.35}Fe_2O_4$, J. Appl. Phys. 115 (2014) 243904. https://doi.org/10.1063/1.4885420.

[18] S. Kumari, N. Ortega, A. Kumar, S.P. Pavunny, J.W. Hubbard, C. Rinaldi, G. Srinivasan, J.F. Scott, R.S. Katiyar, Dielectric anomalies due to grain boundary conduction in chemically substituted $BiFeO_3$, J. Appl. Phys. 117 (2015) 114102. https://doi.org/10.1063/1.4915110.

[19] C.R. Cena, A.K. Behera, B. Behera, Structural, dielectric, and electrical properties of lithium niobate microfibers, J. Adv. Ceram. 5 (2016) 84–92. https://doi.org/10.1007/s40145-015-0176-7.

[20] C.G. Koops, On the Dispersion of Resistivity and Dielectric Constant of Some Semiconductors at Audiofrequencies, Phys. Rev. 83 (1951) 121–124. https://doi.org/10.1103/PhysRev.83.121.

[21] M. Ahmad, M.A. Rafiq, K. Rasool, Z. Imran, M.M. Hasan, Dielectric and transport properties of bismuth sulfide prepared by solid state reaction method, J. Appl. Phys. 113 (2013) 043704. https://doi.org/10.1063/1.4781004.

[22] P. Thongbai, S. Tangwancharoen, T. Yamwong, S. Maensiri, Dielectric relaxation and dielectric response mechanism in (Li, Ti)-doped NiO ceramics, J. Phys. Condens. Matter. 20 (2008) 395227. https://doi.org/10.1088/0953-8984/20/39/395227.

[23] S. Patra, P. Sengupta, A. Ray, A. Roy, S. Das, Discrete dipole approximation for calculating optical properties of ZnO nanoparticles and ZnO-PVP composites, Ceram. Int. 44 (2018) 14236–14241. https://doi.org/10.1016/j.ceramint.2018.05.027.

[24] J. Liu, C.-G. Duan, W.-G. Yin, W.N. Mei, R.W. Smith, J.R. Hardy, Dielectric permittivity and electric modulus in $Bi_2Ti_4O_{11}$, J. Chem. Phys. 119 (2003) 2812–2819. https://doi.org/10.1063/1.1587685.

[25] X.Z. Zuo, J. Yang, B. Yuan, D.P. Song, X.W. Tang, K.J. Zhang, X.B. Zhu, W.H. Song, J.M. Dai, Y.P. Sun, Magnetic, dielectric properties, and scaling behaviors of Aurivillius compounds $Bi_{6-x/3}Fe_2Ti_{3-2x}(WCo)_xO_{18}$ ($0 \leq x \leq 0.15$), J. Appl. Phys. 117 (2015) 114101. https://doi.org/10.1063/1.4915089.

[26] D.K. Rana, S.K. Singh, S.K. Kundu, S. Roy, S. Angappane, S. Basu, Electrical and room temperature multiferroic properties of polyvinylidene fluoride nanocomposites doped with nickel ferrite nanoparticles, New J. Chem. 43 (2019) 3128–3138. https://doi.org/10.1039/C8NJ04755C.

[27] G.C. Psarras, E. Manolakaki, G.M. Tsangaris, Dielectric dispersion and ac conductivity in—Iron particles loaded—polymer composites, Compos. Part A Appl. Sci. Manuf. 34 (2003) 1187–1198. https://doi.org/10.1016/j.compositesa.2003.08.002.

[28] D.K. Rana, S.K. Singh, S.K. Kundu, S. Roy, S. Angappane, S. Basu, Electrical and room temperature multiferroic properties of polyvinylidene fluoride nanocomposites doped with nickel ferrite nanoparticles, New J. Chem. 43 (2019) 3128–3138. https://doi.org/10.1039/C8NJ04755C.

[29] B.E. Jun, H.K. Kim, Y.H. Hwang, B.C. Choi, J.H. Jeong, J.S. Bae, C.H. Kim, Electric modulus scaling behaviors of the near stoichiometric potassium lithium niobate crystal, J. Korean Phys. Soc. 49 (2006) 2408–2412.

[30] S.R. Elliott, A.c. conduction in amorphous chalcogenide and pnictide semiconductors, Adv. Phys. 36 (1987) 135–217. https://doi.org/10.1080/00018738700101971.

[31] N. Vol, review article The universal ' dielectric response, Nature. 267 (1977) 673–679.

[32] M.S. Sheikh, A.P. Sakhya, P. Sadhukhan, A. Dutta, S. Das, T.P. Sinha, Dielectric relaxation and Ac conductivity of perovskites $CH_3NH_3PbX_3$ (X = Br, I), Ferroelectrics. 514 (2017) 146–157. https://doi.org/10.1080/00150193.2017.1359023.

CHAPTER 5

5. Influence of Activation Energy on Charge Conduction Mechanism and Giant Dielectric Relaxation of Sol-gel Derived $C_3H_7NH_3PbBr_3$ Perovskite; Act as High Performing UV Photodetector

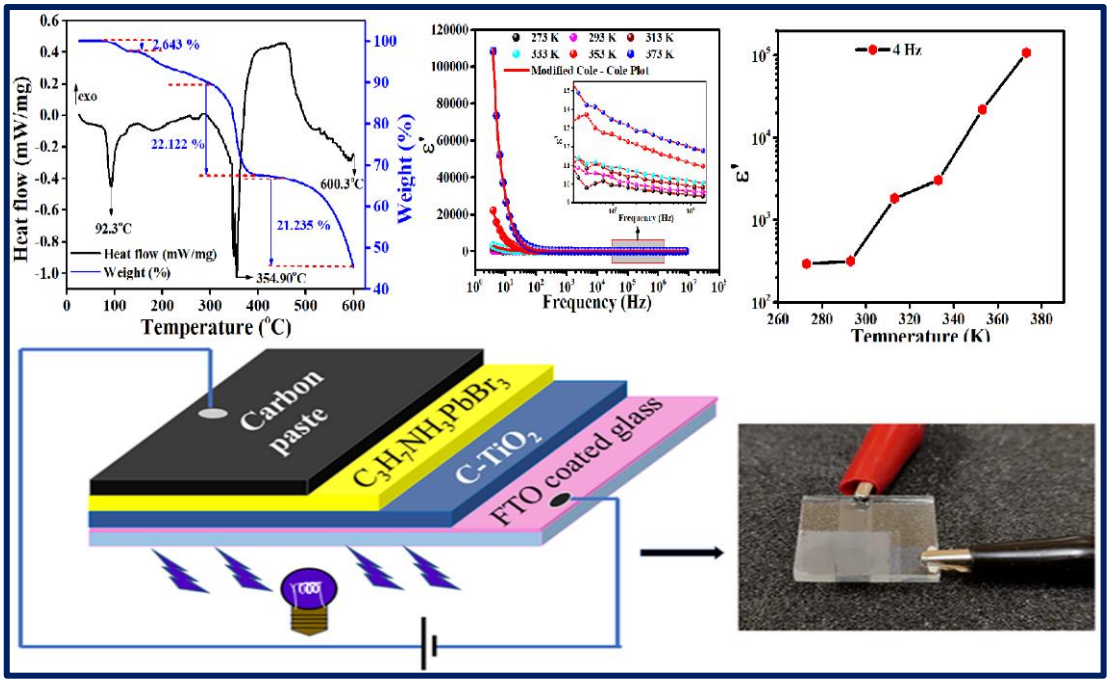

5.1. Introduction

Organic-inorganic hybrid perovskites are a class of perovskites which drawn immense attention in recent years in the field of optoelectronic applications including photovoltaics, photodetectors, lasers, etc. These organometallic perovskites are semiconductor compounds which possess a certain crystal structure having inorganic anions in an organic framework with a general formula of ABX_3 where A refers to the organic cation, B denotes metallic or inorganic ion and X stands for halide anion. High absorption efficiency, tunable band gap, long charge diffusion distance, etc. make these hybrid halide perovskites attractive for commercialization in optoelectronic devices [1]. The inorganic components of these hybrid perovskites are strongly interactive with organic cations. Hence, electronic properties like band gap, and mobility of charge carriers of these organometallic perovskites can be tuned by substituting metal ions, organic cations, or halide anions. Though the interactivity between organic and inorganic components of hybrid structure has not yet been analyzed, nowadays researchers are dealing with various types of alkylammonium lead halides [2,3]. Propylammonium lead bromide, a simple single (1-dimensional) chain structure perovskite, is one of the promising hybrid perovskites. This compound is visibly white and possesses a wide range of energy band gap of ~ 3 eV [4]. Moreover, this perovskite shows appreciable thermal stability. The structural simplicity and optimal band gap make this perovskite potential for optoelectronic applications like UV detectors. To the best of our knowledge, the enthralling response of this material under UV irradiation is reported here for the very first time. Charge conduction through the material significantly participates in the determination of its efficiency in electrical and optoelectronic applications. Dielectric behavior is quite important to depict the nature of AC conduction through the widespread frequency and temperature driven sample which will help to understand the nature of the compound.

In this report, propylammonium lead bromide ($PAPbBr_3$) has been prepared by solution gel method. Besides the structural and optical properties, a detailed analysis of the electrical properties of the proposed perovskite has been carried out in this work. The thermally active dielectric response of $PAPbBr_3$ can deliver adequate information regarding the charge transport mechanism, movement of the localized charge carriers, relaxation time, permittivity, behavior of electric modulus, etc. The experimental consequences of electrical properties have been analyzed meticulously using various available theoretical models to extract different parameters like dielectric constant, relaxation time, activation energy, charge conductivity, etc.

5.2. Experimental details

5.2.1. Materials

n – Propylamine ($C_3H_7NH_2$, 98 %) was purchased from Spectrochem. Hydrobromic acid (57 wt. % in water) was bought from Loba Chemie. 99.8% Anhydrous Dimethylformamide (DMF) and lead bromide ($PbBr_2$) were purchased from Merck Chemicals and Loba Chemie respectively. All the reagents employed here were used as their receiving form and each of them was of analytical grade.

5.2.2. Preparation of propylammonium lead bromide ($C_3H_7NH_3PbBr_3$)

First of all, propylammonium bromide ($C_3H_7NH_3Br$) was prepared by mixing propylamine ($C_3H_7NH_2$) and hydrobromic acid (HBr) in equimolecular ratio at 0 ^oC and stirred continuously for two hours. The obtained solution was then evaporated and splashed thrice with diethyl ether to eliminate unreacted HBr molecules. Lastly, the propylammonium bromide was obtained by drying the solution under vacuum for 12 hours.

For the synthesis of propylammonium lead bromide, an equimolar ratio of propylammonium bromide and lead bromide were dissolved in DMF at 60 ^oC followed by continuous stirring for 10 hours. Then the solution was sieved to separate the precipitate and the clear solvent thus obtained was vaporized at 65 ^oC to form the desired white powder ($C_3H_7NH_3PbBr_3$).

5.2.3. Fabrication of UV photodetector

The fluorine incapacitated tin oxide (FTO) coated glass substrate was cleaned at first and ultrasonicated in deionized water and isopropyl alcohol for 20 min each and then dried in air. Next, a mildly acidic solution of titanium isopropoxide (TiO_2) was spin coated on the cleaned FTO substrate at 3000 rpm for 60 s followed by consecutive annealing in ambient conditions at 100 ^oC for 15 min and 500 ^oC for 30 min, respectively. Hence, the layer of compact TiO_2 form which serve as an electron transportation layer (ETL). A thin layer of $PAPbBr_3$ is spin coated on C-TiO_2 at 1000 rpm for 20 s and 4000 rpm for 20 s respectively. Then, the substrate containing multi-layers was annealed at 100 ^oC for 10 min. Next, a layer of carbon paste was then blade coated onto the perovskite layer to form the sandwich structure and annealed at 100

^{o}C for 5 min. The carbon paste contains 1 gram carbon black, 3 grams of graphite nanopowder, 40 mg carbon nano tube (CNT) in 8 grams α-terpeniol and 10 ml of ethanol.

5.2.4. Characterization

The structural study of the as synthesized sample has been carried out with high resolution synchrotron X-Ray power diffraction data from PETRA III beam line (λ = 0.207430 Å) at DESY, Germany. The sample was loaded carefully in a glass capillary tube and then sealed on both sides to avoid further damage. The sample loaded capillary tube was subjected to move from left to right so that the x-ray could irradiate different portions of the sample. The microstructural morphology has been categorized by scanning electron microscopy using FESEM (Zeiss, Germany, model: SUPRA 40) with a spatial resolution of 2 nm. Ultraviolet – visible spectroscopy has been conducted to determine the band gap of the sample using PerkinElmer (λ = 1050 Å). X-ray Photoelectron Spectroscopy (XPS) has been undergone with the help of XPS facility (VSW Ltd., UK) connected in a UHV companionable nanocluster deposition unit to determine the compositional information of the sample. The internal pressure of XPS chamber was maintained at 5×10^{-10} mbar. Mg K_{α} of energy 1253 eV was employed in this experiment and produced photoelectrons were analyzed with a hemispherical electron analyzer operating at 20 eV with a stay time of 1 s. Thermal stability analysis was carried out NETZSCH make TG – DSC (model: 449C). Differential scanning calorimetry (DSC) and thermogravimetry studies were performed from 30 ^{o}C to 625 ^{o}C (at a ramp up rate of 10 K/min). The IV curve of the so formed device was recorded with a Kiethley 2602B in dark or illuminated mode. White light was supplied with an array of white LEDs. A UV laser was used for UV light. For response time measurement, the photo detector was subjected to a pulsating UV light and the output photo voltage of the photo detector was recorded with a Tektronix digital storage oscilloscope. The nature of dielectric response, relaxation time, impedance study, electric modulus, loss tangent, activation energy, AC conductivity, etc. was analyzed with the help of complex impedance spectra which was obtained by inserting a sample pellet of diameter 8 mm between a pair of Cu electrode in Hioki LCR Q meter (IM3536). The dielectric measurement was carried out at range of temperatures ($273\ K \leq T \leq 373\ K$) as a function of frequency ($4\ Hz \leq f \leq 8\ MHz$).

5.3. Results and discussions

5.3.1. Structural, microstructural, and optical behavior

We have performed initial Lebail refinement using triclinic space group (P -1) symmetry using FullProf software [5,6]. The profile shape has been modeled using pseudo-voigt function. The observed, calculated, and the difference between observed and calculated data is shown in Fig.

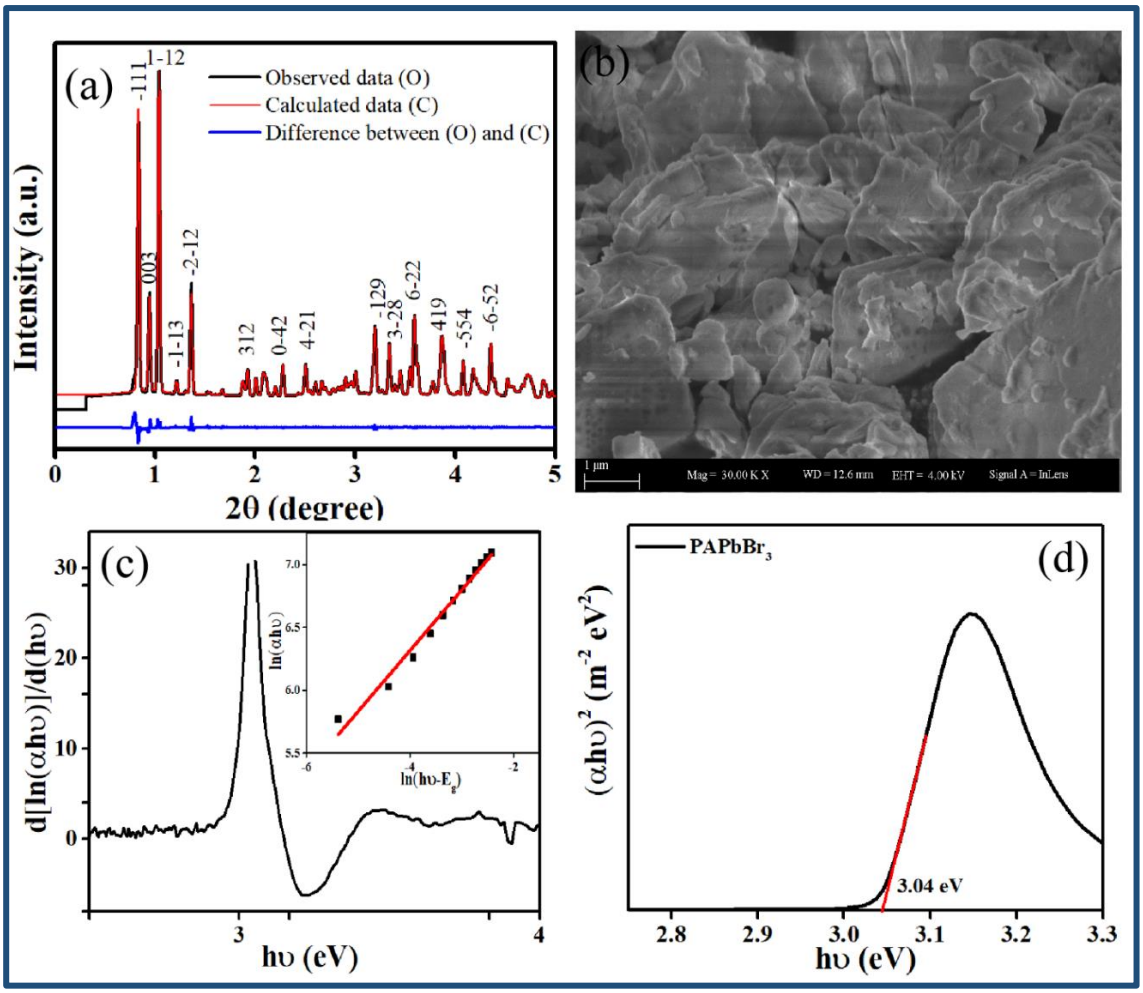

Fig. 5.1.(a) X-ray diffraction pattern of synthesized sample, (b) SEM image showing microstructure of $PAPbBr_3$, (c) $\left[\frac{d(ln(\alpha h\vartheta))}{d(h\vartheta)}\right]$ vs. $h\vartheta$ plot showing discontinuity, inset of (c) $ln(\alpha h\vartheta)$ is plotted against $ln(h\vartheta - E_g)$, (d) Band gap calculation from $(\alpha h\vartheta)^2$ vs. $(h\vartheta)$.

5.1a. The difference between calculated and observed data is almost flat as can be noticed and all the peaks are well indexed with the space group (P -1) symmetry with lattice parameters a

= 21.414425 Å, b = 21.563747, c = 36.350903, α = 92.003860°, β = 93.686470 ° and γ = 90.545921°. The space group matches with the previously reported data [4]. Fig. 5.1b shows the microstructural morphology of the as synthesized sample. The optical band gap of this sample is evaluated using equation 5.1.

$$\alpha = \left(\frac{A}{h\vartheta}\right)(h\vartheta - E_g)^m \quad (5.1)$$

Here, α refers to the optical absorption coefficient, A is a constant, $h\vartheta$ represents the incident energy and m determines the nature of optical transition. Though most of the hybrid perovskites exhibit allowed direct optical transition, the nature of transition may vary. Thus, avoiding the pre-assumption, the nature of transition has been determined here first. Equation 1 can be also written as equation 5.2.

$$\ln(\alpha h\vartheta) = \ln A + m\ln(h\vartheta - E_g) \quad (5.2)$$

$$\left[\frac{d(\ln(\alpha h\vartheta))}{d(h\vartheta)}\right] = \frac{m}{(h\vartheta - E_g)} \quad (5.3)$$

The plot of $\left[\frac{d(\ln(\alpha h\vartheta))}{d(h\vartheta)}\right]$ vs. $h\vartheta$ shows a signature discontinuity which indicates a transition at 3.04 eV (Fig. 5.1c) and the value of E_g has been evaluated from the divergence of the plot. m is estimated as 0.48 (slightly lesser than 0.5) from the slope of $\ln(\alpha h\vartheta)$ vs. $\ln(h\vartheta - E_g)$ signifying allowed direct transition in the representative spin coated film (inset of Fig. 5.1c). The exact value of the direct energy band gap of the sample is finally assessed as 3.04 eV (Fig. 5.1d) from the intersection of the absorption axis $(\alpha h\vartheta)^2$ to the energy axis $(h\vartheta)$ using Tauc plot equation [7].

5.3.2. XPS investigation

Fig. 5.2a indicates the entire XPS survey spectrum of $PAPbBr_3$ consisting of overriding peaks of C 1S (binding energy (B.E.) = 285 eV), O 1s (532 eV), Pb 4f doublets (138.9 eV and 143.6 eV), Br 3d doublets (68 eV – 70 eV) with submissive peaks of Br 3p doublets (182 eV, 189.6 eV) and Si 2p (98.6 eV). As the synthesized sample was dispersed on a Si substrate, a peak of Si was found in the survey spectrum. The elemental peaks accompanied by corresponding satellite peaks are deconvoluted and analyzed from high resolution (HR) spectra of Pb 4f, Br 3d, and Br 3p as shown in Fig. 5.2(b, c, d). Peaks of Pb $4f_{7/2}$ (138.9 eV) and Pb $4f_{5/2}$ (143.6 eV) emerge from untainted Pb present in $PAPbBr_3$.This investigation confirms the non-existence

of any other Pb-oxide compound within the sample. Twin peaks of Br 3p (Br $3p_{3/2}$ and Br $3p_{5/2}$)

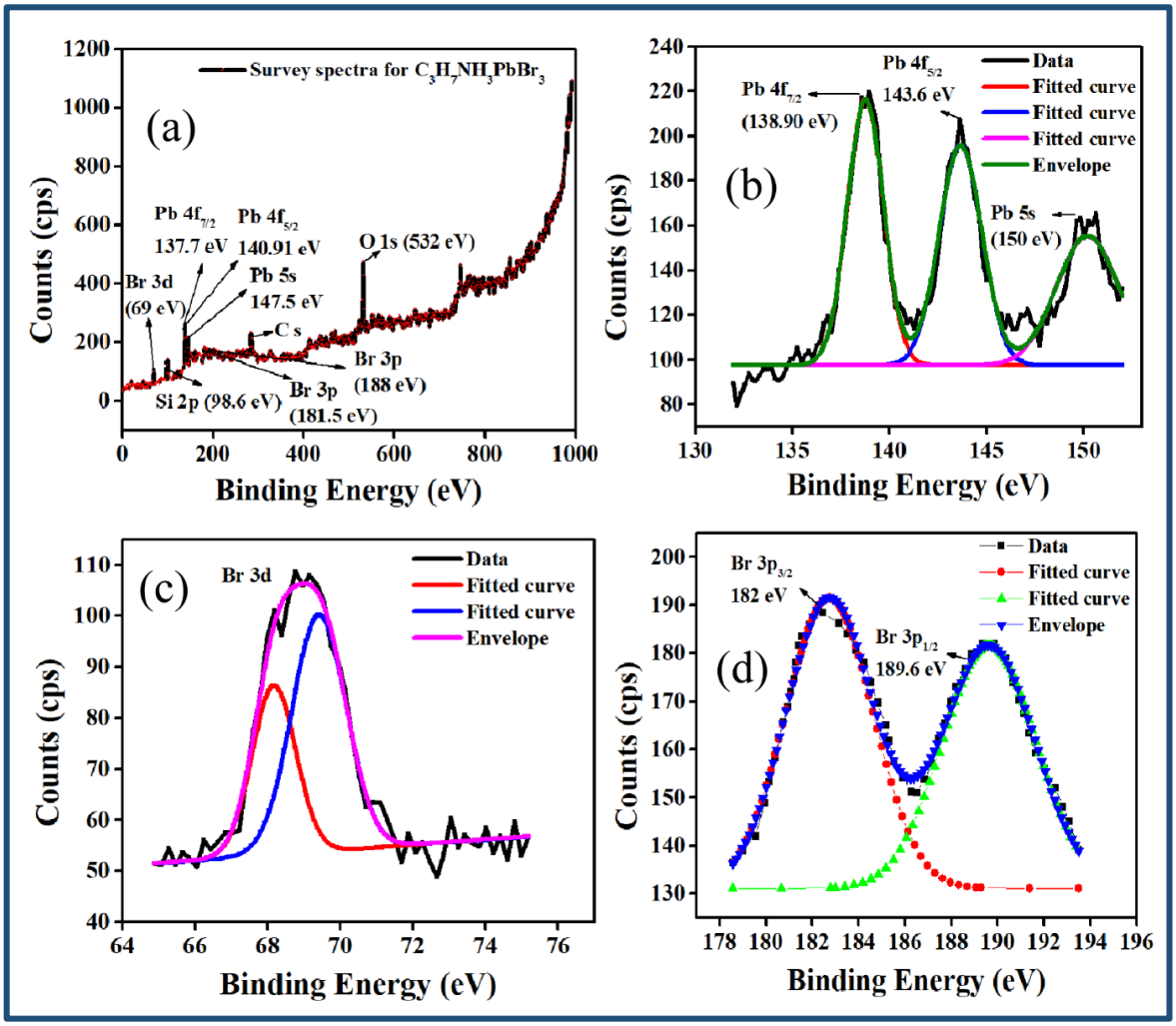

Fig. 5.2.(a) XPS survey spectrum of the sample, (b) High resolution spectrum of Pb and its deconvoluted curves, (c) and (d) High resolution spectra containing deconvoluted curves of Br 3d and Br 3p, respectively.

do not participate in bond formation with Pb. Br 3d peaks and Pb $4f_{5/2}$ appear from $PbBr_2$ compound.

5.3.3. Thermal stability study

Thermogravimetric analysis (TGA) is employed to investigate the thermal stability of $PAPbBr_3$. It can be observed from Fig. 5.3a that weight loss of the sample occurred in three steps ranging between (i) 76 – 130 ^oC, (ii) 301 – 393 ^oC, and (iii) 456 – 600 ^oC. 2.64% weight loss in the 1st step is merely because of the removal of absorbed moisture in the sample [8]. No thermal degradation occurred in the 1st stage. Sequential decomposition in the sample is found

to initiate in the 2nd step as organic component propylammonium bromide undergoes thermal

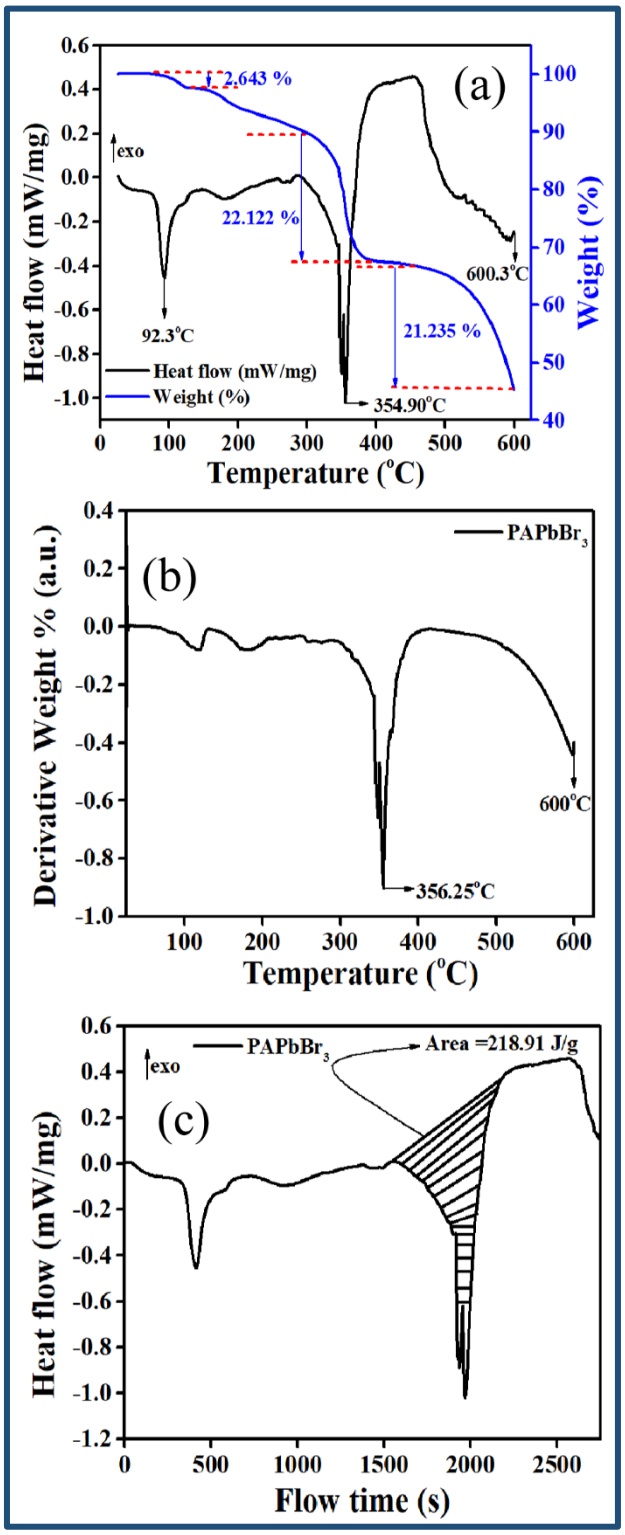

Fig. 5.3(a) DSC and TGA curve of the sample, (b) Derivative weight % vs. temperature curve of the sample, (c) Heat flow vs. flow time curve of the sample.

degradation and weight loss of HBr and propylamine takes place [8]. Thus, amine group is found to be combined more tightly in perovskite structure in comparison with HBr. The TGA weight loss profile shows complete mass loss in the 3rd step due to the sublimation of lead

bromide within this temperature range. The DSC shows no significant endothermic or exothermic reaction occurs below 300 ^{o}C. The second endothermic peak with sublimation at 354.9 ^{o}C found in DSC curve implies the thermal stability of the concerned perovskite up to 300 ^{o}C since the first endothermic peak indicates only the release of absorbed moisture in the perovskite sample. Derivative weight % shows the prominent thermal behavior of the sample (Fig. 5.3b). Enthalpy (ΔH) of the endothermic reaction is found to be 218.91 J/g (Fig. 5.3c).

5.3.4. UV photodetector

Having a wide band gap, $PAPbBr_3$ shows its potential in the application of optoelectronic devices particularly as UV photodetector. The architecture of the fabricated device follows the well conventional sandwich structure (Fig. 5.4a) where the intermediate layer of $PAPbBr_3$ acts as active material which is used to absorb the incident photons and produce electron–hole pairs under the light illumination. The carbon paste layer is used as an effective back contact electrode as well as the hole transport layer (HTL). The intimate connection between the $PAPbBr_3$ and carbon layer boosts the performance of the device by easing the assortment of photo-excited holes at the perovskite layer. This HTL cum back electrode configuration in a single package makes the device architecture simple and efficient by eliminating a dedicated HTL and reducing subsequent capacitive and resistive effects that slow down the photodiode under operation. C-TiO_2 layer deposited on FTO substrate performs as hole blocking layer and averts the shorting of electrodes.

The current-voltage (IV) characteristic curve of the so formed photo diode in dark and illuminated conditions is shown in Fig. 5.4b. The IV curve in the dark condition shows a very good diode profile, confirming a good rectifying interface inside the device. Under white light illumination of intensity 80 mW / cm^2, the device shows a very slight change in the IV curve concerning the dark condition. However, the device exhibits a remarkable change in photocurrent when exposed to UV laser with an intensity of just 5 mW / cm^2. The slight change in photocurrent under white light excitation is due to the minor presence of UV rays in a white light source. The interesting fact is that the device is not influenced by any external wavelength filter. This device possesses an impressive response in UV light illumination due to the wide band gap of $PAPbBr_3$. It has been noticed that the photocurrent follows the conventional diode response. In forward bias conditions, the current does not show much improvement under increasing bias voltage both in the dark and under illumination. But in the reverse bias, photocurrent is found to increase at pretty higher rate with applied voltage (see Fig. 5.4b).

When the device is irradiated with UV laser, a large number of excitons form at the perovskite

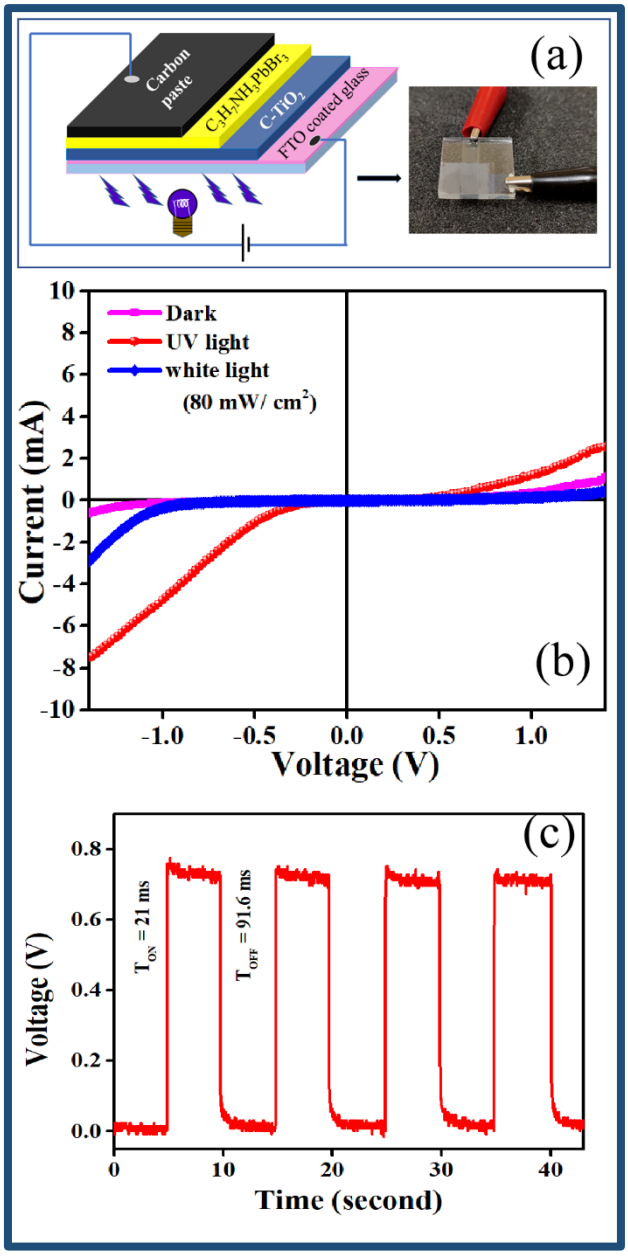

Fig. 5.4(a) Schematic illustration and digital photograph of the photodetector, (b) IV characteristics of the photodetector under dark, white light and UV light irradiation, (c) Transient response characteristics of the photodetector.

layer. Then, the excitons split up to generate free electrons and holes at both of the interfacing layers. Now in reverse bias, the depletion region increases with the increase in reverse bias voltage, and hence photons incident on a larger area and get converted proficiently in electric current. At a reverse bias of -1 V, the current is observed to be - 0.134 mA in dark mode while illuminated by white light, photocurrent becomes - 0.29 mA. The photocurrent enhances substantially in UV exposure and its value becomes - 4.7 mA at that same voltage.

Another important parameter of the photodiode is transient response time. The rise and decay time needed by the fabricated photodiode to shift from 10 % to 90 % and 90 % to 10 % of maximum photocurrent when illuminated in UV laser are 21 ms and 91 ms respectively (Fig. 5.4c). C-TiO_2 slows down the decay time with the diffusion current. Moreover, no external voltage is employed here during measurement, and hence this device executes itself as a promising self-biased voltage driven UV photodiode.

5.3.5. Complex impedance spectroscopy (CIS) analysis

The potential ionic transportation and estimation of the independent influence of grain and grain boundary over the total impedance within the material is investigated using CIS analysis. Commonly, semicircles in the Nyquist plot correspond to the involvement of grain, grain boundary and electrode - material interface to the entire impedance. Fig. 5.5a shows the Cole-Cole plot or Nyquist plot of $PAPbBr_3$ at mentioned temperatures. The semicircles are suppressed at its center owing to the non - Debye type dipolar relaxation of the concerned sample. Though the contributions of grain boundary and grain are designated by the semicircles appear in low and high frequency domain respectively, it is highly troublesome to distinguish their distinct impact from the solo suppressed semicircle at temperature in bare eyes as they are closely overlaid with each other. For $PAPbBr_3$, the impact of electrode – material interface on the total resistance is completely absent since no semicircle is detected in ultra – low frequency region [9]. The desired equivalent circuit for this hybrid perovskite (Fig. 5.5a) encompasses of parallel combination of a pair of resistances (R_g, R_{gb}) and capacitance (C_g, C_{gb}). All these CI spectra are resolved by EC lab software and the derived data regarding the individual involvement of grain and grain boundary to the total impedance are enlisted in Table 5.1. It has been observed from Fig. 5.5(a) that the diameters of the depressed semicircles diminish significantly with the escalation of temperature which specifies the augmentation of DC conductivity with temperature.

The frequency dependent complex impedance can be expressed as

$$Z(\omega) = Z'(\omega) + jZ''(\omega) \tag{5.4}$$

Where $Z'(\omega)$ and $Z''(\omega)$ denote the real and imaginary of impedance.

$$Z'(\omega) = \frac{R_g}{[1+(\omega R_g C_g)^2]} + \frac{R_{gb}}{[1+(\omega R_{gb} C_{gb})^2]} \tag{5.5}$$

$$Z"(\omega) = \frac{\omega C_g R_g^2}{[1+(\omega R_g C_g)^2]} + \frac{\omega C_{gb} R_{gb}^2}{[1+(\omega R_{gb} C_{gb})^2]} \quad (5.6)$$

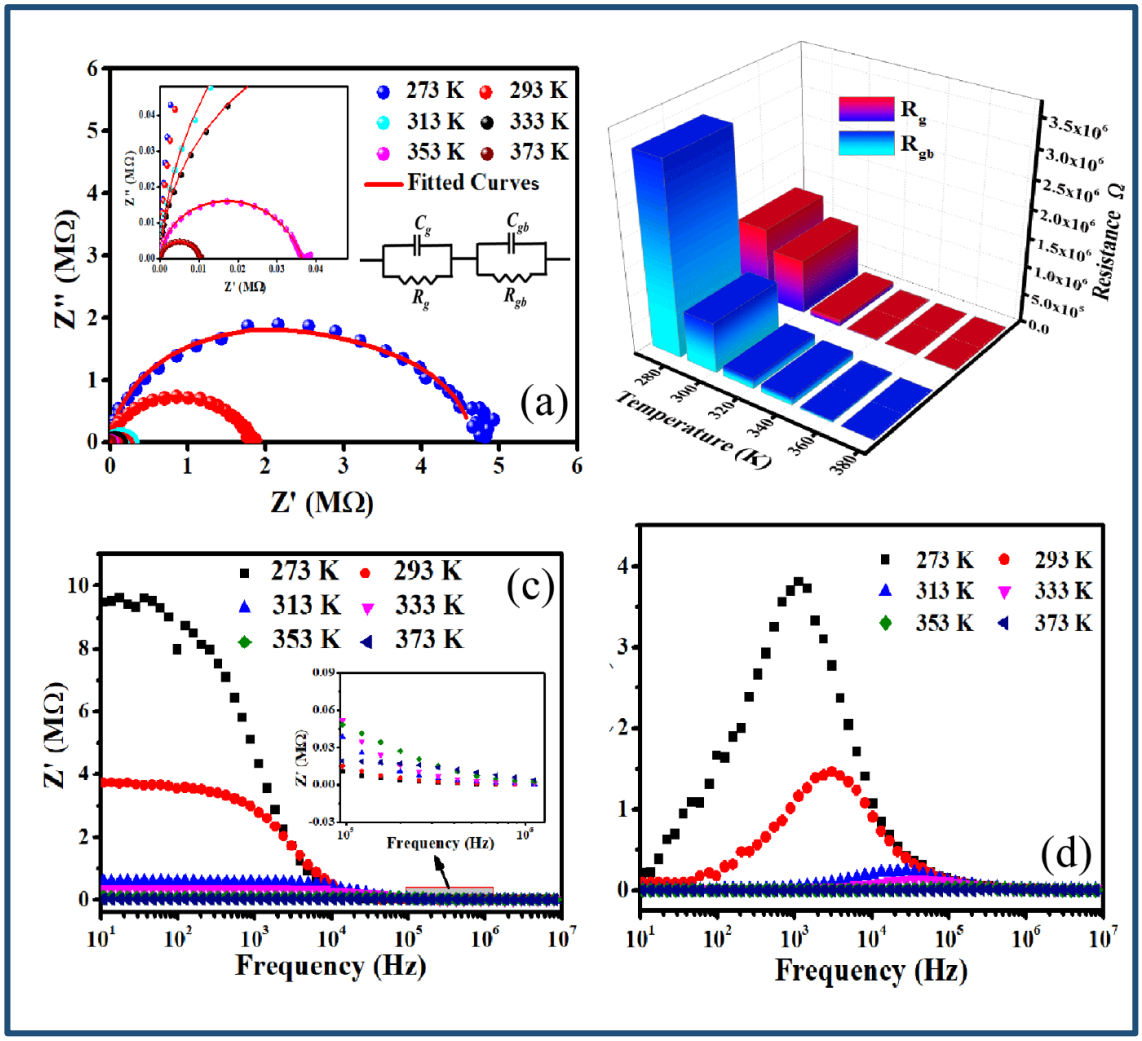

Fig. 5.5(a) Cole-Cole plot of PAPbBr₃ at different temperature, Inset of (a) Maxwell Wagner equivalent circuit, (b) variation of R_g and R_{gb} with temperature, (c) Frequency dependence of $Z'(\omega)$ at different temperature, (d) Variation of $Z''(\omega)$ as a function of frequency of the PAPbBr₃.

Here, R_g and R_{gb} denote the distribution of grain and grain boundary to the total electrical behavior of $PAPbBr_3$ while C_g and C_{gb} refer to the impact of the grain and grain boundary on the total capacitance of the sample. Fig. 5.5b represents the thermally triggered contribution of grain and grain boundary.

The variation of $Z'(\omega)$ of $PAPbBr_3$ as a function of temperature is illustrated in Fig. 5.5c which depicts that the magnitude of $Z'(\omega)$ forms a sigmoidal nature with enhancement of temperature. The higher magnitudes of $Z'(\omega)$ in low frequency region are found to abate gradually with the increment of frequency and temperature and this behaviour corresponds to

the effect of negative temperature coefficient of resistance (NTCR). Semiconducting materials typically exhibit NTCR effect and for $PAPbBr_3$, this effect is quite prominent. Such performance specifies the lower contribution of grain boundary to the total resistance in high frequency region which in turn is responsible for the growth of AC conductivity in high frequency region. At the higher frequency domain, values of $Z'(\omega)$ for all temperatures are found to combine signifying the probable release of space charges and reducing the barrier potential which may lead to the rise in AC conductivity (inset of Fig. 5.5c) [9–14]. Fig. 5.5d exhibits the variation of $Z"(\omega)$ as a function of temperature. This loss spectrum divulges the information about the relaxation time of charge carriers along with the mechanism of charge conduction. Frequency dependent $Z"(\omega)$ spectra exhibit distinct relaxation peaks for all temperature. These relaxation peaks appear at resonance i.e. when the frequency of localized charge carriers becomes almost equivalent to the frequency of applied electric field [9]. These peaks are found to move towards high frequency domain by the rise in temperature [15].

Table 5.1. The values of resistances and capacitances for all the temperatures.

Temperature (K)	R_g (Ω)	R_{gb} (Ω)	$C_{overall}$ (F)	Goodness of fitting factor
273	1.29×10^6	3.35×10^6	4.278×10^{-10}	0.05291
293	9.53×10^5	8.79×10^5	1.522×10^{-10}	0.02384
313	1.13×10^5	1.76×10^5	1.717×10^{-9}	0.02557
333	1.55×10^4	1.32×10^5	1.631×10^{-9}	0.01603
353	2.69×10^3	3.35×10^4	3.197×10^{-9}	0.01164
373	7.12×10^3	3.11×10^3	1.784×10^{-9}	0.005793

5.3.6. Dielectric properties

The complex dielectric behavior is used to inspect several polarization responses, dielectric relaxation, and conductivity of the sample which can be expressed as follows

$$\varepsilon(\omega) = \varepsilon'(\omega) - j\varepsilon"(\omega) \quad (5.7)$$

The dispersion of frequency dependent dielectric constant $\varepsilon'(\omega)$ and dielectric loss $\varepsilon"(\omega)$ for 273 K ≤ T ≤ 373 K are presented in Fig. 5.6a and Fig. 5.6c, respectively. The dielectric constant refers to the energy stored in the system and the dielectric loss denotes the

amount of energy debauched from the system. This real and imaginary part of complex dielectric response can be articulated as equation (5.8, 5.9) respectively.

$$\varepsilon'(\omega) = \frac{Z''}{\omega C_0(Z'^2+Z''^2)} \quad (5.8)$$

$$\varepsilon''(\omega) = \frac{Z'}{\omega C_0(Z'^2+Z''^2)} \quad (5.9)$$

Here, C_0 ($C_0 = \varepsilon_0 \frac{A}{d}$, $\varepsilon_0$is the permittivity of the vacuum, A is the area of the corresponding electrode, and d denotes the thickness of the pellet) designates the free space capacitance. $PAPbBr_3$ exhibits a giant dielectric constant, a fascinating physical behavior, near room temperature at low frequency limit. When the real part of the dielectric permittivity of a material at low frequency region becomes very large ($\varepsilon'(\omega) > 1000$) around room temperature, the material is supposed to possess a giant dielectric constant (GDC) [16]. The origin of GDC might be a topic of debate since it can be attributed to several reasons. But in this context both PA^+ and Br^- migration play important roles in the giant dielectric phenomenon. The nature of dielectric constant $\varepsilon''(\omega)$ in low frequency region is regulated by interfacial polarization which plays crucial role in ionic conduction [17]. Apart from the interfacial polarization, the entire bulk effect from the grain side is responsible for this dielectric behavior [18]. The variation of dielectric constant can be emphasized by the theory of Maxwell-Wagner interfacial polarization in association with Koop's phenomenological theory which concludes that dielectric materials consist of a relatively high conducting layer of grains detached by a high resistive layer of grain boundary [19]. As a result, the charge carriers get stuck at the edge of the grain boundary developing interfacial polarization. Defects and imperfections present in the material compel the positive and negative space charges to hop from their original position to their new position [10,19]. Thus, in the presence of an applied electric field, the core of propylammonium cations ($C_3H_7NH_3^+$) gets displaced towards the core of inorganic anions. Consequently, a huge number of oscillating dipoles are generated which can accumulate and align themselves at the interface along the way of the external electric field. So, this dielectric constant is very high due to the influence of interfacial polarization in low frequency region ($\omega << 1/\tau$) which confirms the non-Debye type nature of $PAPbBr_3$ as displayed in Fig. 5.6a [13,14,20]. But, with the rise in frequency, dipoles fail to chase the direction of the applied electric field and hence dielectric constant decreases gradually with the increase in frequency [21]. The behaviour of dielectric constant in high frequency region is controlled by ionic and electronic polarization effect. Thermally triggered charged carriers enhance the dielectric constant with temperature. In the case of $PAPbBr_3$, GDC is found to reach up to 10^5 with the

escalation of temperature which can be attributed to the existence of thermally stimulated

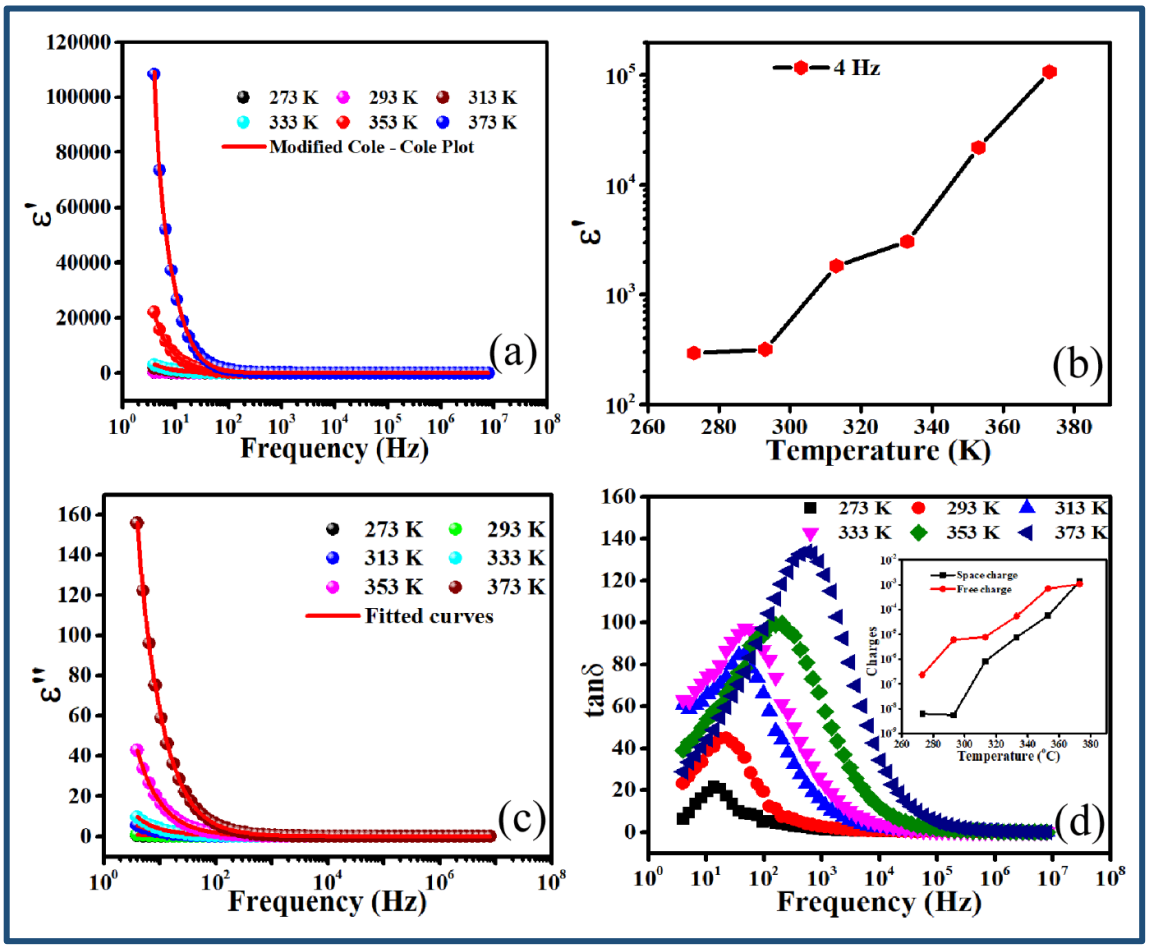

Fig. 5.6(a) Variation of real part of dielectric constant of the sample at various temperatures fitted by modified Cole-Cole fit, (b) Variation of dielectric constant at lower frequency limit, (c) Variation of imaginary part of dielectric constant of the material at several temperatures fitted by modified Cole-Cole fit, (d) $\tan\delta$ vs. angular frequency spectra of $PAPbBr_3$.

charge carriers as well as dipole moments. In the presence of external electric field organic cations ($C_3H_7NH_3^+$) with thermally active dipole moments reorient triggering energy fluctuation. As a consequence, ε' rapidly enhances with the temperature at low frequency domain which is exhibited in Fig. 5.6b [18].

Table 5.2. The values of β, m, τ estimated from the fitting of modified Cole-Cole model of ε' and ε'' of $PAPbBr_3$

	Temperature					
Parameters	273K	293K	313K	333K	353K	373K
τ	0.081	0.050	0.0312	0.02341	5.1×10^{-3}	1.95×10^{-3}
β	0.9917	0.9864	0.8617	0.8943	0.7630	0.8512
m	0.6167	0.6984	0.8688	0.7664	0.8991	0.9132

ε'' is also observed to reduce as frequency increases. According to Koop's theory, deformities and contaminants present in the sample construct a potential barrier which restricts the conduction of charge carriers. Therefore, under the effect of space charge polarization, charges are confined at the grain boundary in low frequency region. Subsequently, electrons consume more energy to hop and overcome the barrier giving rise to huge dielectric loss in low frequency region. In high frequency region, the effects of high conducting grain layers become prominent, and hence electrons need lesser energy to hop. As a result, dielectric loss at each temperature reduces gradually in high frequency domain [22,23].

The obtained experimental data of ε' and ε'' are fitted with a modified Cole – Cole model with which complex permittivity (ε^*) can be expressed as

$$\varepsilon^* = \varepsilon_\infty + \frac{\varepsilon_s - \varepsilon_\infty}{1+(j\omega\tau)^\beta} - \frac{j\sigma^*}{\epsilon_0 \omega^m} \tag{5.10}$$

Here, ε_s and ε_∞ represent low and high frequency dielectric constants, τ refers to the relaxation time, ω is the angular frequency, $0 < \beta < 1$, m is the exponent, σ^* is the summation of space charge (σ_{sp}) and free charge (σ_{fc}) conductivity [20,24]. The dielectric constant and dielectric loss are articulated as

$$\varepsilon' = \varepsilon_\infty + \left[\frac{(\varepsilon_s - \varepsilon_\infty)\left\{1+(\omega\tau)^\beta \cos\left(\frac{\beta\pi}{2}\right)\right\}}{1+2(\omega\tau)^\beta \cos\left(\frac{\beta\pi}{2}\right)+(\omega\tau)^{2\beta}}\right] + \frac{\sigma_{sp}}{\epsilon_0 \omega^m} \tag{5.11}$$

$$\varepsilon'' = \left[\frac{(\varepsilon_s - \varepsilon_\infty)(\omega\tau)^\beta \sin\left(\frac{\beta\pi}{2}\right)}{1+2(\omega\tau)^\beta \cos\left(\frac{\beta\pi}{2}\right)+(\omega\tau)^{2\beta}}\right] + \frac{\sigma_{fc}}{\epsilon_0 \omega^m} \tag{5.12}$$

Consequently, the ratio of dielectric loss to dielectric constant is defined as loss tangent ($\tan(\delta) = \frac{\varepsilon''(\omega)}{\varepsilon'(\omega)}$). Fig. 5.6c depicts the variation of $\tan(\delta)$ with frequency over the range of selected temperatures. The fitted values of m, β, σ^* are enlisted in Table 5.2. Loss tangent decreases in higher frequency region and becomes constant for each temperature. The peak of

loss tangent arises due to the supremacy of dipolar polarization. Hence, charge carriers become thermally excited, and electrical conductivity increases with the rise in temperature [25].

5.3.7. Study of Electric modulus

To understand the relaxation process of space charge distribution within a material in the absence of an electrode effect, a complex electric modulus is employed.

$$M^* = \frac{1}{\varepsilon^*} = M' + iM'' \qquad (5.13)$$

Here, M' and M'' signifies the real and imaginary part of the electric modulus, respectively [20,24].

The variation of M' as a function of frequency and temperature is exposed in Fig. 5.7a which depicts that the values of M' of all temperatures are approaching zero initially for its

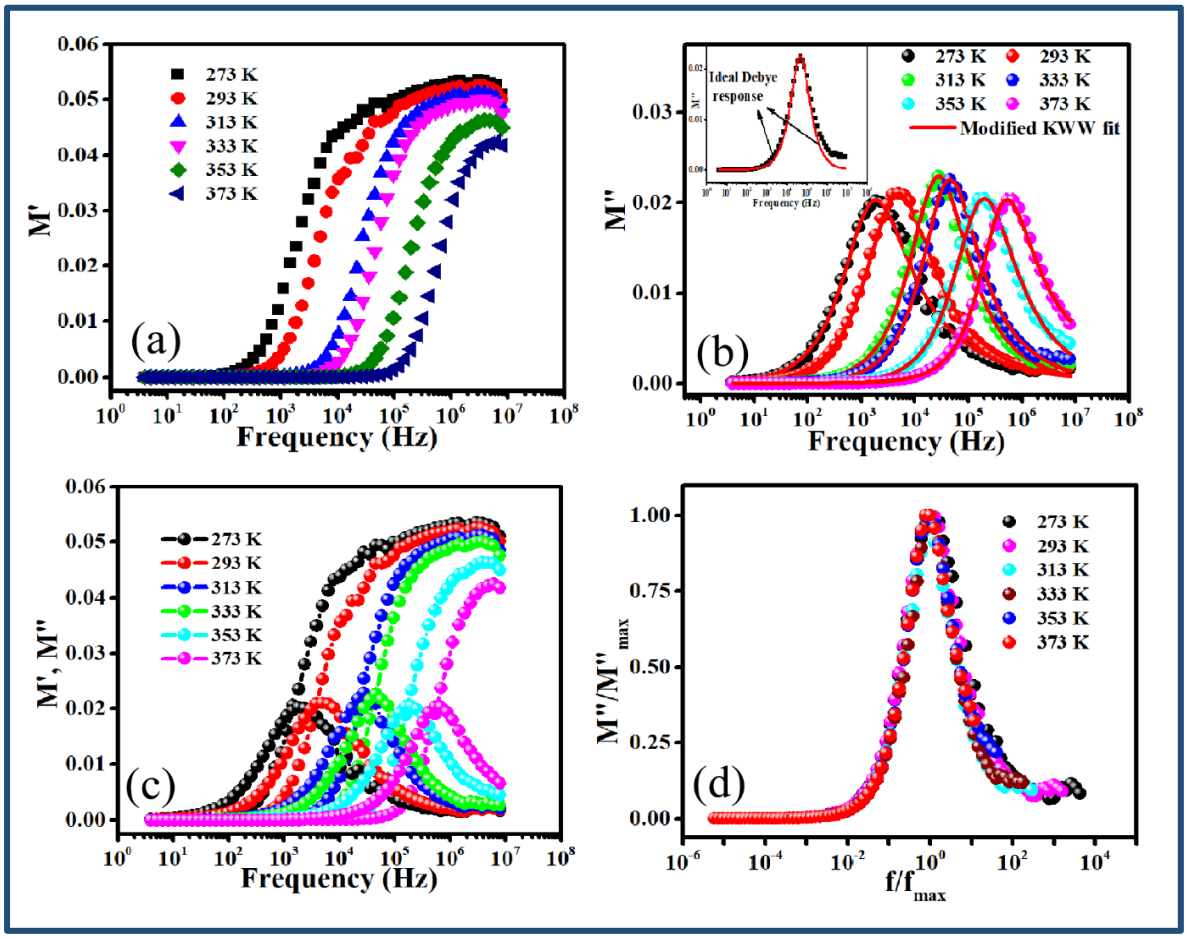

Fig. 5.7 Frequency dependence of (a) real part (b) imaginary part of electric modulus of $PAPbBr_3$, Inset of (b) indicates deviation from ideal Debye response of experimental data at 353K, (c) Variation of $M'(\omega)$ and $M''(\omega)$ versus frequency at different temperature, (d) Normalised imaginary electric modulus M''/M''_{max} vs. f/f_{max} at different temperatures.

enthrallingly high ε' in low frequency region. The curves adopt a sigmoidal type nature as frequency rises. The reason behind this nature is the long range transportation of charge carriers as well as the absence of electrode polarization. As temperature ascends, the peaks that appear in high frequency region are found to shift slightly. M'' achieves its maximum value at high frequency region producing a comprehensive, significant peak which is commonly referred to as a relaxation peak (Fig. 5.7b). Since charge carriers can move keenly from one location to its neighboring site i.e. charge carriers enjoy successful hopping in low frequency region, no occurrence of peak in M'' is found. But, in the high frequency domain, charge carriers are restricted to localized movement within its potential well. Therefore, the journey of charge carriers from long range to short range translational motion is responsible for the formation of peaks in M'' on high frequency region and the peaks drift distinctly towards high frequency domain with the enhancement of temperature. Since ε_s always acquires larger values than that of ε_∞, the relaxation time for the electric modulus of $PAPbBr_3$ is smaller than that of dielectric permittivity. Thus, the relaxation peak of electric modulus shifts towards high frequency region in comparison with dielectric permittivity [26]. However, it has been noticed that M'' peaks are asymmetrical in nature resembling the non – Debye behaviour of $PAPbBr_3$. Modified KWW function, proposed by Bergman, resolve the diversion of M'' spectra from ideal Debye behaviour. [20,24]. The KWW function stated in equation 5.12 contains two independent shape parameters a and b in low and high frequency sides respectively and a smoothing parameter (c).

$$M''(\omega) = \frac{M''_{max}}{\frac{(1-c)}{(a+b)}\left[b\left(\frac{f}{f_{max}}\right)^{-a} + a\left(\frac{f}{f_{max}}\right)^{b}\right] + c} \qquad (5.14)$$

Table 5.3. Evaluated values of shape parameters a and b from the fitting of frequency and

Temperature (K)	***a***	***b***
273	0.7822	0.3473
293	0.8014	0.4518
313	0.84	0.5952
333	0.8597	0.6267
353	0.9052	0.7177
373	0.9159	0.7363

For the ideal Debye response, $a = b = 1$ and $c = 0$, and equation 5.12 is reduced in the form of equation 5.15.

$$M"(\omega) = \frac{M"_{max}}{\frac{1}{2}[\left(\frac{f_{max}}{f}\right)+\left(\frac{f}{f_{max}}\right)]} \quad (5.15)$$

The extracted values of a and b are enlisted in Table 5.3 for every specified temperature. The values of a and b are noted to increase up to unity with the rise in temperature which conforms to the shift of non–Debye to Debye type behavior of the material with the enhancement of temperature. The diversion of the actual experimented value from the ideal Debye response at 333 K is shown in the inset of Fig. 5.7b.

M' and $M"$ is plotted as a function of frequency and illustrated in Fig. 5.7c for stated temperatures. It has been perceived that there exist two kinds of relaxation process – Debye type relaxation process at lower frequency side and non–Debye type relaxation at higher frequency side for low temperatures [27]. Non-Debye type relaxation process tends to shift towards Debye type relaxation as the temperature rises for both higher and lower frequency values [28]. To investigate the scaling behavior of the concerned sample, the normalized imaginary part of complex electric modulus is plotted against normalized frequency for 273 K ≤ T ≤ 373 K as shown in Fig. 5.7d. This figure gives an insight into the co-existence of long-range relaxation along with localized movement within the sample. Charge carriers can traverse long distances on the lower frequency side and conduct a hopping mechanism from one position to its neighboring position whereas, in high frequency portion, charge carriers are confined in a potential well and restricted to performing localized movement within the well. The peak positions illuminate the long range to short range translational motion of charge carriers [28]. The concurrence of all the peaks for selected temperatures confirms the temperature dependent dynamic process of the system.

5.3.8. Study of electrical conductivity

To comprehend the charge transport procedure, frequency and temperature dependent AC conductivity of the concerned sample have been carried out. The AC conductivity follows a generic relation $\sigma_{ac} = \omega\varepsilon'\varepsilon_0 tan\delta$ where ε_0 refers to the free space permittivity. Fig. 5.8a delineates the fact that the curves are frequency and temperature independent in low frequency region and become wider with the rise in temperature which is accredited to the DC conductivity [23]. However, in high frequency domain, the curves were found to exhibit strong frequency dispersion for all selected temperatures which is due to the influence of AC

conductivity. Hopping frequency (ω_p), the frequency at which slope of conductivity transits, is found to move along high frequency domain with the upsurge in temperature. The frequency dependent AC conductivity along with the frequency independent DC conductivity i.e. the overall electrical conductivity is described and analyzed by jump relaxation model (JRM) designed by Funk [13]. Conferring to this model, the ion after hopping from its originally relaxed and stable native configuration will not be able to be in equilibrium with its neighboring ions. The neighboring ions need to shift accordingly to relax and accommodate the ion in its new site. In this way, the ions are capable of hopping efficaciously to their neighboring vacant positions in low frequency region. Long range mobility of ions is responsible for successful hopping in low frequency region which contributes to DC conductivity. Sometimes, after hopping, the ion needs to jump back (forward – backward – forward position) to its initial position to relax the new configuration partially giving rise to unsuccessful hopping. Unsuccessful hopping increases with temperature and in high frequency region, both successful and unsuccessful hopping occurs. Eventually, dispersive conductivity initiates in the high frequency region as the successful hopping takes over the unsuccessful part. Jonscher's power law is an effective tool to analyze the frequency dependent AC conductivity. This is based on the universal dielectric model (UDR) and named after its designer Jonscher. [29,30],

$$\sigma_{ac} = \sigma_{dc} + \sigma_0 f^s \tag{5.16}$$

where σ_{ac} and σ_{dc} signify the AC and DC component of electrical conductivity of the sample, σ_0 is a temperature dependent pre-factor and s refers to frequency exponent (FE), ($0 < s < 1$). The measured data of the electrical conductivity of the sample is fitted with UDR model (Fig. 5.8a). It has been depicted in the inset of Fig. 5.8b that frequency exponent is inversely proportional to the temperature which is ascribed to the correlated barrier hopping (CBH) conduction mechanism expressed as,

$$S = 1 - \frac{6K_\beta T}{W_m - K_\beta T ln(\frac{1}{\omega\tau_0})} \tag{5.17}$$

Here, W_m refers to the maximum barrier height, K_β is the Boltzmann constant, ω denotes the angular frequency and τ_0 represents to the relaxation time. Fitting equation 5.18 on frequency exponent vs. temperature yields W_m = 0.352 eV.

$$S = 1 - \frac{6K_\beta T}{W_m} \tag{5.18}$$

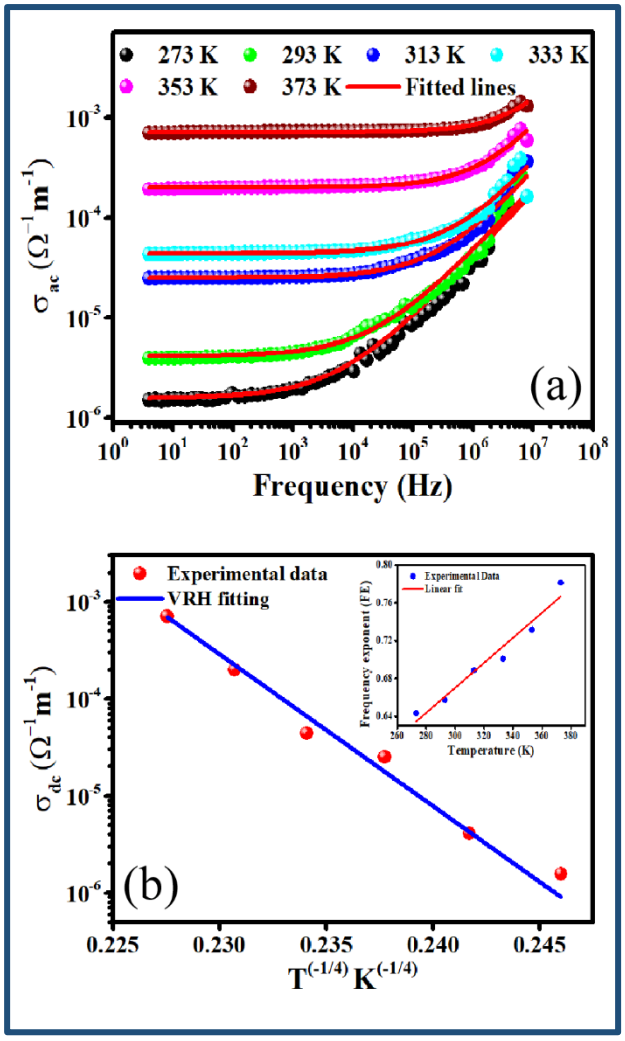

Fig. 5.8(a) Variation of AC conductivity with frequency at different temperatures of $PAPbBr_3$, (b) Variation of temperature dependent DC conductivity fitted with VRH model, Inset of (b) depicts variation of frequency exponent with temperature.

The value of W_m is high in this case in comparison with propylammonium lead iodide [7]. Here, S is calculated as 0.79831 at 373 K showing deviation from ideal dielectric behavior. S attains unity for ideal dielectric material implying ideal Debye type dipolar interaction.

The values of DC conductivity obtained from Jonscher's power law fitting of AC conductivity is analyzed and tailored with Mott's three dimension variable range hopping model (VRH) expressed as equation over specified temperatures.

$$\sigma = \sigma_0 \exp\left[-\left(\frac{T_0}{T}\right)^{\frac{1}{4}}\right] \qquad (5.19)$$

Here, σ_0 represents conductivity at infinite temperature. Mott proposed in this model that charge carriers hop from the residing state to the neighboring vacant state near the Fermi level [31]. The DC conductivity vs. temperature is shown in Fig. 5.8b.

5.3.9. Activation energy

Migration of constituting ions of the sample builds the basis of activation energy. In this context, any of Pb^{2+}, PA^{+}, Br^{-} may migrate. Moreover, further ions like H^{+} or any combined ion may migrate due to contamination or degradation. The migration rate (r_m) of ions inside the material is affected by the activation energy (E_a) of the ions as it follow the following relationship,

$$r_m \; \alpha \; \exp\left(\frac{E_a}{K_\beta T}\right) \qquad (5.20)$$

Activation energy is influenced by the ionic radius, charges of ions, etc. Ions with smaller ionic radius and having vacant interstitial positions can easily migrate. The values of activation energies of I^{-}, Br^{-}, Pb^{2+}, MA^{+} (methylammonium ion) have been reported in many articles. The majority of these articles claim that experimentally as well as computationally obtained activation energy of halide ion is very low which plays and hence performs significantly in ion conduction. Though the ionic radius of bromine is smaller than that of iodine, the electronegativity of bromine is higher which helps to increase the interaction with cations and other anions. Hence, the activation energy of bromine is higher than that of iodine. Pb^{2+} (ionic radius ~ 6.28 Å) possesses a very high activation energy of 2.31 eV which restricts easy migration of Pb^{2+} within the material and hence makes these ions almost immobile [32]. Moreover, the high value of E_a decreases its diffusion capability and make it a rate controlling component in crystal growth mechanism [33]. On the other hand, it has been reported in many articles that methylammonium cation ($CH_3NH_3^{+}$) (ionic radius ~ 1.8 Å) possesses activation energy of the order of ~ 1 eV (nearly 0.84 eV) and its high level orientational motion hinders the long-range mobility of this ion. Propylammonium cation ($C_3H_7NH_3^{+}$) having a larger chain might possesses higher ionic radius which suggests negligible diffusion of this ion [33,34]. Thus, $PAPbBr_3$ is a mixed ionic-electronic conductor in which Br^{-} is the majority ionic carrier. The mobile ionic species are associated with vacancy sites in the lattice. The activation energy has been calculated from the Nyquist plot using the Arrhenius relation $\tau_m = \tau_0 \exp(\frac{E_a}{K_\beta T})$ where τ_m is estimated as $\tau_1 = C_g R_g$ and $\tau_2 = C_{gb} R_{gb}$ respectively. The values of activation energies thus obtained from the fitted $ln\tau_m$ vs. 1000/T data (Fig. 5.9a) ($\tau_m = \tau_1, \tau_2$ respectively) are 0.595 eV and 0.492 eV respectively. The contribution of grain is significant in higher frequency domain although grain boundary subsidizes in low frequency domain. Despite of the very close values of acquired activation energies, the value of E_a is

detected to be suppressed in low frequency zone which suggests that ions migrate faster though

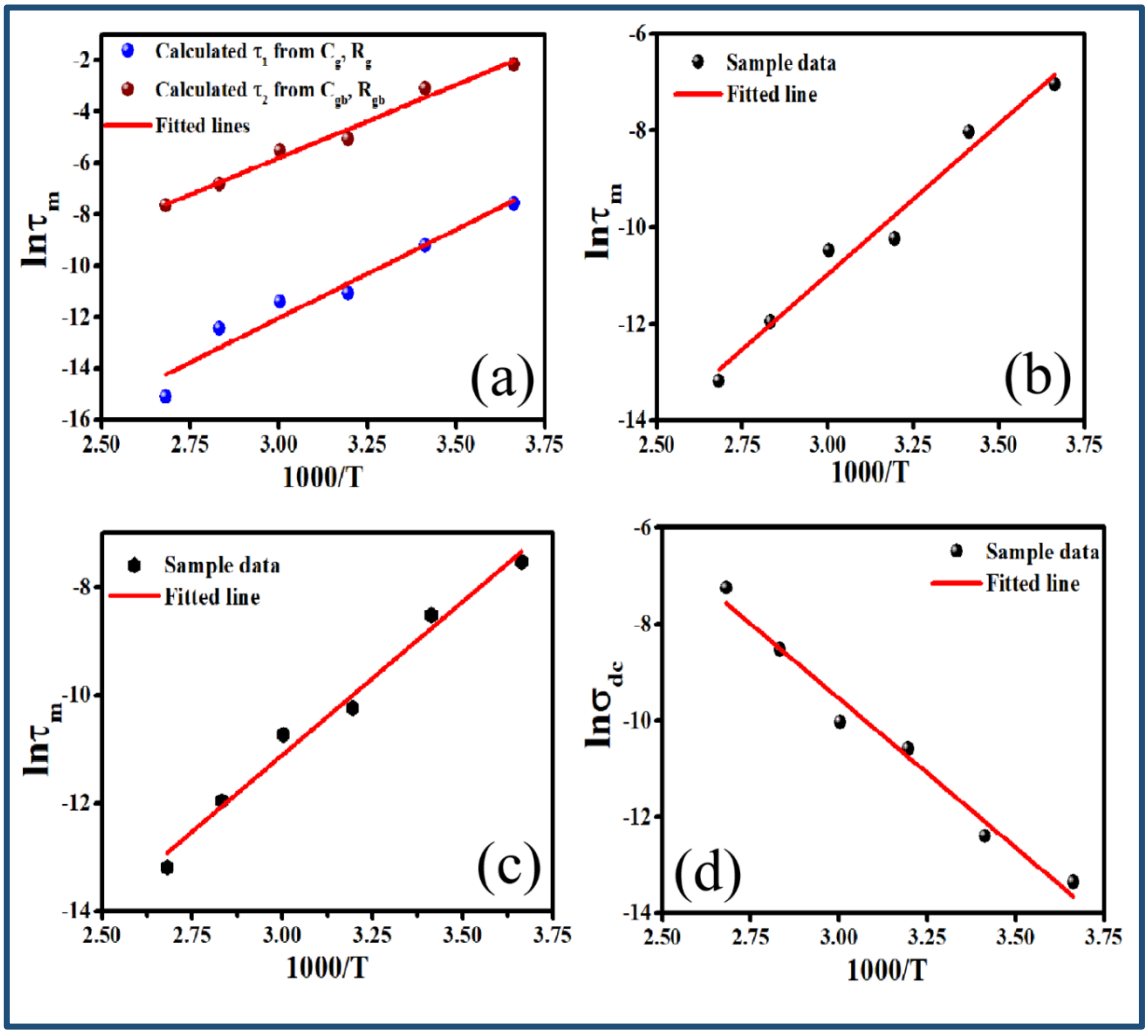

Fig. 5.9(a) Arrhenius plot using the values of R_g, R_{gb}, C_g and $C_{gb}$from Nyquist diagram, (b) Arrhenius plot using the peak of $Z''(\omega)$, (c) $ln\tau_m$ vs. 1000/T plot of PAPbBr$_3$ using the peak values of electric modulus, (d) σ_{dc} vs. 1000/T plot of PAPbBr$_3$.

grain boundaries than via grain or bulk of the perovskite [35]. Using the peak values of $Z"(\omega)$ and $M"(\omega)$ for all temperatures, the activation energies are derived from fitted plot of $ln\tau_m$ vs. $1000/T$ (Fig. 5.9b and Fig. 5.9c respectively) employing the stated Arrhenius relation. The values of E_a thus observed are 0.537 eV and 0.491 eV respectively also indicate bromine ion migration within the sample. Moreover, the values of σ_{dc} for all temperatures are extracted from σ_{ac} using equation 5.14. Fig. 5.9d denotes the least square fit of $ln\sigma_{dc}$ vs. $1000/T$ which provides the value of E_a as 0.534 eV. The similarities among the values of E_a suggest that dielectric polarization as well as electric conduction is identical for this sample. Ionic migration contributes appreciably to the hysteresis behavior of perovskite solar cells. This hysteresis can go high enough to create a difference of almost 90% power conversion efficiency between its

forward and reverse scan. Along with this reversible effect, some irreversible effect like the decomposition of halogen also takes place. Therefore, ionic conduction-oriented complexity decreases with the increase in activation energy value. In this work, E_a is found to be higher than that of propylammonium lead iodide [7].

5.4. Conclusion

In brief, the temperature dependent electrical properties of sol gel-derived propylammonium lead bromide have been investigated in detail. The exceptional thermal stability and fascinating response under UV irradiation make this concerned perovskite a deserving entrant in energy harvesting. Nyquist diagram depicts the role of grain and grain boundary on the total impedance. This material may appear as an attractive perovskite with its appreciably higher ε' and lesser ε'' in room temperature in low frequency zone. It has been depicted from a modified Cole-Cole plot that space charge and free charge conductivity are proportional to temperature. $M"$ is found to be asymmetric and evaluation of the KWW equation assures the non-Debye response of $PAPbBr_3$. Moreover, it has been concluded that the non-Debye nature of $M"(\omega)$ decreases and shifts towards Debye type response as temperature escalates though ideal Debye type nature could not be attained. The electrical conductivity has been analyzed and illuminated comprehensively on JRM model and CBH conduction mechanism. Temperature dependent DC conductivity is fitted with VRH model. The acquired activation energy explains the ion migration and ionic conduction within the sample. The higher values of activation energy calculated from different experimental data conclude that this sample is stable enough to be employed in energy harvesting. Thus, the detailed studies on dielectric constant, relaxation behavior, AC conductivity, and activation energy of the material construct a pathway for further studies and employing the concerned material in energy harvesting systems.

References

[1] D.O. Demchenko, N. Izyumskaya, M. Feneberg, V. Avrutin, Özgür, R. Goldhahn, H. Morkoç, Optical properties of the organic-inorganic hybrid perovskite CH3NH3PbI3: Theory and experiment, Phys. Rev. B. 94 (2016) 1–9.

[2] Y.F. Ding, Q.Q. Zhao, Z.L. Yu, Y.Q. Zhao, B. Liu, P. Bin He, H. Zhou, K. Li, S.F. Yin, M.Q. Cai, Strong thickness-dependent quantum confinement in all-inorganic perovskite Cs2PbI4 with a Ruddlesden-Popper structure, J. Mater. Chem. C. 7 (2019) 7433–7441.

[3] M. Wang, Z. Zang, B. Yang, X. Hu, K. Sun, L. Sun, Solar Energy Materials and Solar Cells Performance improvement of perovskite solar cells through enhanced hole extraction : The role of iodide concentration gradient, Sol. Energy Mater. Sol. Cells. 185 (2018) 117–123.

[4] X. Ren, X. Yan, A.S. Ahmad, H. Cheng, Y. Li, Y. Zhao, L. Wang, S. Wang, Pressure-induced phase transition and band gap engineering in propylammonium lead bromide perovskite, J. Phys. Chem. C. 123 (2019) 15204–15208.

[5] R.C. Nederland, A profile refinement method for nuclear and magnetic structures, (1969).

[6] J. Rodriguez-carvajal, neutron powder diffraction, 192 (1993) 55–69.

[7] P. Sengupta, P. Sadhukhan, A. Ray, R. Ray, S. Bhattacharyya, S. Das, Temperature and frequency dependent dielectric response of $C_3H_7NH_3PbI_3$: A new hybrid perovskite, J. Appl. Phys. 127 (2020) 204103.

[8] A. Mishra, Z. Ahmad, F. Touati, R.A. Shakoor, M.K. Nazeeruddin, One-dimensional facile growth of $MAPbI_3$ perovskite micro-rods, RSC Adv. 9 (2019) 11589–11594.

[9] A. Ray, A. Roy, S. Bhattacharjee, S. Jana, C.K. Ghosh, C. Sinha, S. Das, Correlation between the dielectric and electrochemical properties of TiO_2-V_2O_5 nanocomposite for energy storage application, Electrochim. Acta. 266 (2018) 404–413.

[10] M. Ahmad, M.A. Rafiq, M.M. Hasan, Transport characteristics and colossal dielectric response of cadmium sulfide nanoparticles, J. Appl. Phys. 114 (2013) 133702.

[11] N. Ortega, A. Kumar, P. Bhattacharya, S.B. Majumder, R.S. Katiyar, Impedance spectroscopy of multiferroic $PbZr_xTi_{1-x}O_3/CoFe_2O_4$ layered thin films, Phys. Rev. B - Condens. Matter Mater. Phys. 77 (2008) 1–10.

[12] Z. Imran, M.A. Rafiq, M.M. Hasan, Charge carrier transport mechanisms in perovskite CdTiO3 fibers, AIP Adv. 4 (2014) 067137.

[13] D.K. Pradhan, P. Misra, V.S. Puli, S. Sahoo, D.K. Pradhan, R.S. Katiyar, Studies on structural, dielectric, and transport properties of $Ni_{0.65}Zn_{0.35}Fe_2O_4$, J. Appl. Phys. 115 (2014) 0–9.

[14] D.K. Pradhan, S. Kumari, V.S. Puli, P.T. Das, D.K. Pradhan, A. Kumar, J.F. Scott, R.S. Katiyar, Correlation of dielectric, electrical and magnetic properties near the magnetic phase transition temperature of cobalt zinc ferrite, Phys. Chem. Chem. Phys. 19 (2017) 210–218.

[15] S. Kumari, N. Ortega, A. Kumar, S.P. Pavunny, J.W. Hubbard, C. Rinaldi, G. Srinivasan, J.F. Scott, R.S. Katiyar, Dielectric anomalies due to grain boundary conduction in chemically substituted $BiFeO_3$, J. Appl. Phys. 117 (2015) 117.

[16] E.J. Juarez-perez, R.S. Sanchez, L. Badia, G. Garcia-belmonte, Y.S. Kang, I. Mora-sero, J. Bisquert, Photoinduced Giant Dielectric Constant in Lead Halide Perovskite Solar Cells, J. Phys. Chem. Lett. 5 (2014) 2390–2394.

[17] C.R. Cena, A.K. Behera, B. Behera, Structural, dielectric, and electrical properties of lithium niobate microfibers, J. Adv. Ceram. 5 (2016) 84–92.

[18] W. Li, Z. Man, J. Zeng, L. Zheng, G. Li, A. Kassiba, C : Plasmonics ; Optical , Magnetic , and Hybrid Materials The Relationship of Giant Dielectric Constant and Ion Migration in $CH_3NH_3PbI_3$ Single Crystal Using Dielectric Spectroscopy The Relationship of Giant Dielectric Constant and Ion Migration in CH_3N, J. Phys. Chem. C. 124 (2020) 13348–13355.

[19] C.G. Koops, On the dispersion of resistivity and dielectric constant of some semiconductors at audiofrequencies, Phys. Rev. 83 (1951) 121–124.

[20] P. Thongbai, S. Tangwancharoen, T. Yamwong, S. Maensiri, Dielectric relaxation and dielectric response mechanism in (Li, Ti)-doped NiO ceramics, J. Phys. Condens. Matter. 20 (2008) 395227.

[21] S. Patra, P. Sengupta, A. Ray, A. Roy, S. Das, Discrete dipole approximation for calculating optical properties of ZnO nanoparticles and ZnO-PVP composites, Ceram. Int. 44 (2018) 14236–14241.

[22] J. Liu, C.G. Duan, W.G. Yin, W.N. Mei, R.W. Smith, J.R. Hardy, Dielectric permittivity and electric modulus in Bi2Ti4O11, J. Chem. Phys. 119 (2003) 2812–2819.

[23] X.Z. Zuo, J. Yang, B. Yuan, D.P. Song, X.W. Tang, K.J. Zhang, X.B. Zhu, W.H. Song, J.M. Dai, Y.P. Sun, Magnetic, dielectric properties, and scaling behaviors of Aurivillius compounds $Bi_{6-x/3}Fe_2Ti_{3-2x}(WCo)_xO_{18}$ ($0 \leq x \leq 0.15$), J. Appl. Phys. 117 (2015) 0–7.

[24] D.K. Rana, S.K. Singh, S.K. Kundu, S. Roy, S. Angappane, S. Basu, Electrical and room temperature multiferroic properties of polyvinylidene fluoride nanocomposites doped with nickel ferrite nanoparticles, New J. Chem. 43 (2019) 3128–3138.

[25] G.C. Psarras, E. Manolakaki, G.M. Tsangaris, Dielectric dispersion and ac conductivity in - Iron particles loaded: Polymer composites, Compos. Part A Appl. Sci. Manuf. 34 (2003) 1187–1198.

[26] F. Tian, Electric Modulus Powerful Tool for Analyzing Dielectric Behavior, IEEE Trans. Dielectr. Electr. Insul. 21 (2014) 929–931.

[27] N.H. Vasoya, P.K. Jha, K.G. Saija, S.N. Dolia, K.B. Zankat, K.B. Modi, Electric Modulus, Scaling and Modeling of Dielectric Properties for Mn^{2+}-Si^{4+} Co-substituted Mn-Zn Ferrites, J. Electron. Mater. 45 (2016) 917–927.

[28] A. Molak, M. Paluch, S. Pawlus, J. Klimontko, Z. Ujma, I. Gruszka, Electric modulus approach to the analysis of electric relaxation in highly conducting $(Na_{0.75}Bi_{0.25})(Mn_{0.25}Nb_{0.75})O_3$ ceramics, J. Phys. D. Appl. Phys. 38 (2005) 1450–1460.

[29] S.R. Elliott, A.c. conduction in amorphous chalcogenide and pnictide semiconductors, Adv. Phys. 36 (1987) 135–217.

[30] N. Vol, review article The ' universal ' dielectric response, Nature. 267 (1977) 673–679.

[31] L. Essaleh, S.M. Wasim, G. Marín, C. Rincón, S. Amhil, J. Galibert, CuIn3Te5 semiconductor compound Mott type variable range hopping conduction and magnetoresistance in p -type $CuIn_3Te_5$ semiconductor compound, J. Appl. Phys. 122 (2017) 015702.

[32] Y. Yuan, J. Huang, Ion Migration in Organometal Trihalide Perovskite and Its Impact on Photovoltaic Efficiency and Stability, Acc. Chem. Res. 49 (2016) 286–293.

[33] C. Eames, J.M. Frost, P.R.F. Barnes, B.C. O'Regan, A. Walsh, M.S. Islam, Ionic transport in hybrid lead iodide perovskite solar cells, Nat. Commun. 6 (2015) 2–9.

[34] N.G. Park, Perovskite solar cells: An emerging photovoltaic technology, Mater. Today. 18 (2015) 65–72.

[35] R. García-Rodríguez, D. Ferdani, S. Pering, P.J. Baker, P.J. Cameron, Influence of bromide content on iodide migration in inverted $MAPb(I_{1-X}Br_x)_3$ perovskite solar cells, J. Mater. Chem. A. 7 (2019) 22604–22614.

CHAPTER 6

6. Tailoring of dielectric and transport properties of $C_3H_7NH_3PbI_xBr_{3-x}$

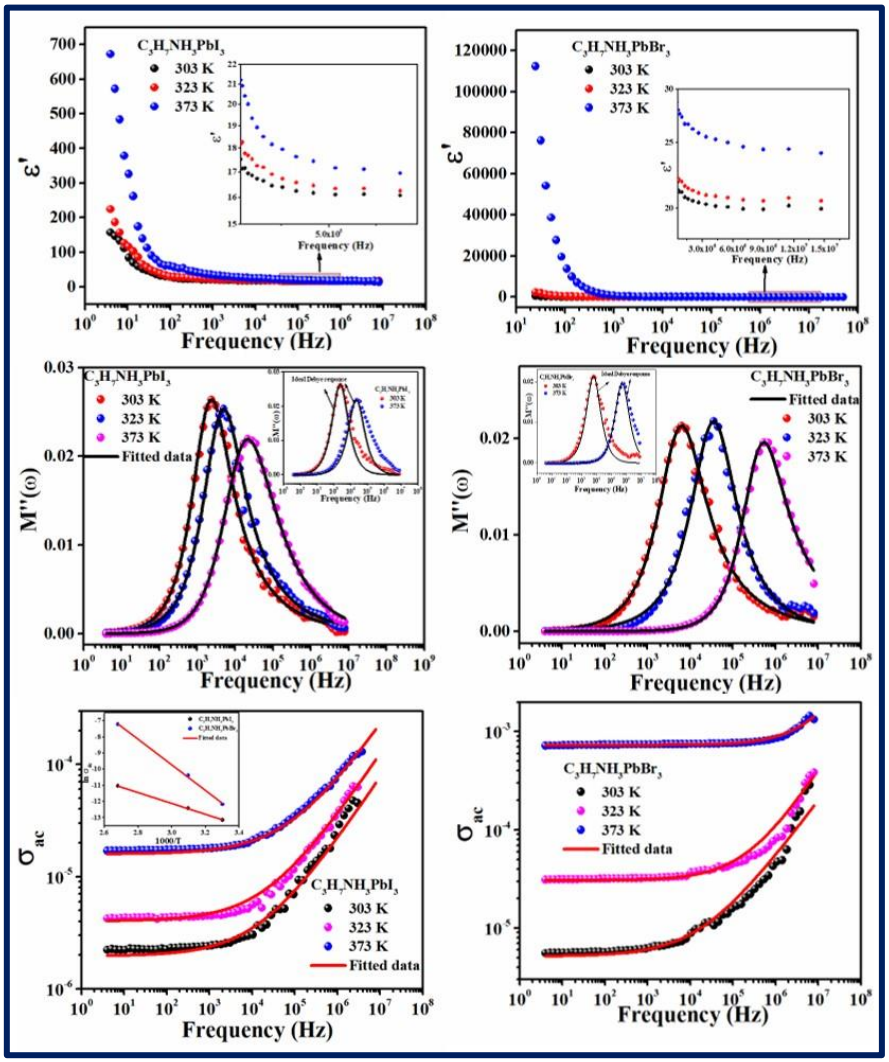

6.1. Introduction

Hybrid perovskites are a group of popular semiconductors exhibiting attractive features like the ease in fabrication method, cost effectiveness, high power conversion efficiency, long charge diffusion distance, tunable band gap, and used in a wide array of applications in solar energy harvesting, optoelectronic devices, etc [1]. These perovskites follow a general structure ABX_3 where A refers to organic cation, B represents bivalent inorganic cation and X denotes halogen ion. Despite the mentioned striking properties, the stability of these hybrid perovskites is still a point of concern [2]. Though methylammonium lead iodide is the most prevalent hybrid perovskite to date, researchers nowadays are dealing with other alkylammonium lead mixed halide hybrid perovskites to explore and overcome the limitations. $C_3H_7NH_3PbI_xBr_{3-x}$ $(0 \leq x \leq 3)$ are encouraging candidates with appreciable stability. A comparative study of temperature and frequency dependent on the electrical properties has been reported here. It shows the significant influence of halogen ions over dielectric constants, conductivity, etc.

6.2. Materials and methods

Both the samples were synthesized by sol–gel process. Firstly, stoichiometric amounts of $C_3H_7NH_2$ and HI / HBr were stirred for 3 hours in an ice bath to form a homogeneous solution. The solutions thus formed were dried and cleaned with diethyl ether to remove unreacted HI / HBr. Finally, the resultants were dried and evaporated to form $C_3H_7NH_3I$ and $C_3H_7NH_3Br$ respectively.

Next, $C_3H_7NH_3I$ and $C_3H_7NH_3Br$ are mixed with PbI_2 and $PbBr_2$ respectively in equimolar ratio in DMF and stirred for 12 hours at 65 ^oC. The homogeneous mixtures thus dried at 65 ^oC in a vacuum to yield yellow-colored $C_3H_7NH_3PbI_3$ and visibly transparent $C_3H_7NH_3PbBr_3$.

5.3. Characterizations

The structural characterization of both the samples were carried out by X-ray diffraction method using Rigaku miniflex – 600 benchtop diffractometer. The electrical properties of $C_3H_7NH_3PbI_xBr_{3-x}$ $(x = 0, 3)$ were measured in the temperature range $300\ K \leq T \leq 373\ K$ within $4\ Hz \leq f \leq 8\ MHz$ using Hioki LCR Q meter (IM3536) system.

6.4. Result & Discussions

6.4.1. Structural analysis

The X-ray diffraction patterns (XRD) measured at room temperature in the range 20^0 - 40^0 of

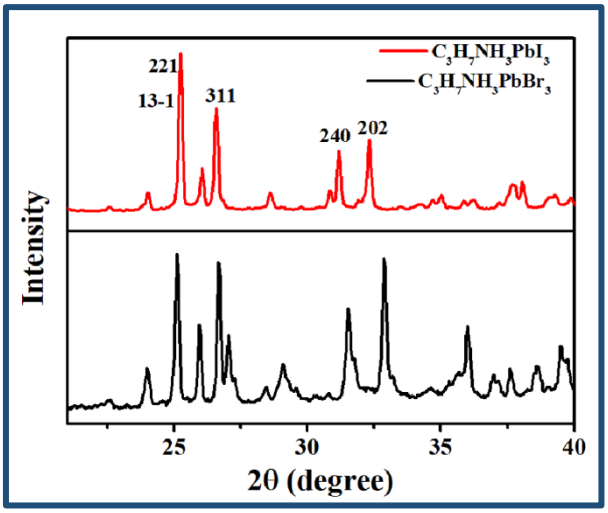

Fig. 6.1. XRD pattern of $C_3H_7NH_3PbI_xBr_{3-x}$ $(x = 0.0, 3.0)$.

2θ for $C_3H_7NH_3PbI_xBr_{3-x}$ $(x = 0.0, 3.0)$ is illustrated in Fig. 6.1. All lines are unambiguously indexed for different (h k l) planes corresponding to the preovskite structured $C_3H_7NH_3PbI_xBr_{3-x}$ [2–4]. As the ionic size of I (~0.220 nm) is more than that of Br (~0.196 nm), the introduction of I in place of Br in hybrid perovskite causes the lattice expansion. This in turn causes a shift of the XRD peaks of $C_3H_7NH_3PbI_3$ towards the smaller angle of diffraction. Thus, Fig. 6.1 may confirm the successful introduction of I in ABX_3 lattice [2].

6.4.2. Dielectric study

Fig. 6.2a-b shows the temperature and frequency dependence of the dielectric constant of $C_3H_7NH_3PbI_xBr_{3-x}$ $(x = 0, 3)$. $\varepsilon'(\omega)$ of $C_3H_7NH_3PbBr_3$ is observed to be much higher than that of $C_3H_7NH_3PbI_3$ for all temperatures. $\varepsilon'(\omega)$ of both the samples exhibit an ascending tendency with an increase in temperature. The behaviour of dielectric constant at low frequency domain can be demonstrated by Maxwell -Wagner interfacial polarization in association with Koop's phenomenological theory. The theory states that dispersion of dielectric constant in low frequency region appears due to the presence of double layers (high conducting layer of grain which is separated by a highly resistive layer of grain boundary). Hence, charge carriers get stuck at the interface of the grain boundary. In the low frequency domain, dipoles follow the

applied electric field ($\omega \ll 1/\tau$) properly and quasistatic $\varepsilon'(\omega)$ is attained. But, with the rise

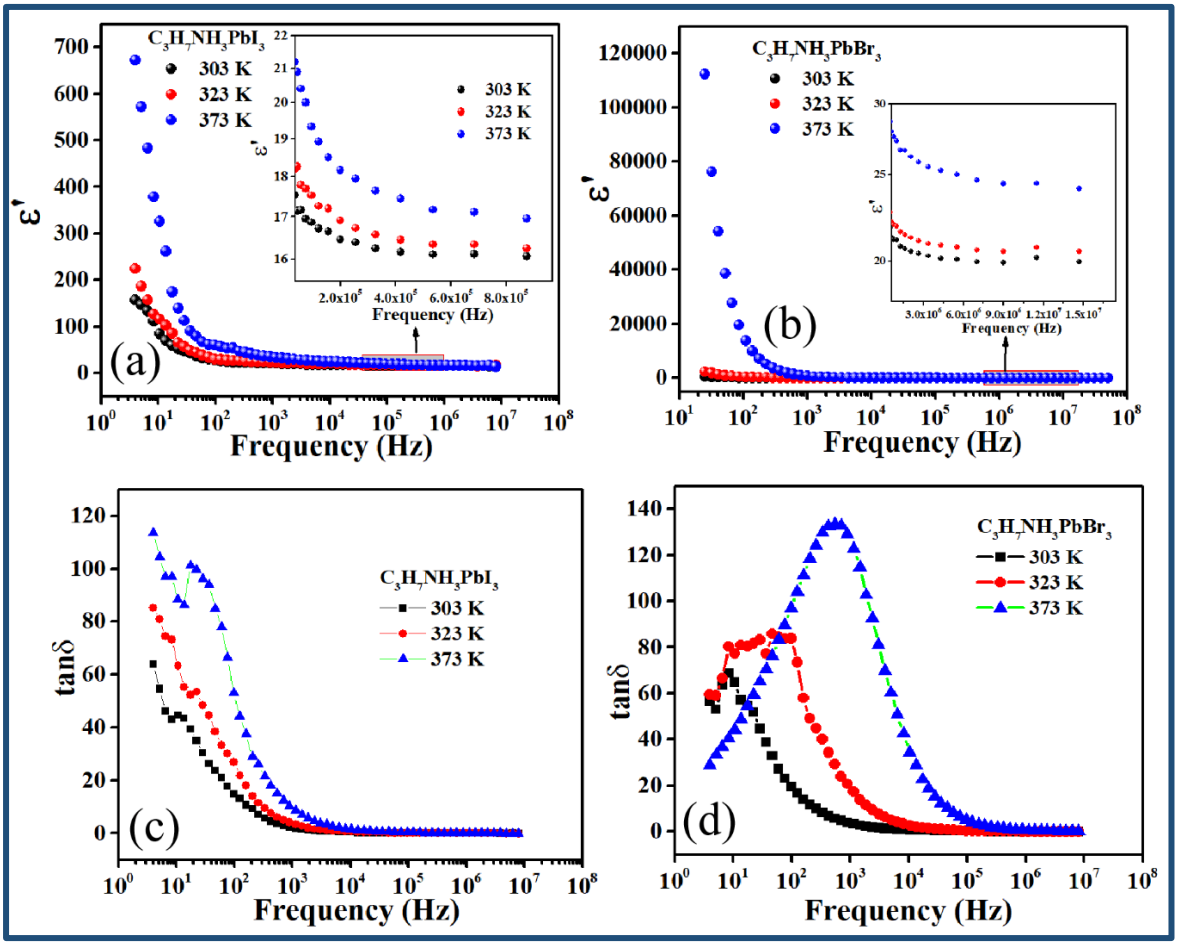

Fig. 6.2a and b shows the variation dielectric constant of $C_3H_7NH_3PbI_xBr_{3-x}$ $(x = 0.0, 3.0)$ as a function of frequency, inset of Fig. 6.2a and b refers to the enlarged portion of high frequency region. Fig. 6.2 c and d denote the loss tangent spectra of both samples.

in frequency, dipoles fail to track the applied AC field and hence the movement of the charge carriers becomes delimited near the grain boundary lowering the value of the dielectric constant [5,6].

Fig. 6.2c and d exhibit the variation of loss tangent with frequency for different temperatures. No peak is observed within the frequency range of investigation for $C_3H_7NH_3PbI_3$. On the other hand, for $C_3H_7NH_3PbBr_3$, peaks are observed as shown in Fig. 6.2d and found to shift towards higher frequency region with an increase in temperature. This infers the lowering of relaxation time with the increase of temperature.

6.4.3. Electric modulus analysis

Complex electric modulus construes the relaxation procedure of the materials and is expressed as

$$M^* = \frac{1}{\varepsilon^*} = \frac{1}{\varepsilon' + i\varepsilon''} \quad (6.1)$$

Here, all the symbols follow their usual significance. The inverse of the complex

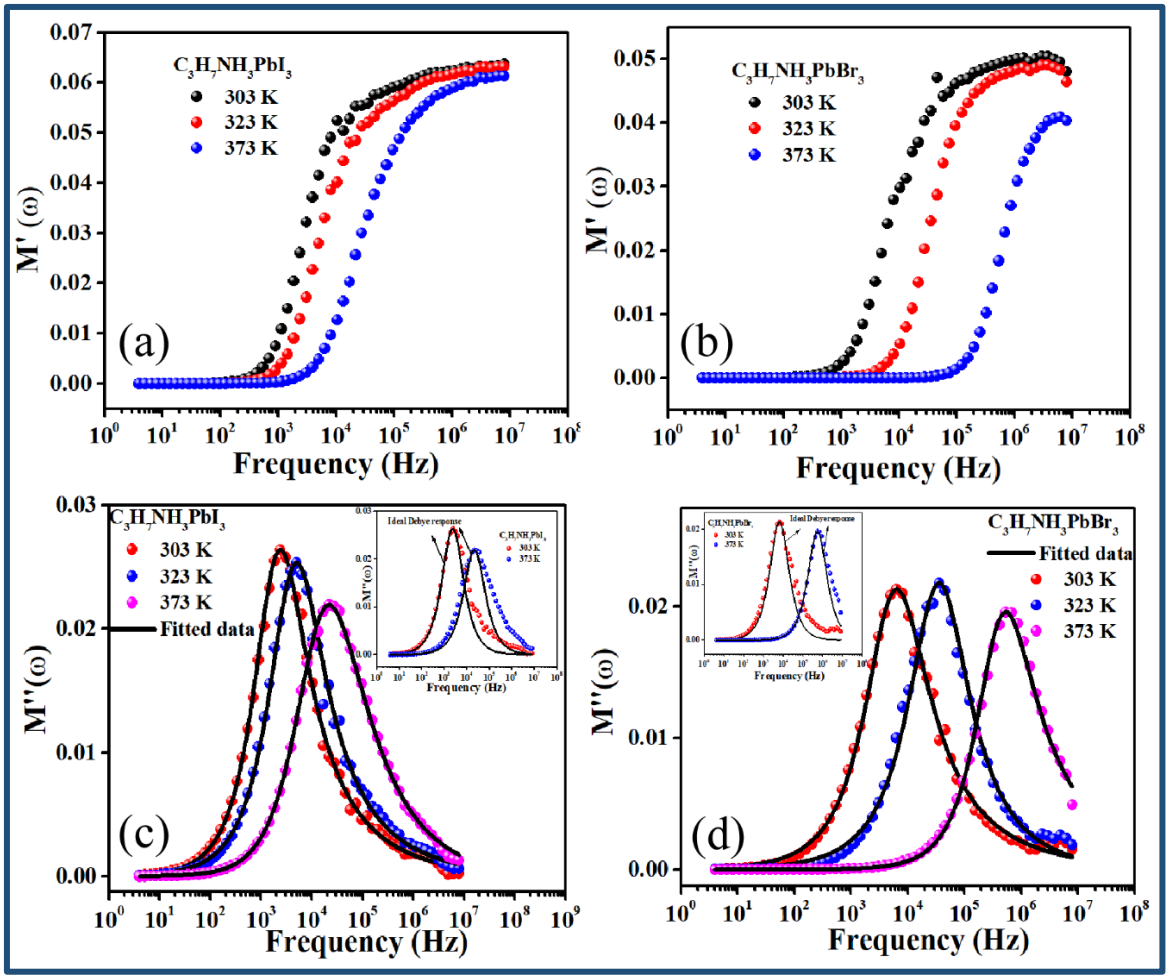

Fig. 6.3a and b indicate the variation of frequency dispersed real part of electric modulus of $C_3H_7NH_3PbI_xBr_{3-x}$ $(x = 0, 3)$. Fig. 6.3c and d exhibits the variation of KWW model fitted data of imaginary part of electric modulus with frequency. Inset of Fig. 6.3c and d shows the deviation from ideal Debye response.

dielectric constant depicts the impacts of space charge distribution in the relaxation mechanism. Fig. 6.3a-b shows the dispersion of the real part of the electric modulus $M'(\omega)$ of both materials with frequency. It has been noticed that in low frequency region, $M'(\omega)$ attain almost zeros value and with the rise in frequency, the values of $M'(\omega)$ are found to increase and obtain a

sigmoidal shape. The shape of $M'(\omega)$ indicates the dominance of long range mobility of charge carriers and suppresses the influence of electrode polarization.

Fig. 6c-d show the variation of temperature dependent imaginary part of the electric modulus ($M''(\omega)$) of both the samples with frequency. It has been observed that $M''(\omega)$ obtains its maximum value at a certain frequency commonly known as relaxation frequency. For both samples, the peaks are observed to arise at high frequency domain attributing to the confined movement of charge carriers within the potential well. The peaks thus imply clearly that the charge carriers can hop spontaneously from one position to its neighbouring position following the long range translational motion in low frequency domain and with the enhancement of frequency, charge carriers only follow the short range mobility. The nature of $M''(\omega)$ is asymmetric confirming the non-Debye type behavior of both samples. Kohlrausch – Williams – Watts (KWW) function is employed to detect the qualitative deviation from the ideal Debye type response. KWW equation stated as [6]

$$M''(\omega) = \frac{M''_{max}}{\left(\frac{1-c}{a+b}\right)\left[b\left(\frac{f}{f_{max}}\right)^{-a}+a\left(\frac{f}{f_{max}}\right)^{b}\right]+c} \qquad (6.2)$$

a and b are two shape parameters that acquire values of near unity for both samples at 303 K indicating the reduction of deviation from ideal Debye type response. c is referred to here as a smoothing parameter. The fitted data reveals that the materials shift their responses from non-Debye type to nearly ideal Debye type with the escalation of temperature. The Inset of Fig. 6.3c-d clearly depicts the deviation of $M''(\omega)$ from ideal Debye type response for $C_3H_7NH_3PbI_xBr_{3-x}$ at 303 K and 373 K respectively.

6.4.4. Conductivity

The variation of frequency dispersed conductivity of $C_3H_7NH_3PbI_xBr_{3-x}$ ($x = 0, 3$) is shown in Fig. 6.4a-b. In low frequency domain, the curves are frequency independent and flat ascribing to DC conductivity. At hopping frequency, conductivity increases appreciably addressing AC conductivity. $C_3H_7NH_3PbBr_3$ indicates substantially higher AC conductivity than $C_3H_7NH_3PbI_3$ for all concerned temperatures. The hopping frequency is temperature dependent, i.e. as temperature increases, hopping frequency is found to move slightly toward high frequency region. The overall conductivities of both samples obey Jonscher's power law (universal dielectric response (UDR)) [7]. The conduction mechanism can be described here with the jump relaxation model. According to this model, the flattened nature of DC conductivity is due to the successful hopping of ions possessing long-range translational

motion. When an ion hops from its relaxed site, the neighboring ions shift apart to soothe the

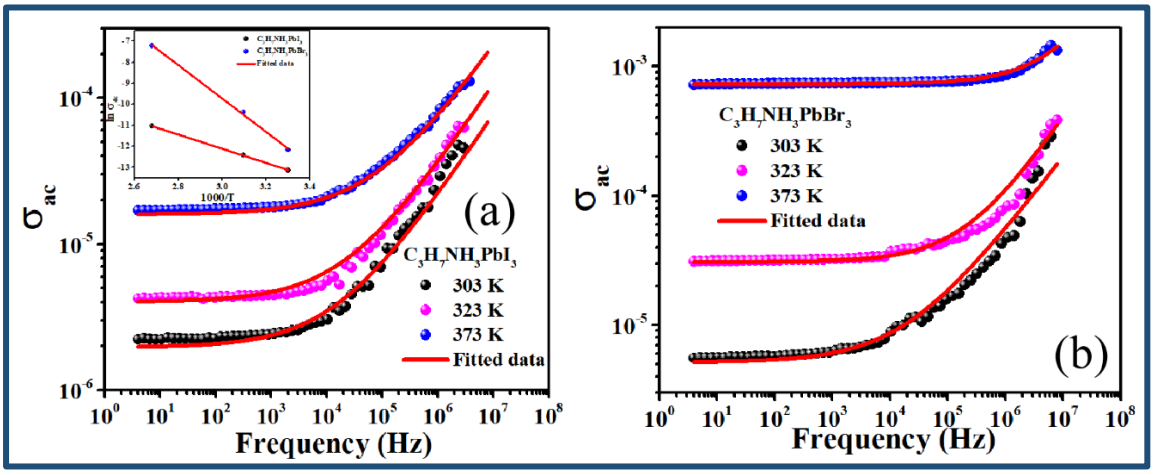

Fig. 6.4a and b depicts the distribution of Jonscher's power law fitted AC conductivity $C_3H_7NH_3PbI_xBr_{3-x}$ $(x = 0, 3)$ with frequency. Inset of Fig. 6.4a shows the σ_{dc} vs. 1000/T for two samples.

hopping ion. But sometimes, the hopping ion moves back to its initial state to partially stable the configuration initiating unsuccessful hopping. In high frequency domain, both successful and unsuccessful hopping participants and dispersive conductivities are observed. σ_{dc} obtained from the fitted data using UDR is plotted against $1000/T$ for both materials and hence the values of activation energy of both samples are evaluated. The Inset of Fig. 6.4a shows that the activation energies are 0.29118 eV and 0.6853 eV respectively.

6.5 Conclusion

$C_3H_7NH_3PbI_xBr_{3-x}$ $(x = 0, 3)$ are synthesized via sol gel method. Dielectric constant of $C_3H_7NH_3PbBr_3$ is much higher than that of $C_3H_7NH_3PbI_3$. With the help of KWW equation, the deviation of non – Debye type response of the imaginary part of the electric modulus from the ideal Debye type response is well explained for both the samples. It has also been found that this deviation diminishes substantially with rise in temperature. $C_3H_7NH_3PbBr_3$ possesses much higher conductivity than $C_3H_7NH_3PbI_3$ for all concerned temperatures. The comparative study of different electrical properties of $C_3H_7NH_3PbI_xBr_{3-x}$ $(x = 0.0, 3.0)$ will help to comprehend the nature of these relatively less explored potential perovskites.

References

[1] P. Sadhukhan, S. Kundu, A. Roy, A. Ray, P. Maji, H. Dutta, S.K. Pradhan, S. Das, Solvent-Free Solid-State Synthesis of High Yield Mixed Halide Perovskites for Easily Tunable Composition and Band Gap, Cryst. Growth Des. 18 (2018) 3428–3432. https://doi.org/10.1021/acs.cgd.8b00137.

[2] P. Sengupta, P. Sadhukhan, A. Ray, R. Ray, S. Bhattacharyya, S. Das, Temperature and frequency dependent dielectric response of $C_3H_7NH_3PbI_3$: A new hybrid perovskite, J. Appl. Phys. 127 (2020) 204103. https://doi.org/10.1063/1.5142810.

[3] M. Safdari, A. Fischer, B. Xu, L. Kloo, J.M. Gardner, Structure and function relationships in alkylammonium lead iodide solar cells, J. Mater. Chem. A. 3 (2015) 9201–9207. https://doi.org/10.1039/C4TA06174H.

[4] X. Ren, X. Yan, A.S. Ahmad, H. Cheng, Y. Li, Y. Zhao, L. Wang, S. Wang, Pressure-Induced Phase Transition and Band Gap Engineering in Propylammonium Lead Bromide Perovskite, J. Phys. Chem. C. 123 (2019) 15204–15208. https://doi.org/10.1021/acs.jpcc.9b02854.

[5] D.K. Pradhan, S. Kumari, V.S. Puli, P.T. Das, D.K. Pradhan, A. Kumar, J.F. Scott, R.S. Katiyar, Correlation of dielectric, electrical and magnetic properties near the magnetic phase transition temperature of cobalt zinc ferrite, Phys. Chem. Chem. Phys. 19 (2017) 210–218. https://doi.org/10.1039/C6CP06133H.

[6] D.K. Rana, S.K. Singh, S.K. Kundu, S. Roy, S. Angappane, S. Basu, Electrical and room temperature multiferroic properties of polyvinylidene fluoride nanocomposites doped with nickel ferrite nanoparticles, New J. Chem. 43 (2019) 3128–3138. https://doi.org/10.1039/C8NJ04755C.

CHAPTER 7

7. Improved energy harvesting ability of $C_3H_7NH_3PbI_3$ decorated PVDF nanofiber based flexible nanogenerator

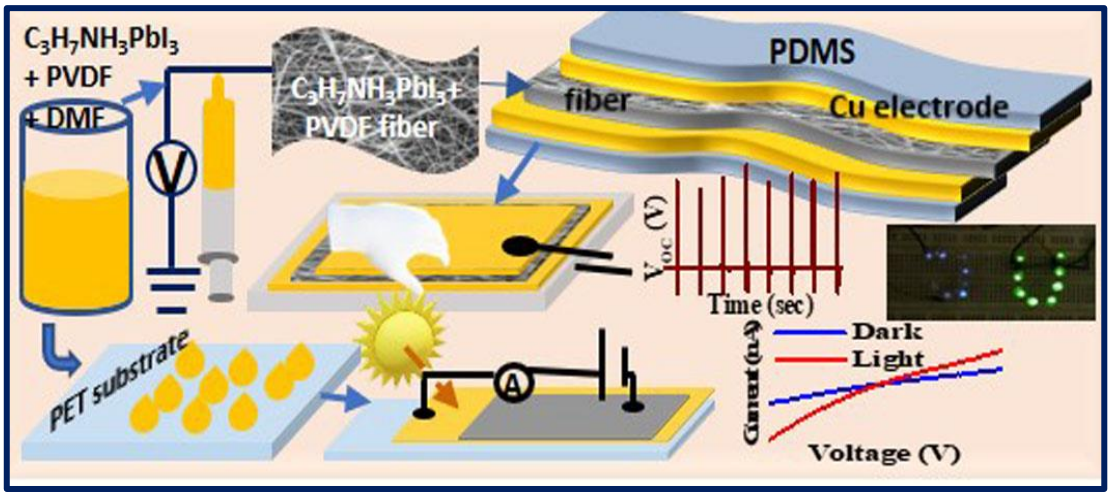

7.1. Introduction

Nowadays, sustainable, green energy resources have garnered immense attention globally to accomplish our inflated daily power needs and to confront various alarming challenges like non-renewable energy limitations, climate changes, and frightening growth of environmental pollution caused by excessive usage of fossil fuels. Among various sources of renewable energy like solar, wind, mechanical, tide, geothermal, etc., solar and mechanical energy sources are very popular due to their environmental friendliness and abundance in the surroundings. Converting the mechanical and vibrational energies obtained from persistent sources around us to electrical signals can be a fitter, biocompatible, and safer option. During the last few years, the rapid development of microelectronics with microchips and MEM-based sensors has emerged a new era in the field of miniaturization. All these miniature instruments like flexible medical devices, body sensors, pressure sensors, communication devices, environmental monitoring devices, etc. run on minimal power but require recharging and often include photo sensors for intended functioning [1,2]. Lightweight, flexible, self-driven, portable, wearable, simple-structured piezoelectric energy harvesters can be an optimum solution here to perform without any peripheral voltage sources. Piezoelectric materials-based nanogenerators (PNG) accumulate energy to produce piezoelectric potential when exposed to dynamic strain and consequently, a transient current generates in the attached circuit. Several semiconducting materials like $BaTiO_3$, $ZnSO_3$, lead zirconium titanate (PZT), ZnO, CdS, GaN, etc. have been studied and well explored over the years [3–5]. Despite high piezoelectric efficacy and high-power output, these inorganic piezoelectric materials have various limitations like cost-intensiveness, complicated rigorous synthesis process, rigidness, brittle nature, etc. Piezoelectric nanogenerators using these inorganic nanomaterials, therefore, face challenges in modern practical implementations of portable electronic appliances and Internet-of-Things (IoTs). On the contrary, piezo-active ferroelectric polymers and their copolymers can be appropriate and competent due to their fabrication simplicity, cost-effectivity, and ability to be designed in the desired shape and size. Despite having all these advantages, the low piezoelectric coefficients and efficacy of these polymers restrict their performance in PNGs made of these polymers. To get the enhanced performance, and to achieve the sturdiness necessary to run self-powered, wearable devices, integrating ferroelectric polymer matrix with suitable organic-inorganic hybrid nanofillers in a sole unit is the new trend. Among various polymers like cellulose, poly-L-Lactide (PLLA), polyvinylidene difluoride (PVDF), etc., PVDF and its copolymers are widely used in PNGs on

account of their easy synthesis technique with a superior piezoelectric response, flexibility, and biocompatibility [6–8]. In semi-crystalline PVDF, the polarized β phase (TTTT conformation) is mostly responsible for its piezo and ferroelectric activity with the highest dipole moment per unit volume among four different phases α (TGTG conformation), β, γ (T_3GT_3G conformation), and δ (polarised α). In general, the non-polar α phase is prevalent in PVDF. To bring out the dominance of the electroactive β phase, various methods like stretching [9,10] PVDF in the high electric field, annealing in high temperatures [11] hydrated salt addition [12], etc. are followed. Roopa et al. [10] reported that the mechanical stretching of the films causes non-uniformity due to a lower stretching ratio and can face difficulty in maintaining a constant temperature. Moreover, annealing at high temperatures may ruin the film's quality and durability [9,10]. On the contrary, the electrospinning method can be an ideal and expedient alternative to produce ultra-thin, flexible, feathery PVDF nanofibers with improved β phase. Although the high stretching ratio to convert α phase to β phase during electrospinning is similar in some way with the mechanical stretching, but some conditional parameters like distance between tip of the needle and the collector plate, flow rate, electrospinning temperature can control the fiber quality and consistency. But the partial transition from the non-electroactive α phase to the highly electroactive β phase somehow draws a limitation in the piezoelectric application. The formation of β phase in PVDF nanofiber can be enhanced significantly by incorporating suitable filler in the precursor solution. Optically active hybrid perovskite materials (generic structure ABX_3, A-organic cation, B-inorganic cation, and X-halide anion) which have gained immense popularity in recent years due to their synthesis simplicity, low expense, tunable bandgap, appreciable optical and electrical properties and wide application in energy harvesting, can be a fascinating choice for this job [13–15]. These perovskites show ferroelectricity that improves the β phase induction of the PVDF matrix and also contributes to better separation of the photogenerated electron-holes inside the perovskite for photodetection. Though intensive research has been carried out on the hybrid perovskites in solar cell applications, the mechanical energy harvesting domain using these perovskites is still less explored. To date, few works have been reported using methylammonium lead halide, formamidinium lead, and tin halide as additives in the polymer matrix [15–20]. Strong polarization in these perovskites can also be induced by using a large organic cation in the A-site that can deform the BX_6 octahedra of the perovskite structure. Propylammonium ion is much larger than methylammonium ion. Propylammonium lead iodide ($C_3H_7NH_3PbI_3$) is a promising candidate that possesses a high dielectric constant indicating strong polarizability of the material and needs to be studied more. Besides, this particular hybrid perovskite exhibits

far better stability in presence of humidity and UV light [21] compared to methylammonium lead halide. Propylammonium lead iodide ($PAPbI_3$) decorated PVDF exhibiting excellent mechanical stability can be employed in a multifaceted device that can harvest mechanical and solar energy simultaneously or separately. Thus, in short, this perovskite as the key filler in PVDF nanofiber not only improves the piezoelectric activity of the system but also enhances the light absorption capability of the fabricated photodetector.

In this report, we have synthesized $PAPbI_3$ doped PVDF nanofibers by the electrospinning technique. The doping of $PAPbI_3$ enhances the degree of crystallinity of electrospun nanofibers substantially and converts almost solely the non-polar phase to polar phase content. The fabricated nanogenerator using $PAPbI_3$@PVDF nanofibers exhibits exotic mechano-sensitivity as well as energy conversion efficiency. The optimal energy band gap and fascinating behavior of $PAPbI_3$@PVDF composite under light illumination certify its ability as a piezo-active photodetector. Thus, this report includes the striking response of $PAPbI_3$ doped PVDF composite-based flexible, self-powered nanogenerator and justification of its credibility as a deserving candidate for scavenging mechanical energy as well as intended photodetection.

7.2. Materials and methods

7.2.1. Materials

To synthesize $PAPbI_3$, n-Propylamine ($C_3H_7NH_2$, 98%), N, N-dimethylformamide (DMF, anhydrous, 99.8%), hydroiodic acid (57 wt.% in water), and lead iodide (PbI_2) were purchased from Spectrochem, Merck Chemicals, Loba Chemie and Alfa Aesar, respectively. PVDF powder, required for nanofiber formation, was bought from Alfa Aesar. All the chemicals used in the experiment were of analytical grade.

7.2.2. Synthesis of $PAPbI_3$

At first, propylamine ($C_3H_7NH_2$) was mixed in an equimolar ratio with hydroiodic acid (HI) and stirred in an ice bath for 2 hours. The formed solution was then dried and cleaned with diethyl ether thrice to pull out unreacted acid if any. The resultant mixture was then dried overnight at 60 ^oC to yield propylammonium iodide salt ($C_3H_7NH_3I$).

$C_3H_7NH_3I$ and lead iodide (PbI_2) were taken in stoichiometric ratio and dissolved in DMF in an open ambiance and stirred for 10 hours at 65 ^oC. The solution was then filtered and dried at 65 ^oC to obtain the required yellow $PAPbI_3$.

7.2.3. Formation of electrospun nanofibers (NFs)

To prepare the stock solution, 10 wt% PVDF was dissolved in a mixture of DMF and acetone (3:5) by stirring continuously for 3 hours at 60 ^oC. A transparent solution was formed in which 3.21, 4.76, and 6.20 wt% (w/w) of previously synthesized $PAPbI_3$ was added and stirred for another 3 hours at the same temperature. The presence of DMF turns the transparent solution into yellow colour with the addition of $PAPbI_3$ as shown in Fig. 7.1.

For electrospinning, a 10 ml hypertonic syringe of diameter 8 mm was filled with the

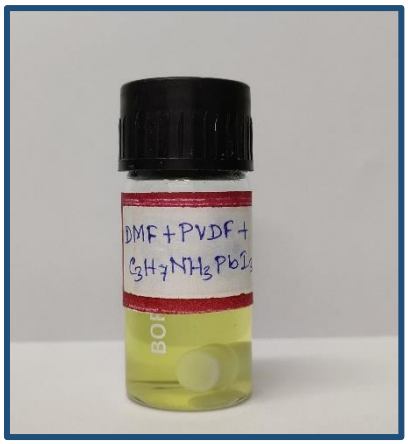

Fig. 7.1. $C_3H_7NH_3PbI_3$ – PVDF solution in the mixture of DMF and acetone.

homogeneous solutions and placed in the electrospinning set-up. The solution was squeezed out by the pump through the needle of the syringe at a flow rate of 0.8 ml/hour and so formed nanofibers were deposited on the aluminium foil-wrapped collector plate. The temperature of the collector plate was sustained at 70 ^oC to evaporate the solvent. The distance between the collector plate and the needle tip of the syringe was maintained at 6.5 cm during the formation of nanofibers. All the nanofibers were prepared under a high voltage of 19 kV. The prepared nanofibers were collected from the aluminium foil for further characterization and device fabrication. $PAPbI_3$@PVDF nanofibers are denoted as PANF (3.21), PANF (4.76), and PANF (6.20) considering the $PAPbI_3$ w/w concentrations.

7.2.4. Fabrication of piezoelectric nanogenerators (NGs)

A very lightweight, cost-effective, flexible, nanogenerator (effective area ~ 25 mm × 15 mm) was fabricated by employing PANF (4.76) as an electroactive material. PANF (4.76) was sandwiched between two copper (Cu) electrodes and two copper wires were soldered on the electrodes. Finally, the fabricated nanogenerator, configured as Cu electrode / PANF (4.76) / Cu electrode, was laminated by PDMS (polydimethylsiloxane) layer to enhance its durability. Another nanogenerator using undoped PVDF, named PVNF, was also fabricated following a similar configuration for the comparative study of performance.

7.2.5. Fabrication of Photo piezo-active energy garner (PPEG)

At first, the prepared PVDF-PAPbI$_3$ (4.76) solution was cast drop-wise slowly on an ITO-coated flexible PET substrate and kept at 90 ^{o}C for 2 hours. The coated ITO serves as a top electrode of the obtained film. An aluminium electrode is attached to the other side to design a sandwich structured PAPPEG (effective exposed area ~ 25 mm × 15 mm). Finally, the device is laminated to provide a safeguard and to increase its lifetime.

7.3. Characterization

The structural property of synthesized nanofibers was examined by X-ray powder diffractometer (Bruker D8). The FTIR spectrum was obtained from PerkinElmer, Spectrum – 2000. The surface morphology of the samples and the detection of constituent elements were performed by FESEM (FEI, INSPECT F50) and EDX (Bruker). TEM image and SAED pattern of PANF (4.76) were gained from JEOL (JEM, 2100). The photoluminescence property of PANF (4.76) at room temperature was attained from Fluoromax–4C_1505D-33. DSC thermographs of the concerned fibers were analysed by Waters India (TA), DSC Q2000. The tensile strength of the samples was measured using Tinius Olsen H50KS at a strain rate of 1 mm/min. The fibers were sandwiched between two Au electrodes (diameter~1 cm) and the dielectric properties of the fibers were analysed by Hioki LCR Q meter (IM3536). The open circuit voltage response was recorded using a digital storage oscilloscope (Keysight, 1052A) and the short circuit current was measured using Kiethley 2602B. The values of d_{33} were

obtained using a wide range of d_{33} meter. We have used AM1.5G, a standard solar spectrum of a solar simulator to illuminate PPEG.

7.4. Results and discussions

7.4.1. Structural characterization and quantification of ferroelectric phase content

The X-ray diffraction pattern of as-synthesized $PAPbI_3$ using Cu K_α radiation is shown in Fig. 7.1a. All the peaks in the diffraction pattern could be indexed by the monoclinic structure with the space group of *Cc* as reported earlier by Sengupta et al. [21]. Thus, the XRD data confirms the absence of any detectable impurity phase. A digital photograph of the sol-gel derived, yellow colored, $PAPbI_3$ is shown in the inset of Fig. 7.2a. This perovskite is used as the key filler with different concentrations in the PVDF matrix to produce nanofibers.

For the quantitative estimation of the electroactive β phase in the electrospun nanofibers, the FTIR analysis was carried out for all the samples. The FTIR spectra of the nanofibers made of pure PVDF (PVNF), and its composites PANF (1.55), PANF (3.21), and PANF (4.76), are shown in Fig. 7.2b. PVNF is mainly composed of α- and β -crystalline phases with the characteristic absorption peaks observed at 1121, 976, 796, 764, 612 cm^{-1} (non-polar α phase), and 1281 cm^{-1}, 843 cm^{-1} (polar β phase) [6]. In general, pure PVDF contains a low percentage of β phase which limits its usage in energy harvesting applications. The inclusion of $PAPbI_3$ as filler in the PVDF matrix reduces the intensity of these characteristic α peaks significantly. On the contrary, the intensity of the absorbance peak of the polar β phase (1281 cm^{-1} and 843 cm^{-1}) enhances gradually in the presence of $PAPbI_3$ up to 4.76 wt%. Moreover, a tiny semi-polar γ phase characterized by an absorption peak at 1238 cm^{-1} is found to appear in PANF (4.76) in contrast to PVNF.

The electroactive phase content (F_{EA}) of the concerned samples are calculated using the relation [22–24]

$$F_{EA} = \frac{A_{EA}}{(\frac{K_{843}}{K_{764}})A_{764}+A_{EA}} \times 100\% \qquad (7.1)$$

Here, A_{EA} and A_{764} correspond to the integral area of the absorbance bands at 843 and 764 cm^{-1}

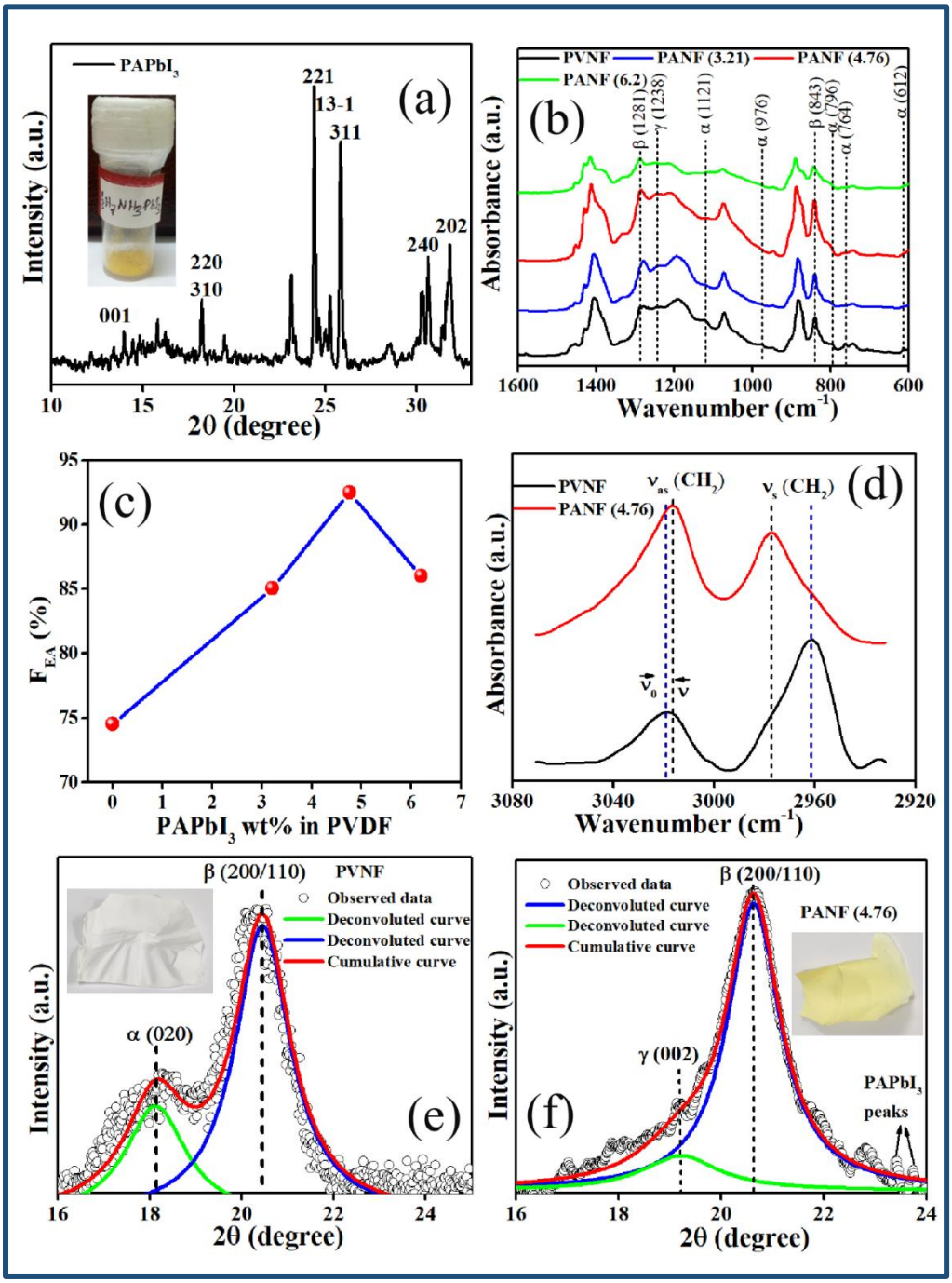

Fig. 7.2. (a) The XRD pattern of sol-gel synthesized $PAPbI_3$. Inset of (a) is the corresponding digital photograph of $PAPbI_3$. (b) The FTIR spectra of PVNF and PANF with different wt% of $PAPbI_3$ in the range of 1600-600 cm^{-1}. (c) The variation of electroactive phase content with different wt% of $PAPbI_3$ in PVDF. (d) The FTIR spectra PVNF and PANF (4.76) within 3080-2920 cm^{-1}. (e)-(f) The deconvoluted XRD curves of PVNF and PANF (4.76), respectively. Inset of (e) and (f) are the digital photographs of PVNF and PANF (4.76), respectively.

^{1}, respectively and K_{843} and K_{764} are the absorption coefficient of these respective bands

($K_{843} = 7.7 \times 10^4\, cm^2/mol$, $K_{764} = 6.1 \times 10^4\, cm^2/mol$). The variation of electroactive phase content of $PAPbI_3$@PVDF due to the incorporation of $PAPbI_3$ with a different concentration is shown in Fig. 7.2c. It is found to be maximum for 4.76 wt% loading of the perovskite. The maximum value of F_{EA} is estimated to be 92.5 % for PANF (4.76) whereas that of PVNF is as low as 74.5 %.

The interaction between the surface charges of $PAPbI_3$ and -CH_2- dipoles of the PVDF chain in PANF is primarily responsible for the conversion of non-polar phase content to polar phase content. Interestingly, the filler up to 4.76 wt %, is dispersed uniformly throughout the PVDF which results in better interaction between the positive and negative charges as well as smooth bead defect-free nanofibers. An attempt was made to prepare nanofibers with 6.20 wt% $PAPbI_3$ filler in the polymer matrix. However, due to the higher concentration, agglomeration of $PAPbI_3$ occurred within the PVDF chain which in turn ruined the formation of nanofibers and effectively reduced the electroactive phase content as illustrated in Fig. 7.2c. In the presence of the solvent, ABX_3 structured perovskite $C_3H_7NH_3PbI_3$ breaks into propylammonium cation ($C_3H_7NH_3^+$) along with PbI_3^- anion. The inorganic PbI_3^- framework exhibits negative charge density due to the presence of electronegative iodine atoms, whereas $C_3H_7NH_3^+$ possesses mono-cationic charge due to a highly electronegative nitrogen atom. Thus, PbI_3^- interacts electrostatically with -CH_2- dipoles which introduce and play a key role in the formation of electroactive β phases. Moreover, the lone pair of fluorine atoms in PVDF participates in the formation of crystallinity of the polymer matrix. Each fluorine atom consists of three lone pairs which may participate as coordination centers. During electrospinning, PVDF molecules attract the cations of $C_3H_7NH_3PbI_3$ precursors due to the presence of the electronegative -CF_2- group. In this way, ABX_3 structured $C_3H_7NH_3PbI_3$ interacts with PVDF to the nucleation of the polarized β phase. Interfacial interactions between the aforesaid filler and -CH_2- dipoles of PVDF can be closely observed within the range 3070 – 2930 cm^{-1} due to the asymmetric (ϑ_{as}) and symmetric (ϑ_s) stretching vibrational bands as shown in Fig. 7.2d for PVNF and PANF (4.76). These vibrational bands are not united with any other vibrational modes and thus shifting of these bands toward low frequencies can be attributed to a sort of disruption of vibration. The presence of the external filler in the PVDF chain improves the interfacial interaction which effectively increases the effective mass of -CH_2- dipoles and reduces the stretching frequency. Such interactions originate damping and relate to vibrational frequencies as follows

$$\omega^2 = \omega_0^2 - r_{dc}^2 \qquad (7.2)$$

Here, ω is the frequency of damped vibration, ω_0 is the frequency of free vibration and r_{dc} denotes the damping factor. Equation (7.2) can be written in terms of wavenumber as

$$\bar{\vartheta} = \sqrt{[\overline{\vartheta_0^2} - (\frac{r_{dc}}{2\pi c})^2]} \quad (7.3)$$

The maximum value of the damping constant is obtained as 5.65×10^{12} sec^{-1} for PANF (4.76). With the addition of the perovskite in the polymer matrix, the damping factor r_{dc} gets enhanced as expected. This behavioral trend indicates the significant β phase formation within PVDF in the presence of $PAPbI_3$ filler is owing to the dipole interactions between the filler and polymer. Thus, PANF (4.76) acquiring satisfying electroactive phase content can be an appropriate choice for harvesting piezoelectric energy.

To analyze further the crystallinity of the electrospun nanofibers, XRD studies of PVNF and PANF (4.76) are performed. The diffraction peak of PVNF at 18.1^o refers to the non-polar α phase (020) whereas, the deconvoluted peak at 20.6^o is assigned to the dual characteristics of β and γ phases as shown in Fig. 7.2e. Interestingly, this non-polar α content is found to disappear completely in PANF (4.76) along with an appearance of a trace amount of semi-polar γ phase at 19.2^o (002). The polar β phase is significantly enhanced in PANF (4.76) as depicted in Fig. 7.2f. To further assess the total degree of crystallinity ($\times_{ct}$ %) of PANF (4.76) and PVNF, the respective XRD curves are deconvoluted. The values of $\times_{ct}$ % of the concerned samples are achieved using the following equation [16].

$$\times_{ct} = \frac{\sum A_{cryst}}{\sum A_{cryst} + \sum A_{amph}} \times 100\ \% \quad (7.4)$$

Here, $\sum A_{cryst}$ and $\sum A_{amph}$ represent the integral area of crystalline phases and amorphous portions of the samples. The evaluated $\times_{ct}$ % of PANF (4.76) and PVNF are 78.8 % and 62.6 %, respectively. Thus, the result of enhanced crystallinity of PANF (4.76) is in tune with that of the FTIR result. The presence of some additional diffraction peaks in PANF (4.76) assigned as that of $PAPbI_3$ confirms the non-degradation of the filler within the polymer.

7.4.2. FESEM imaging and TEM analysis

The surface morphology of PVNF and PANF (4.76) are illustrated in Fig. 7.3a and b, respectively. With the filler load of 4.76 wt%, it can be observed that the randomly oriented fibres are smooth and lump-free. Moreover, the absence of surface bead defects and cracks within the fibre strengthens its durability. The average diameters of PVNF and PANF (4.76)

are ~ 400 nm and ~ 150 nm, respectively (inset of Fig. 7.3a and b). The prominent decrease in

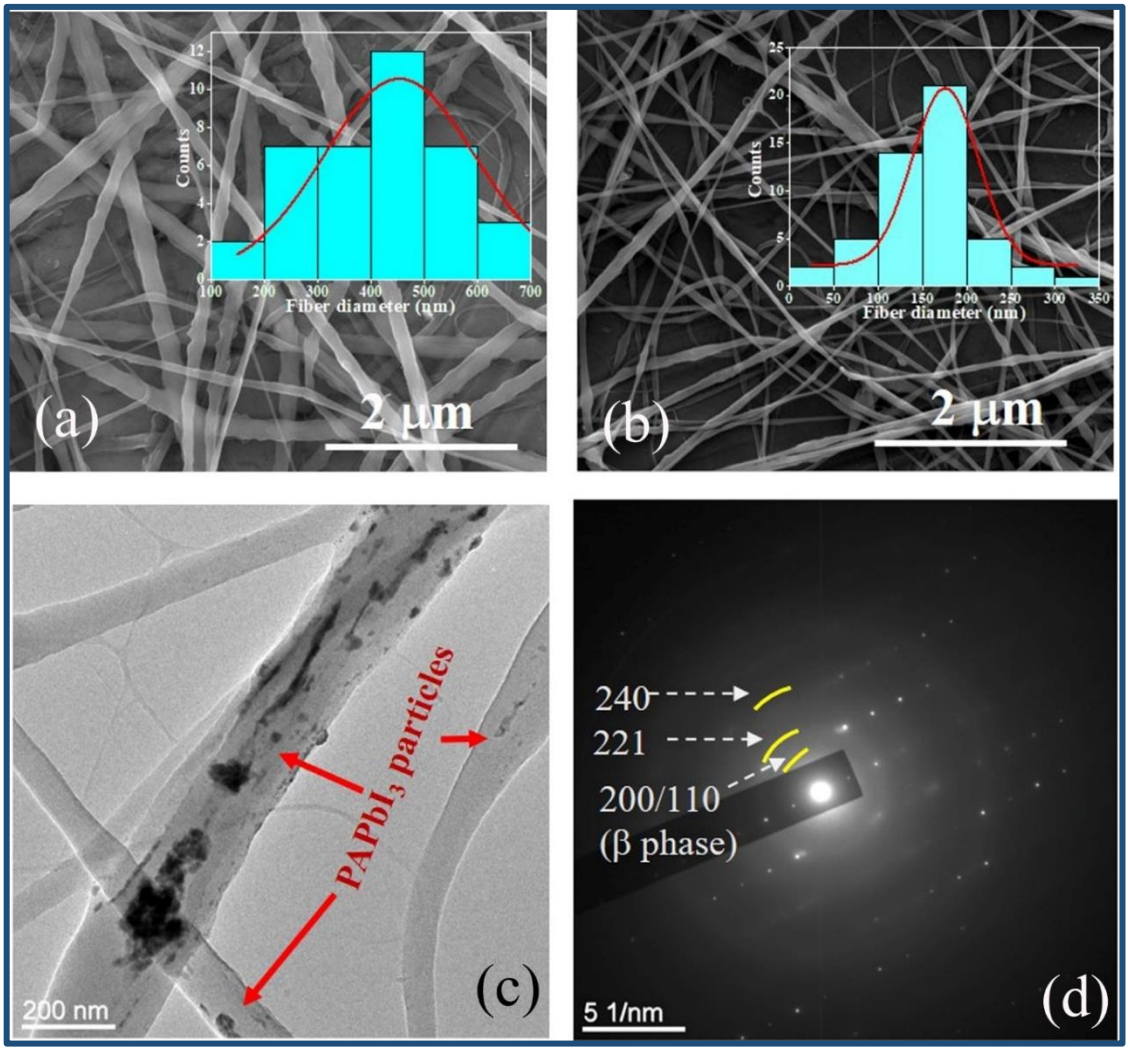

Figure 7.3. (a)-(b) The FESEM images of PVNF and PANF (4.76). Distribution of the fiber diameters of PVNF and PANF (4.76) are shown in the inset of (a)-(b). (c)-(d) The TEM image and SAED pattern of PANF (4.76), respectively.

the diameter of PANF (4.76) is ascribed to the uniform distribution of $PAPbI_3$ in PVDF solution which boosts the charge density of the electrospinning solution. Consequently, under an applied high voltage, the filler-contained solution is triggered with immense force in an electrified jet and produces fibers with a reduced diameter than PVNF. The reduced diameter improves the efficacy as well as the mechanical stability of PANF (4.76). The energy dispersive X-ray (EDX) analysis of PANF (4.76) confirms the presence and well distribution of $PAPbI_3$ in the polymer medium. The corresponding constituent elements (C, N, F, Pb, I) embedded in the nanofibers are mapped as depicted in Fig. 7.4a(i-vii).

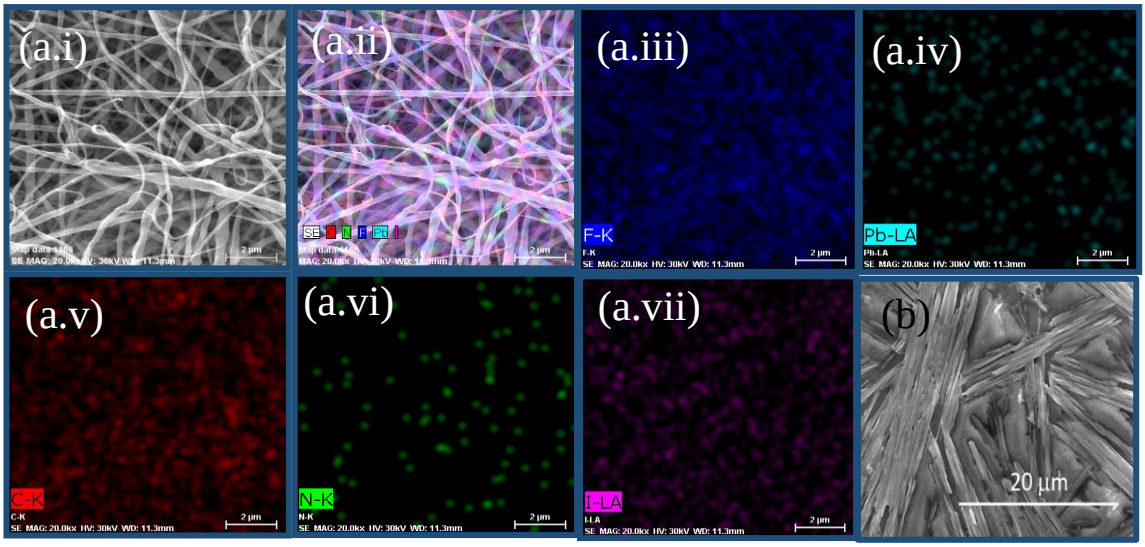

Fig. 7.4a(i-vii) represents the chemical mapping of PANF (4.76), b shows the SEM image of $PAPbI_3$.

The incorporation along with the good dispersion of $PAPbI_3$ in the PVDF matrix is also evident from the TEM image of PANF (4.76) (as shown in Fig. 7.3c). An interesting fact can be observed that the sol-gel processed $PAPbI_3$ possesses a rod-like structure and the average length of the rods is in the micrometer range (as illustrated in Fig. 7.4b). But when the filler is dissolved in DMF in the presence of PVDF, cations, and anions of the filler get separated and PVDF covers the filler as a capping agent. After electrospinning, during the evaporation of the solvent, $PAPbI_3$ recrystallizes and embeds within PVDF, and then PVDF restricts the crystallite size of $PAPbI_3$ in nanometer order. Therefore, the primarily prepared micro crystallite $PAPbI_3$ is finally limited to the nanometer range surrounded by PVDF in PANF (4.76) and improves the β phase efficacy noticeably. The resolved circular pattern and sharp diffraction spots found from the selected area electron diffraction (SAED) pattern as displayed in Fig. 7.3d describe PANF (4.76) as polycrystalline. The planes corresponding to the β phase of PVDF and crystalline $PAPbI_3$ are labeled and thus it supports the co-existence of both. The mechanism of improved crystallinity of PVDF in the presence of $PAPbI_3$ is schematically described in Fig 7.5.

7.4.3. Photoluminescence study

To study the luminescence property, room temperature photoluminescence (PL) of PANF (4.76) was carried out. An emission peak at 558.7 nm is detected in PL spectra as in Fig. 7.6a which suggests that the energy band gap of PANF (4.76) is 2.22 eV. The emission peak of $PAPbI_3$ was found at 546.2 nm as mentioned in the previous report which is fairly close to the

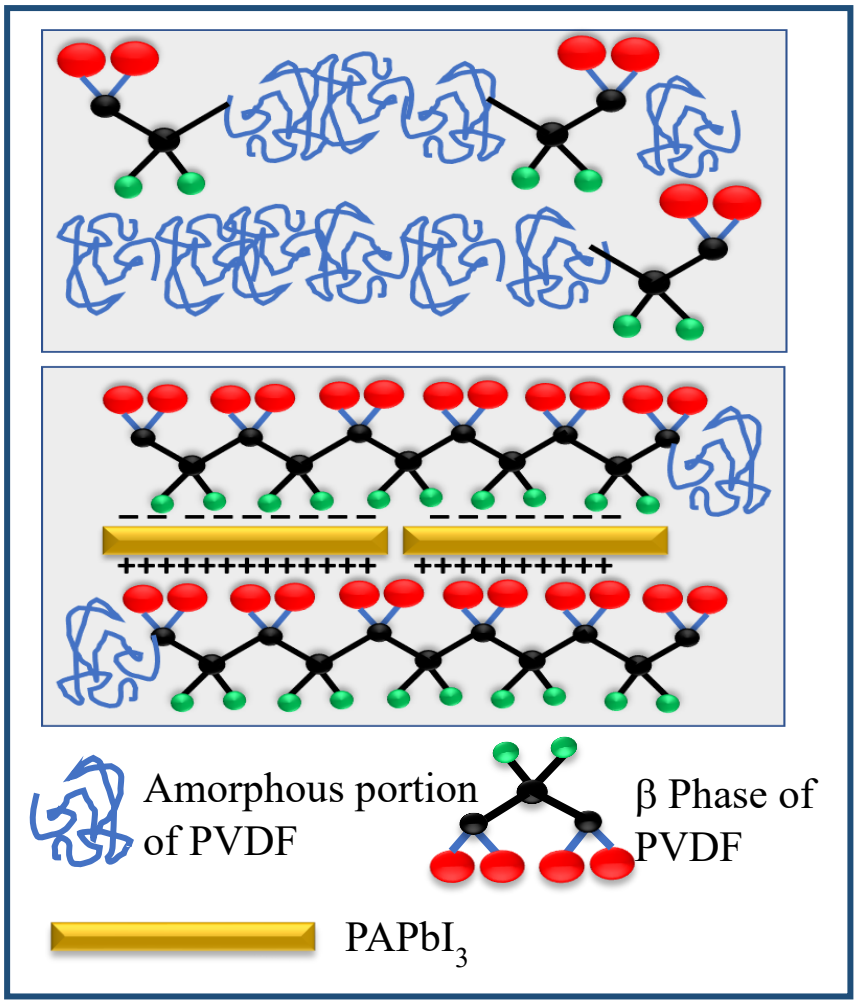

Fig. 7.5 demonstrating schematic diagram of improved crystallinity of PVDF in presence of $PAPbI_3$.

peak obtained for PANF (4.76) [21]. This recommends that the filler being enclosed by PVDF medium retained its original optical behavior. This property, on the other hand, can be utilized in the formation of multi-functional devices.

7.4.4. Thermal stability

The overall change in thermal stabilization on the incorporation of $PAPbI_3$ in PVDF is assessed by the DSC thermograph. The melting point of PVNF is observed as 157.78 ^oC due to the predominant non-polar α phase. The addition of $PAPbI_3$ in pure PVDF introduced the nucleation of β phase adequately and hence the melting point of PANF (4.76) is increased by 1.36 ^oC as shown in Fig. 7.6b. The degree of crystallinity of both nanofibers may be assessed using the following equation [7]

$$x_c\ (\%) = \frac{\Delta H_m}{\Delta H_{100}} \times 100 \qquad (7.5)$$

Here, ΔH_m and ΔH_{100} denote the melting enthalpy of the concerned samples and

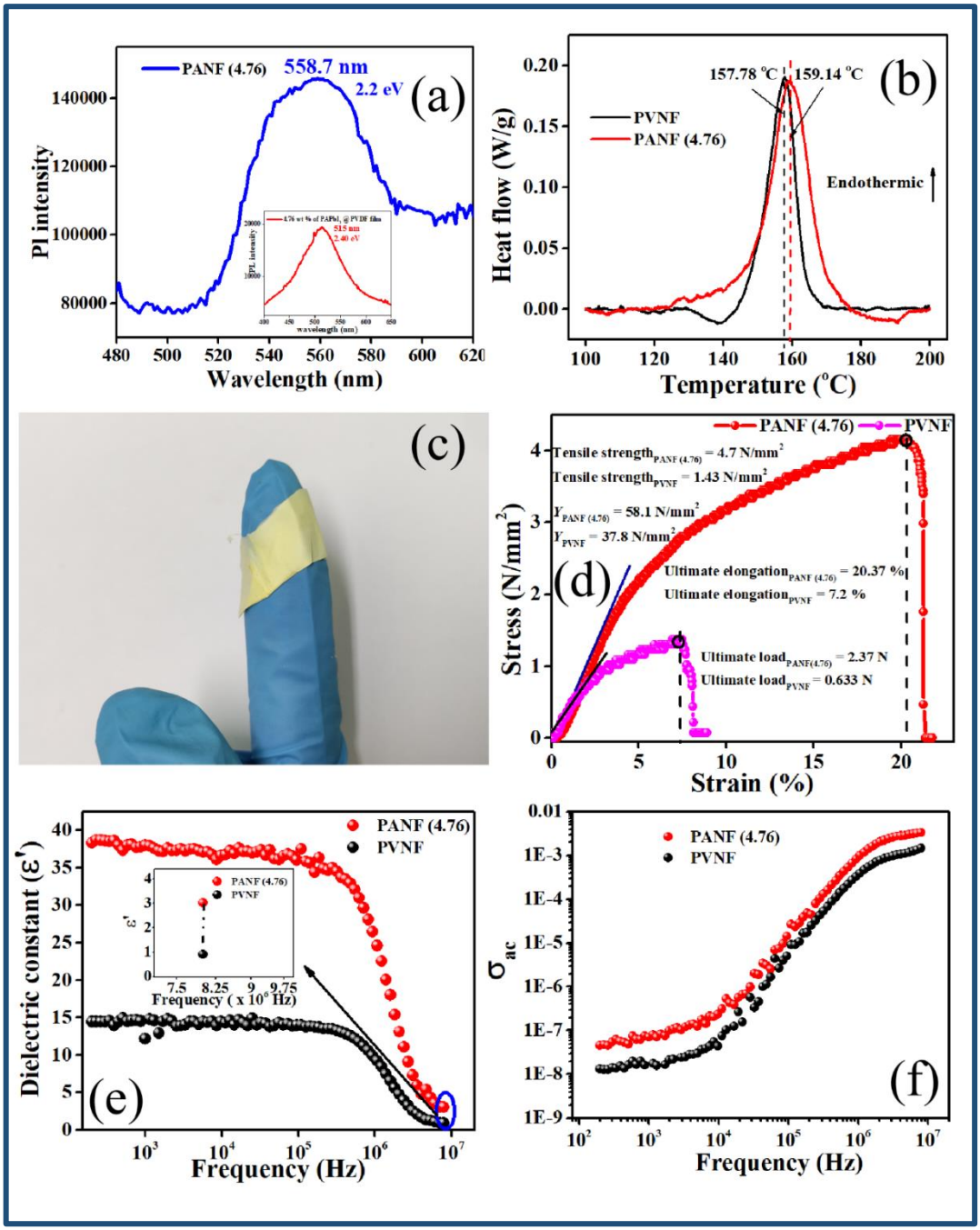

Fig. 7.6. (a) The PL spectra of PANF (4.76). Inset of (a) denotes the PL spectra of 4.76 wt% of $PAPbI_3$@PVDF film. (b) The DSC thermographs of PVNF and PANF (4.76). (c) Photograph illustrating the ultra-flexibility of PANF (4.76) is by wrapping it around a finger. (d) The stress-strain curve of the electro-spun PVNF and PANF (4.76). (e)-(f) the dielectric properties and conductivity studies of PVNF and PANF (4.76), respectively. Inset of (e) shows the change in ε_r in high frequency region.

melting enthalpy of 100 % crystallite PVDF (ΔH_{100} = 104.5 J/g). The x_c (%) of PVNF and PANF (4.76) are evaluated as 25.36 % and 34.5 %, respectively. The improvement of

crystallinity due to the incorporation $PAPbI_3$ agrees with the outcome of the XRD and FTIR investigation.

7.4.5. Investigation of mechanical and electrical properties

The elastic properties of the nanofibers are assessed by the stress-strain relationship as displayed in Fig. 7.6d. The values of Young's modulus (Y) of PANF (4.76) and PVNF are calculated to be 58.1 MPa and 37.8 MPa respectively. Possessing a higher value of Y, PANF (4.76) attains better mechanical stability. Furthermore, the ultimate elongation at break load improves from 7.2 % (for PVNF) to 20.37 % (for PANF (4.76)), resulting PANF (4.76) with much better mechanical toughness. The interaction between PVDF and 4.76 wt% of $PAPbI_3$ yields a significant improvement in the tensile strength and makes it an appropriate choice for mechanical energy harvesting. A digital photograph of wrapping a piece of PANF (4.76) around a finger is shown in Fig. 7.6c demonstrating its desired ultra-flexibility.

The electrical behavior of the nanofibers is investigated at room temperature in the frequency range $200\,Hz \leq f \leq 8MHz$. Figure 7.6e demonstrates that the real part of permittivity (ε_r), which is enhanced by 2.53 times due to 4.76 wt% $PAPbI_3$ doping in pure PVDF in the low-frequency region. The large value of the dielectric constant (ε_r), in the low-frequency domain owing to the interfacial polarization effect as explained by Maxwell Wagner polarization [25]. Charge carriers get trapped at the interface of $PAPbI_3$ grain surrounded by the poorly conducting grain boundary of PVDF. The molecules of $PAPbI_3$ having permanent dipole moment can change their orientation along the direction of the applied field in low frequency region resulting in a high dielectric constant in that region. With the rise in frequency, the dipoles become unable to follow the direction of the applied field and hence dielectric constant gradually decreases. With the increase in frequency, ε_r of both samples, decreases gradually. Interestingly, even at high frequency, the value of ε_r of PANF (4.76) is higher than that of PVNF as depicted in the inset of Fig. 7.6e. The conductivity of PANF (4.76) is found to increase significantly than that of PVNF as displayed in Fig. 7.6f. In the low-frequency region, the flattened, frequency-independent portion of the curves refers to the DC conductivity whereas the conductivity in the high-frequency domain is attributed to AC conductivity. It can also be observed that DC conductivity for both samples is very low. The

interaction between the charges of the filler and the PVDF results in the improvement of both ε_r and conductivity.

7.4.6. Piezoelectric response

To examine the piezoelectric performance, a piezoelectric nanogenerator employing PANF (4.76) as piezo-active material (PANG) was fabricated. The schematic layer-by-layer sandwich structure of PANG is exhibited in Fig. 7.7a. Another nanogenerator using PVNF was also designed (RNG) to perform a comparative study on their respective piezo responses. Figures 7.7b, c, d, and e exhibit that PANG yielded 60 V open circuit voltage (V_{OC}) and 27.54 μA short

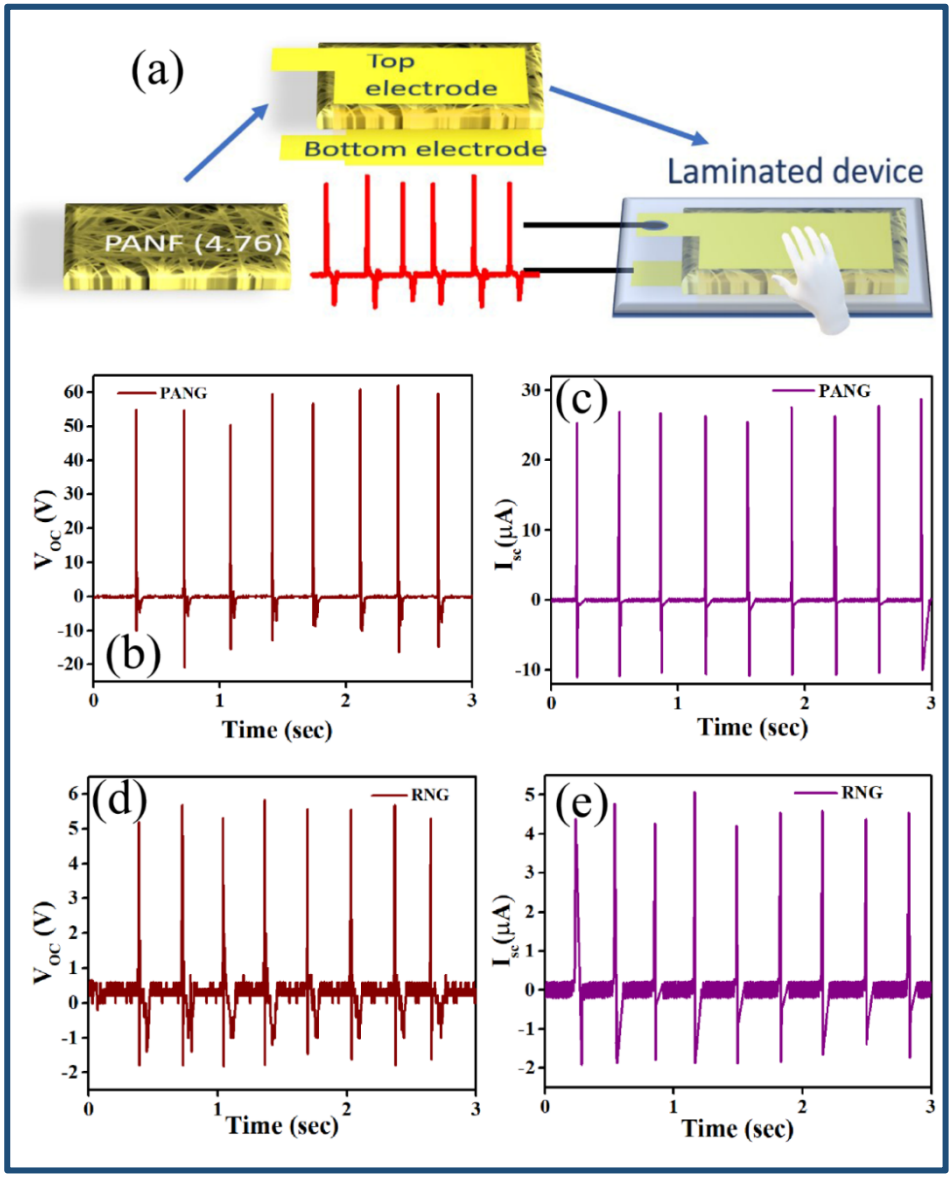

Fig. 7.7. (a) The schematic diagram of device fabrication. (b)-(e) The variation of open circuit voltage and short circuit current of PANG and RNG, respectively as a function of time under hammering with free hand.

circuit current (I_{SC}) (current density 7 μA/cm^2) under repetitive hammering with a free hand in

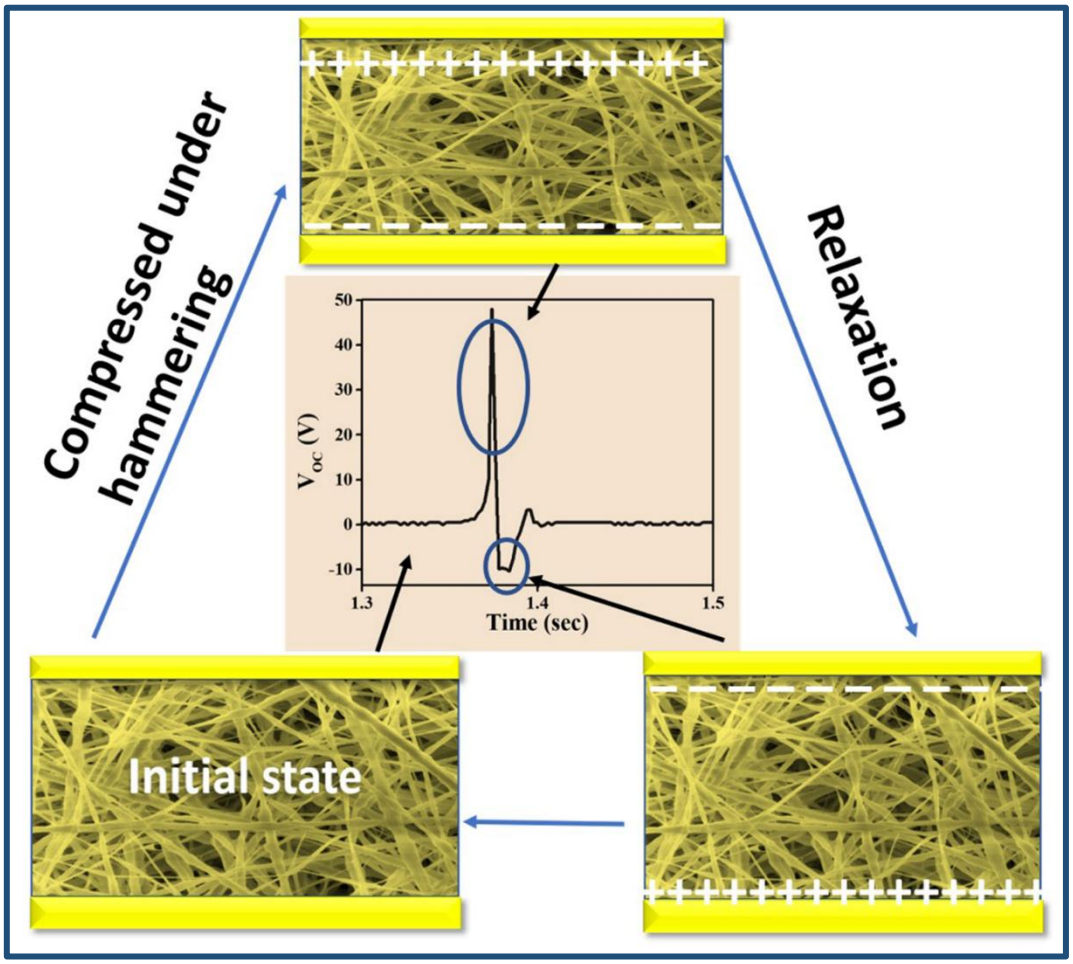

Figure 7.8. The working mechanism of PANG.

a vertical direction whereas RNG under similar pressure in an identical direction provides 5 V (V_{OC}) and 5 μA (I_{SC}). The improved electroactivity of PANF (4.76) reflected in the piezo response as PANG produces 12 times higher V_{OC} voltage and 5 times higher I_{SC} than that of RNG under identical mechanical strain. This occurs due to the enhancement of the β phase of PVDF in the PANF (4.76). A possible reason behind this phenomenon is the generation of potential differences due to temporal distortions under applied mechanical strain. To compensate for this potential developed by the dipoles, an electrical potential difference may occur between the two electrodes that have been delivered as the output signal. On removal of this external strain, the accumulated charges on opposite sides of the nanofibers flow back in the direction opposite to the accumulation process, thus generating an electric impulse in the reverse direction. The working mechanism of the nanogenerator is demonstrated in Fig. 7.8. A comparative study on the output voltage, current, and power density produced by the composite of different lead-based organo-halide perovskites and PVDF are enlisted in table 7.1. It has

been observed that under free-hand hammering, the output response of PANG is satisfactorily large. The asymmetry in the obtained positive and negative peaks of V_{OC} and I_{SC} with time is

Table 7.1: A comparative study of output open circuit voltage (V_{OC}), short circuit current (I_{SC}), generated power of different organic-inorganic hybrid perovskite filler used in PNGs. NA refers to "Not Available".

Filler	Applied pressure	V_{OC} (V)	I_{SC} (Current / Current density)	Output power / Power density	References
$MAPbI_3$	50 N	17.8	2.1 μA/cm^2	NA	[15]
$MAPb_xFe_{1-x}I_3$ x = 0.07	NA	4.52	0.50 μA/cm^2	NA	[36]
$MAPbI_3$	NA	2.7	140 nA/ cm^2	NA	[37]
$FAPbBr_2I$	0.5 MPa	85	30 μA	10 μW/cm^2	[20]
$FAPbBr_3$	0.5 MPa	30	6.2 μA/cm^2	27.4 μW/ cm^2	[17]
$FAPbBr_3$	0.5 MPa	8.5	3.8 μA/cm^2	12 μW/ cm^2	[18]
$MAPbI_3$	Finger tapping	5	60 nA	0.28 μW/ cm^2	[16]
$PAPbI_3$	10 N	60	7 μA/cm^2	9.8 mW/m^2	Present work

ascribed to the difference between the applied external force on the device at the time of approaching and the restoring force of the device at the time of releasing. The charge (Q) produced by PANG during repeated hammering with the free hand (an applied force of 10 N, measured by load cell) is evaluated as 2.68 nC by integrating I_{SC} per unit area ($Q = \int J_{SC}\, dt$) in the positive half which contributes to the piezoelectric coefficient ($|d_{33}| = \frac{Q}{F}$) [26]. The value of $|\widetilde{d_{33}}|$ is calculated as 268 pC/N for PANG and 32.4 pC/N for RNG using the aforesaid equation. This calculated value of $|\widetilde{d_{33}}|$ may be overestimated due to some tribo-electrification effect during the attachment of electrodes on both sides of the devices. Therefore the piezoelectric coefficient ($|d_{33}|$) of PANG and RNG are measured directly with a d_{33} meter. The value of d_{33} for PANG is obtained as 138 pC/N which is still strikingly high [27,28] compared to that of RNG (24.4 pC/N). As a consequence, the voltage conversion coefficient ($g_{33} = \frac{d_{33}}{\varepsilon_r \varepsilon_0}$, [29] ε_0 refers to the permittivity of free space, ε_r denotes the dielectric constant (37.8 for PANF (4.76) and 15 for PVNF at 1 KHz)) is also substantially enhanced for PANG (0.41 Vm/N) as compared to RNG (0.18 Vm/N). Finally, the piezoelectric figure of merit ($F_O M_P \sim d_{33} \times g_{33}$) [30] is assessed to be 5.658 × 10^{-11} Pa^{-1} for PANG which is 12.88 times than that of RNG (4.392 × 10^{-12} Pa^{-1}). This outcome ensures the credibility of PANG with PANF (4.76) as high performing piezoelectric generator.

Furthermore, the piezoelectric sensitivity of PANG was assessed by repeated hammering with a few lightweight objects such as a piece of thermocol, a piece of folded tissue, a pen, etc. at a fixed distance of 5 cm from the device. Figure 7.9a exhibits the corresponding voltages generated as a function of time and the insets show the static state of the objects on PANG. The consistent responses of PANG on the applications of these light forces confirm that this designed NG is ultrasensitive, stable, and a potential candidate for nano-tactile sensing. The sensitivity of PANG under the application of several forces ranging from 0.015 N to 14 N is depicted in Fig. 7.9(b). The responding capability under different mechanical provocations is enumerated by mechano-sensitivity (S_M) which can be expressed as $\frac{\Delta V_{OC}}{\Delta F}$ [30]. As observed

Table 7.2: A comparative study on the mechano-sensitivity exhibited by different PNGs. NA refers to "Not Available"

Structure	Composite materials	Mechano-sensitivity	References
Nanowire	P(VDF-TrFE)	458 mV/N	[38]
Microfiber	P(VDF-TrFE)	269.4 mV/N	[39]
Micropiller	PVDF-TrFe/$BaTiO_3$	257.9 mV/N	[40]
Nanofiber	PVDF	60.5 mV/N	[41]
Triboelectric nanogenerator		28 mV/N	[42]
Nanofiber	Pt-PVDF	600 mV/N	[30]
NA	BTS-GFF/PVDF	1.23 V/N	[43]
Necklace like particle chain	PZT	1.13 V/N	[44]
Nanofiber	$C_3H_7NH_3PbI_3$-PVDF	6.3 V/N-12.12 V/N	Present work

in Fig. 7.9b, two distinct linear response curves with distinct slopes in low and high forces regions are obtained. The values of S_M in low-force and high-force regions are 6.3 V/N and 12.12 V/N respectively. A comparative study based on the previous reports was performed and briefed in Table 7.2. It is noteworthy that the mechano-sensitivity of PANG is far superior to piezo-active films made of PVDF and its copolymers, piezo-active nanofibers, nanowires, etc. The exotic value of S_M further approves the potential of PANG as a smart, lightweight, nano tactile sensor cum power generator. In addition, the bending and twisting of PANG not only generate a response as displayed in Fig. 7.9c, and 7.9d but also exhibit its flexibility. Such flexibility suggests that PANG can be employed as a wearable mechanical energy scavenger. The upper surface of PANG was rubbed with a finger continually from one end to the other end of the device and the result is depicted in Fig. 7.9e. At room temperature, PANG was

attached to the outer surface of a beaker full of water and subjected to an ultrasonic probe

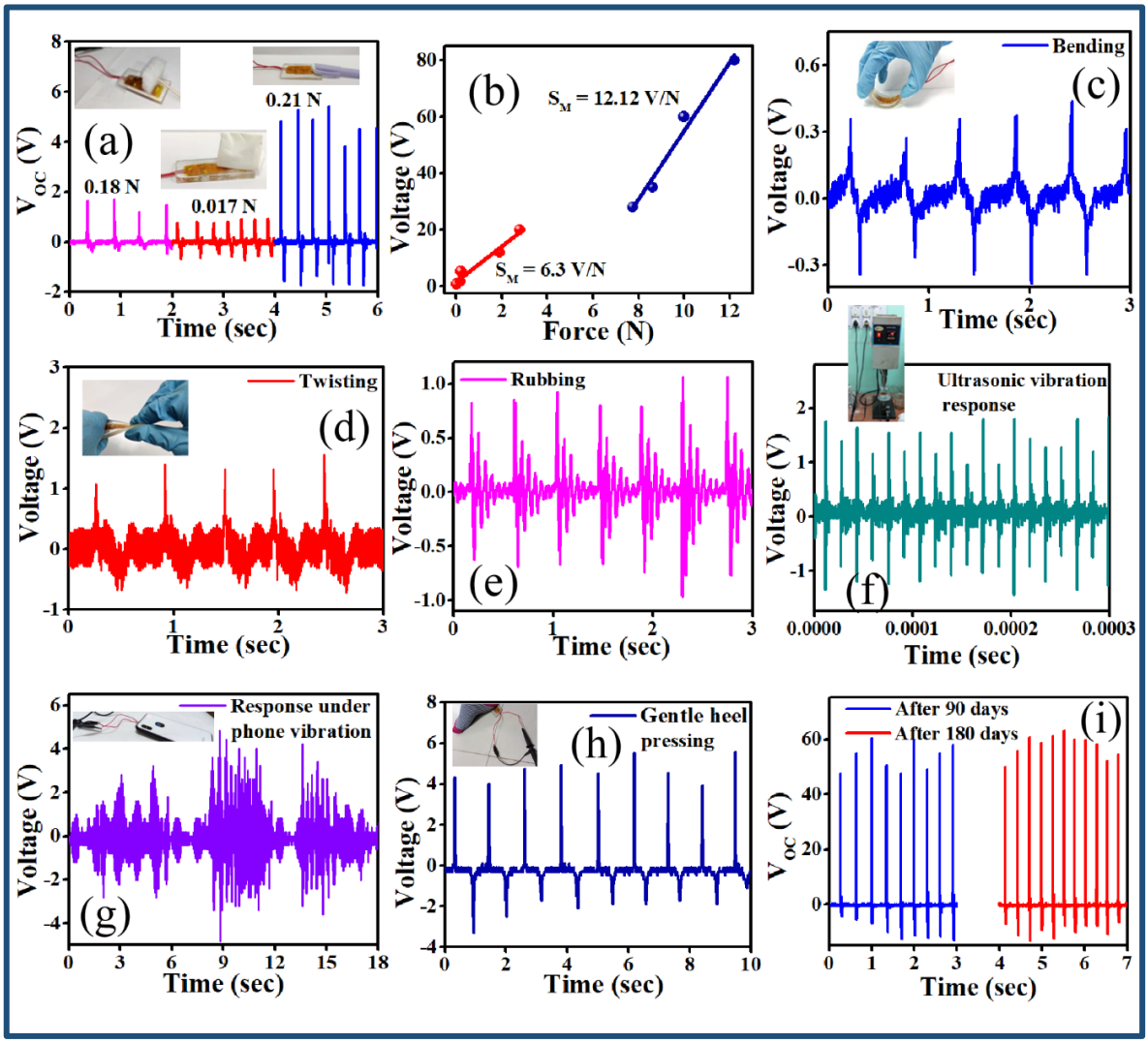

Fig. 7.9. (a) The plot of voltage responses under different applied force. Insets of (a) are the digital photographs of the device under various forces. (b) The mechano-sensitivity of PANG. (c)-(e) The voltage responses as a function of time while bending, twisting and rubbing the PANG, respectively. (f)-(g) The sensitivity of PANG under ultrasonic vibration and phone vibration, respectively. Digital photograph of ultrasonic vibration is shown in the inset of (f). (h) The voltage response of PANG under gentle heel pressing. Corresponding digital photographs are shown in the insets of respective Figs. (i) The response of PANG under hammering with hand after 3 and 6 months of fabrication of the device.

sonicator to detect the ultrasonic vibration. The voltage response is exhibited in Fig. 7.9f. Moreover, the generated voltage of PANG under phone vibration is exhibited in Fig. 7.9g. The vibration sensing ability of PANG recommends it as a potential candidate as a vibration sensor, even in the ultrasonic range. The output response of PANG under gentle heel pressing is also observed and shown in Fig. 7.9h. Moreover, the open circuit voltage produced by PANG

(illustrated in Fig. 7.9i) under free hand imparting after 3 and 6 months of fabrication exhibits significant stability of the device.

To compute the effective electric output power, PANG was connected (inset of Fig. 7.10b) to various external load resistances ranging from 3KΩ to 12.5MΩ. The output power density (P) is calculated using the relations (7.6) and (7.7).

$$I_L = \frac{V_{pp}}{A \times R_L} \tag{7.6}$$

$$P = V_{pp} \times I_L \tag{7.7}$$

Here, V_{pp} is the peak-to-peak voltage across each load resistance (R_L), I_L is the corresponding current density and A is the effective contact area. The variation of output voltage (V_L) and power density with the load resistance is illustrated in Fig. 7.10b and 7.10c, respectively. The maximum output power density of 9.81 mW/m^2 is attained at 4.03 MΩ. Therefore, the internal resistance of PANG (R_{int}) may be considered as 4.03 MΩ using the maximum power transfer theorem [31]. The energy conversion efficiency (η_{piezo}) of PANG can be estimated as the ratio of generated electrical energy to applied mechanical energy i.e. $\eta_{piezo} = \frac{E_{elec}}{E_{mech}} \times 100$ %. The generated electrical energy per cycle across R_{int} (= 4.03 MΩ), is given by $E_{elec} = \int \frac{V(t)^2}{R_{int}}\, dt$, where $V(t)$ is the instantaneous voltage response as shown in Fig. 7.7b.) is estimated as 282 nJ. The applied mechanical energy per cycle of under hammering with free hand can be estimated as $E_{mech} = F\varepsilon L$, where F = 10 N, $\varepsilon = \frac{\sigma_a}{Y} = \frac{0.03\ MP_a}{58.1\ MP_a} = 4.47\times10^{-4}$, L = 150 μM, the thickness of the device [29]. E_{mech} for PANG comes out to be 671 nJ. Thus, the appraised value of η_{piezo} of fabricated PANG is 42.03 % which is not only greater as compared to several commercials along with experiment-derived PNGs, but also proves its superiority in the mechanical energy harvesting segment [17,30,32,33].

To utilize PANG as mechanical energy garner, the device was connected with a full bridge rectifier circuit as in Fig. 7.10a. This instantaneous output power, generated under the hammering with a free hand, is adequate to illuminate several blue and green LEDs without any peripheral storage system (inset of Fig. 7.10c). Here, in PANG, PANF (4.76) acts as a production unit of charges (q) connected in parallel with internal capacitance (C_i) and resistance (R_i). Moreover, on pressing with hand, the instantaneous produced electricity was stored in several commercially available external capacitors. As displayed in Fig. 7.10d, the

momentary response of the 2.2 μF capacitor reached 5.3 V (V_C) in 74 sec. The corresponding

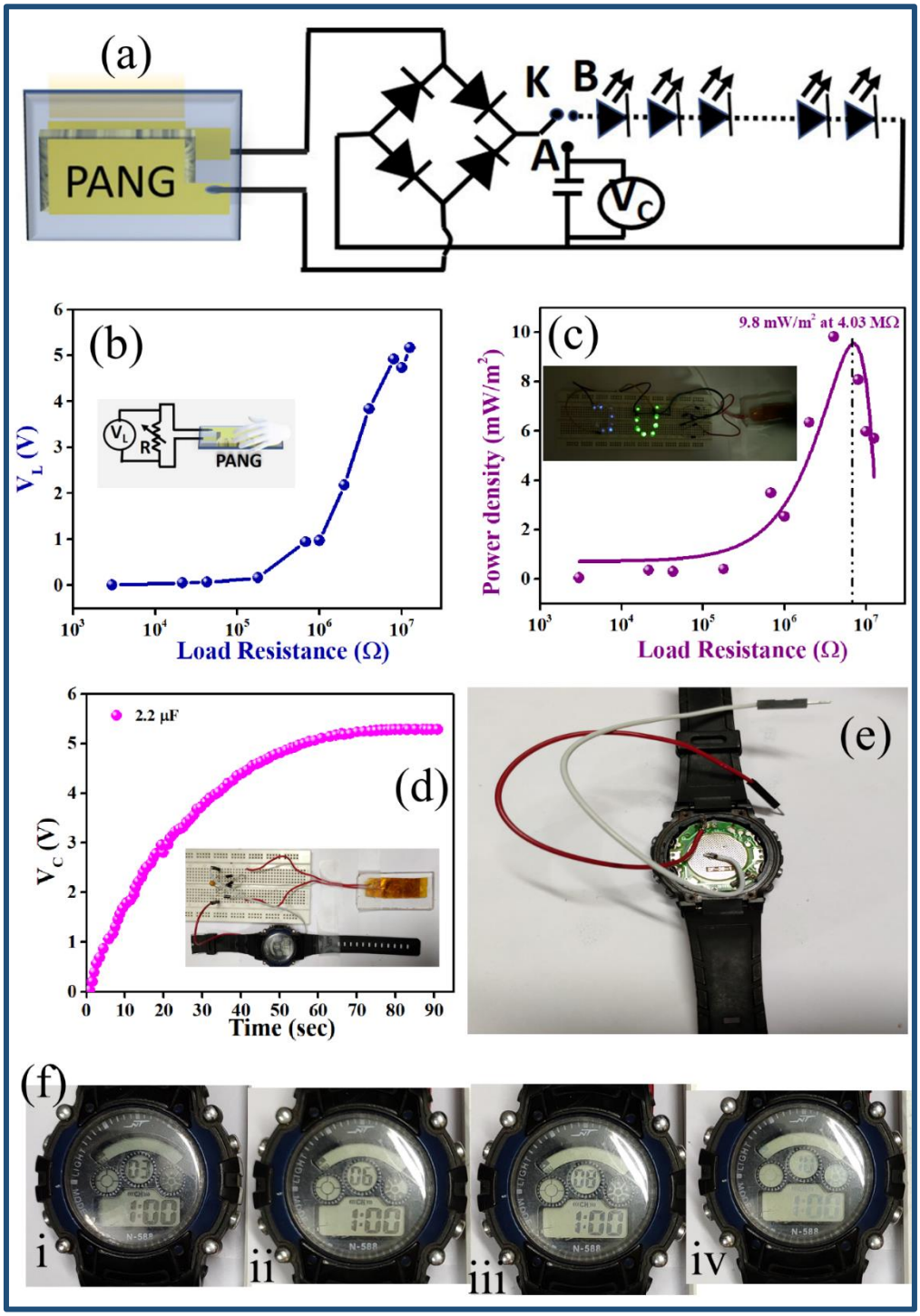

Fig. 7.10. (a) the bridge rectifier circuit designed to light up LEDs as well as to charge the capacitors. (b)-(c) the plots of output load voltage and output power density across various load resistances, respectively. Insets of (b) and (c) are the schematic circuit of PANG with different load resistances and the glowing LEDs showing "JU", respectively. (d) The response of the capacitors as a function of time. (e)-(f) The powering of wrist watch with charged capacitors.

energy stored in the capacitor ($E = \frac{1}{2}CV_C^2$) [2,25,30] is 30.9 μJ which has been further used to power a digital wristwatch as demonstrated in the inset of Fig. 7.10d. The connection of wrist watch with the charged capacitor is illustrated in Fig. 7.10e. The wristwatch was powered up for 10 sec (Fig. 7.10f). Following the RC circuit model ($\tau = R_{int}C_T$, $C_T = C_i + C$), τ is found to be 27.2 sec, and the total capacitance of the circuit (C_T) is estimated to be 6.74 μF. Thus, the internal capacitance of PANG (C_i) is calculated as 4.54 μF. This combination of internal resistance with high internal capacitance makes PANG an extremely potential entrant in the domain of self-powered devices. All of these measurements were carried out using only one PANG device which ensures the durability of the designed NG.

7.4.7. Photo piezo-active response

The intense wide absorption spectrum as in Fig. 7.6a indicates that $PAPbI_3$ may possess photo-response characteristics. Thus, a photodetector using optically active $PAPbI_3$ (4.76) @ PVDF film has been fabricated as described in Fig. 7.11a and the current-voltage (I-V) characteristic of the photodetector (PAPPEG) under dark and light condition was recorded as shown in Fig. 7.11b. To investigate the piezo response of this photodetector (PAPPEG), the device is customized with ITO coated PET and Al foil as two electrodes. The thickness of PAPPEG device is 140 μm. The I-V characteristic observed here under dark is almost linear following the ohmic response, whereas that under illuminated conditions is non-linear. This non-linearity is attributed to the possible Schottky barrier formation at the metal-semiconductor junction. When exposed to light, $PAPbI_3$ perovskite in the $PAPbI_3$ (4.76) @ PVDF film absorbs the incident photons and generates electron-hole pairs. Under the influence of external bias voltage, the excitons split up to free electrons and holes that move outer electrodes. These photo carriers take part in the generation of photocurrent. However, the generated current in both dark and illuminated conditions is low. It might be due to the insulating behavior of PVDF which limits the charge flow by breaking the interconnected network of semiconducting $PAPbI_3$ (4.76). The difference in magnitude of photocurrent in the presence of the light of intensity ~ 80 mW/cm^2 at any bias voltage is significant. It can be observed in Fig. 7.11b that the current is shifted from zero crossing in both dark and illumination. To get more clearance, hysteresis loops of the I-V curves in both dark and illuminated conditions are measured. The non-zero crossing I-V hysteresis behaviour as depicted in Fig. 7.11c. suggests the capacitive response of the device [34,35]. This capacitive effect which arises due to the charge accumulation at the interface between electrodes and the active layer is found to increase under irradiation.

Therefore, when the external voltage reduces to 0, residual current still appears due to the

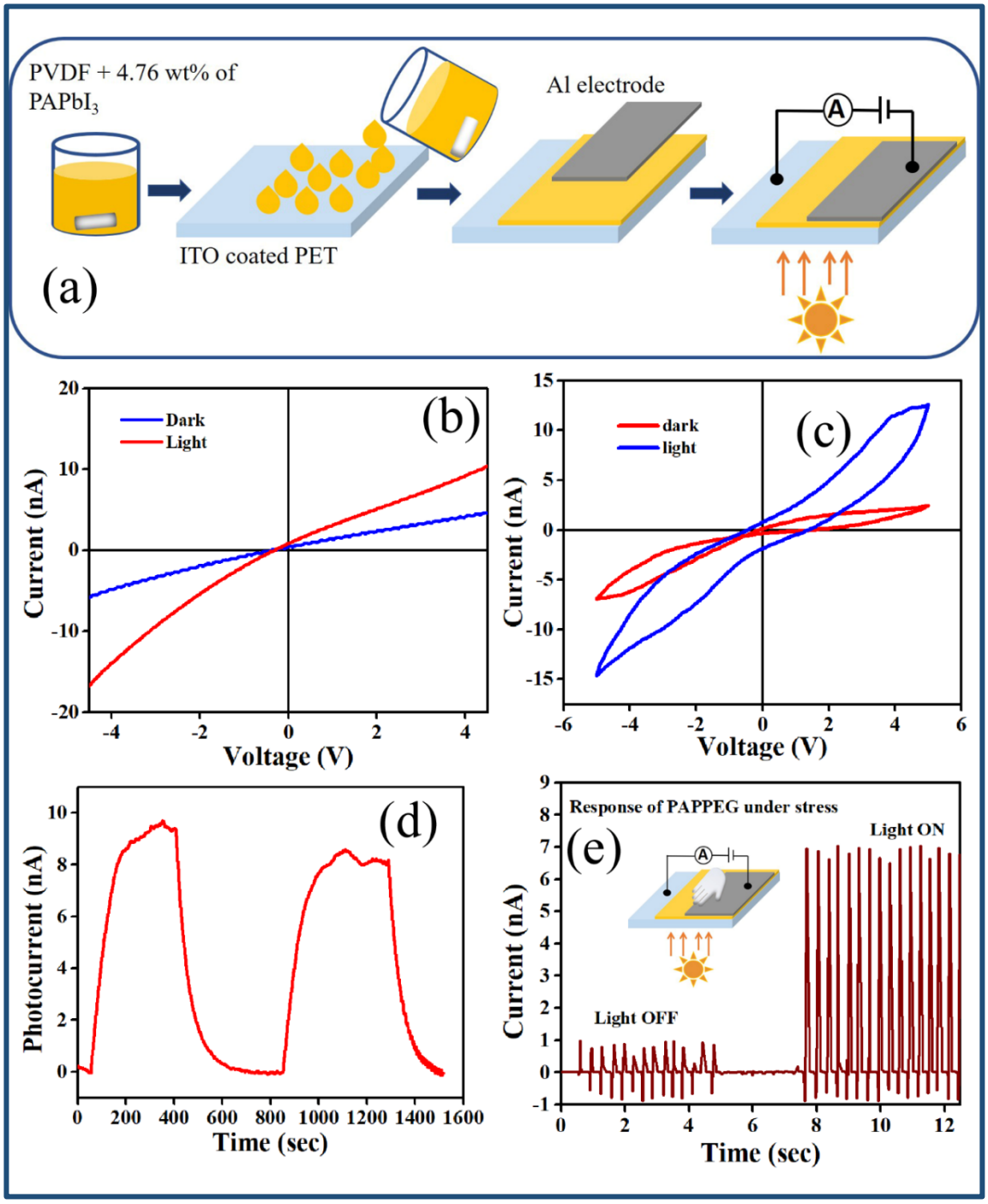

Fig. 7.11. (a) The step-by-step fabrication process of PAPPEG. In PAPPEG, (b) The variation of current with voltage under both dark and illuminated conditions, (c) The hysteresis loop of I-V both in dark and illumination, (d) The response of photocurrent with time, (e) The response of current in dark and illumination under applied stress and inset of (e) is the corresponding schematic diagram.

capacitance effect.

Figure 7.11d depicts the photocurrent as a function of time (I-t) by illuminating the photodetector (PAPPEG) with a white light of intensity ~ 80 mW/cm^2, keeping the bias voltage between two electrodes constant at 5 V. Light illumination was switched on and off periodically with an interval of ~ 350 s through shutter to study the photoresponse of the photodetector. The piezo response is enhanced significantly on the illumination of white light as illustrated clearly in Fig. 7.11e. The short circuit current I_{SC}, measured under dark conditions is smaller than that reported in Fig. 7.8c. This is not only due to the different morphology (e.g. nanofibers and film) of the composite $PAPbI_3$ (4.76)@PVDF present in the PANG and PAPPEG, respectively but also absolutely the different measurement conditions. The piezo response of PAPPEG is measured under gentle finger touch whereas that of PANG is measured under hammering with a free hand.

7.5. Conclusion

$PAPbI_3$ was prepared by the sol-gel method and then incorporated into the PVDF matrix to synthesize electrospun nanofibers (PANF). PANF (4.76) not only enhanced dramatically the degree of crystallinity of PVDF but also transformed solely the non-polar α phase to the polar β phase. This conversion is reflected in the response of PANG under hammering with a free hand in comparison with RNG. The optical properties, tensile strength, thermal stability, and electrical properties of PANF (4.76) are analyzed and found to improve substantially. The PANG exhibits enhanced piezoelectric coefficient, voltage conversion efficiency, and piezoelectric figure of merit. Moreover, PANG shows superior mechano-sensitivity along with energy conversion efficiency. Furthermore, the ultra-sensitive nanogenerator is proficient in ultra-quick charging of various capacitors under external mechanical stimuli which assures its potential as a self-driven, ultra-fast power generator. The $PAPbI_3$ (4.76)@PVDF composite also possesses photo-active characteristics in the presence of white light. The I-V characteristics of the photodetector under both dark and illumination and in the presence of mechanical strain suggest its utility as a photodetector. The overall studies conclude that the proposed composite can be an appropriate choice for designing a hybrid device for mechanical energy harvesting with intended photodetection.

References

[1] S. Bairagi, S. Ghosh, S.W. Ali, A fully sustainable, self-poled, bio-waste based piezoelectric nanogenerator: electricity generation from pomelo fruit membrane, Sci. Rep. 10 (2020) 12121. https://doi.org/10.1038/s41598-020-68751-3.

[2] J. Ma, J. Zhu, P. Ma, Y. Jie, Z.L. Wang, X. Cao, Fish Bladder Film-Based Triboelectric Nanogenerator for Noncontact Position Monitoring, ACS Energy Lett. 5 (2020) 3005–3011. https://doi.org/10.1021/acsenergylett.0c01062.

[3] W. Wu, S. Bai, M. Yuan, Y. Qin, Z.L. Wang, T. Jing, Lead Zirconate Titanate Nanowire Textile Nanogenerator for Wearable Energy-Harvesting and Self-Powered Devices, ACS Nano. 6 (2012) 6231–6235. https://doi.org/10.1021/nn3016585.

[4] C. Huang, J. Song, W. Lee, Y. Ding, Z. Gao, Y. Hao, L.-J. Chen, Z.L. Wang, GaN Nanowire Arrays for High-Output Nanogenerators, J. Am. Chem. Soc. 132 (2010) 4766–4771. https://doi.org/10.1021/ja909863a.

[5] K.-I. Park, J.H. Son, G.-T. Hwang, C.K. Jeong, J. Ryu, M. Koo, I. Choi, S.H. Lee, M. Byun, Z.L. Wang, K.J. Lee, Highly-Efficient, Flexible Piezoelectric PZT Thin Film Nanogenerator on Plastic Substrates, Adv. Mater. 26 (2014) 2514–2520. https://doi.org/10.1002/adma.201305659.

[6] H. Parangusan, D. Ponnamma, M. Al Ali AlMaadeed, Flexible tri-layer piezoelectric nanogenerator based on PVDF-HFP/Ni-doped ZnO nanocomposites, RSC Adv. 7 (2017) 50156–50165. https://doi.org/10.1039/C7RA10223B.

[7] H. Parangusan, D. Ponnamma, M.A.A. Al-Maadeed, Stretchable Electrospun PVDF-HFP/Co-ZnO Nanofibers as Piezoelectric Nanogenerators, Sci. Rep. 8 (2018) 754. https://doi.org/10.1038/s41598-017-19082-3.

[8] H. Gao, P.T. Minh, H. Wang, S. Minko, J. Locklin, T. Nguyen, S. Sharma, High-performance flexible yarn for wearable piezoelectric nanogenerators, Smart Mater. Struct. 27 (2018) 095018. https://doi.org/10.1088/1361-665X/aad718.

[9] L. Li, M. Zhang, M. Rong, W. Ruan, Studies on the transformation process of PVDF from α to β phase by stretching, RSC Adv. 4 (2014) 3938–3943. https://doi.org/10.1039/C3RA45134H.

[10] T. Roopa, H.N. Murthy, D. Harish, A. Jain, G. Angadi, Properties of PVDF films stretched in machine direction, Polym. Polym. Compos. 29 (2021) 198–206. https://doi.org/10.1177/0967391120910592.

[11] D. Yang, Y. Chen, β-phase formation of poly(vinylidene fluoride) from the melt induced by quenching, J. Mater. Sci. Lett. 6 (1987) 599–603. https://doi.org/10.1007/BF01739296.

[12] M. Benz, W.B. Euler, O.J. Gregory, The Role of Solution Phase Water on the Deposition of Thin Films of Poly(vinylidene fluoride), Macromolecules. 35 (2002) 2682–2688. https://doi.org/10.1021/ma011744f.

[13] P. Sadhukhan, S. Kundu, A. Roy, A. Ray, P. Maji, H. Dutta, S.K. Pradhan, S. Das, Solvent-Free Solid-State Synthesis of High Yield Mixed Halide Perovskites for Easily Tunable Composition and Band Gap, Cryst. Growth Des. 18 (2018) 3428–3432. https://doi.org/10.1021/acs.cgd.8b00137.

[14] P. Sengupta, P. Sadhukhan, A. Ray, S. Mal, A. Singh, R. Ray, S. Bhattacharyya, S. Das, Influence of activation energy on charge conduction mechanism and giant dielectric relaxation of sol-gel derived $C_3H_7NH_3PbBr_3$ perovskite; Act as high performing UV photodetector, J. Alloys Compd. 892 (2022) 162216. https://doi.org/10.1016/j.jallcom.2021.162216.

[15] V. Jella, S. Ippili, J.-H. Eom, J. Choi, S.-G. Yoon, Enhanced output performance of a flexible piezoelectric energy harvester based on stable $MAPbI_3$-PVDF composite films, Nano Energy. 53 (2018) 46–56. https://doi.org/10.1016/j.nanoen.2018.08.033.

[16] A. Sultana, M.M. Alam, P. Sadhukhan, U.K. Ghorai, S. Das, T.R. Middya, D. Mandal, Organo-lead halide perovskite regulated green light emitting poly(vinylidene fluoride) electrospun nanofiber mat and its potential utility for ambient mechanical energy harvesting application, Nano Energy. 49 (2018) 380–392. https://doi.org/10.1016/j.nanoen.2018.04.057.

[17] R. Ding, X. Zhang, G. Chen, H. Wang, R. Kishor, J. Xiao, F. Gao, K. Zeng, X. Chen, X.W. Sun, Y. Zheng, High-performance piezoelectric nanogenerators composed of formamidinium lead halide perovskite nanoparticles and poly(vinylidene fluoride), Nano Energy. 37 (2017) 126–135. https://doi.org/10.1016/j.nanoen.2017.05.010.

[18] R. Ding, H. Liu, X. Zhang, J. Xiao, R. Kishor, H. Sun, B. Zhu, G. Chen, F. Gao, X. Feng, J. Chen, X. Chen, X. Sun, Y. Zheng, Flexible Piezoelectric Nanocomposite Generators Based

on Formamidinium Lead Halide Perovskite Nanoparticles, Adv. Funct. Mater. 26 (2016) 7708–7716. https://doi.org/10.1002/adfm.201602634.

[19] R. Pandey, G. SB, S. Grover, S.K. Singh, A. Kadam, S. Ogale, U. V Waghmare, V.R. Rao, D. Kabra, Microscopic Origin of Piezoelectricity in Lead-Free Halide Perovskite: Application in Nanogenerator Design, ACS Energy Lett. 4 (2019) 1004–1011. https://doi.org/10.1021/acsenergylett.9b00323.

[20] A.A. Khan, M.M. Rana, G. Huang, N. Mei, R. Saritas, B. Wen, S. Zhang, P. Voss, E. Rahman, Z. Leonenko, S. Islam, D. Ban, Maximizing piezoelectricity by self-assembled highly porous perovskite–polymer composite films to enable the internet of things, J. Mater. Chem. A. 8 (2020) 13619–13629. https://doi.org/10.1039/D0TA03416A.

[21] P. Sengupta, P. Sadhukhan, A. Ray, R. Ray, S. Bhattacharyya, S. Das, Temperature and frequency dependent dielectric response of $C_3H_7NH_3PbI_3$: A new hybrid perovskite, J. Appl. Phys. 127 (2020) 204103. https://doi.org/10.1063/1.5142810.

[22] C. Wang, J. Zhang, S. Gong, K. Ren, Significantly enhanced breakdown field for core-shell structured poly(vinylidene fluoride-hexafluoropropylene)/TiO_2 nanocomposites for ultra-high energy density capacitor applications, J. Appl. Phys. 124 (2018) 154103. https://doi.org/10.1063/1.5049405.

[23] J. Zhang, X. Du, C. Wang, K. Ren, Poly(vinylidene fluoride-hexafluoropropylene) based blend film for ultrahigh energy density capacitor applications, J. Phys. D. Appl. Phys. 51 (2018) 255306. https://doi.org/10.1088/1361-6463/aac55f.

[24] B. Jaleh, A. Jabbari, Evaluation of reduced graphene oxide/ZnO effect on properties of PVDF nanocomposite films, Appl. Surf. Sci. 320 (2014) 339–347. https://doi.org/10.1016/j.apsusc.2014.09.030.

[25] P. Sengupta, R. Ray, Tailoring of dielectric and transport properties of $C_3H_7NH_3PbI_xBr_{3-x}$, Mater. Lett. 302 (2021) 130456. https://doi.org/10.1016/j.matlet.2021.130456.

[26] A. Sultana, S.K. Ghosh, M.M. Alam, P. Sadhukhan, K. Roy, M. Xie, C.R. Bowen, S. Sarkar, S. Das, T.R. Middya, D. Mandal, Methylammonium Lead Iodide Incorporated Poly(vinylidene fluoride) Nanofibers for Flexible Piezoelectric–Pyroelectric Nanogenerator, ACS Appl. Mater. Interfaces. 11 (2019) 27279–27287. https://doi.org/10.1021/acsami.9b04812.

[27] A.A. Khan, G. Huang, M.M. Rana, N. Mei, M. Biondi, S. Rassel, N. Tanguy, B. Sun, Z. Leonenko, N. Yan, C. Wang, S. Xu, D. Ban, Superior transverse piezoelectricity in organic-inorganic hybrid perovskite nanorods for mechanical energy harvesting, Nano Energy. 86 (2021) 106039. https://doi.org/10.1016/j.nanoen.2021.106039.

[28] S. Ippili, V. Jella, J.-H. Eom, J. Kim, S. Hong, J.-S. Choi, V.-D. Tran, N. Van Hieu, Y.-J. Kim, H.-J. Kim, S.-G. Yoon, An eco-friendly flexible piezoelectric energy harvester that delivers high output performance is based on lead-free $MASnI_3$ films and $MASnI_3$-PVDF composite films, Nano Energy. 57 (2019) 911–923. https://doi.org/10.1016/j.nanoen.2019.01.005.

[29] C. Ghosal, S.K. Ghosh, K. Roy, B. Chattopadhyay, D. Mandal, Environmental bacteria engineered piezoelectric bio-organic energy harvester towards clinical applications, Nano Energy. 93 (2022) 106843. https://doi.org/10.1016/j.nanoen.2021.106843.

[30] S.K. Ghosh, D. Mandal, Synergistically enhanced piezoelectric output in highly aligned 1D polymer nanofibers integrated all-fiber nanogenerator for wearable nano-tactile sensor, Nano Energy. 53 (2018) 245–257. https://doi.org/10.1016/j.nanoen.2018.08.036.

[31] I. Kim, H. Roh, J. Yu, N. Jayababu, D. Kim, Boron Nitride Nanotube-Based Contact Electrification-Assisted Piezoelectric Nanogenerator as a Kinematic Sensor for Detecting the Flexion–Extension Motion of a Robot Finger, ACS Energy Lett. 5 (2020) 1577–1585. https://doi.org/10.1021/acsenergylett.0c00451.

[32] C. Chang, V.H. Tran, J. Wang, Y.-K. Fuh, L. Lin, Direct-Write Piezoelectric Polymeric Nanogenerator with High Energy Conversion Efficiency, Nano Lett. 10 (2010) 726–731. https://doi.org/10.1021/nl9040719.

[33] Y. Song, N. Wang, C. Hu, Z.L. Wang, Y. Yang, Soft triboelectric nanogenerators for mechanical energy scavenging and self-powered sensors, Nano Energy. 84 (2021) 105919. https://doi.org/10.1016/j.nanoen.2021.105919.

[34] B. Sun, Y. Chen, M. Xiao, G. Zhou, S. Ranjan, W. Hou, X. Zhu, Y. Zhao, S.A.T. Redfern, Y.N. Zhou, A Unified Capacitive-Coupled Memristive Model for the Nonpinched Current–Voltage Hysteresis Loop, Nano Lett. 19 (2019) 6461–6465. https://doi.org/10.1021/acs.nanolett.9b02683.

[35] B. Sun, M. Xiao, G. Zhou, Z. Ren, Y.N. Zhou, Y.A. Wu, Non–zero-crossing current-voltage hysteresis behavior in memristive system, Mater. Today Adv. 6 (2020) 100056. https://doi.org/10.1016/j.mtadv.2020.100056.

[36] S. Ippili, V. Jella, J. Kim, S. Hong, S. Yoon, Enhanced piezoelectric output performance via control of dielectrics in Fe^{2+}-incorporated $MAPbI_3$ perovskite thin films: Flexible piezoelectric generators, Nano Energy. 49 (2018) 247–256. https://doi.org/10.1016/j.nanoen.2018.04.031.

[37] Y.-J. Kim, T.-V. Dang, H.-J. Choi, B.-J. Park, J.-H. Eom, H.-A. Song, D. Seol, Y. Kim, S.-H. Shin, J. Nah, S.-G. Yoon, Piezoelectric properties of $CH_3NH_3PbI_3$ perovskite thin films and their applications in piezoelectric generators, J. Mater. Chem. A. 4 (2016) 756–763. https://doi.org/10.1039/C5TA09662F.

[38] X. Chen, J. Shao, N. An, X. Li, H. Tian, C. Xu, Y. Ding, Self-powered flexible pressure sensors with vertically well-aligned piezoelectric nanowire arrays for monitoring vital signs, J. Mater. Chem. C. 3 (2015) 11806–11814. https://doi.org/10.1039/C5TC02173A.

[39] X. Chen, H. Tian, X. Li, J. Shao, Y. Ding, N. An, Y. Zhou, A high performance P(VDF-TrFE) nanogenerator with self-connected and vertically integrated fibers by patterned EHD pulling, Nanoscale. 7 (2015) 11536–11544. https://doi.org/10.1039/C5NR01746G.

[40] X. Chen, X. Li, J. Shao, N. An, H. Tian, C. Wang, T. Han, L. Wang, B. Lu, High-Performance Piezoelectric Nanogenerators with Imprinted P(VDF-TrFE)/$BaTiO_3$ Nanocomposite Micropillars for Self-Powered Flexible Sensors, Small. 13 (2017) 1604245. https://doi.org/10.1002/smll.201604245.

[41] C. Lang, J. Fang, H. Shao, X. Ding, T. Lin, Electrospun Nano-nonwoven Acoustic Sensors, Mater. Today Proc. 4 (2017) 5306–5311. https://doi.org/10.1016/j.matpr.2017.05.040.

[42] Z. Yuan, T. Zhou, Y. Yin, R. Cao, C. Li, Z.L. Wang, Transparent and Flexible Triboelectric Sensing Array for Touch Security Applications, ACS Nano. 11 (2017) 8364–8369. https://doi.org/10.1021/acsnano.7b03680.

[43] D. Yu, Z. Zheng, J. Liu, H. Xiao, G. Huangfu, Y. Guo, Superflexible and Lead-Free Piezoelectric Nanogenerator as a Highly Sensitive Self-Powered Sensor for Human Motion Monitoring, Nano-Micro Lett. 13 (2021) 117. https://doi.org/10.1007/s40820-021-00649-9.

[44] S. Zhang, X. Lin, H. Liu, Z. Yuan, Y. Huan, X. Yuan, S. Huang, X. Cheng, High-performance flexible piezoelectric nanogenerator based on necklace-like PZT particle chains, Int. J. Energy Res. 45 (2021) 6213–6226. https://doi.org/10.1002/er.6242.

CHAPTER 8

8. $C_3H_7NH_3PbI_3$@PVDF porous piezo-active film: A wearable phototronic potential bio-sensor

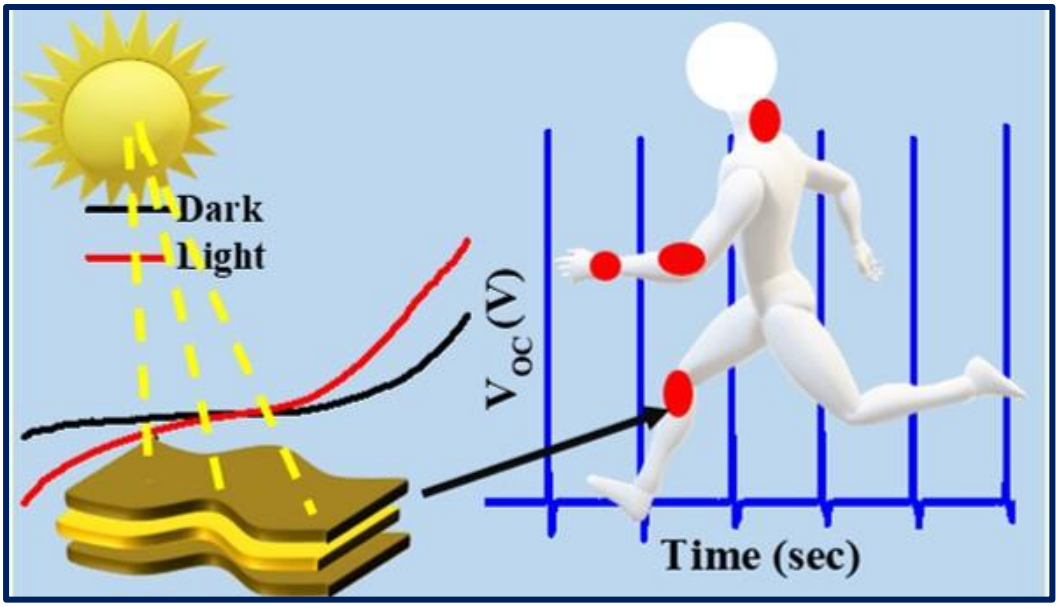

8.1. Introduction

To address the alarming energy crisis, harvesting renewable energy from our surroundings to run these wide range of self-powered, portable electronic devices has gained keen research as well as trade interest. Collecting mechanical energy from human motions, acoustic noise, vibration from vehicles, etc., and converting it to electrical signals is one of the optimum choices among green sources of energy to fight against the energy calamities and several environmental issues triggered by fossil fuels. Moreover, a large number of miniaturized devices such as wireless transmitters, environment monitoring sensors, wearable sensors, biomedical devices, etc. which have become very popular during the last few years require minimal power to be operated, and can be powered up using this piezoelectric energy without the need of any external battery part.[1] The removal of the peripheral battery portion effectively eliminates the effort and time required to recharge these devices at regular intervals. Furthermore, most of these miniaturized devices frequently comprise photosensors for envisioned operation. Solar energy is another persistent and abundant source of sustainable energy. Harvesting mechanical and solar energy follow distinctly different working mechanisms. Various piezoelectric ceramics and perovskites like PZT (lead zirconate titanate), GaN, $BaTiO_3$, $KNbO_3$, $NaNbO_3$ have shown their superior potential in this segment owing to their high piezoelectric constant, enhanced energy conversion efficiency, etc. and are well-studied over the years.[2] Despite being potential candidates, these ferroelectric materials possess several disadvantages like high expense, brittle nature, non-biocompatibility, etc. These drawbacks somewhat put a limitation on the large-scale production of piezoelectric devices using these piezo-active ceramics. Researchers have put dedicated effort in recent years to find suitable light-weight, flexible, environmentally friendly alternatives to fabricate piezoelectric energy harvesters (PEHs). Polyvinylidene difluoride (PVDF) and its copolymers are the most widely used polymer due to their cost-effectivity, flexibility, durability, biocompatibility, etc among various piezoelectric polymers.[3–5] PVDF is a semi-crystalline polymer in which at least four polymorphs exist. Among them, non-polar α phase (TGTG conformation) is the most stable and predominant in PVDF but the polar β phase (TTTT conformation) is the electroactive one. To achieve the dominance of β phase in PVDF, several methods like annealing at high temperatures, mechanical stretching at a high electric field, etc. have been studied which exhibit that these techniques may ruin the flexibility of the PVDF films.[2] In addition, these techniques are expensive and time-consuming and hence not

preferable for large-scale commercialization of PEHs. On the other hand, self-poled, hassle-free, piezo-active PVDF films are trendy now which can be accomplished by the incorporation of appropriate external agents in definite proportion to PVDF. The presence of suitable filler reacts with the -CH_2- and -CF_2- dipoles of PVDF and leads to the huge formation of the most desired crystalline β phase in PVDF.

Hybrid perovskites (generic formula ~ ABX_3, A represents an organic cation, B denotes inorganic ion and X refers to the halide anion) have been illuminated to the research interest over the past few years due to their low expense, ability to tune the energy band gap by altering the cations and/or anions, high light absorption efficiency, long charge diffusion length, etc.[6,7] Moreover, these hybrid perovskites are optically active and possess wide applications in optoelectronic devices.[8,9] The incorporation of a hybrid perovskite within PVDF matrix not only results in the formation of β phase in a significant proportion but also can act as a solar energy harvester owing to its light absorbing property. The main disadvantage of these organo-halide perovskites which restricts their performance over a long span is their stability in the presence of moisture and UV light. Despite facing the stability issue, methylammonium lead iodide ($CH_3NH_3PbI_3$) is one of the most enlightened hybrid perovskites on which several studies have been performed over the years. On the other hand, propylammonium lead iodide ($C_3H_7NH_3PbI_3$) is less explored and is a promising hybrid perovskite that exhibits excellent stability in the presence of moisture.[10] Moreover, the optimal wide energy band gap (~ 2.38 eV) of $C_3H_7NH_3PbI_3$ ($PAPbI_3$) makes it an appropriate candidate to be decorated within PVDF to fabricate an integrated package or separated systems of the mechanical and solar energy harvester. The capping of $PAPbI_3$ by the polymer may protect the environment from the toxicity of lead.

In this work, we include the response of self-poled, flexible PEHs employing $PAPbI_3$@PVDF porous films. The fabricated PEH exhibits a significant response under hammering with a free hand. The significant response of piezo-active photodetector of the concerned composite is also studied extensively to understand the intrinsic properties of the composite along with the device. The flexibility of the devices makes them wearable and the output response corresponding to different human motion ensures its utility as a potential biosensor.

8.2. Experimental details

8.2.1. Materials

N-propylamine ($C_3H_7NH_2$, 98%) was purchased from Spectrochem whereas hydroiodic acid (HI, 57 wt.% in water), N-N dimethylformamide (DMF, anhydrous, 99.8%) was bought from Merck chemicals. Lead iodide (PbI_2) used in the synthesis of $C_3H_7NH_2PbI_3$ was from Loba Chemie, and PVDF was bought from Alfa Aesar. All the chemicals used in this work were of analytical grade.

8.2.2. Preparation of $PAPbI_3$

The preparation of $PAPbI_3$ is explained in our early reports in detail [7,8].

8.2.3. Formation of $PAPbI_3$@PVDF films

Firstly, 10 wt% of PVDF solution was prepared by stirring PVDF powder in DMF continuously for 3 hours at 60 ^oC. Next, 5, 10, 15, and 20 wt% of freshly synthesized $PAPbI_3$ powder was mixed in the PVDF solution and stirred for another 4 hours at 60 ^oC to form homogeneous precursor solutions of $PAPbI_3$@PVDF composites. Lastly, ferroelectric $PAPbI_3$@PVDF films were achieved by consecutive annealing of the respective precursor solutions at 90 ^oC for 2.5 hours and 130 ^oC for 3.5 hours. The prepared films are designated as PAPI_5, PAPI_10, PAPI_15 and PAPI_20. A reference film using only PVDF was also formed following the same procedure to perform a comparative study.

8.2.4. Fabrication of PEHs

To design the PEHs, the prepared films were sandwiched in between two Cu electrodes. Two Cu wires were soldered on each side of the Cu/ $PAPbI_3$@PVDF films/Cu structure for electrical connection. Finally, the fabricated devices were laminated with PDMS (polydimethylsiloxane) layer to provide safeguard and ensure their durability.

8.2.5. Fabrication of piezo-active photodetector

To fabricate the piezo-active photodetector, precursor solution of $PAPbI_3$ incorporated PVDF was casted on ITO coated PET followed by consecutive annealing at 90 ^oC for 1hour and at

130 ºC for 1 hour. Silver paste was attached on the other side of the film and two Cu wires were soldered on both sides of the electrode.

8.3. Characterization

The structural confirmation of the synthesized perovskite as well as films was investigated by X-ray powder diffractometer (Bruker D8). The FTIR spectrum was obtained from PerkinElmer, Spectrum – 2000. The surface morphology of the samples was detected by FESEM (FEI, INSPECT F50). The photoluminescence property of the composite films at room temperature was attained from Fluoromax–4C_1505D-33. DSC thermograph of all the films were analysed by Waters India (TA), DSC Q2000. The tensile strength of the samples was measured using Tinius Olsen H50KS at a strain rate of 1 mm/min. The open circuit voltage response was recorded using digital storage oscilloscope (Keysight, 1052A) and the short circuit current was measured using Kiethley 2602B. AM-1.5g, standard solar spectrum of solar simulator was used to irradiate the photodetector with intensity 100 mW/cm^2.

8.4. Result and discussion

8.4.1. Structural and microstructural analysis of $PAPbI_3$

The XRD profile of the sol-gel driven $PAPbI_3$ as shown in Fig. 8.1a is similar to that reported in the literature [7,8] which thus ensures the formation of the proposed perovskite. The FESEM image of the micro-sized $PAPbI_3$ powder is illuminated in Fig. 8.1b that depicts the flake/rod like structure of the perovskite. The digital photograph of $PAPbI_3$ powder is displayed in the inset of Fig. 8.1a.

8.4.2. Quantification of ferroelectric phase content and degree of crystallinity

The XRD patterns of PAPI_X@PVDF films, (X = 0, 5, 10, 15, 20) are depicted in Fig. 8.2a that shows the variation of β phase enhancement with the wt% of $PAPbI_3$ in PVDF. It has been observed that β phase enhances significantly and polar α phase decreases effectively with the rise in the $PAPbI_3$ content in PVDF that leads to the overall improvement of the crystallinity of

the concerned films. The overall degree of crystallinity ($\times_{TC}$) of the prepared films was

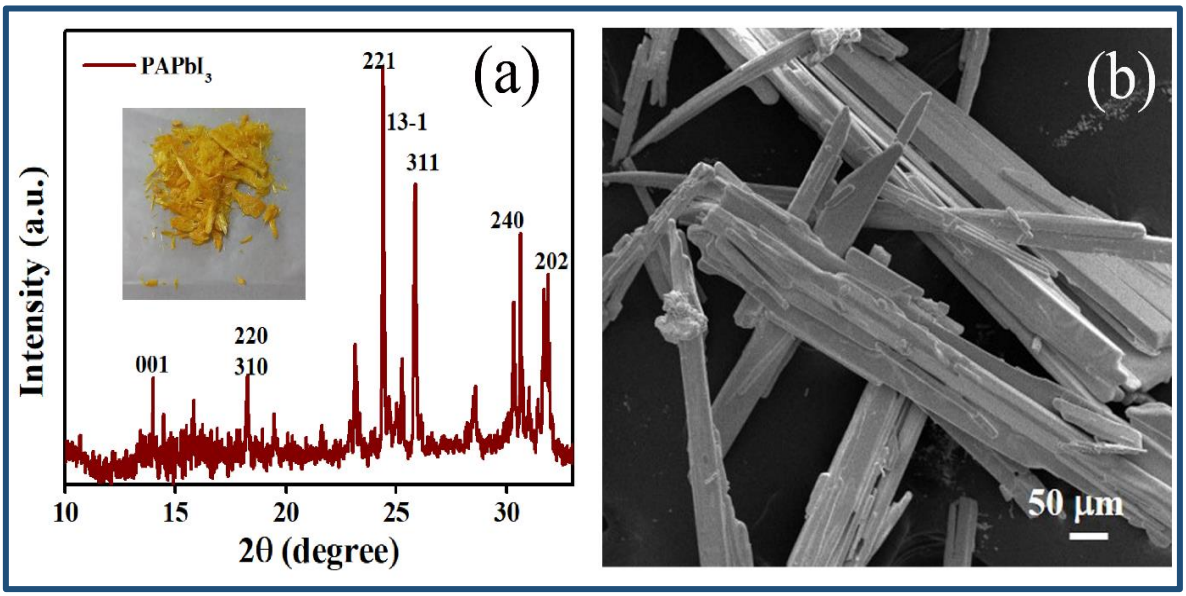

Fig. 8.1. a-b) The XRD pattern and FESEM imaging of the sol-gel derived $PAPbI_3$ powder, Inset of a) The digital photograph of $PAPbI_3$ powder.

computed using the relation

$$\times_{TC} = \frac{\sum A_C}{\sum A_C + \sum A_{amp}} \times 100 \qquad (8.1)$$

Here, $\sum A_C$ denotes the total area of the crystalline portion whereas $\sum A_{amp}$ refers to the total area of the amorphous portion of the films. The variation of the computed value of $\times_{TC}$ with the wt% of the proposed filler in the polymer matrix is exhibited in Fig. 8.2b. PAPI_15 is found to achieve the highest $\times_{TC}$ ~ 69 % among all films.

The FT-IR study has been performed to estimate the β phase content of all the films. Conversion of the non-polar α phase which is predominant in pure PVDF to the polar β phase with the increase in filler concentration evident from Fig. 8.2c. A semi-polar γ phase appears in the filler embedded films in contrast to the neat PVDF film. The ferroelectric active phase content of all the prepared films can be calculated employing the following equation [9]

$$F_{EA} = \frac{A_{842}}{(\frac{K_{842}}{K_{764}})A_{764} + A_{842}} \times 100\% \qquad (8.2)$$

Here, A_{842} and A_{764} represents the integral area of the absorbance bands at 842 and 764 cm^{-1}, respectively and K_{842} and K_{764} are the absorption coefficient of these respective bands ($K_{842} = 7.7 \times 10^4\, cm^2/mol$, $K_{764} = 6.1 \times 10^4\, cm^2/mol$). The evaluated values of F_{EA} is plotted against the variation of filler $PAPbI_3$ as shown in Fig. 8.2d. The rapid

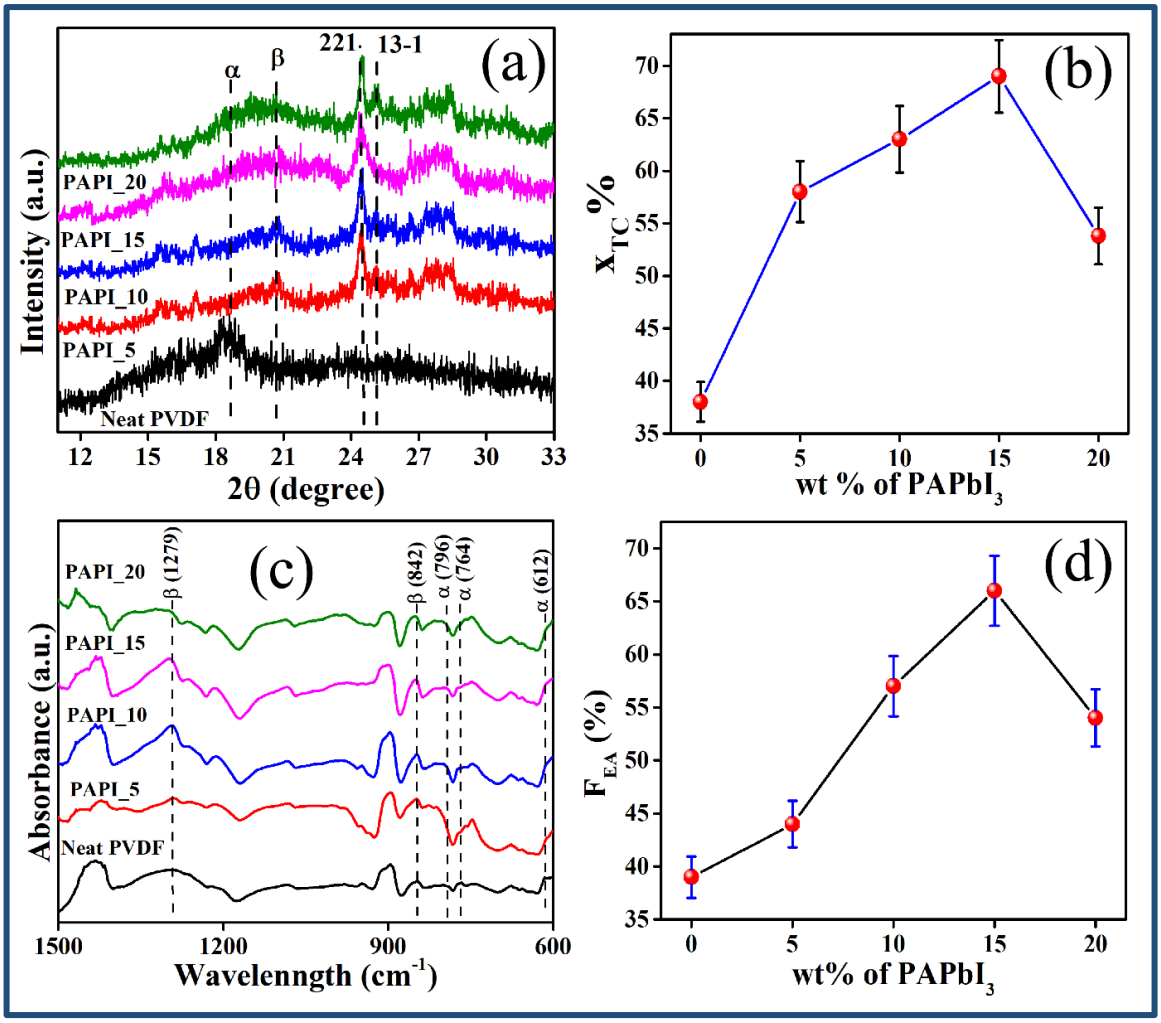

Fig. 8.2. a) The XRD pattern of all the films, b) The variation of degree of crystallinity of all the films, c) The FTIR pattern of all the films, d) The variation of the ferroelectric phase content with the wt. of $PAPbI_3$ in the composite films, e) The stretching of symmetrical and asymmetrical vibrational bands, f) The variation of the values of damping factor with concentration variation of $PAPbI_3$.

enhancement of F_{EA} due to the addition of the filler can be observed that includes the highest value of F_{EA} ~ 66.7 % for PAPI_15. This significant improvement of ferroelectric phase content is owing to the interfacial interaction between the surface charges of $PAPbI_3$ and -CH_2- dipoles of PVDF. In the presence of DMF, $PAPbI_3$ dissociates into $C_3H_7NH_3^+$ and PbI_3^- during the formation of precursor solution and interacts with the -CF_2- and -CH_2- dipoles of PVDF during the evaporation of the solvent that reflects in the appreciable improvement in β phase nucleation.

8.4.3. Surface morphology of the prepared films

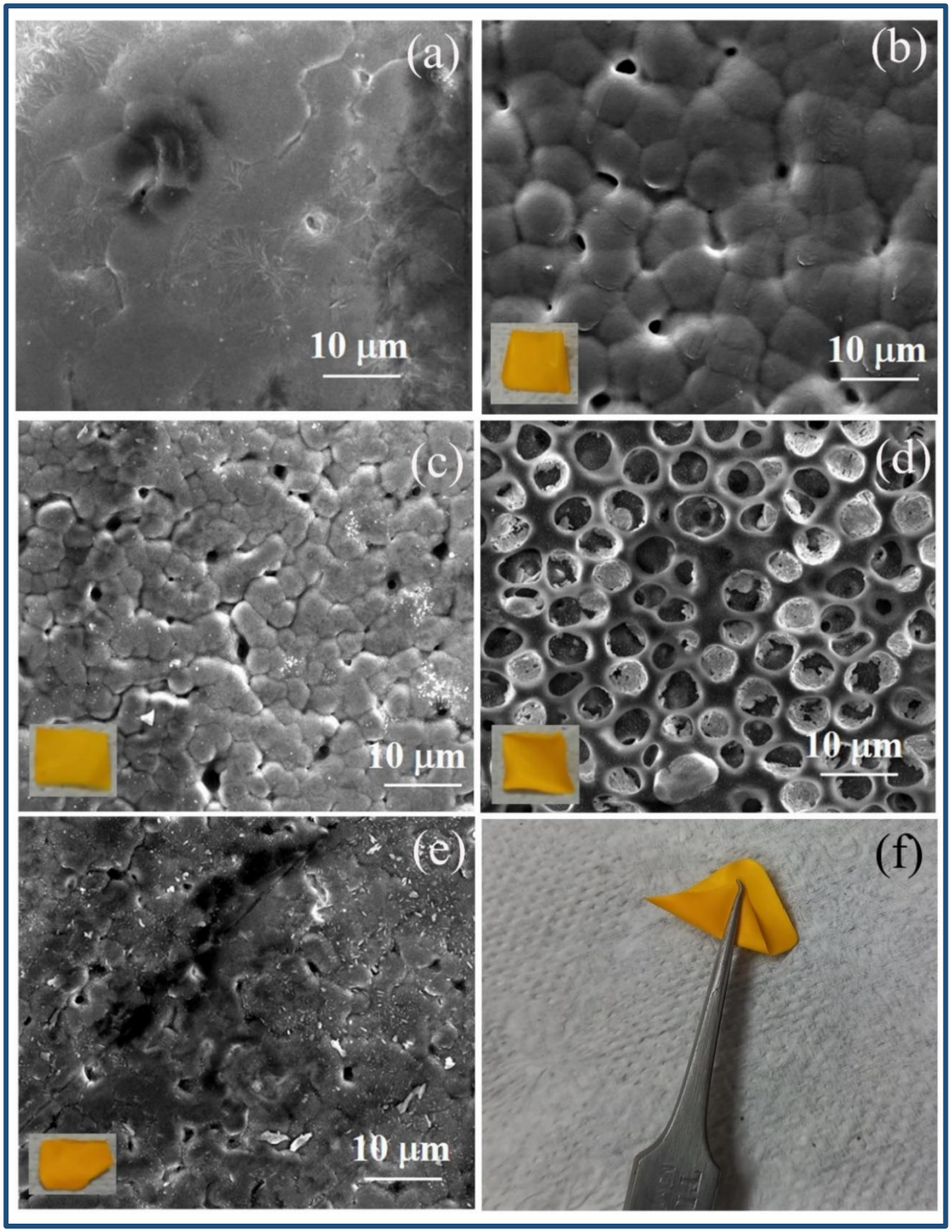

Fig. 8.3. a-e) The FESEM images of all the prepared films. Insets of a-e denotes the digital photograph of the films, f) The flexibility of PAPI_15.

The surface morphologies of the films are exhibited in Fig. 8.3 which shows a smooth, pore-free surface of the neat PVDF film (Fig. 8.3a). On the other hand, the inclusion of $PAPbI_3$

within the PVDF matrix creates pores throughout the surface of the film. $PAPbI_3$ crystallizes faster than the polymer during the process of annealing, more precisely at the time of the evaporation of the solvent, and as a result, the surfaces of filler loaded films are full of pores [10,11]. The sizes and distribution of the pores on the surface of films increase up to 15 wt% of filler loading. The digital photographs of the films are illuminated in the inset of the corresponding diagrams (Fig. 8.3a-e). The digital photograph showing the flexibility of the PAPI_15 is exhibited in Fig. 8.3f.

8.4.4. Optical, elastic, and thermal properties of the films

To investigate the optical properties of the filler loaded films, PL spectra of the films are measured from which we estimated the energy band gap of the films (Fig. 8.4a). The values of the energy band gap of the films lie between 2.30 – 2.32 eV which not only confirms the presence of $PAPbI_3$[7] within PVDF but also suggests that the optical property of the filler remains unaltered even within the polymer framework.

The elastic properties of the film are illustrated in Fig. 8.4b-d. From the stress-strain curve, as shown in Fig. 8.4b, Young's modulus of the films is estimated to be maximum for 15 wt% loading of $PAPbI_3$ as illustrated in Fig. 8.4c. The corresponding evaluated values of Tensile strength are shown in Fig. 8.4d. As the porosity of the films increases, the tensile strength is also found to increase significantly.

The thermal properties and degree of crystallinity of the films are assessed with DSC thermograph analysis. The melting point of the films rises substantially with the rise in filler loading in polymer matrix. The melting point of PAPI_20 is the highest ~ 168.83 ^oC in contrast to neat PVDF 162.97 ^oC as shown in Fig. 8.4e. Furthermore, the crystallization temperature of the films enhances appreciably with the increase in filler content. The melting point of PAPI_20 is as high as 142.80 ^oC in comparison with neat PVDF ~ 133.21 ^oC. The degree of crystallinity of the films are achieved with the help of the following equation [12,13]

$$x_c\ (\%) = \frac{\Delta H_m}{\Delta H_{100}} \times 100 \qquad (8.3)$$

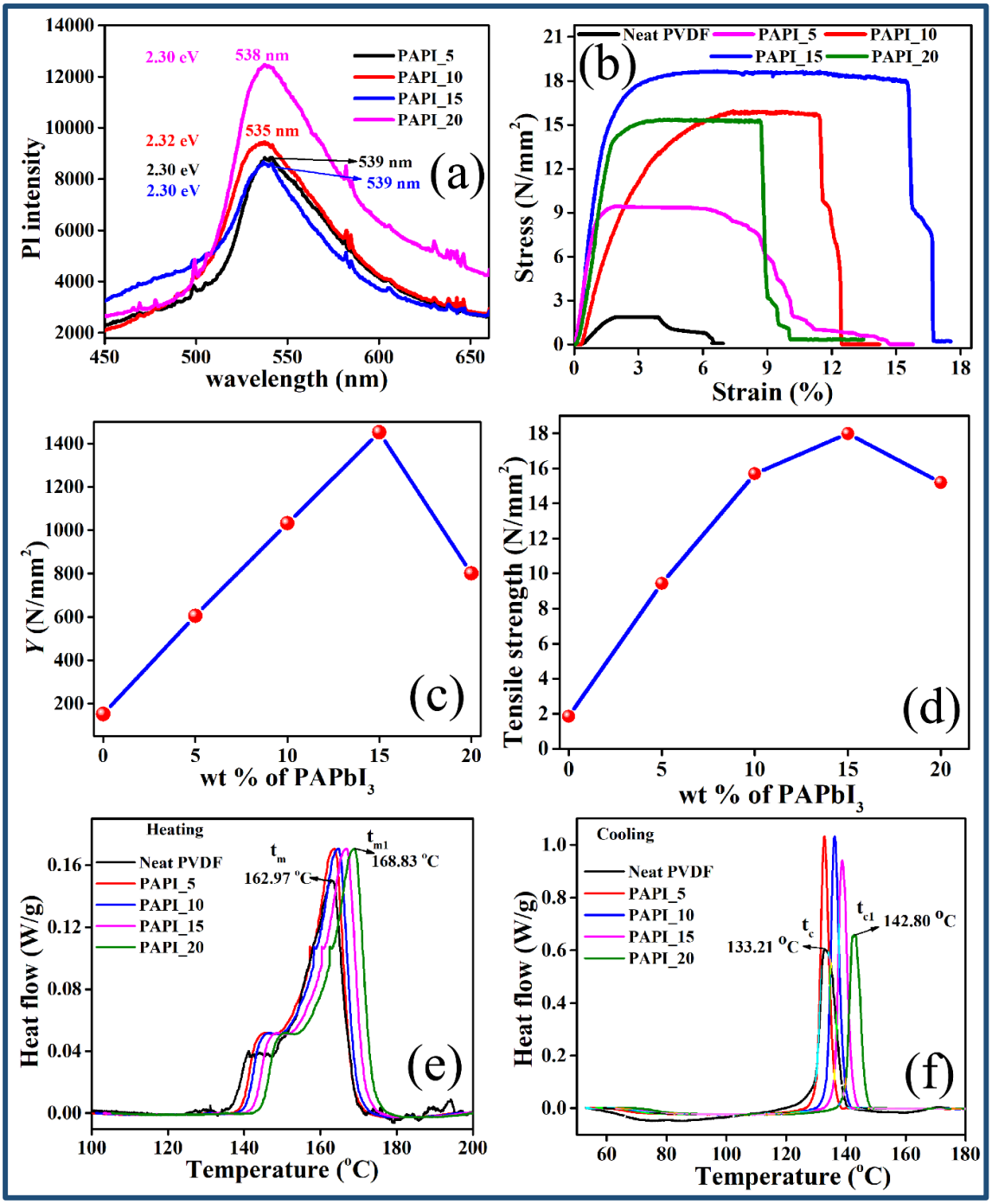

Fig. 8.4. a) The PL spectra of the composite films. b) The stress-strain curve of all the films, c) The variation of the values of Young's Modulus with the variation of $PAPbI_3$ content in the film, d) The values of tensile strength of all the films, DSC thermographs showing e) the heating cycle and f) cooling cycle of the films.

Here, ΔH_m and ΔH_{100} denote the melting enthalpy of the concerned samples and melting enthalpy of 100 % crystallite PVDF (ΔH_{100} = 104.5 J/g). The x_c (%) of the films are evaluated as 25%, 27.8%, 33%, 42% and 37% for neat PVDF, PAPI_5, PAPI_10, PAPI_15,

and PAPI_20 respectively. The significant improvement of crystallinity due to the inclusion $PAPbI_3$ agrees with the results of the XRD and FTIR study.

8.4.5. Piezoelectric response of the devices made of the films

The piezoelectric performance of the PEHs made of all the films (PPEH) is evaluated extensively under the application of various dynamic strain. Fig. 8.5a and 8.5b indicate the superior response of open circuit voltage (V_{OC}) and short circuit current density (J_{SC}) of PPEH_15 under hammering with a free hand. PPEH_15 (effective area ~ 2.5 cm × 1.5 cm, thickness ~ 100 μm) yields as high as ~ 80 V V_{OC} and 17.8 μA/cm^2 J_{SC} in contrast with REH that produces 7 V and 1.9 μA/cm^2 under similar pressure. Since PAPI_15 possesses the highest degree of crystallinity which reflects the highest formation of β phase in this film, the piezoelectric performance of PPEH_15 matches the outcomes of previous studies. Fig. 8.5c reflects the ultra-sensitivity of PPEH_15 as the device was able to detect very lightweight pressure-like tissue that had fallen repeatedly on the device from a height of 7 cm. Next, one edge of the device was attached to an edge of a table in such a way that the other edge was free to move and the response upon repeated hammering on the free edge with a matchstick was measured (Fig. 8.5c). The responses under index finger touch and tapping with a pen were also detected (Fig. 8.5c). Fig. 8.5d denotes the voltage output under twisting of PPEH_15 which demonstrates the flexibility of the device. Fig. 8.5e represents the response of PPEH_15 under gentle foot press whereas Fig. 8.5f illustrates the vibration sensitivity of PPEH_15 even in the ultrasonic range. The behavior of PPEH_15 under various types of external dynamic strain or vibration assures its potential as a promising candidate in the field of IoTs.

To calculate the generated power of PPEH_15 under hammering with bare hand, the device was connected to various external resistance that varies from 3KΩ to 12.5 MΩ. The schematic diagram of the corresponding circuit is exhibited in Fig. 8.6a. The variation of the voltage response under hammering with a free hand is plotted against the resistances as illustrated in Fig. 8.6b. The output power density (P) is calculated from

$$I_L = \frac{V_{pp}}{A \times R_L} \tag{8.4}$$

$$P = V_{pp} \times I_L \tag{8.5}$$

Here, V_{pp} refers to the peak-to-peak voltage across each load resistance (R_L), I_L is the

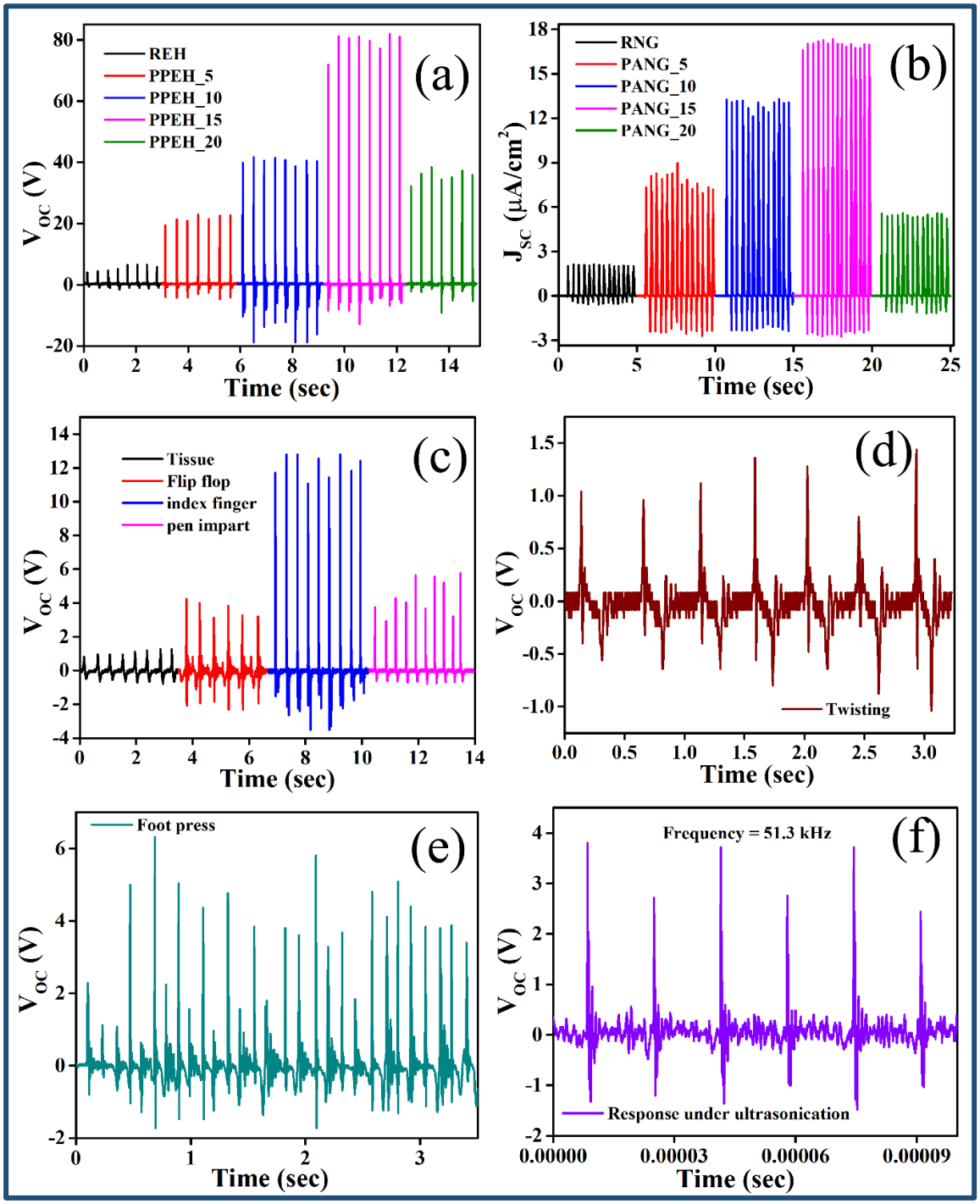

Fig. 8.5. a-b) The output response of V_{OC} and J_{SC} of all the PEHs under hammering with free hand, c) The response of PPEH_15 under the application of very light weight objects, response under d) twisting, e) foot press, f) ultrasonic vibration.

corresponding current density and A is the effective contact area. The maximum power ~ 3.91 mW/cm^2 under hammering with hand was obtained across 1.97 MΩ load (Fig. 8.6c). Thus,

using the maximum power transfer theorem, we estimated the internal resistance of the device

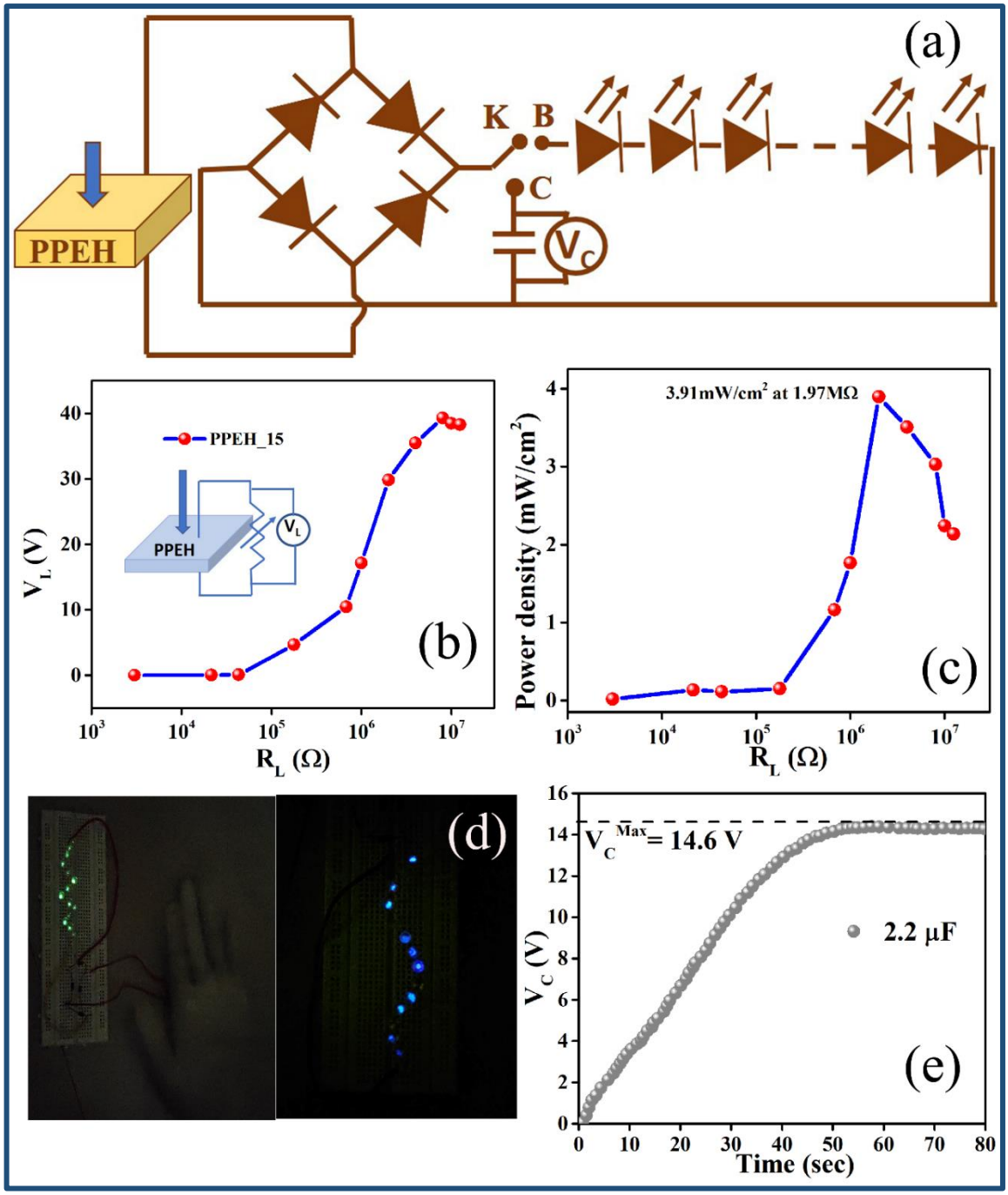

Fig. 8.6. a) The schematic diagram of bridge rectifier circuit attached to the device, b) The variation of load voltage across a range of load resistance, Inset of b) The schematic diagram of the corresponding circuit, c) The variation of output power density across load resistance, d) glowing up several green and blue LEDs, e) charging a capacitor.

(R_i) as 1.97 MΩ.

The generated power is sufficient enough to light up several green and blue LEDs as shown in Fig. 8.6d. Furthermore, this power is used to charge a commercially available

capacitor of 2.2 μF (Fig. 8.6e) that can produce 14.6 V in 55 sec. The corresponding energy stored in the capacitance is ($E = \frac{1}{2}CV_c^2$) 234.476 μJ. The internal capacitance of PPEH_15 was computed using the conventional RC circuit model

$$\tau = R_i C_T \tag{8.6}$$

Here, τ represents the time constant and C_T is the total capacitance. Therefore, the internal capacitance (C_i) of the device thus evaluated ($C_T = C + C_i$) as 11.1 μF.

The flexibility of PPEH_15 helps to detect various physiological measures such as bending of a finger, pulse rate monitoring, detection of abnormal knee jerk reflex, and movement of neck joint at different angles and thus makes it a wearable bio-medical sensor. At rest, no signal was detected whereas, with the movement of the finger, a response was detected as shown in Fig 8.7a. The response changes for different angles of the movement of the finger. Hence, the response with the movement of the finger suggests that this device may be used in detecting arthritis which mainly affects the ball and socket joint. Next, PPEH_15 was placed on the human knee and generated an electric signal in response to a mild hammering at the knee (Fig. 8.7b) can detect the abnormal knee jerk reflex if any. A diminished reflex or exaggerated reflex which implies a lesion/defect in the peripheral nervous system or the central nervous system could be identified by comparing the strength of the electric pulse with that of to normal reflex. The V_{OC} obtained in detecting the radial artery pulse of a healthy human being in normal condition confirms its potential as a pulse monitoring device (Fig. 8.7c). To protect our backbone and spinal cord, maintaining proper body posture while working on a laptop/desktop for a prolonged time is very important. We placed the device at the human neck and the output response was received when the neck was bent at different angles ~ 30^o, 60^o, etc (Fig. 8.7d-e). At different bending angles, the output response is completely different that

assures its use as a posture monitoring system. The response corresponding to the arm joint bending is depicted in Fig. 8.7f.

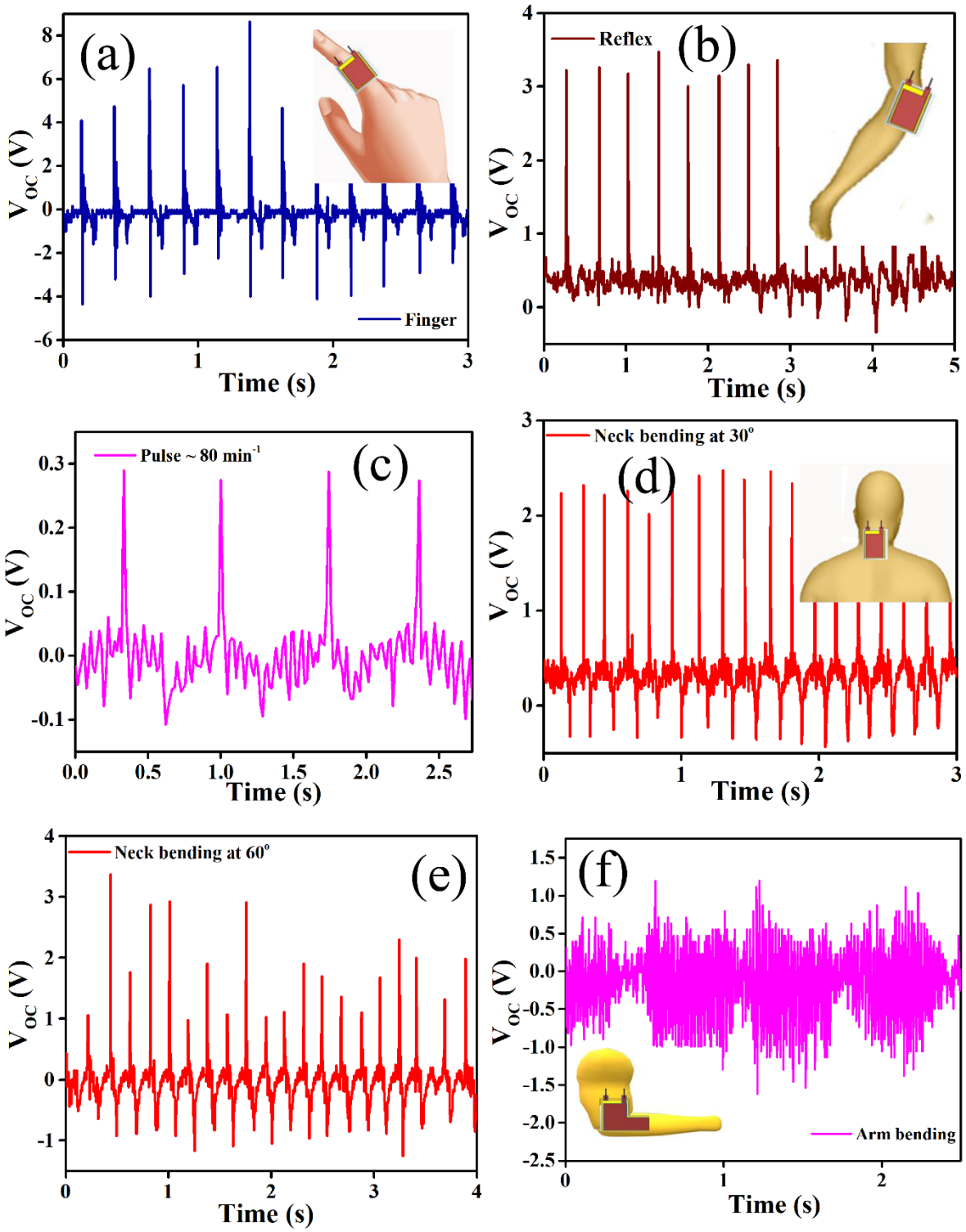

Fig. 8.7. The output response of PPEH_15 under (a) finger bending, (b) knee reflex, (c) pulse, (d-e) neck bending at 30° and 60°, (f) arm joint bending, respectively.

8.4.6. Response of the piezo-active photodetector

PAPI_15 was employed in the fabrication of piezo-active photodetector. The wide absorption

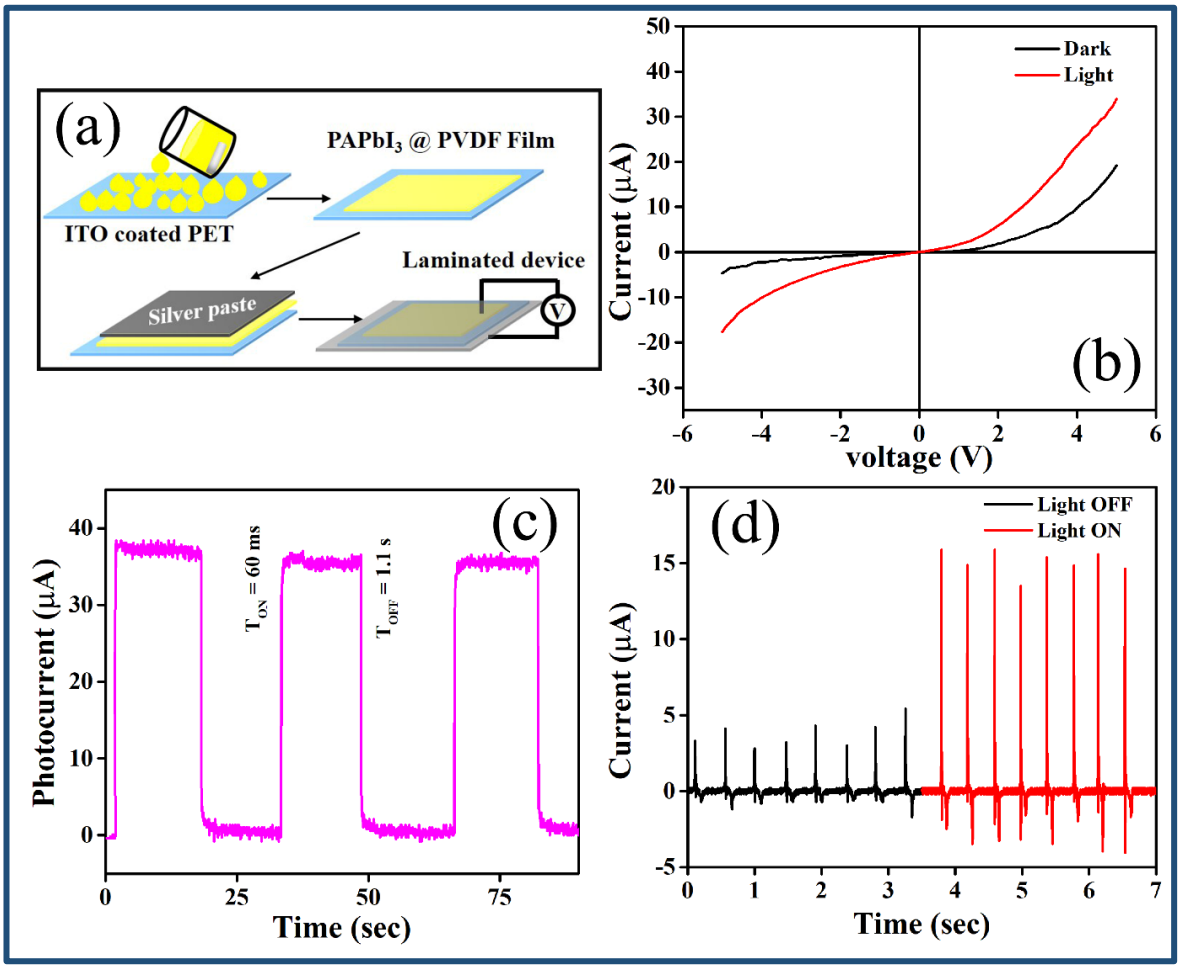

Fig. 8.8. a) The step-by-step schematic diagram of the fabrication of the photodetector. b) I-V characteristics of the device in both dark and irradiated condition. c) The current-time plot of the device, d) The photo-active piezo response of the device.

peak as observed in Fig. affirms its utility as an optically active layer in the photodetector. The schematic step-by-step diagram of designing the photodetector is depicted in Fig. 8.8a. The I-V characteristic of the designed photodetector is shown in Fig. 8.8b in which the difference between the current obtained in dark and illuminated conditions is distinct. The I-V nature in both dark and under irradiation is linear owing to the ohmic response. In the presence of irradiation, a large number of excitons are produced at the absorption layer (exposed area ~ 2.5 cm ×1.5 cm, the thickness of the photodetector ~ 100 μm). In the presence of external bias voltage, the excitons that form during irradiation split up into free holes and electrons and shift toward the outer electrodes. As a result, photocurrent is generated. The periodic switching of photocurrent from OFF state to ON state is exhibited with time in Fig. 8.8c indicating the

appreciably fast response time of the device. The piezo response under gentle touch is also found to be enhanced in the presence of illumination (Fig. 8.8d).

8.5. Conclusion

$PAPbI_3$, a promising, optically active, hybrid perovskite was employed as an external agent in different proportions in PVDF solution to form flexible, porous films that were used in the fabrication of PEH. PPEH_15 was found to be the most electroactive and possess the highest degree of crystallinity among all the films. Moreover, the values of the energy band gap of the films affirm their efficacy as optically active semiconductors. The elastic properties of the films ensure their flexibility. The porosity of the films as observed from SEM image may be responsible for the formation of β phase. The values of V_{OC} and J_{SC} of PPEH_15 are significantly high in contrast to REH. The generated power output is sufficient to light up several green and blue LEDs. This piezo-active flexible film could be used as a biomedical sensor which particularly can monitor pulse rate, can detect abnormal knee-jerk reflexes which may be due to defects in the peripheral nervous system or central nervous system and more precisely bending posture of different parts of our body. Moreover, PAPI_15 was used to design a piezo-active photodetector.

References

[1] V. Jella, S. Ippili, J.-H. Eom, J. Choi, S.-G. Yoon, Enhanced output performance of a flexible piezoelectric energy harvester based on stable $MAPbI_3$-PVDF composite films, Nano Energy. 53 (2018) 46–56. https://doi.org/10.1016/j.nanoen.2018.08.033.

[2] N.R. Alluri, B. Saravanakumar, S.-J. Kim, Flexible, Hybrid Piezoelectric Film ($BaTi_{(1-x)}Zr_xO_3$)/PVDF Nanogenerator as a Self-Powered Fluid Velocity Sensor, ACS Appl. Mater. Interfaces. 7 (2015) 9831–9840. https://doi.org/10.1021/acsami.5b01760.

[3] M. Sharma, V. Srinivas, G. Madras, S. Bose, Outstanding dielectric constant and piezoelectric coefficient in electrospun nanofiber mats of PVDF containing silver decorated multiwall carbon nanotubes: assessing through piezoresponse force microscopy, RSC Adv. 6 (2016) 6251–6258. https://doi.org/10.1039/C5RA25671B.

[4] P. Sadhukhan, S. Kundu, A. Roy, A. Ray, P. Maji, H. Dutta, S.K. Pradhan, S. Das, Solvent-Free Solid-State Synthesis of High Yield Mixed Halide Perovskites for Easily

Tunable Composition and Band Gap, Cryst. Growth Des. 18 (2018) 3428–3432. https://doi.org/10.1021/acs.cgd.8b00137.

[5] P. Sengupta, P. Sadhukhan, A. Ray, S. Mal, A. Singh, R. Ray, S. Bhattacharyya, S. Das, Influence of activation energy on charge conduction mechanism and giant dielectric relaxation of sol-gel derived $C_3H_7NH_3PbBr_3$ perovskite; Act as high performing UV photodetector, J. Alloys Compd. 892 (2022) 162216. https://doi.org/10.1016/j.jallcom.2021.162216.

[6] P. Sadhukhan, D. Ghosh, P. Sengupta, S. Bhattacharyya, S. Das, Unraveling the Charge Transport Mechanism in Mechanochemically Processed Hybrid Perovskite Solar Cell, Langmuir. 37 (2021) 5513–5521. https://doi.org/10.1021/acs.langmuir.1c00200.

[7] P. Sengupta, P. Sadhukhan, A. Ray, R. Ray, S. Bhattacharyya, S. Das, Temperature and frequency dependent dielectric response of $C_3H_7NH_3PbI_3$: A new hybrid perovskite, J. Appl. Phys. 127 (2020) 204103. https://doi.org/10.1063/1.5142810.

[8] P. Sengupta, P. Sadhukhan, S. Saha, S. Das, R. Ray, Improved Energy Harvesting Ability of $C_3H_7NH_3PbI_3$ Decorated Pvdf Nanofiber Based Flexible Nanogenerator, Nano Energy. 109 (2023) 108277. https://doi.org/10.2139/ssrn.4249647.

[9] H. Parangusan, D. Ponnamma, M. Al Ali AlMaadeed, Flexible tri-layer piezoelectric nanogenerator based on PVDF-HFP/Ni-doped ZnO nanocomposites, RSC Adv. 7 (2017) 50156–50165. https://doi.org/10.1039/C7RA10223B.

[10] S. Ippili, V. Jella, J.-H. Eom, J. Kim, S. Hong, J.-S. Choi, V.-D. Tran, N. Van Hieu, Y.-J. Kim, H.-J. Kim, S.-G. Yoon, An eco-friendly flexible piezoelectric energy harvester that delivers high output performance is based on lead-free $MASnI_3$ films and $MASnI_3$-PVDF composite films, Nano Energy. 57 (2019) 911–923. https://doi.org/10.1016/j.nanoen.2019.01.005.

[11] A. Sultana, P. Sadhukhan, M.M. Alam, S. Das, T.R. Middya, D. Mandal, Organo-Lead Halide Perovskite Induced Electroactive β-Phase in Porous PVDF Films: An Excellent Material for Photoactive Piezoelectric Energy Harvester and Photodetector, ACS Appl. Mater. Interfaces. 10 (2018) 4121–4130. https://doi.org/10.1021/acsami.7b17408.

[12] M.M. Abolhasani, S. Azimi, H. Fashandi, Enhanced ferroelectric properties of

electrospun poly(vinylidene fluoride) nanofibers by adjusting processing parameters, RSC Adv. 5 (2015) 61277–61283. https://doi.org/10.1039/C5RA11441A.

[13] H. Parangusan, D. Ponnamma, M.A.A. Al-Maadeed, Stretchable Electrospun PVDF-HFP/Co-ZnO Nanofibers as Piezoelectric Nanogenerators, Sci. Rep. 8 (2018) 754. https://doi.org/10.1038/s41598-017-19082-3.

CHAPTER 9

9. Environmental friendly multifunctional energy harvester along with energy storage application of an oxide perovskite composite

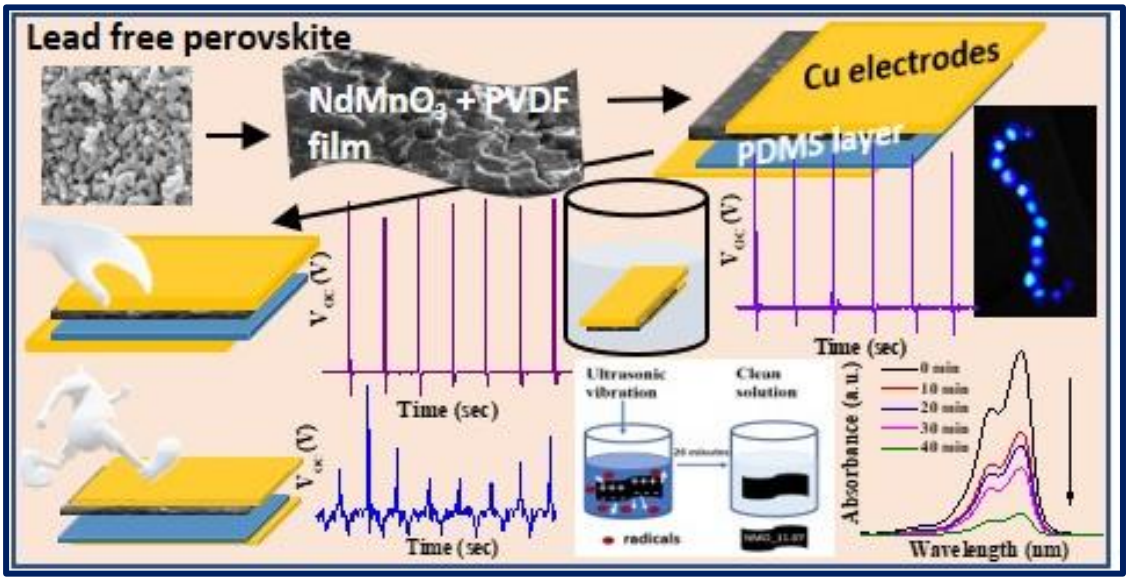

9.1. Introduction

Over the past decade, miniaturized renewable energy harvesting devices have become focal point of interest to power the various self-driven sensors and IoTs based systems [1]. Scavenging abundant mechanical energy from surroundings and converting it to electrical energy can be a perfect choice not only as a promising alternative to batteries, which require periodic replacement but also meet the global concern of the environment pollutions caused by fossil fuels. Inexpensive, portable, maintenance free, wearable, flexible piezoelectric can produce electrical energy when exposed to any dynamic strain in any living ambience irrespective of the day-night cycle, climate, and humidity conditions. In recent years, miniaturized, self-charging supercapacitor devices have garnered keen attention to store energy [2–5]. It can be very interesting to follow a single step to harvest and store energy in a single unit. Various piezoelectric materials like lead zirconate titanate (PZT), lithium niobate ($LiNbO_3$), barium titanate ($BaTiO_3$), Galium nitride (GaN), zinc oxide (ZnO), etc. [6–10] have gained immense popularity over the years due to their high piezoelectric performance. Despite being highly ferroelectric, these materials are brittle and thus restricted in applications. On the other hand, among various semi-crystalline ferroelectric polymers, polyvinylidene difluoride (PVDF) (chemical formula: $-(CH_2-CF_2)-_n$), and its copolymers are diversely used in piezoelectric nanogenerators (PNGs) in recent years owing to their low expense, fabrication simplicity, biocompatibility, light weight, and desired flexibility. There are four crystalline phases α, β, γ and δ of PVDF out of which predominant non-polar phase is α whereas, polar phase β is the highest electroactive component. PVDF can have several nanostructures like fibers, ribbons, wires etc. and each of these is well explored over the years. Despite being considered as piezo-active material, the efficacy of pure PVDF was not up to the mark. To achieve the supremacy of β phase within PVDF, various techniques like mechanical stretching, spin coating, annealing at high temperature, high field electrical poling, etc. have been performed. But these methods are time consuming, tedious, and hence fail to supply wide reaching production of PNGs [11,12]. Enhancement of the β phase of PVDF using the nanofiller is considered to be a smart and convenient choice. The addition of suitable nanofiller helps to orient the $-CH_2/-CF_2$ dipoles in PVDF which induces self-poling. Lead based systems are found to be suitable candidate as nanofiller because of its high piezoelectric constant and coupling factor which provide superior power conversion efficiency [13,14]. However, various regulating agencies across the globe are imposing restrictions on devices containing lead-based materials due to environmental issues. Thus, the development of a lead-

free piezoelectric nanogenerator is required owing to its less toxic nature. Another concern is to store the harvested energy properly to provide an uninterrupted power supply. The rapid development of supercapacitors eliminates the need of batteries and utilized in various applications. Hence, we further propose to fabricate a hybrid self-charging, piezoelectric device that can harvest mechanical and store it simultaneously. In this case, the mechanical energy is converted into the electrical energy which further transmutes to electrochemical energy. Various efforts that includes the conversion of mechanical to electrical to electrochemical energy have been observed in these reports [15–17]. Here, we have used gel electrolyte instead of liquid electrolyte to avoid unnecessary leakage problem, stability issue of the liquid solvent, physical phase of the liquid solvent that may put an obstacle for harvesting mechanical energy, etc.

Perovskite materials have gained immense attention owing to their wide applications in optoelectronic devices [18]. In this report, we include a lead-free rare earth oxide perovskite (ABO_3), neodymium manganate ($NdMnO_3$), as a nanofiller in PVDF matrix. MnO_6 octahedra is the base component of this perovskite structure and the large atomic weight difference of A and B-sited atoms makes it a suitable candidate for mechanical energy harvesting [19,20]. Structural and temperature dependent electrical behavior of $NdMnO_3$ is studied in detail. The XRD and FTIR experimental result of the composite films proves the appreciable enhancement of β phase in PVDF as $NdMnO_3$ is embedded in it. The output response of the fabricated piezoelectric nanogenerator was significantly high that assures the potential of the energy harvester. The appreciably large piezoelectric coefficient and voltage conversion efficiency of $NdMnO_3$@PVDF film confirm the contribution of piezoelectric effect of the films. The required flexibility and striking stability in the water medium make this nanogenerator an appropriate choice for producing wearable sensors/devices. It is noteworthy that the prepared film performs as a promising piezocatalyst for dye degradation even in the dark that can be utilized for industrial purposes. Moreover, a multifaceted self-charging, flexible piezo-active device was designed using the same composite that was capable of harvesting mechanical energy and storing the electrical energy separately/simultaneously as a sole unit.

9.2. Experimental section

9.2.1. Materials

To synthesize $NdMnO_3$, neodymium oxide (Nd_2O_3) (99.99 % trace metal basis) was purchased from Sigma Aldrich whereas manganese acetate tetrahydrate ($((CH_3COO)_2Mn.4H_2O)$), nitric acid (HNO_3), Ethylene glycol and citric acid were bought from Merck Chemicals. N, N-dimethylformamide (DMF, anhydrous, 99.8%), N-methyl pyrrolidine (NMP), PVDF, H_3PO_4, and PVA used in the synthesis of films, were bought from Merck Chemicals and Alfa Aesar, respectively. All the chemicals used to carry out this work maintained analytical grade.

9.2.2. Synthesis of $NdMnO_3$ nanoparticles

$NdMnO_3$ nanoparticles were synthesized by sol-gel method [21]. Nd_2O_3 and $(CH_3COO)_2Mn.4H_2O$) were mixed in stoichiometric ratio and converted to the respective nitrates by adding a few drops of conc. HNO_3 to the precursors. The nitrate solution was allowed to boil for 15 minutes to remove excess HNO_3. To mix the metal ions in an atomic scale, a proper amount of citric acid was added to the solution. Considering that only two of the citrate ions take part in chemical bonding with metal ions, the amount of citric acid was estimated such that all the metal ions form metal citrate [22]. Ethylene glycol was added later on to the mixture and stirred for 4 hours to form a homogeneous solution. The solution was then kept at 80 ^oC for 12 hours to obtain the gel. The gel was kept at 200 ^oC for until it became brownish powder. The powder was heated at 600 ^oC and 800 ^oC respectively, each step for 6 hours, followed by intermediate grinding to form well-crystallized oxides.

9.2.3. Preparation of films

PVDF solution was prepared by dissolving 100 mg pure PVDF in 1 ml DMF by continuous stirring the mixture at 60 ^oC for 4 hours. Next, 3, 5, 7, 10 wt % (w/w) of $NdMnO_3$ nanoparticles were added to the stock solution and kept stirring at room temperature for 24 hours. The transparent stock solution became black on addition of $NdMnO_3$ nanoparticles. The composite precursor solutions were ultrasonicated for 45 mins and then casted on glass slide to obtain the composite films by annealing at 90 ^oC for 2 hours followed by annealing at 130 ^oC for 3 hours [23]. This annealing procedure helps to enhance the piezo-active phase of the film.

$NdMnO_3$@PVDF composite films of different concentrations are designated as NMO_X films with X = 3, 5, 7, and 10.

9.2.4. Fabrication of hybrid piezoelectric and triboelectric nanogenerators (PTNGs)

To design a hybrid piezoelectric-triboelectric nanogenerator (PTNG), a Cu electrode was attached on one side of NMO_X film to form the bottom electrode. Then, a uniform layer of polydimethylsiloxane (PDMS) is casted on a separate Cu electrode and dried at 60 ^{o}C for 2 hours. The hybrid device was structured as Cu electrode/ NMO_X film/ Air gap (~100 μm)/ PDMS layer/ Cu electrode and designated as PTNNG_3 for PTNNG_5, PTNNG_7 and PTNNG_10. An NG using pure PVDF films is also designed following similar steps for reference purposes (RNG). Two Cu wires were soldered on both sides of each of the NG for connection purposes.

9.2.5. Fabrication of piezoelectric nanogenerators (NGs)

To design a piezoelectric nanogenerator, two Cu electrode was attached on either side of NMO_X film to form a sandwich structure. Finally this sandwich is laminated in order to get rid of any air bubble trapped between the film and electrode. Thus the lamination may assure the absence or significant reduction of tribo effect. The nanogenerator was configured as Cu electrode/ NMO_X film/ Cu electrode and designated as NNG_3 for NNG_5, NNG_7 and NNG_10. An NG using pure PVDF films is also designed following similar steps for reference purposes (RNG). Two Cu wires were soldered on both sides of each of the NG for connection purposes.

9.2.6. Piezo-catalysis study

A NMO_7 film of dimension 2.5 cm × 1.5 cm and thickness ~ 40 μm was immersed in 15 ml of 5 ppm aqueous solution of methylene blue (MB) dye. The beaker containing the above mixer was subjected to a bath sonicator so that the film is exposed to ultrasonic waves. After sonication for a desired time, a small portion of the solution was pipetted out. The concentration of residual MB in the filtrate was determined by JASCO V 650 UV–VIS spectro-photometer. The catalytic experiment was carried out in dark to avoid the photo effect and the temperature was maintained at 28 ^{o}C.

9.2.7. Preparation of the electrodes and fabrication of self-charging piezoelectric supercapacitor

At first, as-synthesized $NdMnO_3$, graphite powder, and PVDF were mixed in the ratio 85:10:5 and dispersed in NMP to prepare a homogeneous slurry. The slurry was coated uniformly on the surface of two flexible steel plates used as symmetric electrodes (the effective area of each plate is 1.5 cm × 1.5 cm) and dried at 50 ^oC for 5 hours. To fabricate the self-charging piezoelectric supercapacitor (SCPS), NMO_7 was used as piezo-separator soaked in gel electrolyte H_3PO_4/PVA. The gel electrolyte was prepared by mixing 1g of H_3PO_4, 3g of PVA, and 20 ml of DI water following rigorous stirring at 90 ^oC until a homogeneous solution was achieved. The separator was then sandwiched between two prepared electrodes to design the device. Furthermore, the device was laminated to provide safeguard.

9.3. Characterization

The XRD analysis of synthesized $NdMnO_3$ nanoparticles as well as $NdMnO_3$@PVDF films were obtained from X-ray diffractometer (Bruker D8). The surface morphology of the both the nanoparticles and the composite films was performed by FESEM (FEI, INSPECT F50). The FTIR pattern was obtained from PerkinElmer, Spectrum – 2000. The open circuit voltage response was recorded using digital storage oscilloscope (Keysight, 1052A) and the short circuit current was measured using Kiethley 2602B. The values of d_{33} of the films were measured using a d_{33} meter. UV-Vis spectroscopy was carried out using JASCO V 650 spectrophotometer. The dielectric properties of all the films were analyzed by Agilent 4294A impedance analyzer. The PE loop was measured using a Precision Premier II ferroelectric tester. The electrochemical measurement was carried out with the help of PGSTAT 302N autolab.

9.4. Result and discussions

9.4.1. Structural and morphological characterization of $NdMnO_3$ nanoparticles

The X-ray diffraction pattern of $NdMnO_3$ using CuK_α radiation is illustrated in Fig. 9.1a. We have performed Rietveld refinement using MAUD software that confirms no presence of

impurity or spare peaks in the sample. $NdMnO_3$ possesses orthorhombic phase (JCPDS PDF

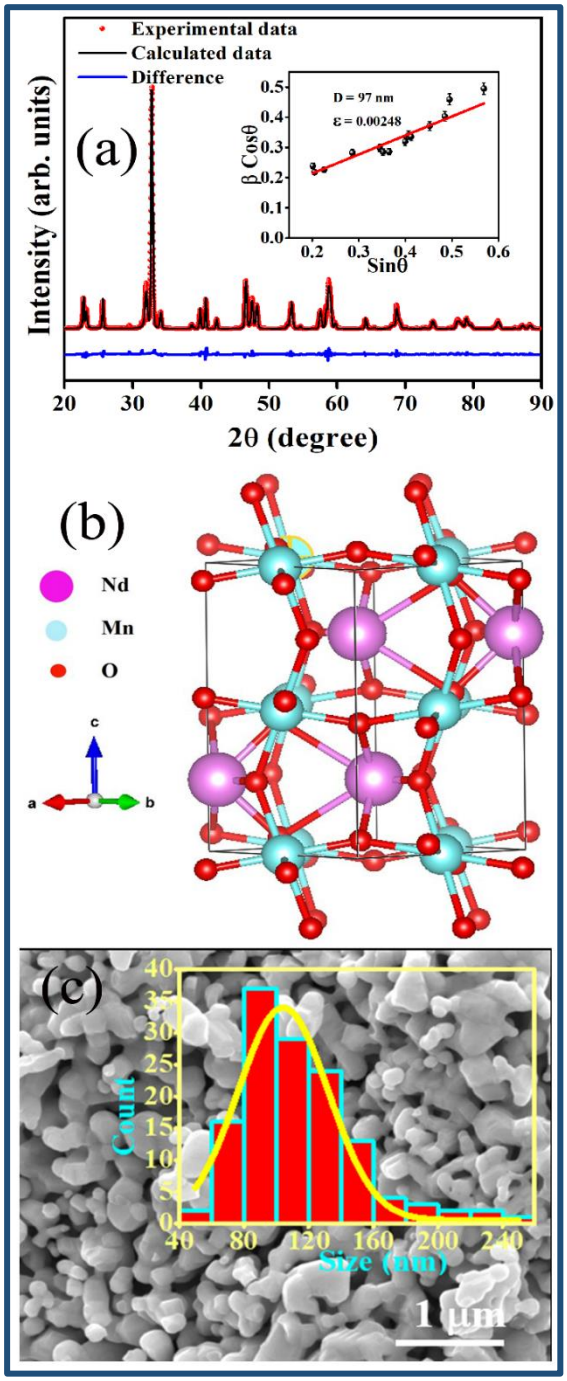

Fig. 9.1. (a) The XRD pattern. Inset of (a) The Williamson Hall plot to determine the crystallite. (b) The atomic model. (c) SEM image. Inset of (c) Distribution of the corresponding particle size size of sol-gel derived black colored $NdMnO_3$.

card no. # 25-0565) that belongs to *Pbnm* space group with a = 5.43010 Å, b = 5.59210 Å, c = 7.65060 Å, unit cell volume 232.3155 $Å^3$. The crystallite size (D) and microstrain (ε) of $NdMnO_3$ are estimated using Williamson and Hall's modified Scherrer's equation [21]

$$\beta cos\theta = \frac{0.89\,\lambda}{D} + 2\varepsilon\, sin\theta \quad (1)$$

Taking under consideration the prominent XRD peaks having uniquely defined FWHM a linear fit of $\beta\cos\theta$ versus $\sin\theta$ plot is shown in the inset of Fig. 9.1a. The average crystallite size and the microstrain of $NdMnO_3$ nanoparticles are estimated to be 97 nm and 0.00248, respectively. The atomic model of the synthesized sample is depleted in Fig. 9.1b. The morphology of the as-synthesized $NdMnO_3$ nanoparticles is characterized by field emission scanning electron microscopy (FESEM). Figure 9.1c depicts the FESEM images of the particles. The size of the particle follows the Gaussian distribution (inset of Fig. 9.1c) with the maximum number of particles around 100 nm which is consistent with the XRD results.

9.4.2. Structural analysis and estimation of electroactive phase: XRD, EDX, and FT-IR studies

The XRD patterns of neat PVDF film and NMO_X films with X = 3, 5, 7, and 10 are illustrated in Fig. 9.2a. The non-polar α phase is found to be absent in NMO_X films. Moreover, the degree of crystallinity of the filler-added and pure PVDF films is quantified by using the relation [24]

$$\times_{C_t} = \frac{\sum A_C}{\sum A_C + \sum A_{amp}} \times 100 \quad (2)$$

Here, $\times_{C_t}$ represents the total degree of crystallinity, where $\sum A_C$ and $\sum A_{amp}$ denote the total crystalline and amorphous area, respectively. Figure 9.2b illustrates the variation of $\times_{C_t}$ of the films with X, the wt % of $NdMnO_3$. It shows that NMO_7 acquires the maximum value of $\times_{C_t}$ ~ 86.67 % amongst all the films.

For elemental analysis of $NdMnO_3$ in the film, NMO_7 as a representative member of the series NMO_*X* was selected, and EDX measurement was performed. Fig. 9.2c depicts the energy-dispersive spectra (EDX). The ratio of oxygen to Nd atom is approximately ~ 3-δ. However, the value of δ may not be claimed with high precision from the EDX experiment only.

The FT-IR spectra of all the films as shown in Fig. 9.2d are investigated to evaluate the electroactive phase content of the films both in the presence and the absence of the perovskite-filler within the PVDF matrix. Figure 9.2e indicates that up to NMO_7, the polar, electroactive β phase (corresponding band at 842 cm^{-1} and 1282 cm^{-1}) significantly enhances and then is

found to decrease in the case of NMO_10. It is also evident that the non-polar α phase is

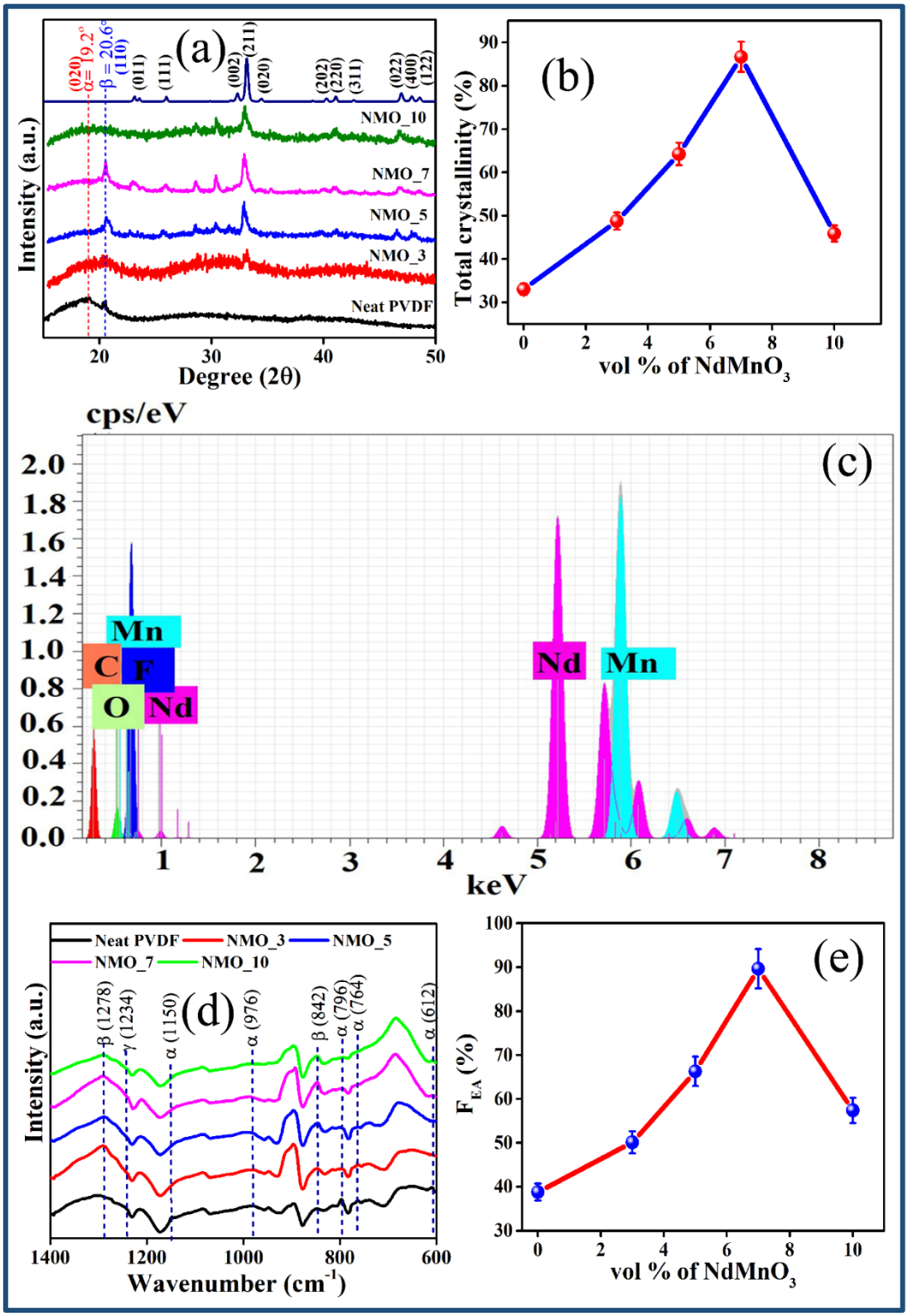

Fig. 9.2. shows (a) XRD patterns of the NMO_X films with X=0, 3, 5, 7, 10. (b) Plot of crystallinity of the films vs. vol. % of the nanofiller. (c) EDX spectra of NMO_7. (d) FTIR spectra of the composite films. (e) Variation of F_{EA}% vs. vol. % of the nanofiller

completely converted to the β phase in NMO_7. Thus, the non-toxic $NdMnO_3$ filler can be an appropriate choice to produce remarkable enhancement of the electroactive phase. The relative electroactive phase component (F_{EA}) of each film is evaluated using the relation [25–27]

$$F_{EA} = \frac{A_{842}}{\left(\frac{K_{842}}{K_{764}}\right)A_{764} + A_{842}} \times 100 \qquad (3)$$

Here, A_{764} and A_{842} are the respective integral area of absorbance bands at 842 cm^{-1} and 764 cm^{-1}, the corresponding absorption coefficients are $K_{842} = 7.7 \times 10^4$ cm^2 mol^{-1} and $K_{764} = 6.1 \times 10^4$ cm^2 mol^{-1}. The variation of $F_{EA}$with X, the wt% of the $NdMnO_3$ in PVDF matrix is shown in Fig. 9.2e. NMO_7 achieves the highest value of F_{EA} ~ 89.71 % which is in tune with the XRD outcome.

9.4.3. Surface morphology of composite films

The surface morphology of neat PVDF and NMO decorated PVDF films are illustrated in Fig. 9.3a–e. The surface of PVDF film is observed as dense, pores-free, and smooth. On the contrary, the surfaces of NMO_X films with X = 0, 3, 5, 7, and 10 films have spherical pores distributed on the surface. During prolonged stirring in open ambiance, water molecules may get absorbed in the solution from the air. These water molecules evaporate quite faster than the solvent DMF due to lower boiling point which results in pores structure throughout the surface of the film. Some of these pores are occupied by $NdMnO_3$ nanoparticles. The homogeneous distribution of $NdMnO_3$ throughout the surface is observed in the films with higher filler content. The inset of Fig. 9.3a-e shows the digital photograph of the prepared films. The flexibility of NMO_7 is illuminated in Fig. 9.3d. Cross-sectional view of the NMO_7 film revealing 40.4 μm thickness is illustrated in Fig. 9.3f.

9.4.4. Dielectric behavior of the composite films

The dielectric response of NMO_X films with X = 0, 3, 5, 7, and 10 over $4\ Hz \leq f \leq 8MHz$ are shown in Fig. 9.3g that depicts the rise in the dielectric constant of PVDF film in presence of $NdMnO_3$. The Inset of Fig. 9.3g depicts that the real part of permittivity increases with the increase in filler content at high frequency region. The interfacial polarization and porous structure of the films play the key role in the dielectric property of the films specifically in low

frequency region[28,29]. The dielectric constant of NMO_10 enhances almost 3 times that of

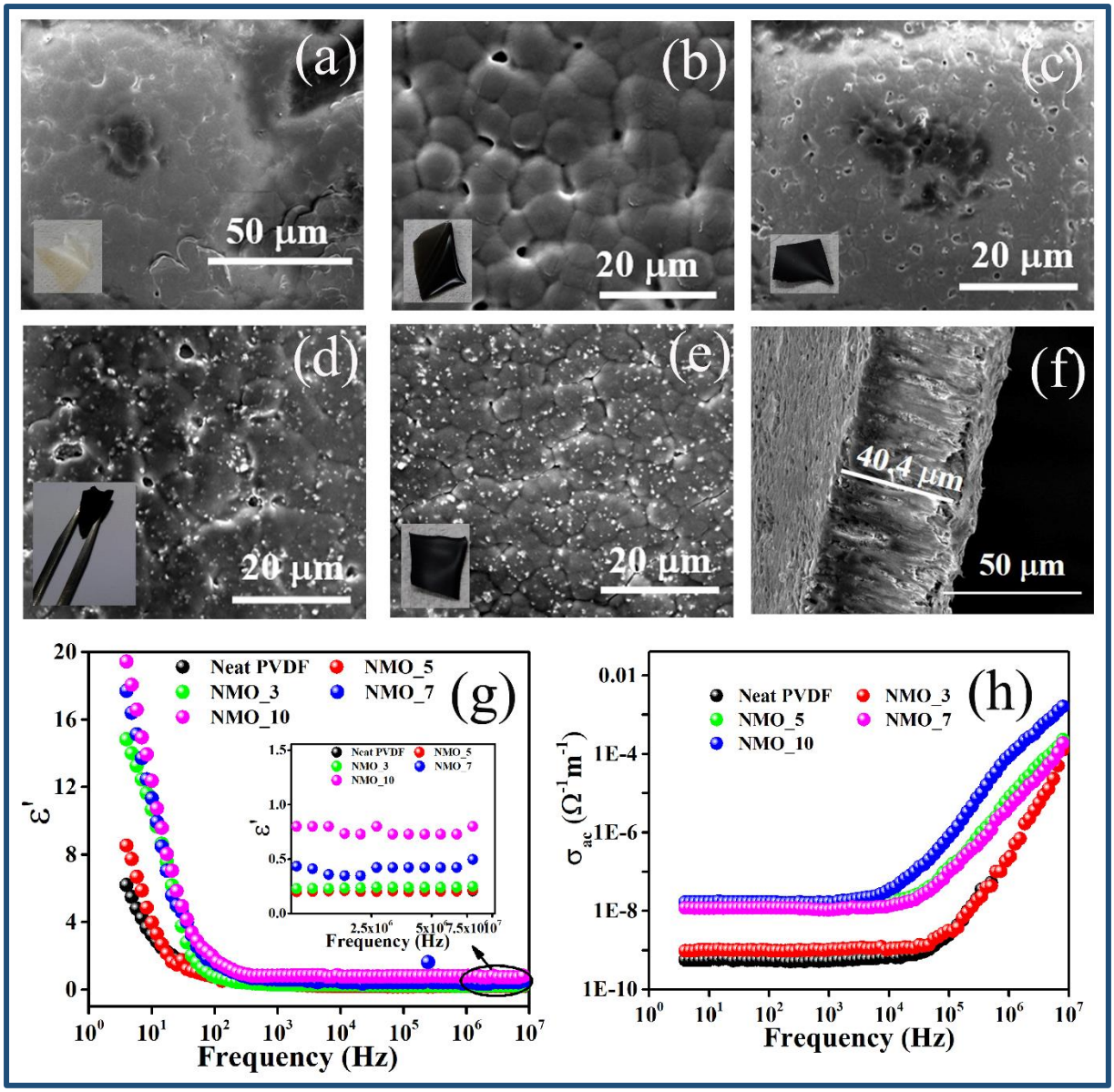

Fig. 9. 3. (a)-(e) SEM images of the pure PVDF and composite films. Digital photographs of the films and the flexibility of NMO_7 are exhibited in the inset of the corresponding SEM images. (f) Thickness of NMO_7 film. (g)-(h) The dielectric behavior and conductivity study of all the films.

pure PVDF film in low frequency domain owing to the contribution of interfacial polarization. NMO_40 is found to achieve the highest dielectric constant too in high frequency region. The conductivity of all the films has been evaluated using $\omega\varepsilon_{0\varepsilon}\varepsilon' tan\delta$ [28,30]. The frequency variation of the AC conductivity of NMO_X films with X = 0, 3, 5, 7, and 10 is shown in Fig. 9.3h. The Inset of Fig. 9.3h illustrates the appreciable enhancement of the AC conductivity with the increase in filler content in the film. The flattened portions of the conductivity curves

in low frequency region represent the DC portion and highly frequency dispersive regions appear owing to the AC contribution.

9.4.5. Output response of the fabricated nanogenerators

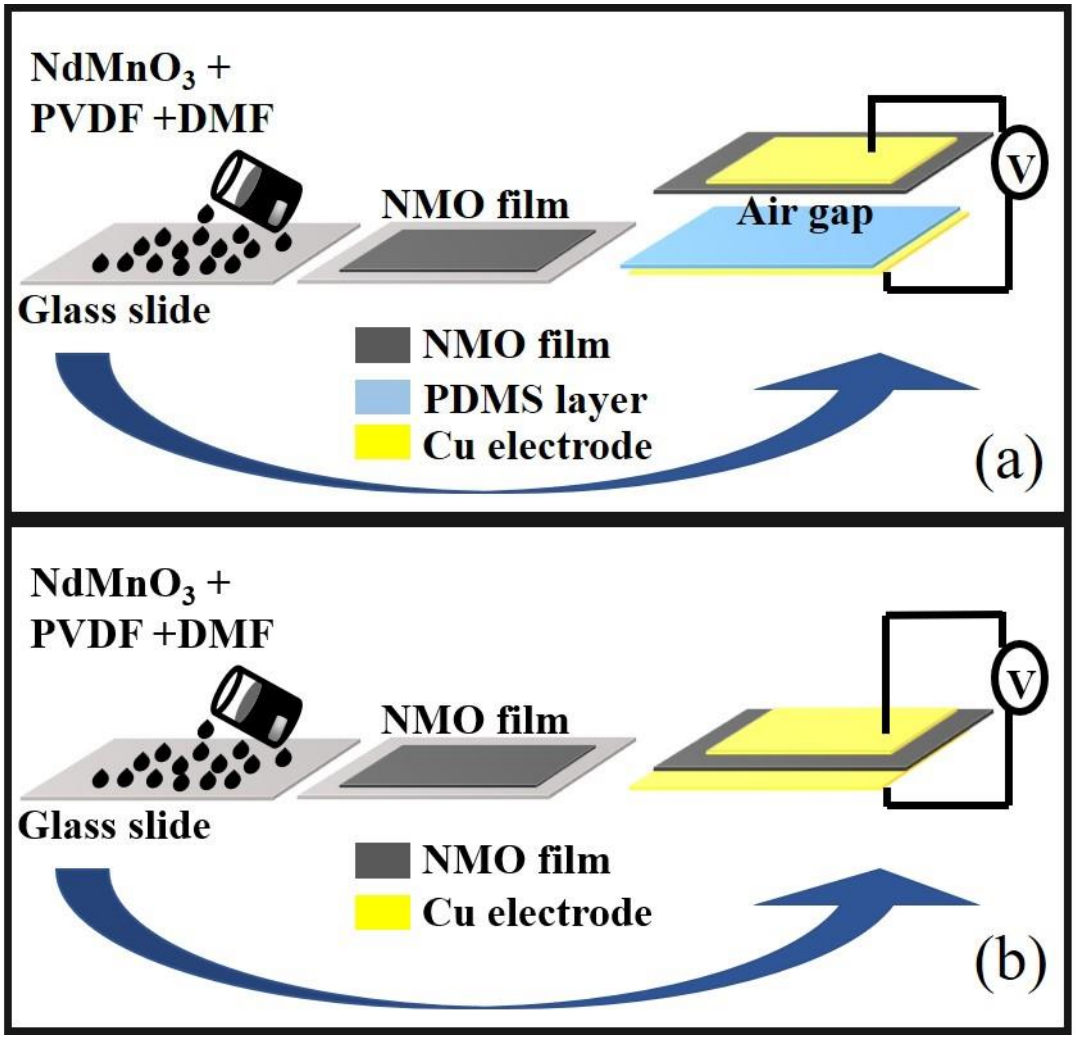

Fig. 9.4. depicts the schematic diagrams of the fabricated nanogenerators.

The step-by-step fabrication process of the PTNGs is illustrated in the form of a schematic in Fig. 9.4a. To have a glimpse of tribo effect, a hybrid device was fabricated as Cu electrode/ NMO_X film/ Air gap (~100 μm)/ PDMS layer/ Cu electrode. This hybrid device (PTNNG_7) exhibits enormously large V_{OC} (~ 160 V) for X = 7 as reported in the Fig. 9.6a.

The working mechanism of the hybrid nanogenerator is illustrated in schematic form in Fig. 9.5. Initially, no potential difference occurs between the two electrodes as no charge is generated in the absence of the relative motion of the layers and the deformation of the

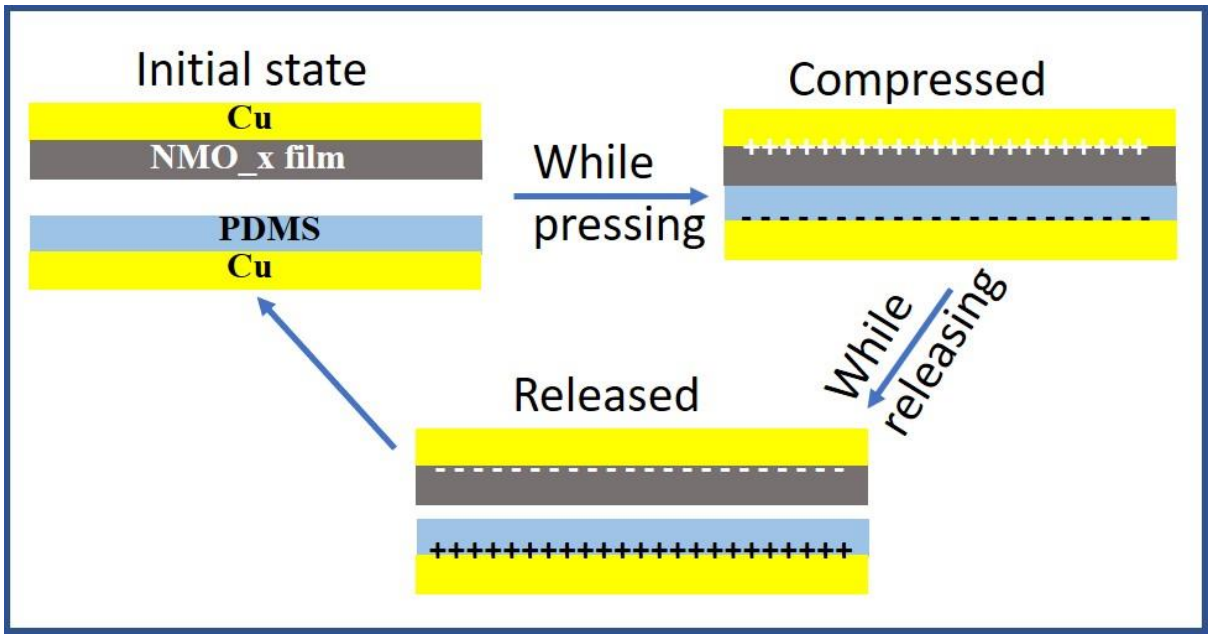

Fig. 9.5. exhibits the working mechanism of the hybrid nanogenerators.

piezoelectric layer. Due to the application of the external mechanical force, different layers ($NdMnO_3$@PVDF and PDMS) come in contact causing the deformation of the device and so the deformation of $NdMnO_3$@PVDF. Firstly, positive, and negative charges are generated in the piezoelectric functional layer under compressive stresses. In the meantime, the PDMS surface which comes in contact with the $NdMnO_3$@PVDF layer is also charged due to the triboelectric effect. On the other hand, the continuous releasing process separates the PDMS layer with an air gap from the NMO layer. The generated potential difference leads to the output electrons flowing in the circuit between two concerned frictional layers. When the two triboelectric layers get separated during the removal of the mechanical force, the charges at the surfaces do not neutralize immediately. Rather, a potential difference occurs between the two concerned electrodes that drive the electron to transfer from one electrode to the other one to generate an electrical signal in the opposite direction. When the separation distance retains its original value, the potential difference is fully offset by the flow of electrons between the electrodes, and hence no electric signal is produced.

In order to study the intrinsic effect of piezoelectricity of the NMO_X film only, tribo

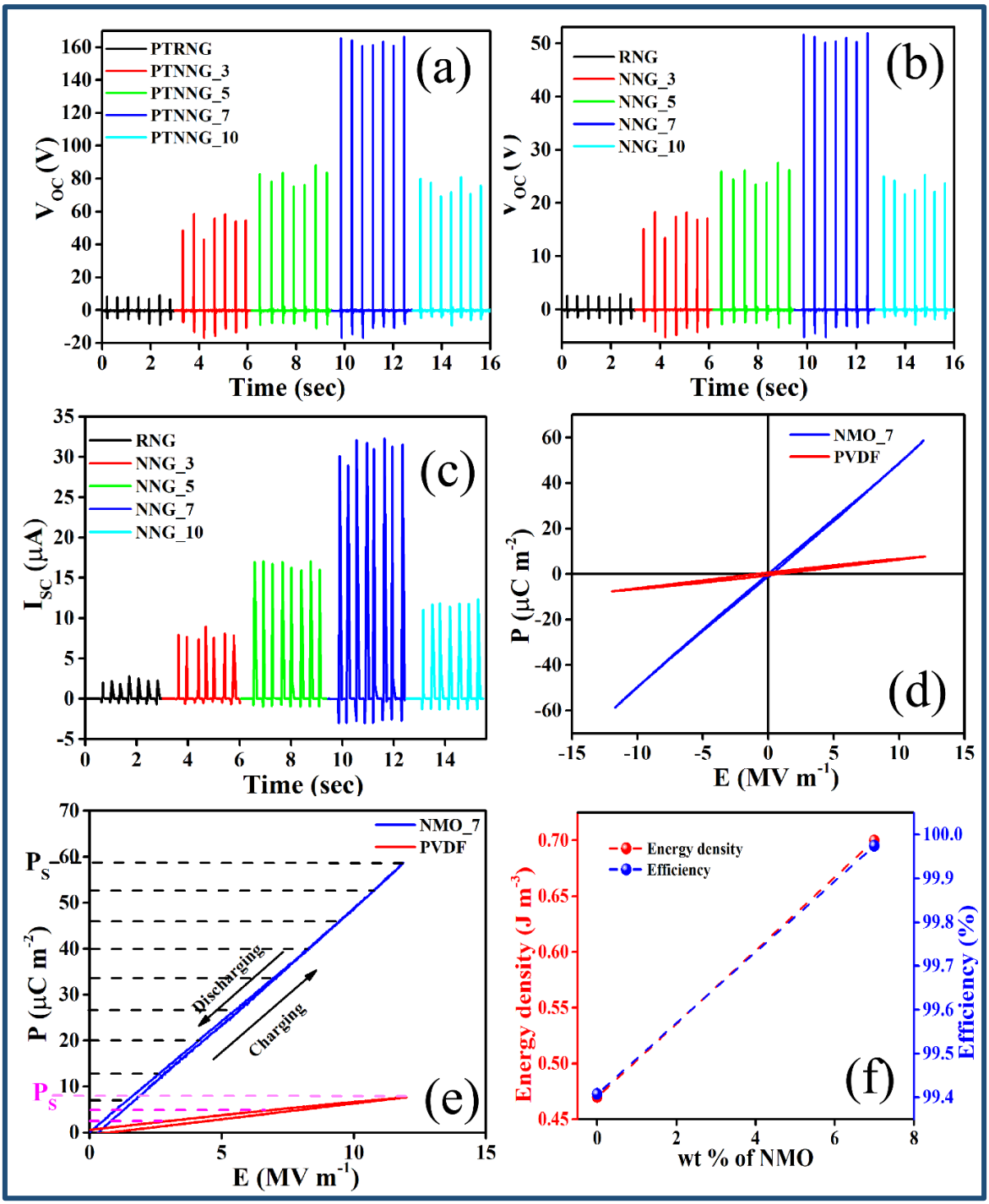

Fig. 9.6. (a) V_{OC} of the designed hybrid nanogenerator. (b)-(c) V_{OC} and I_{sc} of the fabricated NNGs under hammering with free hand. (d) PE loop of NMO_7 and PVDF. (e) Saturation polarization of both the films. (f) Energy density and efficiency of both the films.

effect is to be minimized and so the device was prepared with sincere care to get rid of any air trapped between the film and electrodes as shown in Fig. 9.4b. The piezoelectric response of the fabricated NNGs and RNG are studied to investigate the effect of the $NdMnO_3$ nanofiller

within PVDF matrix. The open circuit voltage (V_{OC}) and short circuit current (I_{sc}) produced by the concerned NGs under repetitive hammering with free hand is illustrated in in Fig. 9.6b and 9.6c, respectively. Amongst all NGs, NNG_7 exhibits the highest response, i.e., 50 V V_{OC} and 30 μA I_{sc} under periodic hammering with a free hand whereas RNG produces 3 V V_{OC} and 2 μA I_{sc} under similar pressure. Almost 17 times V_{OC} and 15 times I_{sc} exhibited by NNG_7 compared to that of RNG complements the β phase enhancement as inferred from XRD and FTIR analysis. To assess the piezoelectric contribution, the piezoelectric coefficient (d_{33}) of NMO_7 was measured by d_{33} meter and obtained as 32.2 pC/N which is effectively very high compared to that of neat PVDF (17.8 pC/N). To determine the ferroelectric nature of the films at room temperature, we have recorded the polarization (P) vs. electric field (E) hysteresis loops for pure PVDF film and NMO_7 (Fig. 9.6d) since NMO_7 not only possess superior electro-active phase content, enhanced crystallinity but also exhibits significantly improved V_{OC} and I_{sc}. Figure 9.6e depicts that the saturation polarization (P_S) of NMO_7 is higher than that of pure PVDF. The shaded regions refer to the energy stored by the films and the corresponding energy density and efficiency have been plotted in Fig. 9.6f.

Since, the output response of the NNG_7 is the highest, this device was used to perform various experiments to understand its sensitivity and efficacy. The sensitivity of the fabricated NNG_7 is examined by hammering it with various lightweight objects like tooth pick, pen, thermocol, etc. is exhibited in Fig. 9.7a that not only indicates its ultra-sensitivity but also confirms its utility in nano tactile sensing. The mechano-sensitivity [31] ($S_M = \frac{\Delta V_{OC}}{\Delta F}$) of the hybrid NNG_7 was considerably high ~7.81 V/N obtained from the voltage response under the application of different forces (forces were measured using a load cell as shown in Fig. 9.7b inset). The voltage outcome of NNG_7 under gentle repeated heel pressing device ensures its potential as a wearable sensor (Fig. 9.7c). Figure 9.7d demonstrates the response of NNG_7 when subjected to a phone vibration. The device was attached on the outer surface of a beaker full of water kept under ultrasonic vibration and the corresponding output response of the device is displayed in Fig. 9.7e. Furthermore, the NNG_7 was placed inside a beaker full of water to assess the sensitivity of the water wave produced due to the ultrasonic vibration (Fig. 9.7f). These outcomes suggest that NNG_7 can be an appropriate choice as a vibration sensor. Furthermore, the device was attached on a mouse connected to the computer. The voltage response on repetitive clicks on the mouse is shown in Fig 9.7g. A piece of paper was placed

on NNG_7 and the illustrated outputs (Fig. 9.7h) on writing a few alphabets assure that the

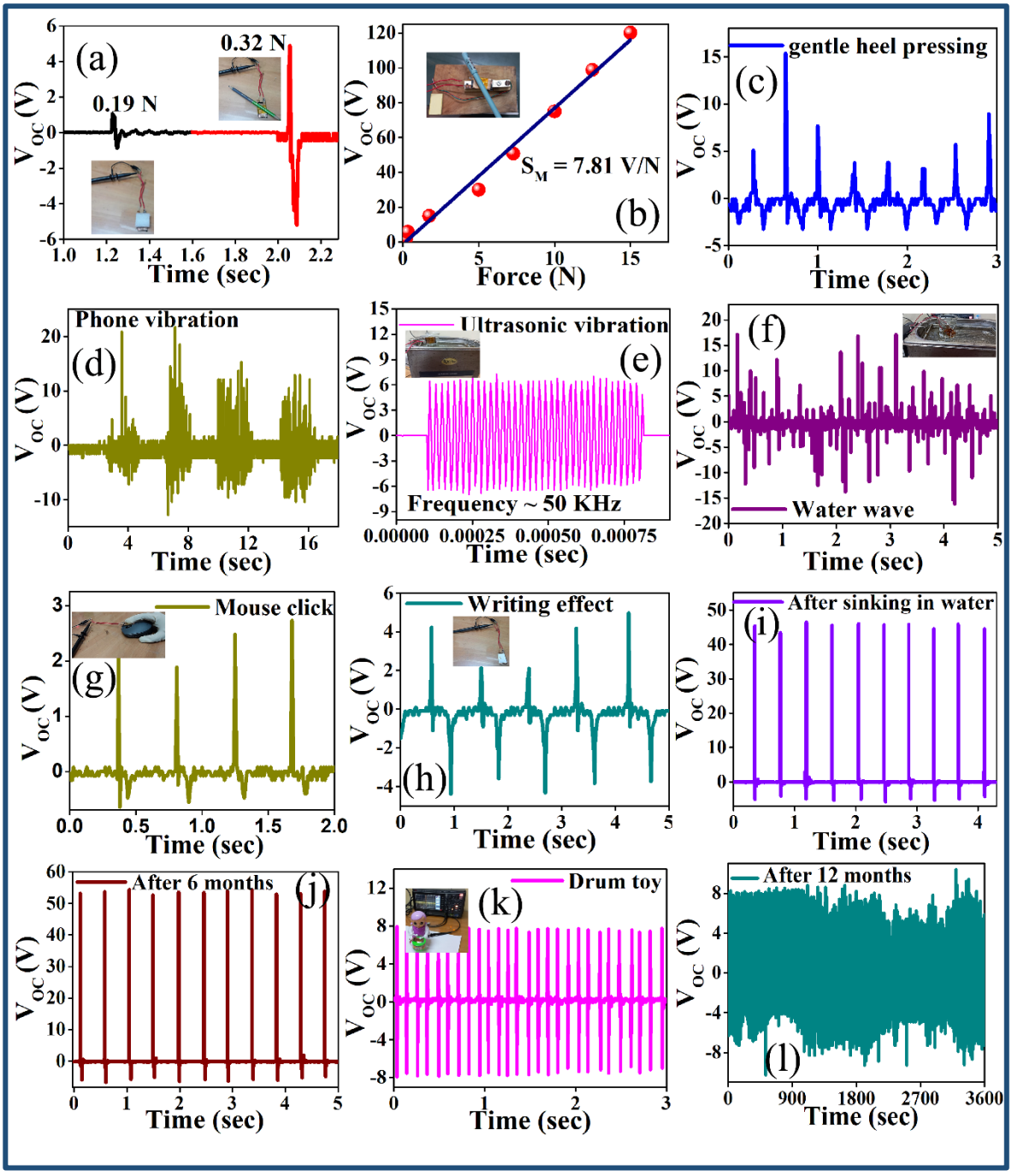

Fig. 9.7. Voltage response of NNG_7 under several conditions (a) pressure imparting with very light weight objects, (b) mechano-sensitivity of NNG_7 computed from load cell, (c) gentle heel pressing, (d) phone vibration, (e) ultrasonic vibration, (f) wave motion, (g) mouse click, (h) writing on a piece of paper placed on the device, (i) hammering with free hand after drowning the device under water for 24 hours, (j) stability checking by hammering with free hand after 6 months of the fabrication, (k) Voltage output of NNG_7 in response to a drum toy at the time of fabrication, (l) Stability test after 12 months of fabrication in large cycle.

device can be used as a smart writing board sensor. Next, the efficacy of the device is further

assessed in water by drowning NNG_7 in a beaker full of water for 24 hours. After 24 hours, measured V_{OC} under periodic hammering with free hand was interestingly obtained as before (Fig. 9.7i). The excellent stability of the device under water makes it a desired wearable sensor in wide applications. Furthermore, the performance of the device was tested after 6 months of the fabrication and observed a similar voltage response (Fig. 9.7j) without any significant decay under similar pressure. To investigate the stability of the NNG_7 in a large cycle, the device was hammered by a toy. The corresponding V_{OC} is exhibited in Fig. 9.7k that was recorded at the time of fabrication of the device. The similar performance of the device obtained in response to the drum toy in an appreciably large cycle after 12 months of fabrication confirms its excellent stability (Fig. 9.7l).

NNG_7 was connected to various load resistances (R_L) ranging from 3KΩ to 20 MΩ and the corresponding voltage response (V_L) was measured as illustrated in Fig. 9.8a to compute the internal resistance of the concerned device. The schematic diagram of this circuit is illustrated in the inset of Fig. 9.8a. The corresponding load current density (I_L) is calculated using the relation

$$I_L = \frac{V_{pp}}{A \times R_L} \qquad (4)$$

Here, V_{pp} refers to the peak-to-peak load voltage and A denotes the effective area of contact of NNG_5 (2.5 cm × 1.5 cm).

The output power density is further evaluated using the relation

$$P = V_{pp} \times I_L \qquad (5)$$

As depicted in Fig. 9.8b, the power density becomes maximum (~35.33 mW/cm^2) for R_L = 3.96 MΩ. This corresponds to the internal resistance (R_i) of NNG_7 using the maximum power transfer theorem [32]. To assess the ability of NNG_7 as a mechanical energy harvester, it was connected to several green and blue LEDs through a full bridge rectifier circuit to light up under simple hammering with free hand. The rectified circuit diagram is illustrated in Fig. 9.8c. The produced instantaneous power is found to be sufficient to glow up these LEDs as observed in Fig. 9.8d. The Generated power output was attempted to store in a commercially available external capacitor. The voltage response of a 3.3 μF capacitor attains a maximum voltage of 13.2 V (V_c^{max}) as depicted in Fig. 9.8e. The equivalent energy ($1/2CV_c^{max\,2}$) stored

in the capacitor is 287.47 μJ. The internal capacitance of NNG_7 is computed using the RC

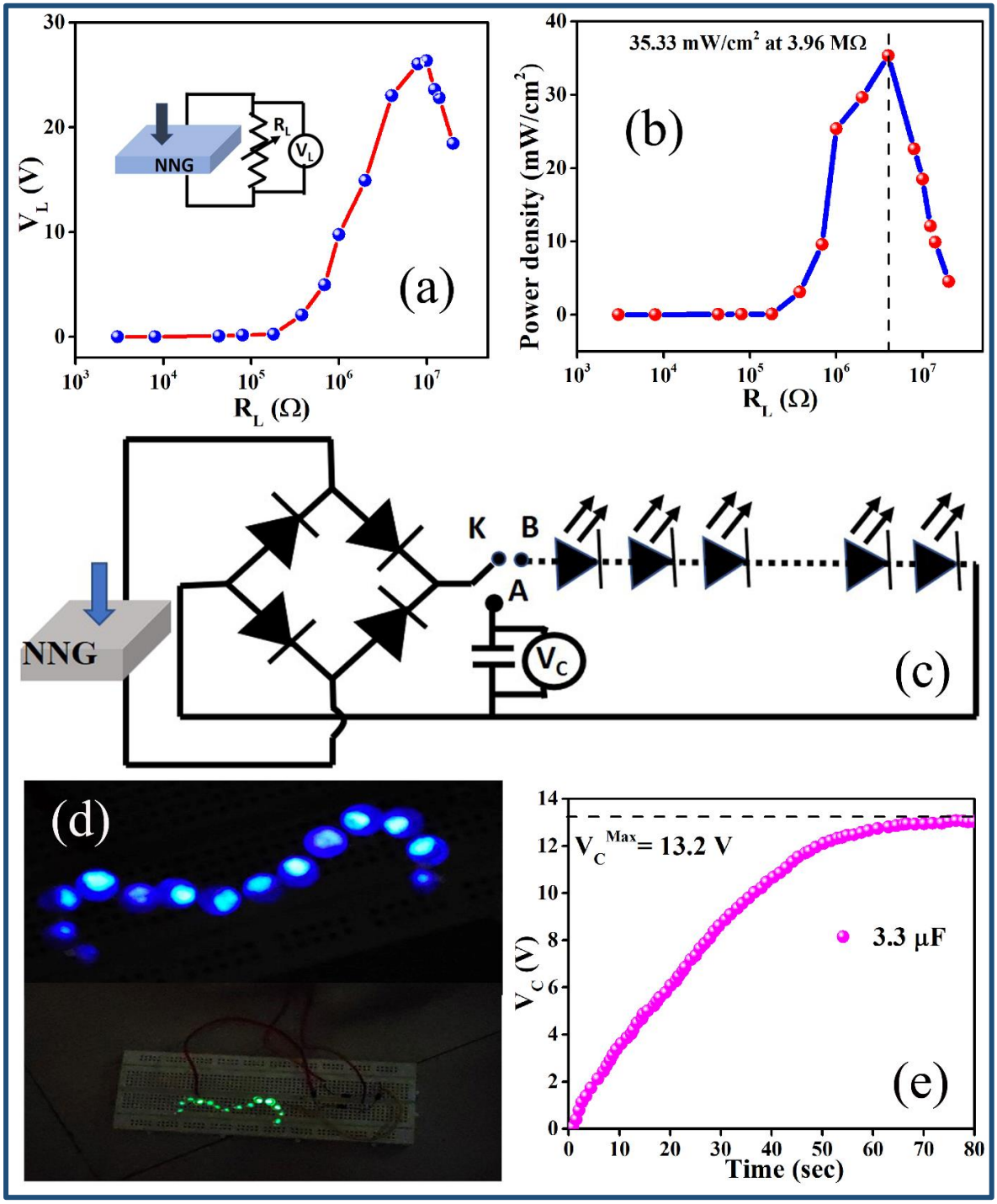

Fig. 9.8. (a) Voltage response of NNG_7 across several load resistances. Inset of (a) Corresponding schematic diagram of the circuit (b) Plotting of power density of NNG_7 across the load resistances. (c) A schematic diagram referring the full bridge rectifier circuit. (d) Glowing up LEDS. (e) Capacitor charging by NNG_7.

circuit model.

$$\tau = R_i C_T \qquad (6)$$

Here, τ, the time constant, is calculated as 28.82 sec. C_T represents the total capacitance of NNG_7. Now, the internal capacitance (C_i) is estimated as 3.9 μF employing the relation [33]

$$C_T = C_i + C \quad (7)$$

The computed R_i and C_i suggest NNG_7 as a potential candidate for energy harvesting. Furthermore, the aforesaid experimental results confirm its ability as an energy source to run small-powered miniature devices. The desired flexibility, ultra-sensitivity, and excellent stability in the air, as well as water medium, ensure its utility not only as a wearable sensor but also in the biomedical industry as it is lead free non-toxic energy harvester.

9.4.6. Piezoelectric dye degradation

To get more insight into the piezoelectric efficacy of NMO_7, the piezocatalytic activity of NMO_7 has been studied by analyzing the degradation of methylene blue (MB) dye aqueous solution under piezoelectric vibration in dark conditions. The schematic diagram of the working process of the dye degradation by the influence of piezocatalysis is illustrated in Fig. 9.9a. The piezoelectric dye degradation was monitored by computing the change in intensity of the characteristic absorption peak of MB at 663 nm (Fig. 9.9b). Moreover, the apparent change in the color of the dye loaded solution was observed visually after 30 min of ultrasonication which confirms the piezocatalytic property of the concerned film. After 40 min, the dye degraded almost completely and an almost clear solution was obtained. In contrast, the concentration of MB dye remains almost unchanged when a neat PVDF film was used in the identical MB dye aqueous solution and exposed to ultrasonic vibration for the same time as observed in Fig. 9.9c The degradation [34] of MB dye defined as $\epsilon = \frac{C_t - C_0}{C_0}$, measures the degradation efficacy of the piezocatalyst (Fig. 9.9d). Here, C_0 is the initial concentration of the dye and C_t denotes the concentration of the residual dye after time t. The variation of degree of degradation ($\frac{C_t}{C_0}$) with the time[35] of ultrasonication (t) is illustrated in Fig. 9.9e that confirms the degradation of MB reaches by ~ 56 % in just 10 min. However, the concerned film exhibits appreciably catalytic activity in the dark with ~ 90 % degradation in 40 min of mechanical stimulus. The piezocatalytic mechanism of MB degradation is explained in Fig. 9.9f. Incorporation of $NdMnO_3$ in PVDF produces self-poled piezoelectric composite. Under the continuous exposure of ultrasonic waves, piezoelectric field is generated across $NdMnO_3$ @PVDF film due to the separation of positive and negative charges. These charges (+ve and -

ve) accumulate on the opposite side of the surface of the film. Oxygen (O_2) molecules dissolved

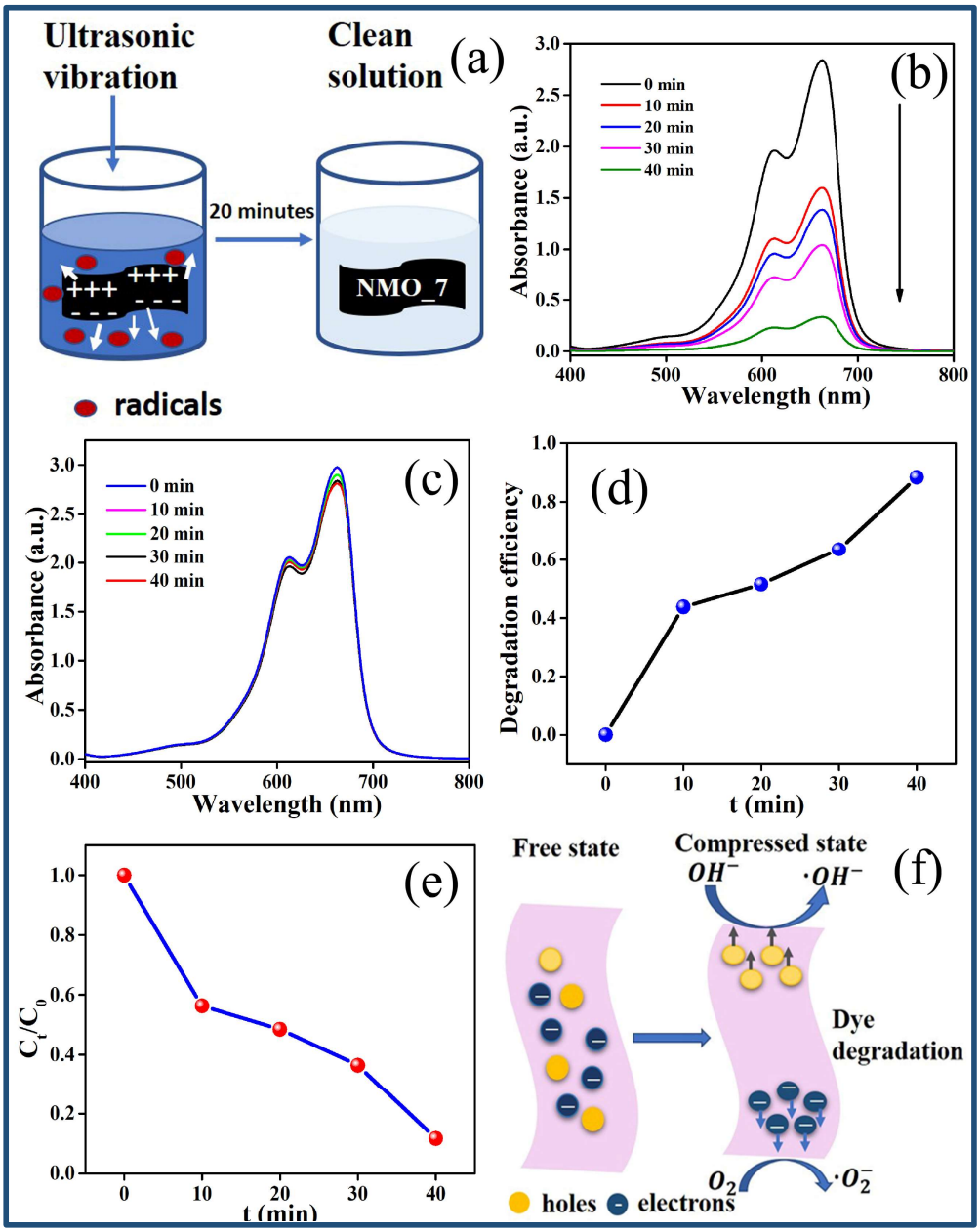

Fig. 9.9. (a) Working mechanism of piezocatalysis, (b) Absorbance spectra in presence of NMO_7 at different interval. (c) Absorbance spectra in presence of neat PVDF at several intervals. (d) Degradation efficiency of NMO_7 is plotted against time. (e) Variation of ($\frac{C_t}{C_0}$) with time. (f) Schematic representation of the reaction mechanism of piezo-catalyst.

in solution, receive the electron from the mechanical vibration induced –ve charges to form superoxide anion radical ($\bullet O_2^-$) while the positive charges get the electron from the surface-

bound H_2O and OH^- to produce hydroxyl radicals (•OH). These $\bullet O_2^-$ and $\bullet OH$ radicals are the main reactive species for the degradation of organic dye MB.

Furthermore, the film used in photocatalysis was employed again to fabricate a piezoelectric generator following the aforesaid similar configuration that exhibited a similar voltage response without any decay under hammering with a free hand. Hence, it can be confirmed that the concerned film is highly stable even in dye containing aqueous solution.

9.4.7. Electrochemical performance of SCPS device

The electrochemical energy storage property of the fabricated flexible SCPS device was investigated using cyclic voltammetry (CV) and galvanostatic charge-discharge (GCD) analysis within working potential window 1.2 V. The quasi-rectangular shape of all the CV curves scanned at different scan rate indicates that the ion-intercalation pseudo capacitance is responsible for the charge storage at the electrode (Fig. 9.10a). The absence of any redox peak in the CV curves confirms the involvement of the non-Faradic charge storage process of the system. The rise in the current range with the increase in the scan rate (2 mV/s to 100 mV/s) illuminates the good capacitive properties of the device. The areal device capacitance is evaluated as 41 mF cm^{-2} using $C_A = \frac{\int I\,dv}{vA\Delta V}$ (C_A denotes the areal capacitance of the device, $\int I\,dv$ represents the integral area of the CV curve, A is the area of the device, v refers to the scan rate and ΔV is the working potential window)[36] at an applied scan rate of 2 mV/s. It has been observed in Fig. 9.10b that the device capacitance decreases gradually with the increase of the applied scan rate. SCPS exhibits 10.59 mF cm^{-2} when the scan rate is increased by 50 times. Furthermore, the device capacitance was also monitored from GCD analysis using $C_A = \frac{I\times\Delta t}{A\times\Delta V}$ (I is the constant discharging current in A, Δt refers to the discharge time and ΔV denotes the working potential window)[36] at different current densities as displayed in Fig. 9.10c. The areal capacitance is found to be 41.37 mF cm^{-2} at a current density of 2 mA. The variation of the areal capacitance with the rise in current density is exhibited in Fig. 9.10d. To check, the device's stability, the device capacitance was scrutinized during 2000 cycles of charging and discharging at a constant discharging current density of 5 mA. The capacitance retention of 99% of its initial value after completing 2000 cycles assures the potential of the concerned electrode for the application of a supercapacitor. The variation of 1st 11 cycles and the last 11 cycles is shown in Fig. 9.10e suggests no significant change in the values of areal capacitance. Figure 9.10f represents the energy–power response of the device in the form of a Ragone plot.

The energy (E) and power (P) of the SCPS were determined from the CD curves using the

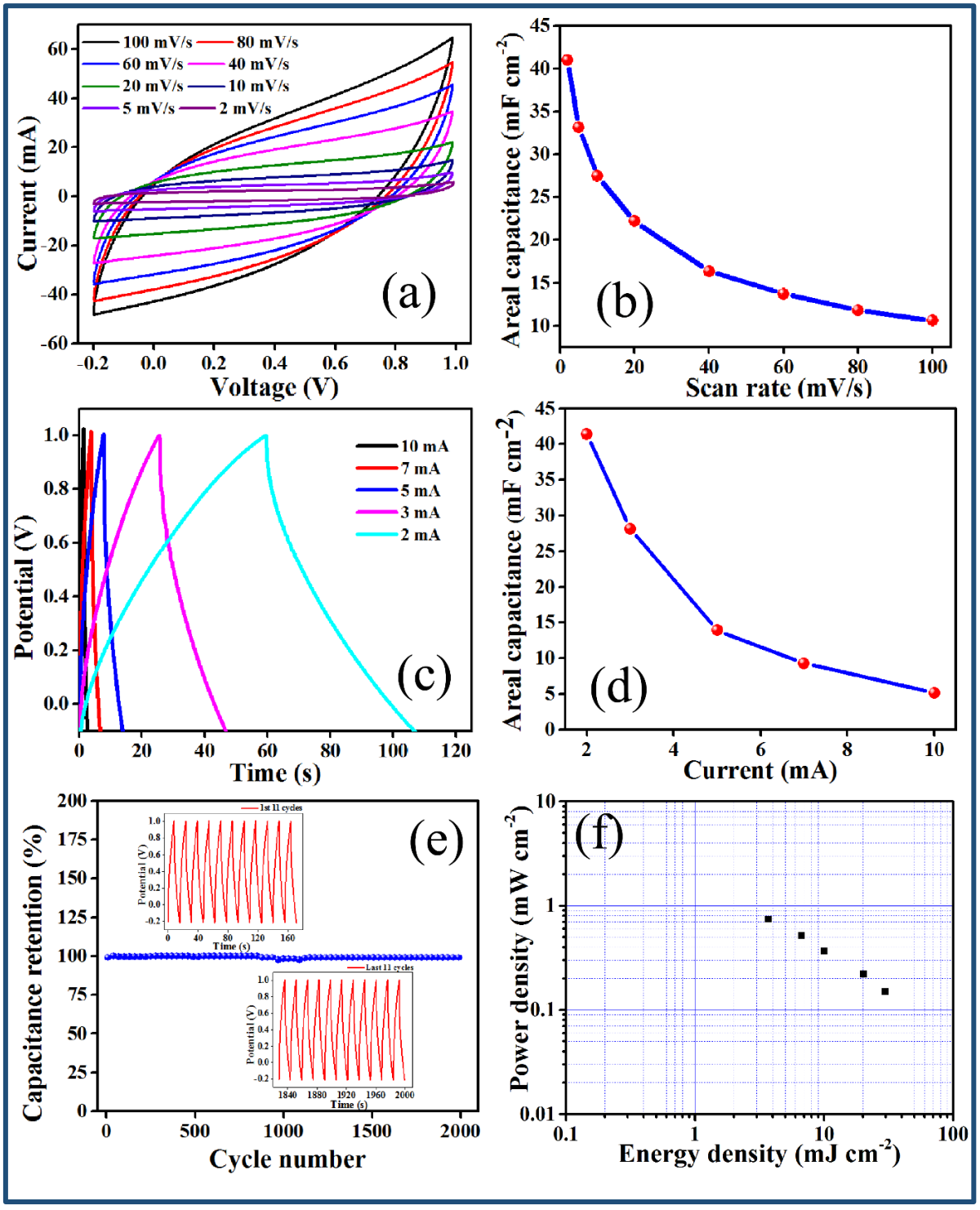

Fig. 9.10. (a) CV curves of SCPS at different scan rate. (b) Variation of areal capacitance of the device with scan rates computed from CV curves. (c) GCD curves of the device at different discharging current. (d) Areal capacitance of the device calculated from GCD spectra. (e) Cyclic stability and capacitance retention of the device. Inset of (e) show the 1st 11 cycles and last 11 cycles. (f) Energy-power performance of the SCPS presented in the form of Ragone plot.

relations[2]

$$E = \frac{C_A \times \Delta V^2}{2} \quad (8)$$

$$P = \frac{E}{\Delta t} \quad (9)$$

9.4.8. Self-charging performance of the fabricated SCPS

Figure 9.11a-c represents the self-charging performances of the as-designed SCPS at different bending angles ranging from 30^o to 90^o. When SCPS is bent repetitively at 30^o, the voltage of the device reaches 436 mV from 23 mV in just 147 that assures its self-charging properties under dynamic strain. The device was further allowed to retain its initial state within 118 s by applying a steady discharge current of 0.1 mA. The device was also periodically bent at 60^o and 90^o to investigate the output self-charging response under mechanical deformation. SCPS attains 590 mV and 890 mV in 146 s when bent at 60^o and 90^o, respectively followed by a discharge to the initial state within 100 s. The increase in the self-charging voltage of the device with the rise in deformation in the form of bending is owing to the piezoelectric effect of the NMO_7. The charging-discharging cycle under periodic bending at 90^o is also checked and displayed in Fig. 9.11d that ensures the device's potential to power various miniaturized instruments run on minimal power. The digital photograph of the illuminating LEDs as illuminated in Fig. 9.11e further assures the storing capacity of the fabricated SCPS.

9.4.9. Working mechanism of SCPS

The self-charging device has been designed using a piezoelectric separator NMO_7 soaked in PVA/H_3PO_4 between two electrodes. Although the working mechanism of the self-charging piezoelectric supercapacitors has been explained in many literatures based on piezoelectrochemical process, the mechanism is still not clear. It can be stated that self-charging piezo-active process lies in the piezoelectrochemical reaction that occurs at the surface of the electrodes and the electrolyte soaked piezoelectric separator. The electrolyte PVA/H_3PO_4 was uniformly spread over the surface of the electrodes and the separator. When the device is subjected to mechanical deformation, positive and negative piezoelectric potential is generated across the piezo-separator that leads to the electrolyte ion migration towards the opposite symmetric electrodes. At the initial state, as an electrochemical equilibrium is

sustained between the two electrodes and the electrolyte, no charge transfer occurs. In the

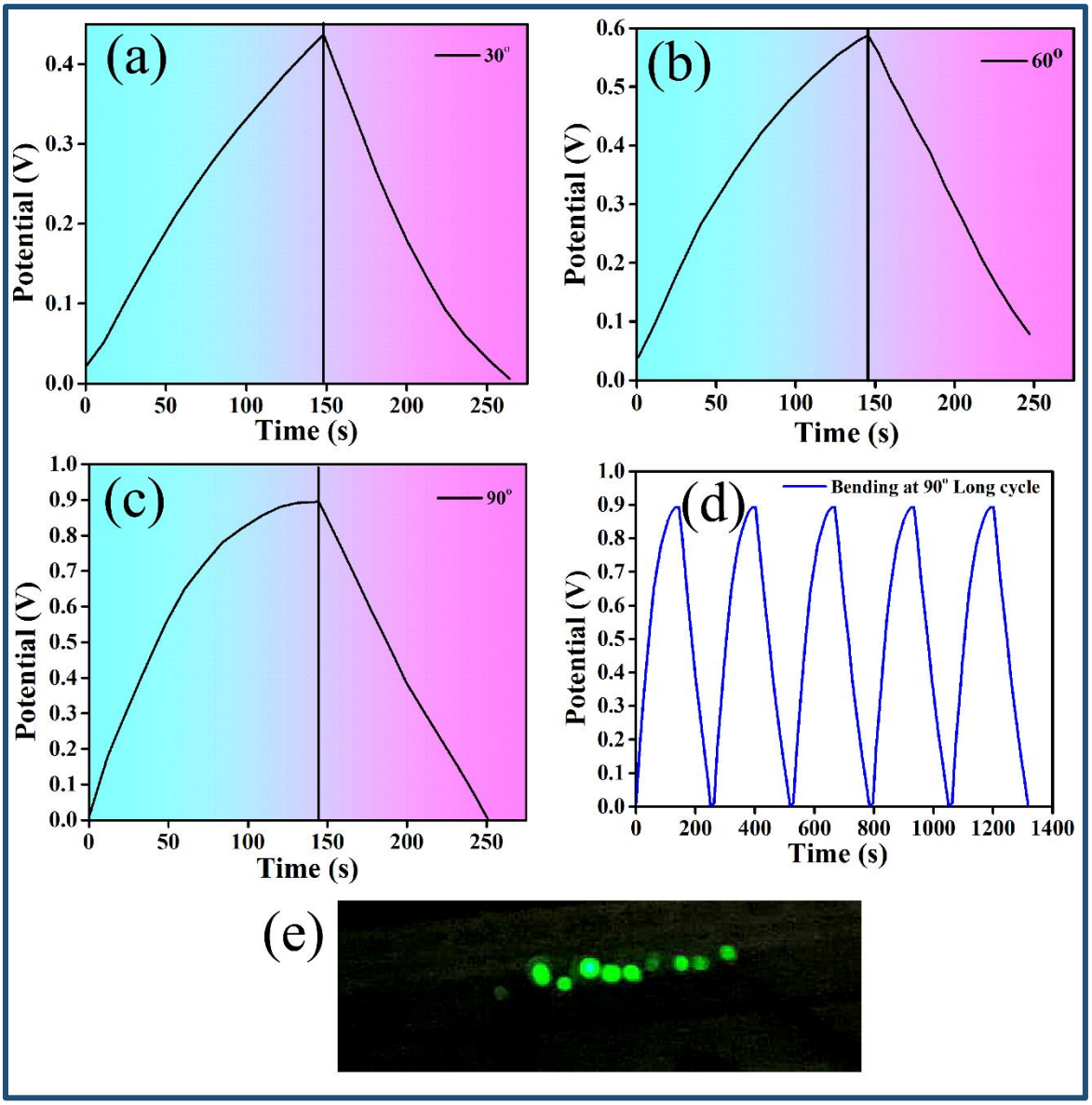

Fig. 9.11. Self-charging properties of SCPS subjected to different bending angle (a) 30°, (b) 60°, (c) 90°, (d) Stability of the self-charging properties of the SCPS under the application of periodic bending at 90°. (e) The LEDs illuminated by SCPS.

presence of external pressure, the equilibrium gets disturbed giving rise to stress-driven potential across the piezo-separator. To compensate for this piezo-potential, cations (H^+) traverse towards the negative electrode through the piezo-active separator. Consequently, the faradic or redox reaction occurs at the surface of both electrodes to attain the chemical equilibrium condition. A reduction reaction occurs at the negative $NdMnO_3$ electrode owing to the insertion of H^+ ions that leads to the accumulation of positive charges at the negative electrode. On the other hand, an oxidation reaction occurs at the positive electrode due to the reduction of H^+ ions which leads to the gathering of free electrons at the interface of positive

electrodes. When the applied pressure is removed, the piezoelectric properties of the separator

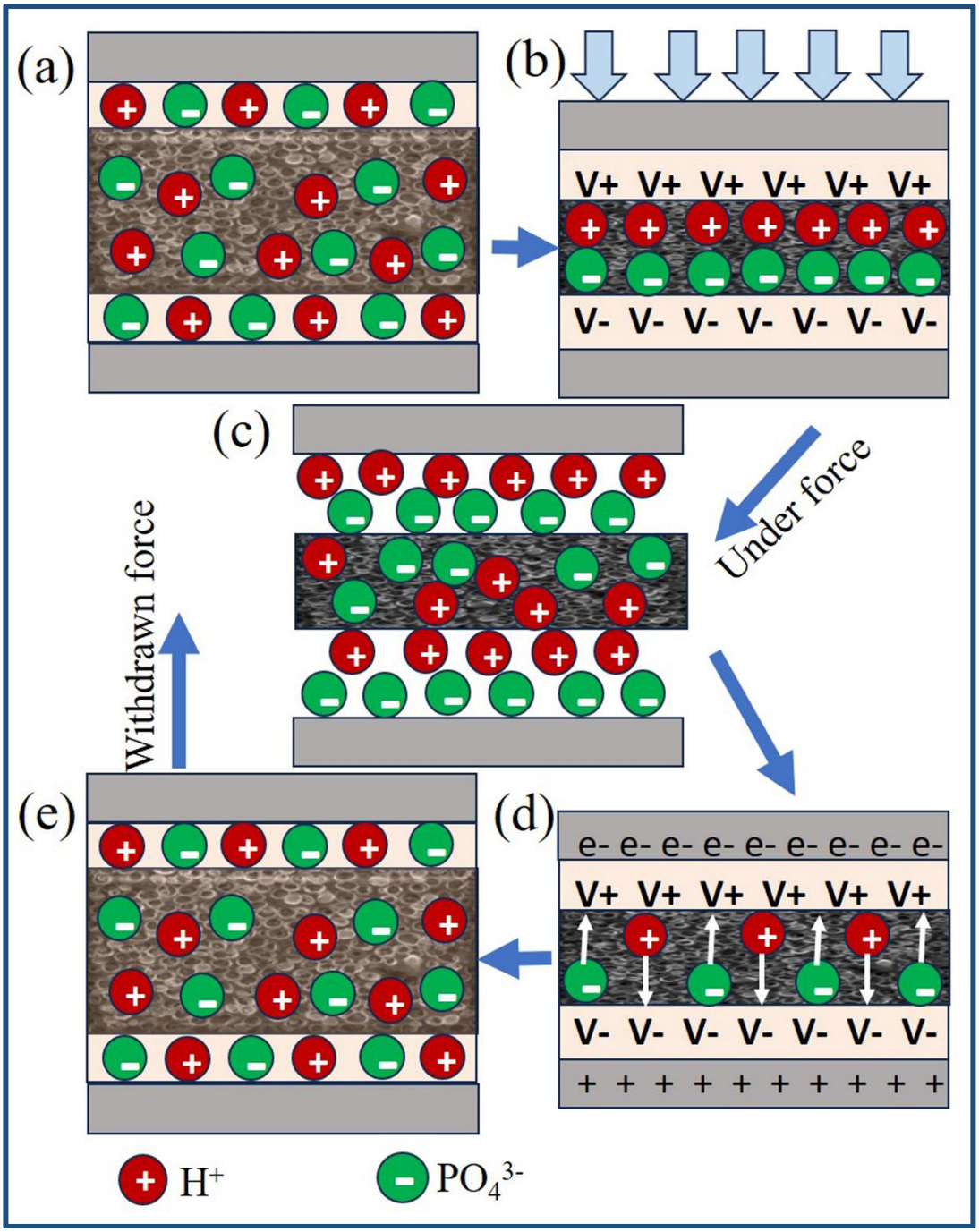

Fig. 9.12. Schematic diagram of the working mechanism of SCPS (a) The original state of SCPS in absence of any applied force. (b) Piezoelectric potential generated by the separator under the influence of external force initiating the electrolyte ion migration. (c) Migration of H^+ and PO_4^{3-} towards the electrodes. (d) An equilibrium state has been achieved between the piezoelectric potential generated and the electrochemical reaction. (e) Withdrawn of external force and piezoelectric potential disappears in the SCPS.

vanish and hence the electrolyte ions are re-distributed uniformly throughout the electrode surface to maintain the equilibrium. In this way, the conversion of mechanical energy to

electrochemical energy takes place. The entire mechanism is illustrated in Fig. 9.12 using a schematic diagram.

9.5. Conclusion

An integrated self-charging piezoelectric nanogenerator is designed using $NdMnO_3$@PVDF composite films and PVA/H_3PO_4 layer to harvest and store energy in a sole unit. The piezoelectric contribution of the $NdMnO_3$@PVDF composite films is estimated from the XRD and FTIR analysis which indicates the significantly enhanced crystallinity and electroactive content of the films owing to the interaction between the nanofiller and the polymer. Variation of $NdMnO_3$ nanoparticles content in the composite reveals that the composite with 7 wt % (w/w) of $NdMnO_3$ viz. NMO_7 achieves the highest crystallinity (~86.67 %) and is found to be the most electro-active film (~89.71 %) among all the prepared films. The fabricated NNG_7 exhibits appreciably high mechano-sensitivity and remarkably high V_{OC} and I_{SC} under free hand hammering. The outstanding stability of the concerned NG under water and striking responses under the application of various low forces ensures its potential application as a mechanical energy harvester. The adequate power generation indicates the usefulness of the device as a power source to run various low-powered devices. It is noteworthy that the non-toxicity of the designed NG meets the eco-friendly need. Moreover, NMO_7 exhibited its efficacy as a promising piezo catalyst that is reusable. The fabricated piezoelectric supercapacitor exhibits 41.37 mF cm^{-2} areal capacitance with 99% capacitance retention even after 2000 cycles. Hopefully, this study will help to show a promising window to fabricate self-powered and self-charging sustainable power sources and storage devices.

References

[1] S. Bairagi, S. Ghosh, S.W. Ali, A fully sustainable, self-poled, bio-waste based piezoelectric nanogenerator: electricity generation from pomelo fruit membrane, Sci. Rep. 10 (2020) 12121. https://doi.org/10.1038/s41598-020-68751-3.

[2] K. Krishnamoorthy, P. Pazhamalai, V.K. Mariappan, S.S. Nardekar, S. Sahoo, S. Kim, Probing the energy conversion process in piezoelectric-driven electrochemical self-charging supercapacitor power cell using piezoelectrochemical spectroscopy, Nat. Commun. 11 (2020) 2351. https://doi.org/10.1038/s41467-020-15808-6.

[3] A.P. Cohn, W.R. Erwin, K. Share, L. Oakes, A.S. Westover, R.E. Carter, R. Bardhan, C.L. Pint, All Silicon Electrode Photocapacitor for Integrated Energy Storage and Conversion, Nano Lett. 15 (2015) 2727–2731. https://doi.org/10.1021/acs.nanolett.5b00563.

[4] P. Pazhamalai, K. Krishnamoorthy, V.K. Mariappan, S. Sahoo, S. Manoharan, S.-J. Kim, A High Efficacy Self-Charging MoSe 2 Solid-State Supercapacitor Using Electrospun Nanofibrous Piezoelectric Separator with Ionogel Electrolyte, Adv. Mater. Interfaces. 5 (2018) 1800055. https://doi.org/10.1002/admi.201800055.

[5] S. Mondal, S. Thakur, S. Maiti, S. Bhattacharjee, K.K. Chattopadhyay, Self-Charging Piezo-Supercapacitor: One-Step Mechanical Energy Conversion and Storage, ACS Appl. Mater. Interfaces. 15 (2023) 8446–8461. https://doi.org/10.1021/acsami.2c17538.

[6] W. Wu, S. Bai, M. Yuan, Y. Qin, Z.L. Wang, T. Jing, Lead Zirconate Titanate Nanowire Textile Nanogenerator for Wearable Energy-Harvesting and Self-Powered Devices, ACS Nano. 6 (2012) 6231–6235. https://doi.org/10.1021/nn3016585.

[7] S. Dussan, A. Kumar, J.F. Scott, R.S. Katiyar, Effect of electrode resistance on dielectric and transport properties of multiferroic superlattice: A Impedance spectroscopy study, AIP Adv. 2 (2012) 032136. https://doi.org/10.1063/1.4746026.

[8] S. Kumari, N. Ortega, D.K. Pradhan, A. Kumar, J.F. Scott, R.S. Katiyar, Effect of thickness on dielectric, ferroelectric, and optical properties of Ni substituted Pb(Zr0.2Ti0.8)O3 thin films, J. Appl. Phys. 118 (2015) 184103. https://doi.org/10.1063/1.4935481.

[9] N. Ortega, A. Kumar, P. Bhattacharya, S.B. Majumder, R.S. Katiyar, Impedance spectroscopy of multiferroic $PbZr_xTi_{1-x}O_3$ Õ$CoFe_2O_4$ layered thin films, Phys. Rev. B. 77 (2008) 014111. https://doi.org/10.1103/PhysRevB.77.014111.

[10] C. Huang, J. Song, W. Lee, Y. Ding, Z. Gao, Y. Hao, L.-J. Chen, Z.L. Wang, GaN Nanowire Arrays for High-Output Nanogenerators, J. Am. Chem. Soc. 132 (2010) 4766–4771. https://doi.org/10.1021/ja909863a.

[11] H. Parangusan, D. Ponnamma, M. Al Ali AlMaadeed, Flexible tri-layer piezoelectric nanogenerator based on PVDF-HFP/Ni-doped ZnO nanocomposites, RSC Adv. 7

(2017) 50156–50165. https://doi.org/10.1039/C7RA10223B.

[12] C. Chang, V.H. Tran, J. Wang, Y.-K. Fuh, L. Lin, Direct-Write Piezoelectric Polymeric Nanogenerator with High Energy Conversion Efficiency, Nano Lett. 10 (2010) 726–731. https://doi.org/10.1021/nl9040719.

[13] S. Ippili, V. Jella, J. Kim, S. Hong, S. Yoon, Enhanced piezoelectric output performance via control of dielectrics in Fe^{2+}-incorporated $MAPbI_3$ perovskite thin films: Flexible piezoelectric generators, Nano Energy. 49 (2018) 247–256. https://doi.org/10.1016/j.nanoen.2018.04.031.

[14] S. Mondal, T. Paul, S. Maiti, B.K. Das, K.K. Chattopadhyay, Human motion interactive mechanical energy harvester based on all inorganic perovskite-PVDF, Nano Energy. 74 (2020) 104870. https://doi.org/10.1016/j.nanoen.2020.104870.

[15] H. He, Y. Fu, T. Zhao, X. Gao, L. Xing, Y. Zhang, X. Xue, All-solid-state flexible self-charging power cell basing on piezo-electrolyte for harvesting/storing body-motion energy and powering wearable electronics, Nano Energy. 39 (2017) 590–600. https://doi.org/10.1016/j.nanoen.2017.07.033.

[16] S. Sahoo, K. Krishnamoorthy, P. Pazhamalai, V.K. Mariappan, S. Manoharan, S. Kim, High performance self-charging supercapacitors using a porous PVDF-ionic liquid electrolyte sandwiched between two-dimensional graphene electrodes, J. Mater. Chem. A. 7 (2019) 21693–21703. https://doi.org/10.1039/c9ta06245a.

[17] A. Rasheed, W. He, Y. Qian, H. Park, D.J. Kang, Flexible Supercapacitor Type Rectifier-free Self-charging Power Unit Based on a Multifunctional PVDF-ZnO-RGO Piezoelectric Matrix, ACS Appl. Mater. Interfaces. 12 (2020) 20891–20900. https://doi.org/10.1021/acsami.9b22362.

[18] D. Sahoo, A.K. Karan, N.B. Manik, Influence of SWCNT on the Electrical Behavior of an Environmentally Friendly $CH_3NH_3SnI_3$ Perovskite-Based Optoelectronic Schottky Device, ACS Appl. Electron. Mater. (2023). https://doi.org/10.1021/acsaelm.3c00086.

[19] S. Saha, S. Chanda, A. Dutta, T.P. Sinha, Dielectric relaxation of NdMnO3 nanoparticles, Mater. Res. Bull. 48 (2013) 4917–4923. https://doi.org/10.1016/j.materresbull.2013.07.027.

[20] S. Yáñez-Vilar, A. Castro-Couceiro, B. Rivas-Murias, A. Fondado, J. Mira, J. Rivas, M.A. Señarís-Rodríguez, Study of the Dielectric Properties of the Perovskite $LaMn_{0.5}Co_{0.5}O_{3-\delta}$, Zeitschrift Für Anorg. Und Allg. Chemie. 631 (2005) 2265–2272. https://doi.org/10.1002/zaac.200570055.

[21] N. Giri, B.S. Biswas, P. Sengupta, R. Ray, Exchange bias and magnetic memory effect in hole doped $Nd_{0.78}Sr_{0.22}CoO_3$ nanoparticles, RSC Adv. 12 (2022) 26470–26475. https://doi.org/10.1039/D2RA04454D.

[22] K. De, R. Ray, R. Narayan Panda, S. Giri, H. Nakamura, T. Kohara, The effect of Fe substitution on magnetic and transport properties of $LaMnO_3$, J. Magn. Magn. Mater. 288 (2005) 339–346. https://doi.org/10.1016/j.jmmm.2004.09.118.

[23] V. Jella, S. Ippili, J.-H. Eom, J. Choi, S.-G. Yoon, Enhanced output performance of a flexible piezoelectric energy harvester based on stable $MAPbI_3$-PVDF composite films, Nano Energy. 53 (2018) 46–56. https://doi.org/10.1016/j.nanoen.2018.08.033.

[24] Y. Zhou, W. Liu, B. Tan, C. Zhu, Y. Ni, L. Fang, C. Lu, Z. Xu, Crystallinity and β Phase Fraction of PVDF in Biaxially Stretched PVDF/PMMA Films, Polymers (Basel). 13 (2021) 998. https://doi.org/10.3390/polym13070998.

[25] H. Parangusan, D. Ponnamma, M.A.A. Al-Maadeed, Stretchable Electrospun PVDF-HFP/Co-ZnO Nanofibers as Piezoelectric Nanogenerators, Sci. Rep. 8 (2018) 754. https://doi.org/10.1038/s41598-017-19082-3.

[26] M.M. Abolhasani, S. Azimi, H. Fashandi, Enhanced ferroelectric properties of electrospun poly(vinylidene fluoride) nanofibers by adjusting processing parameters, RSC Adv. 5 (2015) 61277–61283. https://doi.org/10.1039/C5RA11441A.

[27] N. Soin, T.H. Shah, S.C. Anand, J. Geng, W. Pornwannachai, P. Mandal, D. Reid, S. Sharma, R.L. Hadimani, D.V. Bayramol, E. Siores, Novel "3-D spacer" all fibre piezoelectric textiles for energy harvesting applications, Energy Environ. Sci. 7 (2014) 1670–1679. https://doi.org/10.1039/C3EE43987A.

[28] P. Sengupta, P. Sadhukhan, A. Ray, R. Ray, S. Bhattacharyya, S. Das, Temperature and frequency dependent dielectric response of $C_3H_7NH_3PbI_3$: A new hybrid perovskite, J. Appl. Phys. 127 (2020) 204103. https://doi.org/10.1063/1.5142810.

[29] P. Sengupta, R. Ray, Tailoring of dielectric and transport properties of $C_3H_7NH_3PbI_xBr_{3-x}$, Mater. Lett. 302 (2021) 130456. https://doi.org/10.1016/j.matlet.2021.130456.

[30] P. Sengupta, P. Sadhukhan, A. Ray, S. Mal, A. Singh, R. Ray, S. Bhattacharyya, S. Das, Influence of activation energy on charge conduction mechanism and giant dielectric relaxation of sol-gel derived $C_3H_7NH_3PbBr_3$ perovskite; Act as high performing UV photodetector, J. Alloys Compd. 892 (2022) 162216. https://doi.org/10.1016/j.jallcom.2021.162216.

[31] P. Sengupta, P. Sadhukhan, S. Saha, S. Das, R. Ray, Improved Energy Harvesting Ability of $C_3H_7NH_3PbI_3$ Decorated Pvdf Nanofiber Based Flexible Nanogenerator, Nano Energy. 109 (2023) 108277. https://doi.org/10.2139/ssrn.4249647.

[32] I. Kim, H. Roh, J. Yu, N. Jayababu, D. Kim, Boron Nitride Nanotube-Based Contact Electrification-Assisted Piezoelectric Nanogenerator as a Kinematic Sensor for Detecting the Flexion–Extension Motion of a Robot Finger, ACS Energy Lett. 5 (2020) 1577–1585. https://doi.org/10.1021/acsenergylett.0c00451.

[33] S.K. Ghosh, D. Mandal, High-performance bio-piezoelectric nanogenerator made with fish scale, Appl. Phys. Lett. 109 (2016) 103701. https://doi.org/10.1063/1.4961623.

[34] A. Mondal, N. Giri, S. Sarkar, S. Majumdar, R. Ray, Tuning the photocatalytic activity of ZnO by TM (TM = Fe, Co, Ni) doping, Mater. Sci. Semicond. Process. 91 (2019) 333–340. https://doi.org/10.1016/j.mssp.2018.12.003.

[35] S. Sarkar, N. Giri, A. Mondal, S. Sarkar, R. Ray, Enhanced photocatalytic activity and enormous dielectricity of α-Fe_2O_3/reduced graphene oxide nanocomposites, Indian J. Phys. 93 (2019) 449–458. https://doi.org/10.1007/s12648-018-1308-z.

[36] A. Ray, A. Roy, M. Ghosh, J. Alberto Ramos-Ramón, S. Saha, U. Pal, S.K. Bhattacharya, S. Das, Study on charge storage mechanism in working electrodes fabricated by sol-gel derived spinel $NiMn_2O_4$ nanoparticles for supercapacitor application, Appl. Surf. Sci. 463 (2019) 513–525. https://doi.org/10.1016/j.apsusc.2018.08.259.

10. General Conclusion

In recent years, renewable energy harvesting is not an option, it has been the ultimate future to maintain sustainability. Collecting abundant mechanical energy from the ambiance and converting it to an electrical signal is one of the finest options to run a large number of microelectronics that require low power to operate. Besides mechanical energy, solar energy is another important renewable source that can be acquired in the maximum portions of the earth. It is now in trend to hybridize two or more energy harvesting units in a sole unit to develop a multifaceted, self-powered, portable, and wearable device to perform in a wide horizon that can harvest more than one energy simultaneously or separately. While talking about solar energy harvesting, OIHPs have gained immense attention worldwide owing to their exciting photovoltaic property, tunable band gap, long carrier charge diffusion length, simple synthesis processes, etc. Rare earth oxide perovskites have also been well explored for years in different domains and are an integral option for energy harvesting owing to the high dielectric constant hence polarization, excellent stability, catalytic properties, etc. PVDF is one of the most popular ferroelectric polymers due to its cost-effectiveness, easy synthesis process, and flexibility. The inclusion of appropriate filler such as perovskite materials can enhance the ferroelectric phase content, and degree of crystallinity to an appreciable extent. Generally, an energy system comprises an energy harvesting unit, a power controlling system, and a storage unit. Energy storage is another global concern today to power devices anywhere and everywhere, irrespective of weather, and time. Therefore, it would be very convenient if we integrate energy harvesting and storage units in a single device.

In this thesis work, we have prepared organic-inorganic hybrid perovskite propylammonium lead halide ($C_3H_7NH_3PbX_3$, X = I, Br) via sol-gel method. We got the structural confirmation of the samples from XRD analysis. Despite being popular due to their interesting properties such as easy synthesis process, low expense, high carrier diffusion length, tunable band gap, and appreciable photovoltaic properties, these hybrid perovskites face stability issues in the presence of moisture, high temperature, and UV irradiation that harness the practical implementation of these perovskites in large scale. We have investigated the stability of $C_3H_7NH_3PbI_3$ in moisture ambiance by keeping the bare $C_3H_7NH_3PbI_3$ in saturated NaCl solution for 168 hours. We have found no detectable change in the XRD peaks after 168

hours that ensures the significant stability of this perovskite. $C_3H_7NH_3PbI_3$ possesses an optimal band gap of ~ 2.38 eV that has been calculated from the absorbance peak using the Tauc plot. The extensive study on dielectric properties of the sample over 10 Hz ≤ f ≤ 8 MHz for 273 K ≤ T ≤ 373 K was measured. The contribution of grain and grain boundary over the total impedance was evaluated. The grain and grain boundary resistance is found to decrease with the temperature rise. The asymmetrical behavior of the imaginary part of the electric modulus implies the non-Debye type nature of the sample. From the fitting of the Kohlrausch–Williams–Watts function, it is observed that the non-Debye nature shifts to the Debye type with the rise in temperature.

$C_3H_7NH_3PbBr_3$ which possesses a wide bandgap of ~ 3 eV is also very stable as can be concluded from the DSC thermograph. Despite being stable in high temperatures, this perovskite is also very stable in UV illumination. We have fabricated a UV photodetector using this perovskite as light absorption material. A comparative study on the dielectric properties of both the aforesaid perovskites was performed. It has been observed that $C_3H_7NH_3PbBr_3$ exhibits a giant dielectric constant at room temperature. The AC conductivity is observed to be appreciably high in elevated temperatures. The ionic conduction that plays an important role in the conductivity of the sample has been analyzed by Jonscher's power law. The influence of the activation energy on ionic conduction has been analyzed in detail.

To harvest mechanical energy, we have incorporated $C_3H_7NH_3PbI_3$ in PVDF in different proportions (3.21, 4.76, 6.20 wt %) to produce nanofiber by the method of electrospinning. It has been observed that 4.76 wt% $C_3H_7NH_3PbI_3$ decorated PVDF nanofiber (PANF (4.76)) exhibits the highest electroactive phase content ~ 92.5 % with superior crystallinity ~ 78.8 % among the nanofibers of all concentrations. In contrast, neat PVDF nanofiber (PVNF) possesses electroactive phase content as low as ~ 74.5 % with crystallinity of ~ 62.6 %. Moreover, the remarkably reduced diameter of the nanofiber on the inclusion of 4.76 wt % $C_3H_7NH_3PbI_3$ suggests the significant formation of polarized β phase within the polymer matrix. The optical and elastic properties of the prepared nanofiber are analyzed in detail. The computed band gap of PANF (4.76) ~ 2.2 eV ensures that the perovskite retains its intrinsic properties even in the nanofiber. The melting point of the composite nanofiber is increased effectively due to the presence of the perovskite that has been concluded from the DSC thermograph. We have performed a comparative study on the performance of the fabricated piezoelectric nanogenerators (PNGs) using PANF (4.76) and PVNF (named PANG (4.76) and PVNG, respectively). The lightweight, flexible, durable, cost-effective, self-powered PANG

(4.76) is observed to generate 60 V open circuit voltage, 27.5 μA short circuit current, and 9.81 mW/m^2 power under periodic hammering with a free hand. The generated power is enough to glow up several green and blue LEDs. Moreover, the power output was stored in commercially available capacitors that were further used to run a digital wristwatch. The output response of the device under the influence of various forces is detected. The concerned device demonstrates significant mechano-sensitivity that assures its potential as IoTs and wearable sensors. The optimal energy band gap of the aforesaid composite confirms its efficacy as a piezo-active photodetector. Hence, we can design a multifaceted device using the proposed composite that can harvest both mechanical and solar energy separately or simultaneously.

Next, we prepared self-poled piezoelectric films using $C_3H_7NH_3PbI_3$ and PVDF (5, 10, 15, 20 wt %). The inclusion of $C_3H_7NH_3PbI_3$ in 15 wt% in PVDF produces significant enhancement of degree of crystallinity ~ 88 % and ferroelectric phase content ~ 86 % within the film. The melting point of the composite is also effectively improved. Moreover, the elastic and optical property of the film ensures its flexibility as well as its optical capability to be used in optoelectronic devices. The porosity of the films induces self-polarization and hence improves the transformation of β phase content. This composite was employed in the fabrication of a piezoelectric energy harvester (PPEH_15) that generated ~ 80 V V_{OC} and 17.8 $\mu A/cm^2$ J_{SC} under hammering with a free hand and the obtained outcome is substantially high compared to that of a PEH made of neat PVDF. Finally, the photo-active piezo response of the photodetector made of the aforesaid composite was remarkable enough to serve the photo-detecting purpose.

Next, we have synthesized lead-free oxide perovskite $NdMnO_3$ nanoparticles through sol-gel method. The structural confirmation and surface morphology was obtained from XRD and FESEM analysis. $NdMnO_3$ nanoparticles are embedded in PVDF in different volume fractions (3, 5, 7, and 10 wt %) to prepare self-poled, porous films. The loading of 7 wt % $NdMnO_3$ nanoparticles within PVDF results in significant enhancement of β phase formation ~ 89.71 % which assures its utility in the field of wearable sensors and IoTs. The aforesaid $NdMnO_3$ decorated PVDF film affirms itself as a promising piezocatalyst in the dark to degrade dye effectively. We have designed ultra-sensitive hybrid piezoelectric-triboelectric nanogenerators that are fabricated using $NdMnO_3$ decorated PVDF films and PDMS that exhibit V_{OC} as high as 160 V. The sole contribution of piezoelectric effect was isolated by designing piezoelectric nanogenerator that produced 50 V V_{OC} and 30 μA I_{SC} under free hand hammering. The generated power is adequate to glow up several green and blue LEDs. The

sufficient power generation of the piezo generator confirms its efficacy as a potential power source. Interestingly, the device shows excellent stability even in water medium. We have fabricated an integrated self-powered self-charging piezoelectric supercapacitor using $NdMnO_3$@PVDF composite films to harvest and store energy in a sole unit. The composite film is used as a piezo-active separator in the integrated device that yields 41.37 mF cm^{-2} areal capacitance with 99% capacitance retention even after 2000 cycles.

Payal Sengupta
02.05.2024